FACULTY
OF MATHEMATICS
AND PHYSICS
Charles University

DOCTORAL THESIS

Mgr. Alžbeta Kuižová

Drop coating deposition Raman spectroscopy of biologically important molecules

Institute of Physics of Charles University

Supervisor of the doctoral thesis:	RNDr. Eva Kočišová, Ph.D.
Study programme:	Biophysics, Chemical and Macromolecular Physics

Prague 2024

I declare that I carried out this doctoral thesis on my own, and only with the cited sources, literature and other professional sources. I understand that my work relates to the rights and obligations under the Act No. 121/2000 Sb., the Copyright Act, as amended, in particular the fact that the Charles University has the right to conclude a license agreement on the use of this work as a school work pursuant to Section 60 subsection 1 of the Copyright Act.

In Prague, September 2, 2024 Alžbeta Kuižová

Firstly, I would like to express my deep gratitude to my supervisor, RNDr. Eva Kočišová, Ph.D., whose knowledge, guidance, and encouragement have been invaluable for my research and writing of the thesis. I am thankful to my advisor, prof. RNDr. Marek Procházka, Ph.D., for his insights, approach, and many discussions.

I would like to thank doc. RNDr. Ondřej Kylián, Ph.D. and Anna Kuzminova, Ph.D., both from the Department of Macromolecular Physics, for the preparation and fabrication of a variety of substrates and for their cooperation. My thanks belong to Dr. Franck Sureau for a nice collaboration and Dr. Sergei G. Kruglik for sharing his high level of expertise in Raman tweezer microspectroscopy and for discussions during my research stay in Paris (both from Sorbonne Université, Laboratory Jean Perrin).

Many thanks belong to the entire Division of Biomolecular Physics at the Institute of Physics of Charles University, especially to doc. RNDr. Peter Mojzeš, CSc., RNDr. Václav Profant, Ph.D. and the fellow Ph.D. student Mgr. Štěpán Jílek, for many fruitful discussions and cooperation.

I would like to thank my family for their endless support and always believing in me, as well as all my friends who encouraged me in my journey. Above all, I would like to thank my partner Rado, whose support and understanding have been my constant source of motivation.

Title: Drop coating deposition Raman spectroscopy of biologically important molecules

Author: Mgr. Alžbeta Kuižová

Department: Institute of Physics of Charles University

Supervisor: RNDr. Eva Kočišová, Ph.D., Institute of Physics of Charles University

Abstract: The thesis addresses various applications of drop coating deposition Raman (DCDR) spectroscopy. The first part tackles the capability of detecting agricultural (thiram, bentazon, picloram) and food (melamine) contaminants. Moreover, the detection of melamine from intentionally blended real infant formula was investigated. It was demonstrated that for successful detection, not only the pre-concentration, but also the spatial segregation of compounds together with potential interaction between them could be crucial. DCDR was shown to be a powerful yet simple approach for detecting contaminants. The second part deals with DCDR application for studies of dried phospholipids. It includes the discussion of drying dynamics of liposomal suspension droplet, comparing dried patterns (smooth/nanostructured substrate, homogeneous/non-homogeneous suspension) and analysing the difference between DCDR spectra and Raman spectra acquired directly from suspension (Raman tweezer microspectroscopy). Finally, conformational changes in the dried deposit triggered by heating (the thermotropic behaviour) or by drying at different relative humidity were monitored. DCDR showed great potential to contribute to the investigation of fundamental properties of biomolecules in the absence of water. As straightforward as the method is, it provides valuable information, combining the analysis of the drying process and the observation of the dried pattern with detailed spectroscopic study by Raman spectroscopy.

Keywords: Raman spectroscopy, drop coating deposition Raman (DCDR), hydrophobic substrate, drying dynamics, contaminant, phospholipid, phase transition

Název práce: Ramanova spektroskopie kapkově nanášených povlaků biologicky významných molekul

Autor: Mgr. Alžbeta Kuižová

Katedra: Fyzikální ústav UK

Vedoucí dizertační práce: RNDr. Eva Kočišová, Ph.D., Fyzikální ústav UK

Abstrakt: Práce se zabývá různými aplikacemi Ramanovy spektroskopie kapkově nanášených povlaků (DCDR). První část je věnována detekci jednoho potravinového (melamin) a tří zemědělských (thiram, bentazon, picloram) kontaminantů. Melamin jsme dále zkoušeli detekovat i ze záměrně kontaminovaného vzorku kojenecké výživy. Pro úspěšnou detekci se jako rozhodující ukázalo nejen zakoncentrování, ale také prostorové vydělení a potenciální interakce složek ve vzorku. Ukázali jsme, že DCDR je jednoduchá, ale zároveň účinná metoda pro detekci kontaminantů. Druhá část se zabývá aplikací DCDR ke studiu vyschlých fosfolipidů. To zahrnuje diskusi o dynamice schnutí kapky lipozomální suspenze, srovnání vyschlých depositů (na hladkém/nanostrukturovaném substrátu, schnutí homogenní/nehomogenní suspenze) a analýzu rozdílu mezi DCDR spektrem a Ramanovým spektrem získaným přímo ze suspenze (Ramanova pinzeta). Následně byly pozorovány konformační změny vyschlých fosfolipidů vyvolané zahříváním (termotropní chování) nebo sušením při různých relativních vlhkostech. Metoda DCDR ukázala, že má velký potenciál přispět ke zkoumání základních vlastností biomolekul v nepřítomnosti vody. Jakkoli je metoda přímočará, poskytuje cenné informace, přičemž umožňuje kombinovat analýzu procesu schnutí a pozorování vyschlého depositu s jeho detailním spektrálním rozborem pomocí Ramanovy spektroskopie.

Klíčová slova: Ramanova spektroskopie, metoda kapkově nanášených povlaků (DCDR), hydrofobní povrch, dynamika schnutí, kontaminant, fosfolipid, fázový přechod

Contents

1 Introduction

The phenomenon of inelastic light scattering, Raman scattering (RS), attracts wide attention in the field of chemical and biological analysis. RS spectroscopy is an essential non-invasive technique that carries fingerprint information extracted from recorded Raman spectra. For biological analysis (biologically important molecules and their complexes), RS spectroscopy benefits, in contrast to infrared (IR) spectroscopy, from the minimal interference from water bands in the relevant fingerprint region. Contrarily, the serious drawback of RS is the weak cross-section when the maximum of the inelastically scattered photons is only one from about $10^5 - 10^7$. Thus, relatively highly concentrated samples (more than 1 mM) and large amounts of material (more than 1 μg) are needed to obtain a sufficient signal-to-noise ratio. Particularly for biological samples, these concentrations do not reach physiologically relevant concentrations. There are several options to improve the measured RS intensity enough to be sensitive and specific to detect and identify an analyte of interest at low concentrations.

The surface-enhanced Raman scattering (SERS) spectroscopy is a well-known approach profiting from electromagnetic enhancement in which the incident light induces localised surface plasmon resonance on the metallic plasmonic (mostly Ag, Au or Cu) nanostructures, producing huge enhancement of the Raman signal [1]. The second enhancing mechanism in SERS spectroscopy, which is nowadays widely studied, is a chemical enhancement, explained by photo-induced charge transfer between the adsorbed molecule and the substrate [2]. The SERS method has been significantly developed and is fruitfully used in various studies and applications [3]. However, applicability is not straightforward to any molecule and comes with spectral variations and problematic spectral reproducibility influenced by enhancement mechanisms and used substrates. Thus, an alternative method is presented here to broaden the measurement options and obtain improved Raman signal from low-concentrated solutions or suspensions. Drop coating deposition Raman (DCDR) scattering spectroscopy offers an intensity increase in the acquisition of classical (non-enhanced) Raman spectra [4, 5, 6].

1.1 Principle of drop coating deposition Raman (DCDR) spectroscopy

The DCDR method benefits from a simple process of solvent removal by evaporation from droplet deposited on a hydrophobic substrate. Subsequent analyte pre-concentration into dried patterns allows the acquisition of the classical Raman spectra from pre-concentrated locations (Figure 1.1). The dried patterns can have different forms, such as coffee-ring, small spots or crystals, as will be further discussed. After droplet deposition and completion of evaporation, the substrate with a dried pattern is placed under a microscope objective, where the Raman spectrum is measured. To obtain a spectrum with a high signal-to-noise ratio, a small initial volume of the low-concentrated sample is sufficient. This approach improves sensitivity by several orders of magnitude compared to normal

Raman measurement from solution or suspension [7]. Moreover, Raman spectral mapping can be used to investigate the possible spatial separation of a solution´s constituents and analyse the impact of the drying process on analyte properties in the dried state and potential variations in acquired spectra. The starting point for the method development was very likely the observation of a simple process of drying the spilled liquid drop of coffee (generally droplets containing insoluble particles). The primary mechanism was first more precisely described by Deegan in 1997 [8]. The phenomenon where coffee, initially dispersed over the entire drop volume, becomes, after drying, pre-concentrated into a ring pattern is known as a coffee-ring effect.

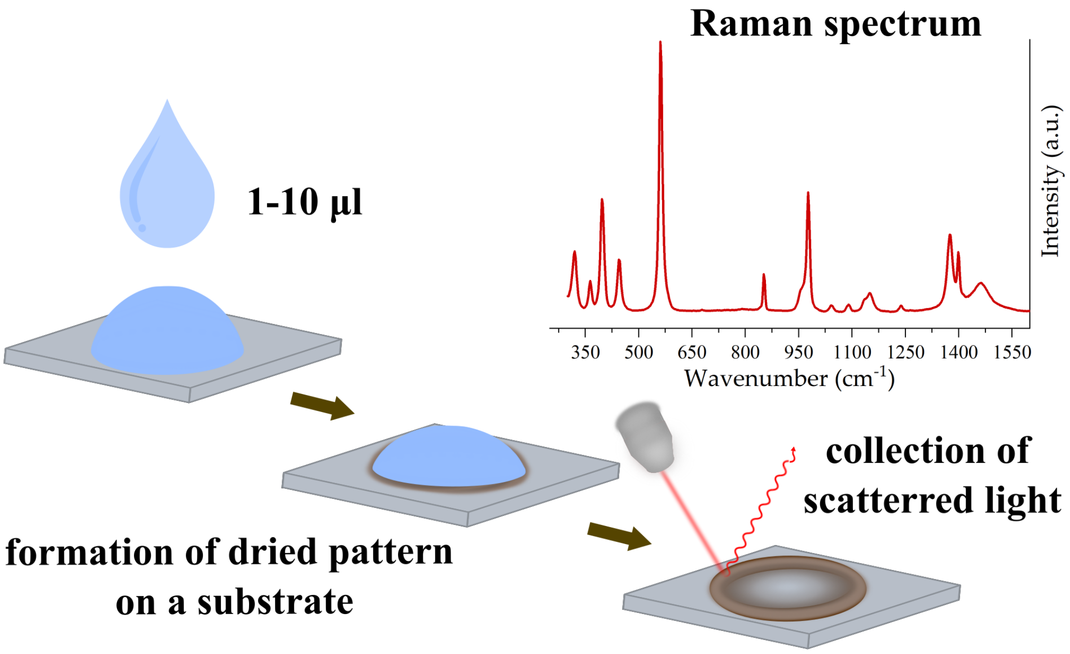

Figure 1.1 The principle of the DCDR method: deposition of a droplet of low-concentrated liquid sample on a hydrophobic (solvophobic) substrate followed by solvent evaporation. The classical Raman spectrum is collected from the formed, dried pattern.

1.2 Formation of dried pattern

Deegan and colleagues stated that capillary flow in drying droplet with pinned contact line on the surface ensures that liquid evaporated from the edges is replenished by liquid from the interior. Outward flow in the drying droplet is thus responsible for carrying dispersed material to the droplet edges to form the coffee-ring dried pattern, as observed for coffee [8]. The mentioned mechanism was assumed to be independent of the used substrate, solvents or deposited solids (solutes) and was explained by only geometrical constraints such as a free surface limited by a pinned contact line. On the other hand, the authors admitted that additional effects not considered in their calculations could significantly modify the deposition pattern [9]. For example, vertical mixing, viscous stresses, solute interaction, diffusion (for smaller solute particles), sedimentation (for larger solute particles) or Marangoni effects were not included. Since then, a number of studies have been conducted to investigate the drying phenomena experimentally with the aim of controlling the morphology of dried patterns after solvent evaporation, although often with no straightforward theoretical explanation [10, 11, 12, 13]. The pattern formation during free drying of a deposited droplet is an intricated process influenced by numerous ways such as solute concentration [14, 15], solute particle size and shape [16], ionic strength [17, 18], different solute mixtures [19], environmental conditions (temperature, pressure, humidity) [20, 21], substrate properties including its temperature, hydrophobicity or roughness [15, 22, 23, 24].

The Marangoni effect, when surface tension gradients drive the additional flow at the liquid-gas interface, is often studied and discussed [13]. The surface tension is typically altered by the nonuniform distribution of solute concentration or temperature variation along the interface or by adding surfactants, which substantially decrease the liquid surface tension [25, 26]. Marangoni flow can overcome the coffee-ring effect to promote spot pre-concentration to the central part of the deposited droplet. In this way, a small spot-like or spot-inside-ring pattern can be formed [13]. However, heating the liquid or adding surfactants is often not a possibility for most biological samples. Generally, the formation of dried patterns, including coffee-ring, often challenges the performance of relevant industrial production processes. Across diverse fields (inkjet printing, biological assays, coatings), there is a high demand for uniform dried patterns, and the question remains how to achieve them. One of the solutions can be to work with a sufficiently high concentration, which is slightly higher than the theoretical concentration for filling the wetted contact area of the deposited droplet [27]. In addition, variation in solution pH modifies the particle-particle and particle-substrate interactions and then, for optimal value, also leads to a uniformly dried pattern [17]. Another outcome of the drying process of small droplets can be analyte crystallization. Crystals are formed mainly from saline solutions but also from molecules susceptible to hydrogen bonding and $\pi - \pi$ interactions. The final dried pattern is composed of small crystals and is influenced not only by initial concentration but also by complex droplet-substrate interactions such as substrate wettability and topological patterns on the substrate. Crystals can accumulate in a coffee-ring or in the centre of the dried droplet. The underlying mechanisms in crystal pattern formation are not fully understood, as there are difficulties in distinguishing the main components of these patterns by current analytical techniques [10, 28].

Generally, there is a wide spectrum of possibilities for dried patterns formed by particles on the substrate (Figure 1.2). The above-mentioned patterns include coffee-ring, spot-like patterns, uniform patterns, crystal patterns or others such as crack patterns, slick-slip patterns [29] or their combination [10]. Some studies also discussed the segregation potential of the evaporation process based on particle size [30]. It was shown that non-interacting particles formed concentric coffee-rings near the contact line with different diameters when the smallest particles were separated to the outermost ring and the biggest to the innermost ring. The separation resolution was strongly dependent on the initial concentrations of solutes, and a higher concentration implies a decrease in separation distance. To test the segregation capability of drying for biological samples, a mixture of fluorescently labelled antimouse IgG antibodies (< 10 nm), Escherichia coli (order of 500 nm), and fluorescently labelled murine B-lymphoma cells (WEHI-231) (order of 5 μm) was suspended in deionized water and left to dry, where the size-dependent separation was successfully demonstrated [30].

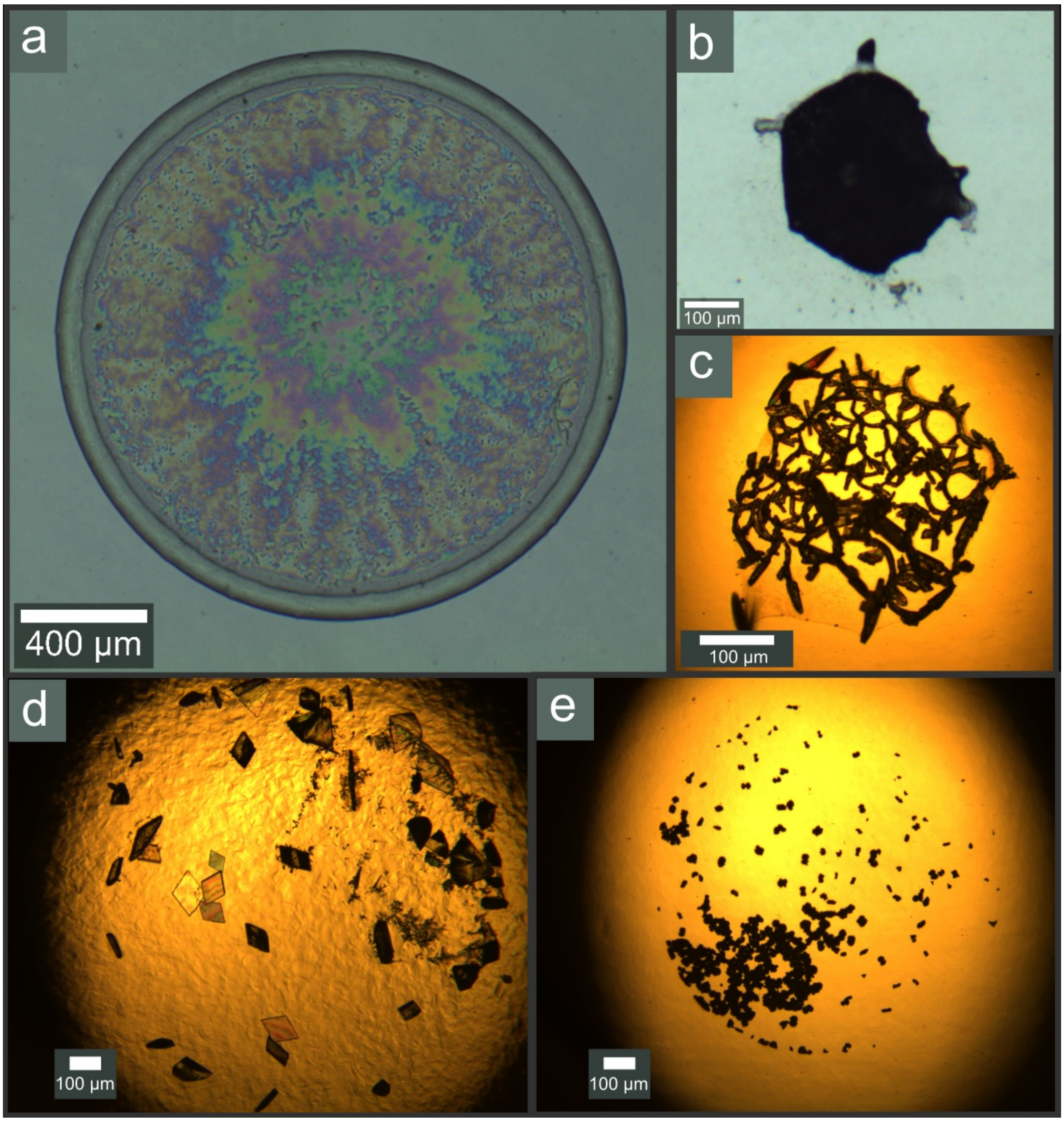

Figure 1.2 White light images of dried patterns of biomolecules and contaminants. (a) lipid dipalmitoylphosphatidylcholine (DPPC), 1 mg/ml, (b) lactose, 1.2 mg/ml, (c) bentazone, 0.5 mg/ml, (d) melamine, 2 mg/ml, (e) picloram, 0.5 mg/ml.

1.3 Substrates used in DCDR

Substrates, as an integral part of DCDR spectroscopy, play an important part in dried pattern formation. The minimal requirements for utilized substrates are low optical absorbance, high optical reflectance and no or minimal Raman signal in the region of interest. An additional relevant feature is substrate wettability, which is the ability of a liquid to maintain in contact with a solid surface. Wettability is characterised by a contact angle of the deposited liquid droplet (Figure 1.3A) and influences the final dried pattern and pre-concentration of the analyte [15].

Generally, the smaller the dried pattern, the better sample pre-concentration, which results in the Raman signal of higher intensity. Throughout DCDR development, various substrates (preferentially hydrophobic) were developed and tested, including two commercially produced:

- SpectRIM^{TM} substrate from Tienta Sciences based on polished stainless steel overcoated with a thin (50 nm) hydrophobic layer with contact angle for the water droplet of 122° (no more available).
- μ-RIM^{TM} stainless steel substrate from BioTools with a contact angle for the water droplet of 108°. This highly reflective surface has no detectable Raman or IR background signal (still available).

Multiple non-commercial substrates with contact angles in the range of about 80°- 120° include polished CaF_2 slides, silanized glass platforms, quartz slides, gold foil, aluminium foil, thiol-modified gold-coated glass, and polytetrafluoroethylene (PTFE) tape. A specific class of hydrophobic substrates are smooth fluorocarbon surfaces produced using a fully solvent-free plasma-based deposition with radio frequency magnetron sputtering of PTFE target, so-called PTFE substrates. We showed that the DCDR performance of the PTFE substrates can be improved by their nanostructuring with invariant chemical composition of the surface. Nanostructuring of the PTFE substrates was achieved by gas-phase synthesis of copper (Cu) nanoparticles (Nps), which were embedded in the PTFE layer. The production process allowed precisely tailoring the roughness and wettability where more Cu Nps were linked with a higher contact angle of the deposited droplet (see Attachment A.6). In this way, highly hydrophobic as well as superhydrophobic substrates can be fabricated. Generally, with a higher contact angle, the pre-concentration of the analyte in dried pattern is more efficient [15, 31].

1.4 DCDR employed on biomolecules, biologically relevant molecules

Everything becomes more difficult when biological systems come into play, where different processes, such as chemical reactions or degradation, can be present. Moreover, water, as an essence of life and the most important biochemical, represents a natural environment for biomolecules such as proteins or lipids, where the desiccation process can lead to structural and packing alterations. Most research on biological samples has been, therefore, conducted in water. The structural integrity and function of biological membranes are undoubtedly dependent on the surrounding water molecules. Dehydration can lead to irreversible or reversible (anhydrobiosis) changes, which are still not fully understood [32]. Biological membranes are the primary sites of different external stresses, such as drying. As hydrophobic interaction is one of the key elements in the structural stability of biomembranes, the removal of water has multiple consequences. Raman spectroscopy is commonly employed in lipid studies, generally for liposome suspension, supported lipid bilayers or other self-assembling aggregates [33, 34, 35].

The first experiments with drying biological fluids started with urine droplets, and in recent years, researchers have paid attention to the pattern formation of

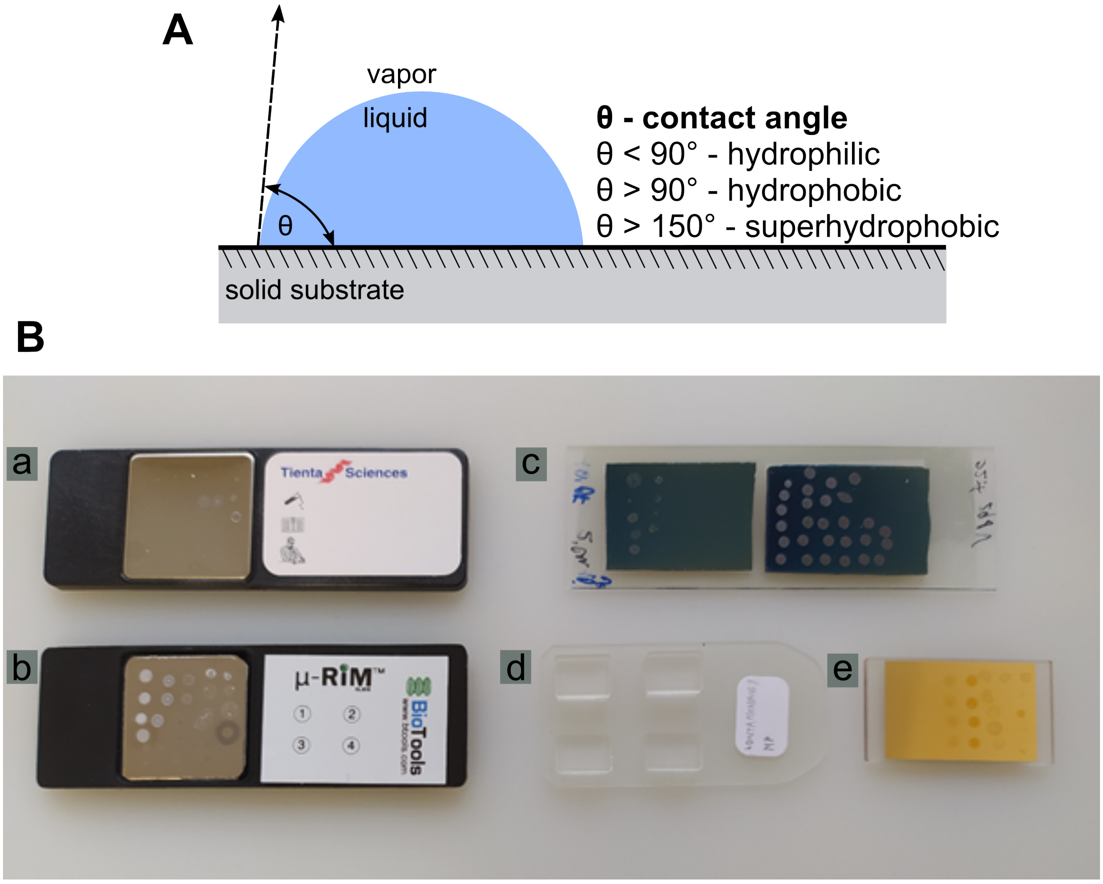

Figure 1.3 (A) Definition of contact angle of a deposited droplet on the solid substrate and (B) several examples of substrates employed in DCDR together with contact angle of water droplet: (a) commercial SpectRIM$^{\mathrm{TM}}$, 122°, (b) commercial μ-RIM$^{\mathrm{TM}}$, 108°, (c) nanoroughened platform with tailored hydrophobicity by embedded metal Nps in PTFE layer, (d) smooth polished CaF_2 glass, 90°, (e) thiol-modified smooth gold coated glass, 110°.

biofluids such as tears, blood or serum with a focus on diagnosis and therapy [36, 37, 38]. The extension of the drying process of biological fluids by analyzing dried patterns using RS was carried out by the pioneering work of Zhang et al. in 2003 on samples of lysozyme and human insulin protein [7]. From that time, more DCDR research followed, focusing on biomolecules and biofluids [39, 40, 41, 42, 43, 44]. However, controlling pattern formation from biologically interesting molecules is still a challenging task. The requirement for DCDR performance and acquisition of Raman spectra is the successful pre-concentration of the analyte *per se*, not the specific pattern. However, being able to predict and control the formation of reproducible dried patterns of the studied analyte would be advantageous for further method development where specific tailored applications would be possible.

Further and detailed information concerning DCDR studies over the last 15-20 years on different biologically important molecules (proteins, lipids, porphyrins etc.) and biological fluids (tears, urine, serum) was summed up in our two review papers (see Attachments A.3 and A.4). We covered the principle, a short history of the method, including its state-of-the-art, and our contribution to the method's development. Moreover, as the droplet deposition process employed for successful pre-concentration has received considerable attention in Raman spectroscopy, we also reviewed the progress of the analytical application of droplet deposition Raman spectroscopy including not only DCDR but also SERS (see Attachment A.5).

2 Aims and objectives of the theses

The main goal of the thesis was to explore the potential of the DCDR method in the study of biomolecules and biologically important molecules. The approach was first mentioned at the beginning of 21st century and was continuously developed also in our research group, including testing and comparing commercial *vs* non-commercial substrates and method application using them [31, 45, 46, 47, 48, 49, 50, 51, 52, 53, 54]. This thesis is a straightforward continuation of the utilization of the DCDR method, along with an outline of its further potential.

2.1 Detection capability of DCDR

The first part focuses on employing the DCDR to detect selected agricultural (thiram, bentazone, picloram) and food (melamine) contaminants from the low-concentrated aqueous solution. The aim was to observe changing dried patterns and to find the characteristic vibration in Raman spectra, which would allow us to detect selected contaminants and determine the lowest DCDR detected concentrations in deposited droplets using commercial SpectRIM^{TM} substrate. Additionally, we compared the achieved DCDR sensitivity with already published SERS detection limits if possible.

Furthermore, the fungicide thiram was analysed for a better understanding of its properties in degraded and undegraded forms. For that, DCDR results were compared and discussed among additional SERS measurements and density functional theory calculations (study done with collaboration).

Focusing on melamine, DCDR's capability to detect melamine from melamine blended infant formula was investigated. Firstly, pure milk infant formula was studied by DCDR, where spatial segregation in the dried pattern was revealed for carbohydrates and lipids. Then, melamine susceptibility to milk infant formula's main constituents, such as lactose and selected lipids, was tested. The simple melamine blended models helped us to predict the melamine behaviour in the melamine blended infant formula and its presence in the dried pattern.

2.2 Properties of dried phospholipids explored by DCDR

The second part deals with employing DCDR on liposomal suspensions, where the effect of the drying process on conformational changes and thermotropic behaviour is studied. Liposomal suspensions composed of fully hydrated bilayer aggregates are generally studied as model biomembranes. However, studying the drying of liposomal suspension can shed some light on processes such as membrane fusion or molecular interaction without the interference of water. Considering applying the DCDR on liposomal suspension, we studied the drying process on different substrates (smooth and nanoroughened) by monitoring the droplet drying dynamics and comparing the dried patterns. Then, we focused on the influence of unilamellar homogeneous *vs* non-homogeneous liposomal suspension (in liposome size, lamellarities and weights) on formed dried patterns. Applying the DCDR approach to liposomal suspension composed of one kind of lipid, we compared single spectra from different locations throughout the dried pattern to better understand the possible inhomogeneity of the coffee-ring patterns. This was followed by the study of the Raman spectral differences between fully hydrated liposomes *vs* dried liposomal suspension. For this purpose, the Raman tweezer microspectroscopy (RTM) approach was applied on liposomal suspension when final spectra were compared with DCDR spectra acquired from dried patterns. Finally, the thermotropic behaviour of dried liposomal suspensions was monitored for selected phospholipids differing in the hydrocarbon chain length or polar head group, with the motivation of discussing changes in the conformational order of dried lipid aggregates when heated. Drying at different relative humidity (RH) was also tested to better understand its influence on final dried patterns and conformational order.

3 Studied samples

3.1 Contaminants

Focusing on the DCDR performance in the detection of agricultural and food contaminants from aqueous solution, the following compounds were selected

Thiram (bis(dimethylthiocarbamyl) disulphide) sulphur-containing fungicide that serves as an animal repellent to protect fruit trees and prevent deterioration of harvested crops in storage or transport from a variety of fungal diseases. This compound can lead to liver damage and digestion issues due to its breakdown to form the carbon disulfide in the body. The European Union has banned the use of thiram in plant protection products on all commodities, as *per* Commission Regulation (EU) 2022/1406, which amended Regulation (EC) No. 396/2005. Therefore, monitoring possible illicit use is necessary.

Bentazone (3-isopropyl-2,1,3-benzothiadiazin-4-one 2,2- dioxide) is a herbicide applied aerially on food crops to control the spread of weeds occurring among the food crops by inhibiting photosynthesis. It can be dangerous due to its toxicity and mutagenic effects.

Picloram (4-amino-3,5,6-trichloro pyridine-2-carboxylic acid) is a systemic herbicide used for broadleaf weed control in pasture and rangeland, wheat, barley, oats, and woody plant species. It causes uncontrolled growth of the plant cells, leading to the plant death.

Melamine (2,4,6-triamino-1,3,5-triazine) is known as a food additive for the apparent elevation of protein content due to its high content of nitrogen, infamous for infant formula contamination in China in 2008 and pet food in 2004 and 2007 [55, 56]. Excessive consumption can lead to the formation of kidney stones.

Furthermore, melamine detection from intentionally blended real infant formula was tested with two types of local infant formula. To investigate the possible chemical reaction of melamine with main infant formula constituents affecting the dried pattern, simple model mixtures of the melamine-lactose and melamine-lipid were prepared.

3.2 Membrane phospholipids

Biological membranes are highly complex and dynamic. They play a key role in the structure and function of all cells. Extensive research has been held focusing on the composition, structure and function of membranes and lipids in a hydrated state since the membrane structure is stabilised by the hydrophobic effect. It is known that five forces contribute to membrane stabilization: a hydrophobic effect (the most prominent), caged tails, head-head interaction, head-water interaction, and van der Waals interaction. It is noteworthy to mention that membranes (and other self-assembling lipid aggregates) are stabilized without any covalent bonds holding them together. Biological membranes are composed primarily of lipids and proteins with significant variations in their relative amounts. Here, we are focused on membrane lipids, particularly phospholipids, as the major components of plasma membranes. Phospholipids are amphipathic molecules in which a hydrophilic head comprises the phosphate-containing group, and the hydrophobic part comprises two fatty acids (FAs) known as an acyl (or hydrocarbon) chain. Most common FAs have an even number of carbons (C), such as C14, C16, or C18 and different degree of unsaturation. Numerous long-range structures (phases) of lipid amphipathic molecules in water are referred to as "lipid polymorphism". Only four lipid phases are believed to be stable at high water content, which are lamellar (bilayer, liposome), inverted hexagonal H_{II}, cubic Q^{224} or Q^{227}. The final phase depends on the molecular shape of the lipids, which is derived from the ratio of the cross-sectional area of the polar head group at the aqueous interface and the cross-sectional area at the bottom of acyl chains [57].

The lamellar phase is the most prominent phase for biological membrane structure. However, even the lamellar phase can exist in several variations depending on the temperature. Upon heating, the lamellar phase undergoes multiple thermotropic phase transitions where the most distinct transition is from a solid-like gel (L_{β}´) to a liquid-like crystalline phase (L_{α}) denoted as melting behaviour (Figure 3.1). Upon heating, rotation of the $C - C$ bonds results in an accumulation of *gauche* kinks in the acyl chain linked with the conformational disorder, which is characteristic of the liquid crystalline phase. Compared to the gel phase, the liquid crystalline phase is, thanks to the *gauche* kinks, more poorly packed, more fluid, more permeable, thinner, less stable, and disordered, and it occupies a larger area *per* lipid. For hydrated lipid structures, the phase transition is highly cooperative and occurs over a very narrow temperature range. The cooperativity of transition decreases with a decrease in lipid purity [58]. The temperature of the main thermotropic phase transition T_{m}, when two phases coexist, is influenced by the length of acyl chains, polar head group and degree of unsaturation. The longer or the more unsaturated acyl chain, the higher T_{m} (for a more detailed description of lipid polymorphism, see [57, 59, 60]). Monitoring the lipid thermotropic phase transitions in the fully hydrated state, has been the subject of numerous studies using different methods, including Raman spectroscopy [61, 62, 63]. However, the behaviour of amphipathic molecules in anhydrous or poorly hydrated form can be different, including the phase transition [64]. Therefore, in our studies, several phospholipids were selected to explore the capabilities of DCDR to investigate the properties of dried lipids focusing on thermotropic phase transitions and the conformational order. We employed DCDR to study dried liposomal suspension of phospholipids differing in the polar head or length of the acyl chain:

DPPC (dipalmitoylphosphatidylcholine, 16:0 PC) - choline head group (neutral), acyl chain contains two saturated C16 FAs, $T_{\mathrm{m}} = 41$ °C (fully hydrated)

DMPC (dimyristoylphosphatidylcholine, 14:0 PC) - choline head group (neutral), acyl chain contains two saturated C14 FAs, $T_{\mathrm{m}} = 24$ °C (fully hydrated)

DOPC (dioleoylphosphatidylcholine, 18:1(Δ9-*cis*) PC) - choline head group (neutral), acyl chain contains two monounsaturated C18 FAs, $T_{\mathrm{m}} = -17$ °C (fully hydrated)

DMPS (dimyristoylphosphatidylserine, 14:0 PS) - serine head group (anionic under physiological conditions), acyl chain contains two saturated C14 FAs, $T_{\mathrm{m}} = 35$ °C (fully hydrated)

DOPS (dioleoylphosphatidylserine, 18:1 PS) - serine head group (anionic under physiological conditions), acyl chain contains two monounsaturated C18 FAs, $T_{\mathrm{m}} = -11$ °C (fully hydrated)

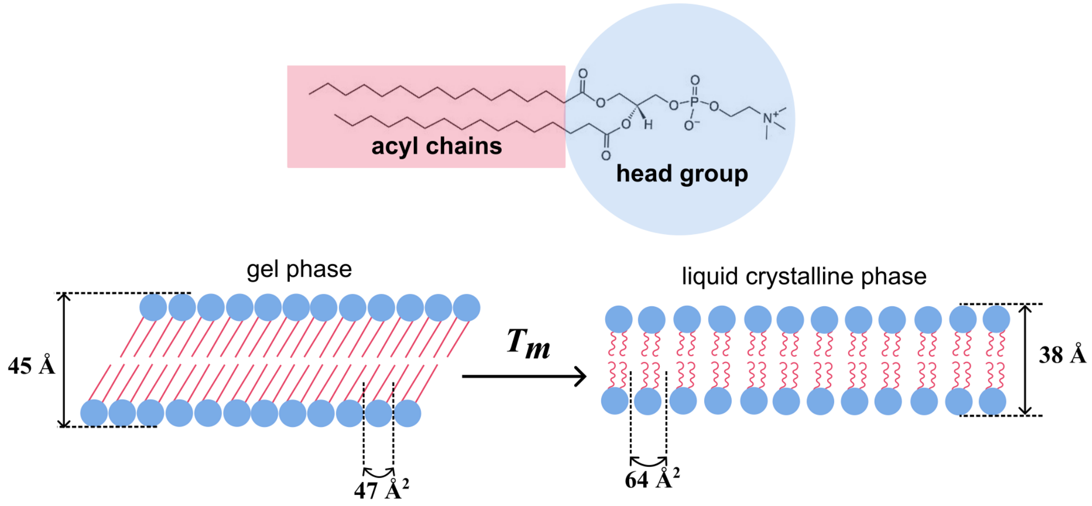

Figure 3.1 Schematic structural characteristics for a fully hydrated DPPC bilayer in a gel phase and liquid crystalline phase [65, 66].

4 Material and methods

4.1 Sample preparation

All studied contaminants and lactose were purchased from Sigma-Aldrich, Inc. in the highest possible purity as powders (product number - PN):

- **thiram** - PN 43966, 99 % purity
- **bentazone** - PN 32052, 99.9 % purity
- **picloram** - PN 36774, 99.6 % purity
- **melamine** - PN M2659, 99 % purity
- **α-lactose monohydrate** - PN L3625, $\geq$99 % purity

Two powdered milk infant formulas **Sunar** (Sun) and **Nutrilon** (Nut) were obtained from the local market. All lipids were purchased from Avanti Polar Lipids, Inc. as powder:

- **DPPC** (1,2-dipalmitoyl-sn-glycero-3-phosphocholine) - PN 850355
- **DMPC** (1,2-dimyristoyl-sn-glycero-3-phosphocholine) - PN 850345
- **DOPC** (1,2-dioleoyl-sn-glycero-3-phosphocholine) - PN 850375
- **DMPS** (1,2-dimyristoyl-sn-glycero-3-phospho-L-serine) - PN 840033
- **DOPS** (1,2-dioleoyl-sn-glycero-3-phospho-L-serine) - PN 840035
- **DOPE** (1,2-dioleoyl-sn-glycero-3-phosphoethanolamine) - PN 850725

Structural formulas of all purchased contaminants and biomolecules (lactose, lipids) are shown in Figure 4.1.

Contaminant stock solutions were prepared by dissolving powders in deionized water in the highest possible concentrations (except melamine, which is highly soluble in water). Stock solutions for each contaminant (thiram - 62 μM, bentazone and picloram - 2 mM, melamine - 16 mM) were subsequently diluted as far as their detection was possible. To obtain DCDR results from pure lactose and infant formulas, powders were dissolved in water (lactose - 1 mg/ml, infant formulas - 7.83 mg/ml). Concerning melamine detection from infant formula, mixture solutions were prepared by mixing powders followed by dissolution in water (details of prepared mixtures can be found in Table 4.1).

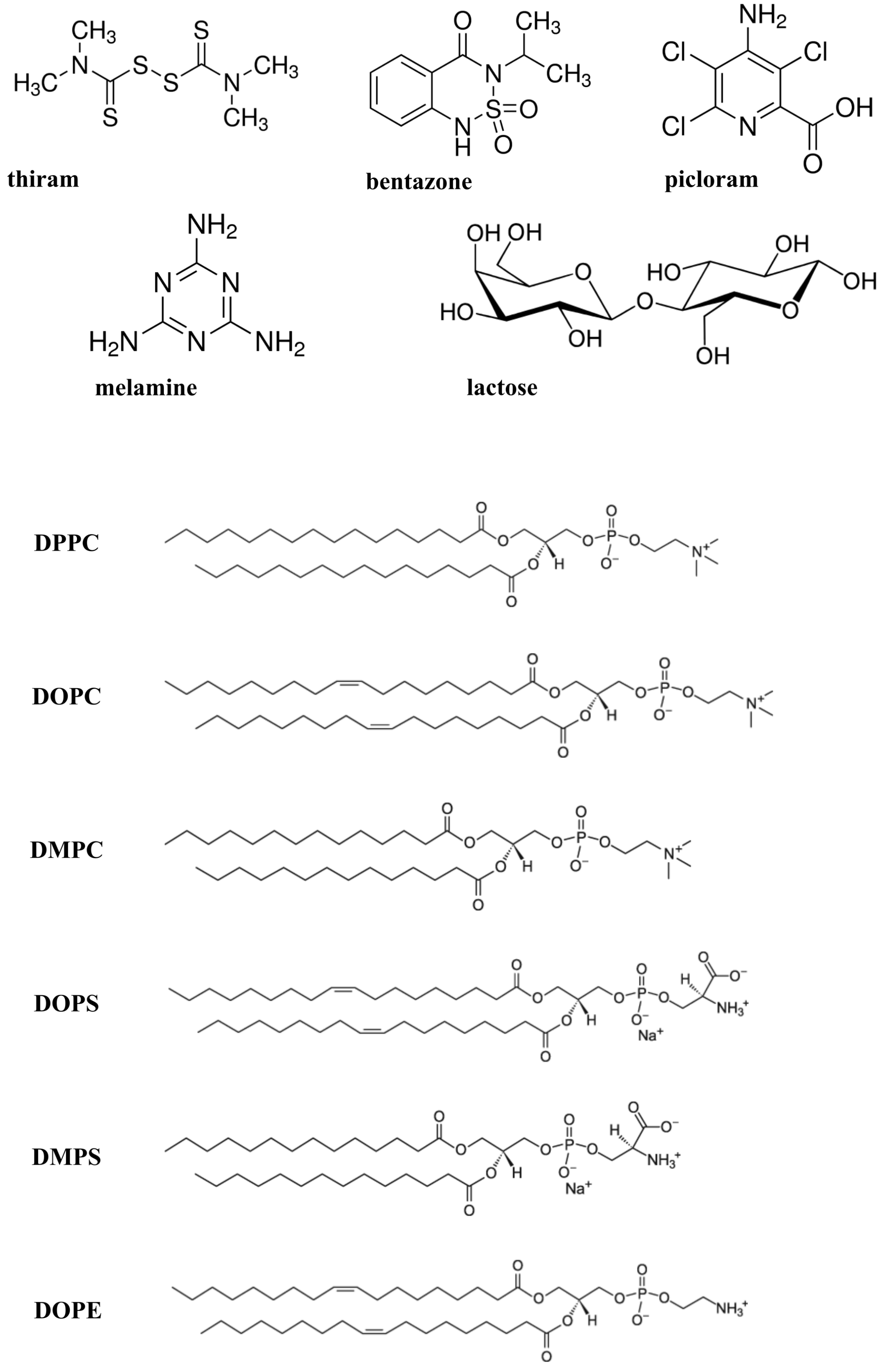

Figure 4.1 Structural formulas of studied samples including contaminants, lactose and lipids.

Table 4.1 Final concentrations of reactants in the mixture for model reactions with melamine

Reactant	Reactant final concentration in aqueous mixture (mg/ml) for DCDR spectroscopy								
	Lac-mel	**DOPC-mel**	**DOPE-mel**	**Sun A**	**Sun B**	**Sun C**	**Nut A**	**Nut B**	**Nut C**
Melamine	0.006	0.006	0.007	0.1	0.05	0.025	0.1	0.05	0.025
Lactose	1	-	-	-	-	-	-	-	-
DOPC	-	1	-	-	-	-	-	-	-
DOPE	-	-	1	-	-	-	-	-	-
Sunar	-	-	-	7.83	7.83	7.83	-	-	-
Nutrilon	-	-	-	-	-	-	7.83	7.83	7.83

Liposomal suspensions were prepared following the standard protocol [67]. Lyophilized lipids were dissolved in an organic solvent (pure chloroform or chloroform/methanol mixture) to achieve complete dissolution in a glass flask. A stream of nitrogen was then used for solvent removal, allowing the formation of a thin layer of lipid spread on a glass surface. Subsequently, deionized water was added to the flask (to achieve the required concentration - 2 mg/ml, 1 mg/ml or 0.5 mg/ml) for lipid hydration and spontaneous vesicle formation. Complete hydration to cloudy liposome suspension was achieved by maintaining the suspension at the temperature above the thermotropic main phase transition for 1 h and finally by applying an ultrasonic bath. To obtain a unilamellar liposomal suspension, an apparatus LiposoFast-Basic$^{\mathrm{TM}}$ (Avestin) was used with a porous polycarbonate membrane filter with 100 nm pores. The liposomal suspension needs to be extruded through a membrane filter approximately thirty-five times above transition temperature to ensure liposomal unilamellarity. Figure 4.2 from Cryogenic electron microscopy (Cryo-Tem) illustrates an example of prepared liposomal suspension.

All solutions and suspension were prepared in deionized water (Milipore-Q 18.2 MΩ), and studied sample was deposited on chosen substrate (non-commercial: CaF_2 glass, polished stainless steel plate or commercial: SpectRIM$^{\mathrm{TM}}$, μ-RIM$^{\mathrm{TM}}$) by micropipette as 2 μl droplet and let to dry freely at room temperature (RT) and approximate RH of 55 % covered with a Petri dish (to avoid dust pollution) for approximately 1 hour. Liposomal suspension dried at RH of 0.5 % was deposited and left to dry in a dry cabinet (model XC-315).

To test the effect of nanoroughened substrate on a drying process and formed dried pattern of liposomal suspension, a non-commercial substrate based on a PTFE layer was used, where sandwiched Cu Nps governed controlled roughness (see Attachment A.6). For temperature-dependent studies with liposomal suspension, polished stainless steel substrates were employed.

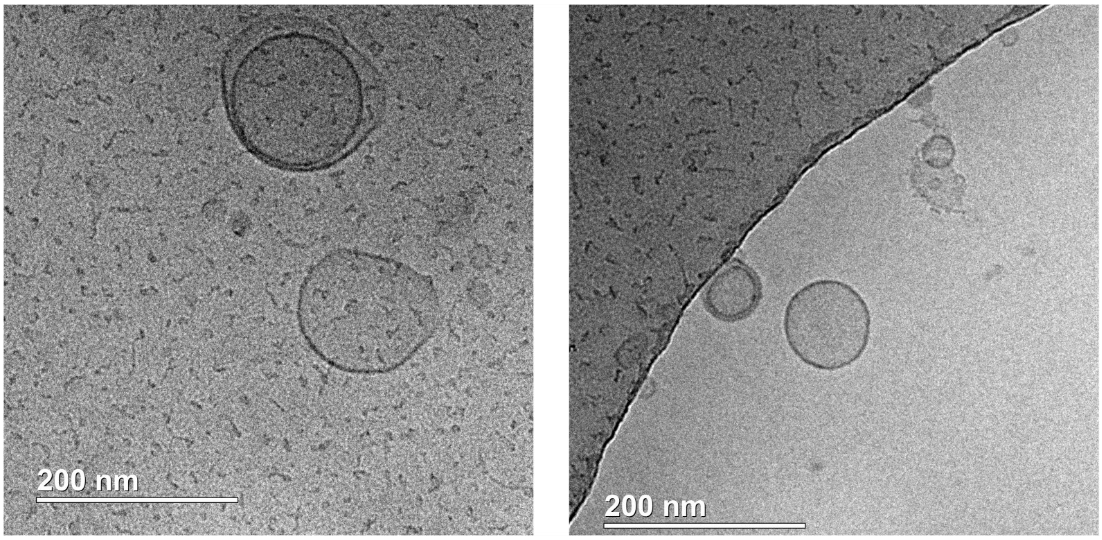

Figure 4.2 Cryo-Tem images of unilamellar homogeneous liposomal suspension (100 nm) prepared from DOPC (0.7 mg/ml).

4.2 Instrumentation

Two confocal Raman microspectrometers were used to study and analyse dried patterns and to acquire Raman spectra (single point spectra, line spectra, spectral maps). LabRAM HR800 (Horiba Jobin Yvon) equipped with 300 grooves/mm grating, a nitrogen-cooled CCD detector and a He-Ne laser (excitation line at 632.8 nm) was used for contaminants´ detection and some lipid studies. For spectra acquisition, 50×ULWD objective with 3 mW laser power on a sample was used with typical single spectrum accumulation of 60 × 1 s. White light images of dried patterns were taken using objectives with magnifications 5× , 10×, and 50×.

The Alpha300 confocal Raman microspectrometer from WiTec (Oxford Instruments) was used to study the melamine blended samples, as well as for the majority of lipid studies. The microspectrometer was used with different excitation lasers (785 nm, 633 nm, and 532 nm) and different gratings (300 grooves/mm, 600 grooves/mm, 1200 grooves/mm) depending on the desired spectral sensitivity in measured wavenumber interval and sample type. A Carl Zeiss 50×/0.55 LD objective was used to focus on the sample and collect back-scattering radiation. The objective reduced laser power on the sample by a factor of 0.689. Images of the dried pattern were taken using objectives with 5× and 50× magnification. Temperature-dependent measurements were conducted at the copper heating stage, calibrated using PT100 element and controlled by the software (stabilised at each measured temperature for 1 min, 1 °C step). Laser powers and acquisition times (single point spectra, line spectra, and spectral maps) were adjusted so as not to degrade the sample (during heating experiments, laser power of only $2-4$ mW prior to the objective was used). For more information about microspectrometer confocality, see Attachment A.1.

Raman tweezer microspectroscopy (RTM) measurements of liposomal suspensions were carried by the Alpha300 confocal Raman microspectrometer from WiTec. RTM successfully combines optical trapping with Raman probing when the same laser is used for optical trap and for the excitation of RS of trapped particles (Figure 4.3). A laser of 785 nm was used with a maximal power of cca 128 mW measured prior to the objective. The laser beam was focused through a water immersion objective (Olympus UPlanSapo 60×/1, 2 W), which was used in direct contact with liposomal suspension (100 μl) placed on a CaF_2 glass. During the measurements, the focal waist is located inside the liquid suspension, serving as an optical trap. The same objective (reducing the power by a factor of 0.730) was used to collect scattered light in back-scattering geometry. The Raman signal from nanosized liposomes is extremely weak and sits on top of the water Raman spectrum as soon as the liposomes are optically trapped. For that, longer acquisition times are needed. Raman spectra were acquired with a grating of 300 g/mm using a time series software feature preserving each measured accumulation. The acquisition time was 3×300 s in three series in total. For water correction, a signal of water was acquired with 3×50 s acquisition in total for each series, while the constant movement of the sample table (liposomal suspension remaining in contact with the objective) minimized the probability of an optical trap while maintaining the same sample environment. The process of optical trapping depends on liposome composition, size, concentration, density and laser power [68, 69]. The lipid concentration in liposomal suspension measured by RTM was 1 mg/ml.

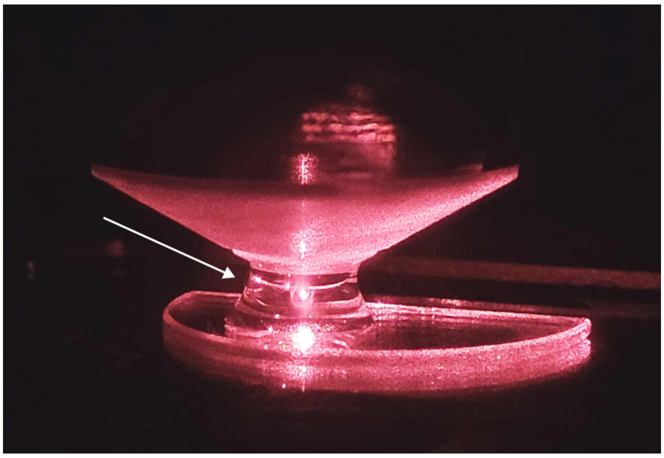

Figure 4.3 Demonstration of optically trapped nanoparticle.

4.3 Data treatment

Spectra measured on an Alpha300 confocal Raman microscope were processed in the associated software from the WITec Suite SIX package with automatic calibration. All raw spectra were first treated with the ”Cosmic Ray Removal” procedure to detect and remove cosmic ray spikes. For processing spectral maps, where appropriate, the “True Component Analysis” tool was used to identify the dominant spectral component of the scanned area. The procedure involves fitting each acquired spectrum with a linear combination of basis spectra using the least squares method. The intensity distribution of different components and their averaged spectra are simultaneously created. Raman spectra of liposomal suspension acquired by the RTM technique were corrected for water background by subtracting the averaged water signal from the signal of liposomal suspension by the appropriate factor. Baseline correction for all measured spectral sets (DCDR, RTM) was applied using in-house-developed software using the orthogonal-differences baseline correction method [70]. To analyse temperature-dependent measurement, factor analysis was employed to determine subtle spectral differences with rising temperature to ascertain the phase transition temperature. ImageJ software was used to determine lateral parameters of dried patterns, such as the width and diameters of coffee-ring patterns. Inkscape 1.2.2 (732a01da63, 2022-12-09) was applied to construct the final images. OriginPro 2024b (OriginLab Corporation) was used for general data treatment, including smoothing methods, Savitzky-Golay or Fourier transform, depending on the character of the treated data, and to create all final graphs.

4.3.1 Factor analysis

Factor analysis is a multivariate statistical method applied to large data sets describing them by extracting all their commonalities into a smaller number of factors [71]. Factor analysis can be performed using different methods, such as principal component analysis or singular value decomposition (SVD), with the same abstract results. The latter was employed here. SVD procedure decomposes matrix A of $m \times n$ to the following matrix multiplication:

$$A = UWV^T \tag{4.1}$$

For a set of single Raman spectra, each column n of the matrix A contains one measured spectrum. In general, a spectrum is represented by a set of intensity values assigned to a corresponding wavenumber. Thus, each row m in the matrix stands for intensity values at a specific wavenumber of individual spectra. SVD procedure applied to matrix A includes solving the eigenvalue equation providing an orthonormal set of subspectra $S_{\mathrm{j}}(v)$, an orthonormal matrix of corresponding scores V_{ij} and a set of singular values or weights W_{j}.

$$Y_i(v) = \sum_{j=1}^{m} W_j V_{ij} S_j(v) \tag{4.2}$$

The output of factor analysis contains the set of subspectra, their statistical weights (singular values), normalised coefficients (scores) indicating the relative contribution of subspectra in individual spectra, and finally, residual errors. The first subspectrum computed using SVD algorithms presents the principal shape common to each spectrum in the measured set. Using least square analysis, it was shown that this subspectrum approximates the measured set in the best possible way [70]. The second and following subspectra reflect various spectral changes in the analysed spectral set. Moreover, information from individual subspectra is independent because of their orthogonality. The more subspectra is considered in the sum 4.2, the better approximation of experimental spectra is achieved with lower residual error. To obtain the factor dimension (number of minimum factors to approximate experimental spectra), singular values or residual errors assigned to the subspectra can be used, where the significant drop in the value is the deciding factor. The number of values before the drop indicates the dimension.

Raman spectral changes related to temperature-dependent measurements of lipids treated by factor analysis are reflected in subspectra (except the first one) and corresponding scores. Furthermore, a simple two-state model can help analyze the thermotropic phase transition by fitting the scores dependencies for individual subspectra.

4.3.2 Simple two-state model for lipid phase transition

A two-state model is an established phenomenological description for lipid phase transitions [72, 73]. Within the model, we presume that both phases, gel and liquid crystalline, behave linearly with temperature in the analysed region. The transition from form A (gel) to form B (liquid crystalline) can be written as follows:

$$A \xrightarrow{K} B, K = \frac{c_{\mathrm{B}}}{c_{\mathrm{A}}} \tag{4.3}$$

Regarding the form concentrations $\mathrm{c_A}$ and $\mathrm{c_B}$, we can write:

$$c_{\mathrm{A}} + c_{\mathrm{B}} = 1, c_{\mathrm{A}} = \frac{1}{K+1}, c_{\mathrm{B}} = \frac{K}{K+1} \tag{4.4}$$

From thermodynamics, we utilized relations between equilibrium constant, temperature, and changes in thermodynamic parameters linked to lipid phase transition:

$$K = e^{-\frac{\Delta G}{RT}}, \Delta G = \Delta H - T\Delta S \tag{4.5}$$

Where $\Delta G, \Delta H, \Delta S$ are changes in Gibbs energy, enthalpy and entropy, R stays for the ideal gas constant, and T represents the absolute temperature.

Temperature of the phase transition is for $K = 1$, which means:

$$T_{\mathrm{m}} = \frac{\Delta H}{\Delta S} \tag{4.6}$$

Finally, using the above-mentioned formulae, we performed fitting on the factor analysis results according to the following relation by the linear least squares method:

$$\sum_{i=1}^{N}\sum_{j=1}^{D}[\sqrt{W_{\mathrm{j}}}V_{\mathrm{ij}} - (a_{\mathrm{j0}} + a_{\mathrm{j1}}t_{\mathrm{i}})c_i^A - (b_{\mathrm{j0}} + b_{\mathrm{j1}}t_{\mathrm{i}})c_i^B]^2 = min \tag{4.7}$$

Where N is the number of analysed spectra, and D stays for the factor dimension of the measured spectral set.

5 Results and Discussions

5.1 DCDR as a tool for contaminant detection

Generally, contaminants can be harmful, and both life and environmentally threatening even in low concentrations. Therefore, their detection and identification, even at trace concentrations, are required. Droplet coating and subsequent pre-concentration of analyte into dried patterns represent a straightforward and simple approach for sensitive detection. We focused on the DCDR detection performance of selected agricultural and food contaminants, together with an assignment of their characteristic vibrational modes according to which they could be detected (detailed information in the Attachment A.7).

5.1.1 Agricultural and food contaminants

DCDR was employed to stock solutions of all selected contaminants (thiram, bentazone, picloram and melamine). Stock solutions were subsequently independently diluted into a series of concentrations for each contaminant according to its DCDR spectra sensitivity. We observed dried patterns in different forms and measured DCDR spectra from pre-concentrated locations (Figure 5.1). Picloram exhibited two types of spectra depending on the deposited concentrations. Using crossed polarization filters, we found out that the first type of spectrum corresponded to amorphous picloram and the second type of spectra to crystalline picloram. Both spectral types shared the distinct band of breathing vibration at 1109 cm^{-1}. To highlight the DCDR capability, the spectra of stock solutions were measured under the same experimental conditions from liquid drops on a microscope slide. As can be seen in Figure 5.2, no spectral features of contaminants are visible except the melamine band at 676 cm^{-1} assigned to its breathing vibration. The lowest deposited concentrations detected by DCDR were determined as 0.31 μM, 20 μM and 2 μM, 6.4 μM for thiram, bentazone, picloram, and melamine, respectively. Thiram was detected due to distinct $S-S$ vibration at 560 cm^{-1}, bentazone was detected due to its partial breathing vibration at 1037 cm^{-1}, picloram was detected due to its breathing vibration at 1109 cm^{-1} and finally, the melamine was detected due to its breathing vibration at 676 cm^{-1}. Concerning thiram, the sophisticated SERS detection using Au@Ag nanoparticles and paper-based microfluidic allowed its detection at 10^{-9} M concentration [74]. Additionally, DCDR measurements of thiram were further extended to analyse the thiram behaviour in solution and solid phases to understand its properties (study done with collaboration). DCDR results were discussed together with our SERS measurements and density functional theory calculations. It was found that the thiram molecule is susceptible to hydrogen bonding with chloroform and can be coordinated to the silver nanostructured SERS substrates not only in the degraded form but also in the undegraded form (more details in the Attachment A.8). SERS detection of melamine using common Ag and Au Nps or solid nanostructures allowed for detection of 10^{-7} – 10^{-8} M concentration [75]. No SERS detection study for comparison was found for bentazone and picloram.

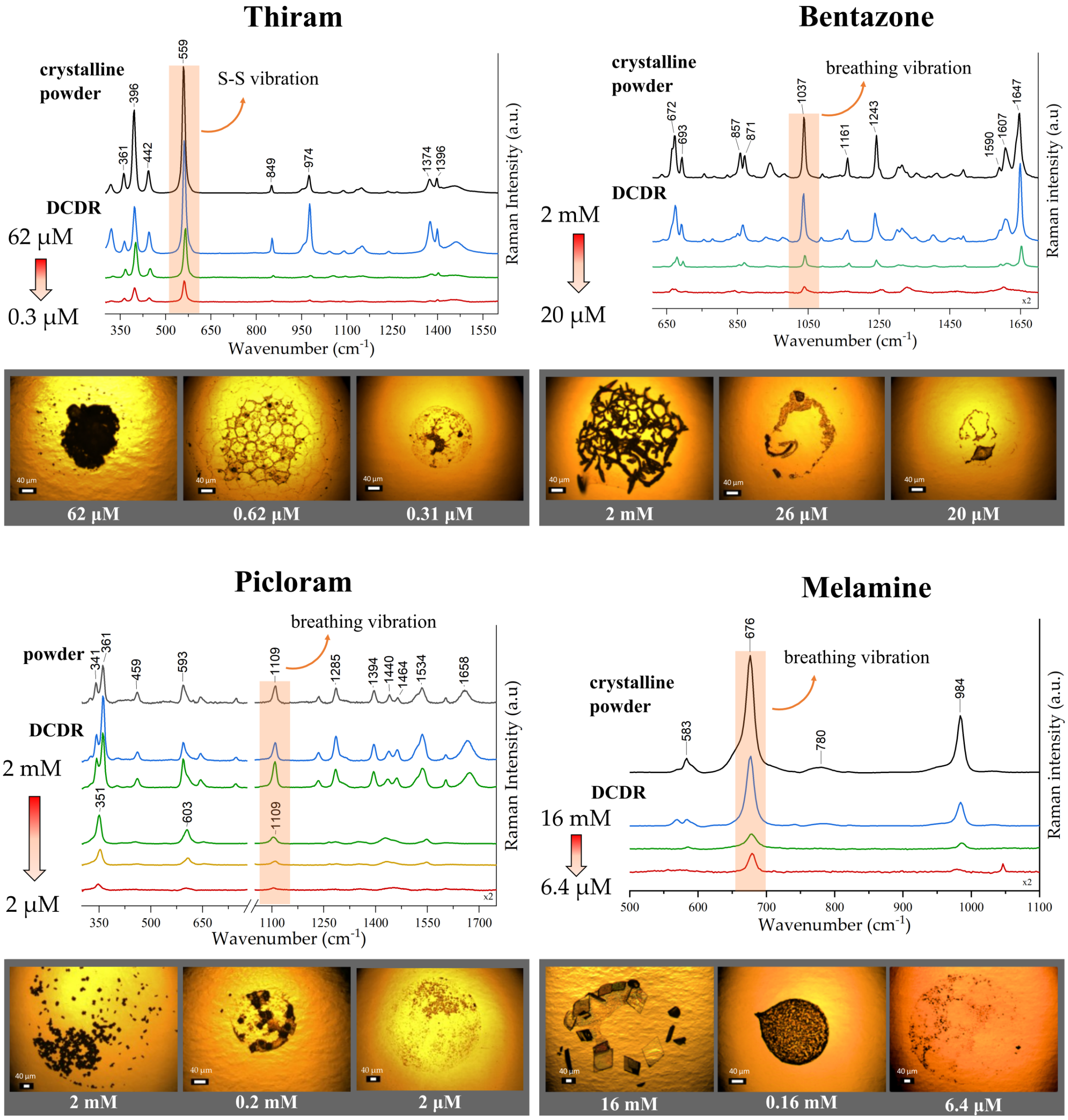

Figure 5.1 Results of DCDR detection of selected contaminants at different concentrations including formed dried patterns, acquired spectra and highlighted characteristic vibrations.

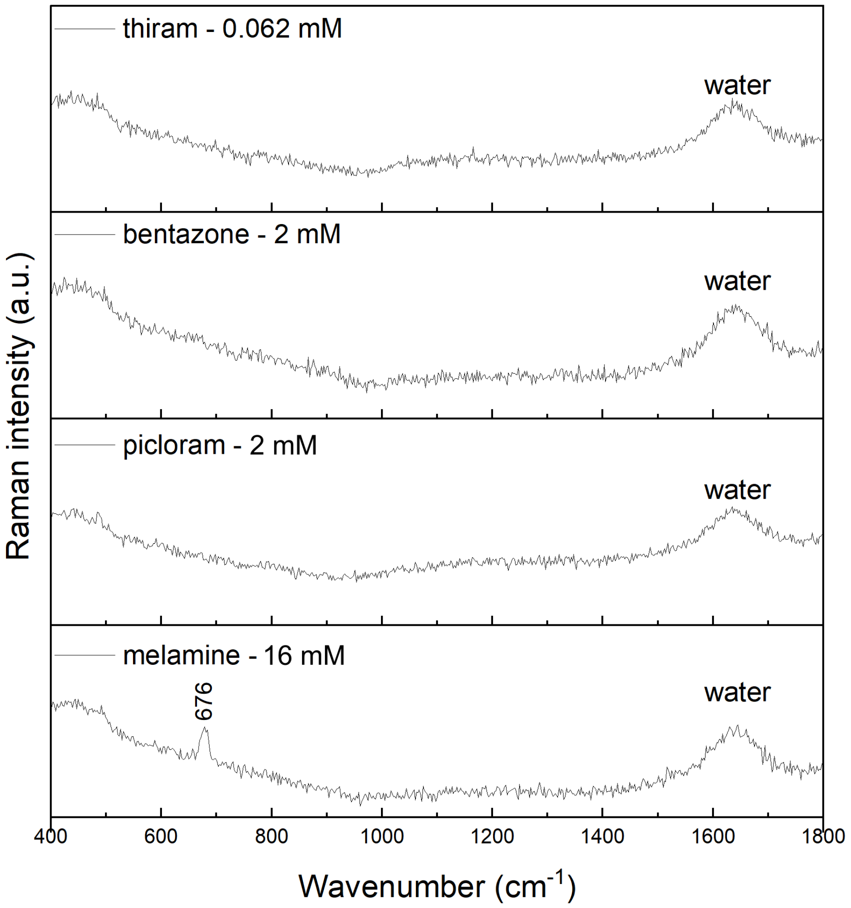

Figure 5.2 Raman spectra of stock solutions of each studied contaminant: thiram, bentazone, picloram and melamine.

5.1.2 Detection of melamine from real infant formula

Melamine DCDR detection from real infant formula was performed with two kinds of pure infant formula (Sun and Nut). For dried patterns from both milk samples, we observed the formation of distinct rings with the remaining thin film spread in the central part as seen in Figure 5.3a and c. Acquired Raman spectra revealed the segregation potential of the drying process. The ring edge was mainly composed of lipids, particularly oleic acid, the most abundant FA in infant formula. The thin central layer was mainly composed of carbohydrates, mostly lactose. Comparing the spectra from both tested milk samples, Sun and Nut, we observed only subtle differences (Figure 5.3b and d). Thus, we could see a similar separation of solution constituents for both studied kinds of milk with slightly different compositions.

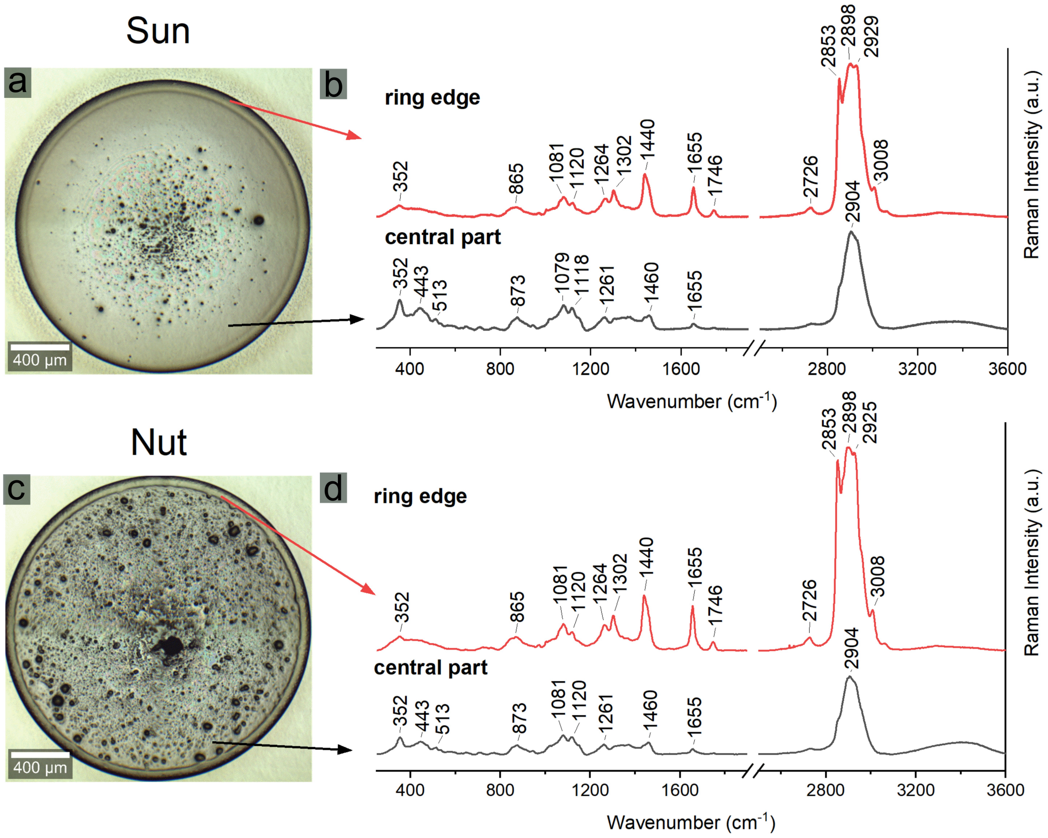

Figure 5.3 White light images of dried patterns of the (a) Sun and (c) Nut with corresponding DCDR spectra accumulated from the edge rings and thin central layer for (b) Sun and (d) Nut.

The main constituents of infant formula are oleic acid as fat and lactose as a carbohydrate. The susceptibility of melamine to these compounds was explored by simple melamine blended models that were prepared for DCDR analysis. Melamine blended lipid mixtures, DOPE-mel and DOPC-mel, were compared with corresponding pure liposomal suspensions from DOPE and DOPC. A distinct coffee-ring dried pattern was formed for each sample, as is generally observed for liposomal suspensions. However, Raman spectral mapping from the DOPE-mel ring pattern treated by the ”True component analysis” procedure (from Witec software) revealed the presence of melamine due to its characteristic breathing vibration at 687 cm^{-1}. From the spatial distribution of calculated components, we determined that DOPE lipid was mainly pre-concentrated in the outer ring pattern, and melamine was partially separated into the inner parts of the ring (Figure 5.4). However, the measured Raman spectral map suggested that melamine partially interacted with DOPE during mixing and drying. We assumed that interaction was due to the DOPE polar head containing an amine group prone to form hydrogen bonds with melamine molecules. To confirm or exclude our assumption, we did the same experiment with DOPC (the same acyl chain, different polar head group). Comparing pure DOPC and DOPC-mel dried patterns, the latter consisted of small spots inside the ring structure absent in the pure DOPC pattern. Acquired Raman spectra revealed, that small spots were formed by melamine, whereas the spectral map from the ring structure exhibited only lipid bands (Figure 5.5). The drying process separated melamine (small spots) from lipids (the coffee-ring pattern). Thus, the incomplete separation of melamine from DOPE was likely a result of the partial interaction of melamine with DOPE, namely with the ethanolamine head group.

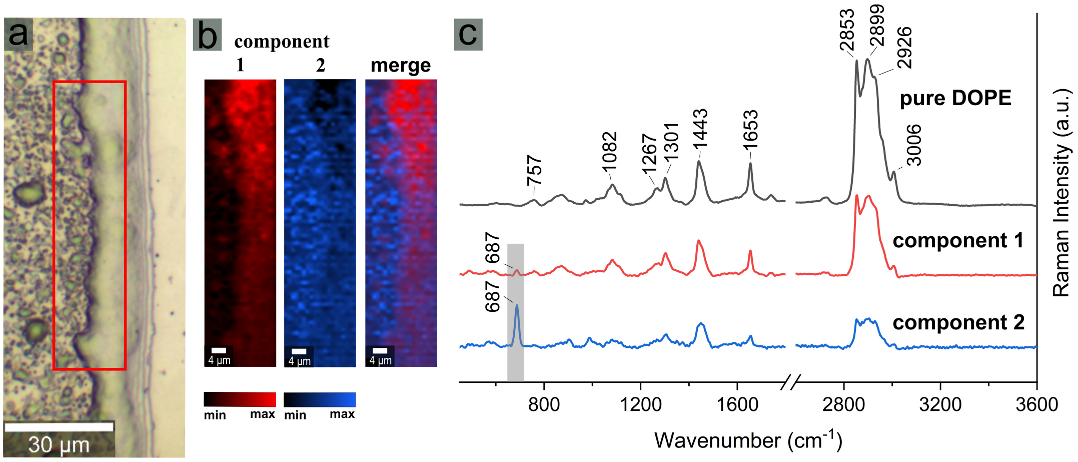

Figure 5.4 a) The white light image of the dried pattern DOPE-mel mixture with indicated area for spectral mapping with (b) showing the spatial distribution of two identified components. c) Average spectrum for both components together with the reference spectrum of DOPE.

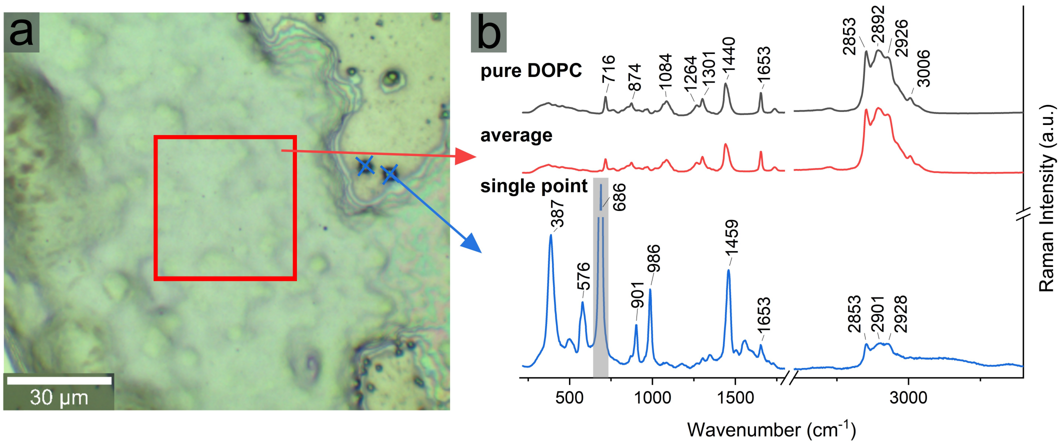

Figure 5.5 a) The white light image of the dried pattern DOPC-mel mixture with indicated area for spectral mapping and b) average spectrum from spectral mapping and single Raman spectrum from the indicated points together with the reference spectrum of DOPC.

Melamine blended lactose mixture, Lac-mel, was also tested and compared with pure lactose. The dried pattern of pure lactose solution had a crystalline character confirmed by crossed polarization filters and Raman spectrum (Figure 5.6a-d). Lac-mel mixture dried into a uniform thin layer pattern with an amorphous character. Moreover, the Raman spectral map exhibited a homogeneous distribution of melamine band at 681 cm^{-1} together with the bands assigned to amorphous lactose (Figure 5.6e-g). The loss of lactose crystalline character and the presence of a melamine breathing vibration band for the Lac-mel mixture suggested an interaction between lactose and melamine. Lactose as a potent reaction partner for melamine was observed and previously reported [76, 77, 78].

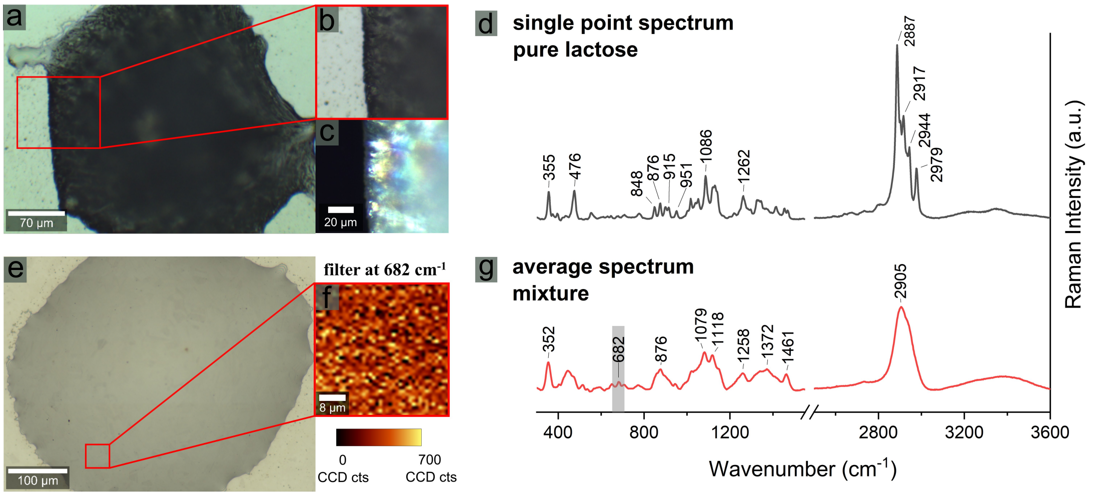

Figure 5.6 a), b) White light images of pure lactose dried pattern with c) the image using crossed polarising filters and d) single point Raman spectrum from pure lactose dried pattern. e) The white light image of Lac-mel mixture dried pattern with the indicated area selected for spectral mapping, f) melamine distribution throughout the scanned area using a spectral filter for the band of melamine breathing vibration at 682 cm^{-1}, and g) average Raman spectrum from selected area.

Finally, two melamine blended kinds of infant formula were tested. Dried patterns formed from blended samples were indistinguishable from the ones of pure infant formula. The acquired Raman spectra revealed the presence of melamine only in the thin film spread in the central part of the blended dried patterns together with carbohydrates, mainly lactose (Figure 5.7 top). Therefore, melamine retained its reaction potential to lactose also in the complex milk mixture while simultaneously separated from lipids. Raman spectral mapping was used to show the homogeneous melamine distribution in the thin central layer (Figure 5.7 bottom). These findings represent a promising utilisation of the DCDR approach as the simple and efficient method for compound detection (as contaminants) based not only on the pre-concentration but also on the spatial distribution in the dried pattern strengthened by its reaction potential in the mixed solution.

Detailed information about the spatial separation of infant formula's main constituents, together with melamine detection from melamine blended samples, can be found in the Attachment A.9.

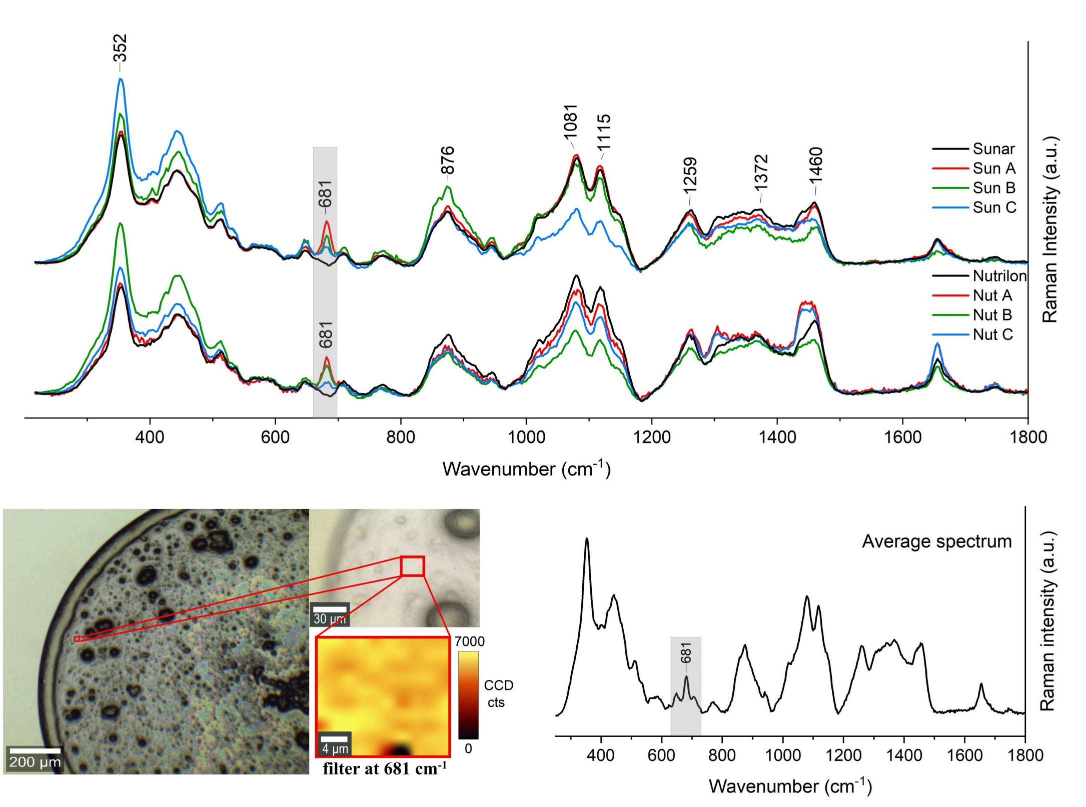

Figure 5.7 Top: DCDR spectra of melamine blended infant formulas at different concentrations (see Table 4.1) with highlighted melamine breathing vibration. Bottom: The white light image of a dried pattern of intentionally blended infant formula (Nut B) with an indicated area for spectral mapping and a demonstration of melamine distribution throughout the scanned area using a spectral filter for the band of melamine breathing vibration at 681 cm^{-1} together with an average Raman spectrum calculated from the scanned area.

5.2 Investigation of lipid properties by DCDR

5.2.1 Drying dynamics of liposome suspension

As previously described, drying of liquid droplets is a complex phenomenon. Here, some aspects of liposomal suspension droplet drying dynamics are discussed in the context of the generally accepted drying modes. Drying dynamics covers observing a contact angle (CA) and a contact radius (CR) changes over time. A common drying process monitored on different kinds of platforms includes several sequential modes: constant contact radius (CCR) mode linked with CA decrease, followed by constant contact angle (CCA) mode linked with CR decrease and a mixed mode when both the CA and CR decrease up to the droplet diminishing [79, 80]. Modifications of drying dynamics influenced by the substrate properties are mainly discussed with respect to water droplets. Here, we present the set of drying dynamics of liposomal suspension droplets (2 μl) composed of unilamellar 100 nm liposomes prepared from DPPC lipids. Non-commercial substrates, smooth PTFE and nanoroughened ones with embedded Cu Nps in the PTFE layer were compared. The deposition time of Cu Nps was 2 and 4 minutes, the corresponding substrates were denoted as NpsCu2 and NpsCu4, respectively. The longer deposition of Nps leads to higher roughness and, thus, a more hydrophobic substrate. Moreover, a set of water droplet drying dynamics on the same substrates is presented for comparison.

A water droplet was deposited and left to dry freely at RT on each substrate (PTFE, NpsCu2, NpsCu4). Figure 5.8a and b shows the time evolution of CA and CR during the drying. We observe different drying dynamics of droplets dried on smooth *vs* nanoroughened substrate. For smooth PTFE substrate (Figure 5.8c), we can clearly determine three separate drying modes as previously described, where CCR mode is followed by CCA and finally by mixed mode to the droplet diminishing. For nanoroughened substrates (Figure 5.8d), only two drying modes could be distinguished: CCR mode followed by mixed mode to the complete droplet disappearance. CCA mode was effectively suppressed. Water droplets remained pinned on the nanoroughened surface for almost the entire evaporation time. This behaviour is in agreement with published results [81].

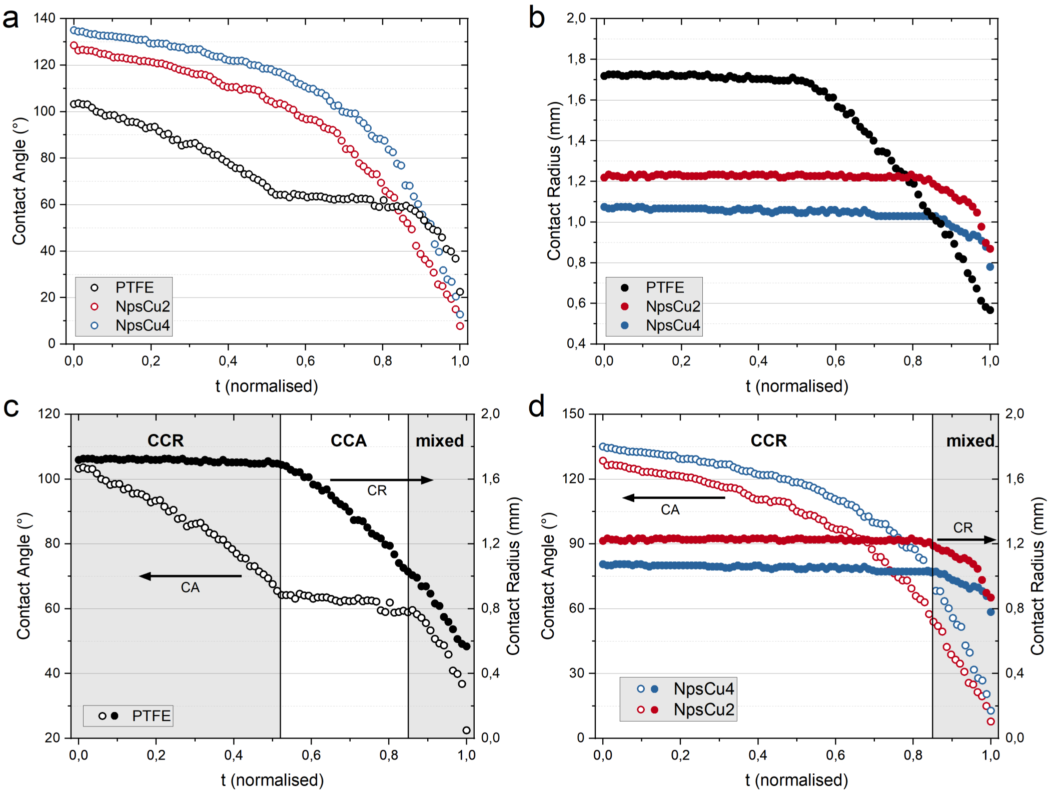

Figure 5.8 Drying dynamics (time evolution of a) CA and b) CR) of a water droplet deposited on a smooth PTFE and nanoroughened NpsCu2, NpsCu4 substrates with designation of the different drying modes (CCR, CCA, mixed) c) on smooth PTFE and d) nanoroughened NpsCu2, NpsCu4 substrates.

Further, drying dynamics of unilamellar liposomal suspension prepared from a 0.5 mg/ml lipid concentration were monitored. The evolution of CA and CR with time for each substrate is shown in Figure 5.9a and b. We observe complete suppression of CCA mode for each drying dynamics. The evolution of CR indicates different drying modes of liposomal suspension on smooth substrate compared to nanoroughened ones. Drying dynamics of liposomal suspension on smooth PTFE substrate express CCR mode followed by mixed mode (Figure 5.9c) as

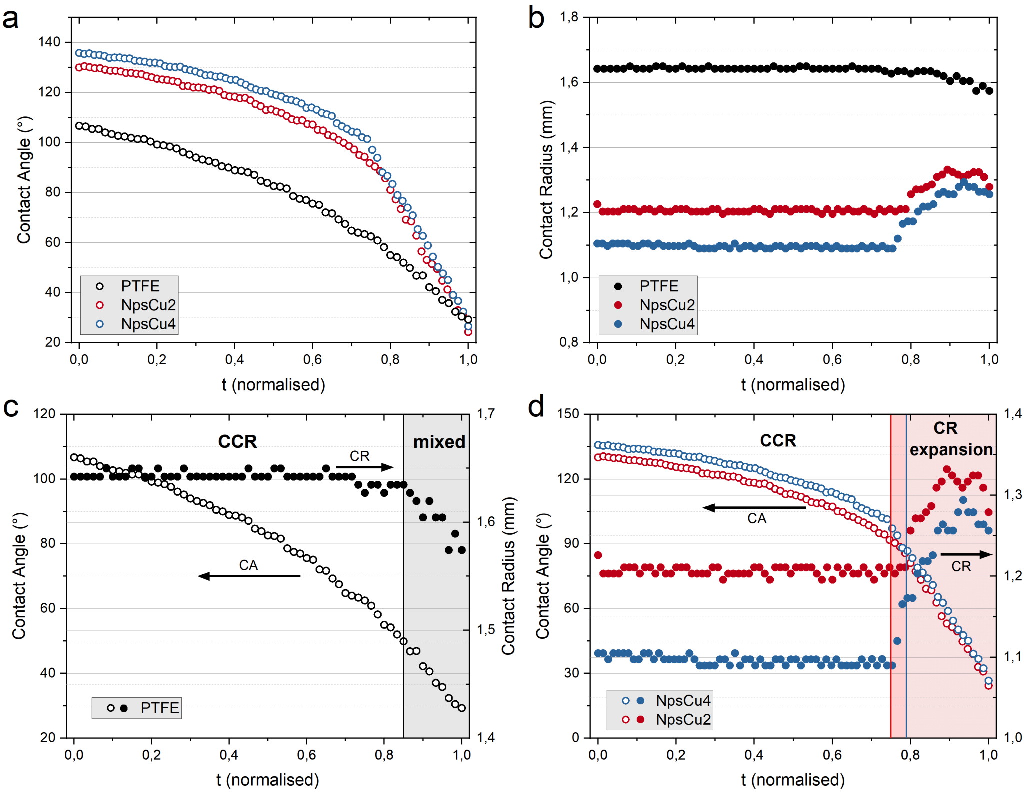

Figure 5.9 Drying dynamics (time evolution of a) CA and b) CR) of a DPPC unilamellar liposomal suspension droplet deposited on a smooth PTFE and nanoroughened NpsCu2, NpsCu4 substrates with designation of the different drying modes (CCR, mixed, CR expansion) on c) smooth PTFE and d) nanoroughened NpsCu2, NpsCu4 substrates.

we could observe for water droplets on the nanoroughened substrate. A droplet remained pinned on the smooth substrate almost to the end of the evaporation process. Drying of liposomal suspension on nanoroughened substrate showed CCR mode followed by CR expansion alongside the steep decrease in CA (Figure 5.9d). Droplets on nanoroughened substrates stayed pinned to the contact radius for approximately three-quarters of the complete evaporation process. After that, droplet CR initially expanded by 10 % for NpsCu2 and 17 % for NpsCu4 and subsequently shrank to droplet diminishing. This behaviour (not reported before) is considerably different from liposomal suspension dried on the smooth substrate and water droplets dried on the nanoroughened substrate, where CCR mode was followed by mixed mode. It suggests that CR expansion mode has to be linked to both the nature of the droplet (liposomal suspension) and the nature of the substrate (nanoroughened).

Generally, drying of liposomal suspension is linked with a gradual increase in liposome concentration as the water evaporates. Thus, we assume that liposomes are warped when not enough water molecules are available to hold the liposome structure *via* hydrogen bonding. Vesicles collapse and, based on simulations, their deposition on hydrophobic substrate leads to unzipping at the substrate and complete transformation into monolayer [82]. Moreover, water or lipid molecules can be partially captured by the nanoroughened layer due to surface protrusions.

From our point of view, both mentioned effects, the collapse of liposome entities and capture by the nanoroughened layer, play an important role in drying dynamics, particularly in CR expansion mode. The observed time evolution is considerably different from the drying dynamics of water or solid Nps suspension described in the literature [83, 84]. However, as no plausible explanation is available to our knowledge, the observed mode needs to be further explored to be fully understood.

An adequate understanding of drying dynamics modes can help control the formation of dried patterns for specific application and analysis. In the context of the DCDR method, we compared and discussed dried patterns from liposomal suspension formed on smooth PTFE substrate and nanoroughened NpsCu2 and NpsCu4 substrates in the Attachment A.6. Drying a liposomal suspension leads to the typical coffee-ring formation after an evaporation process on each tested substrate. By observing dried patterns, we concluded that drying on nanoroughened substrates led to the formation of coffee-rings with a smaller radius of the observed rings together with smaller lateral ring widths (Figure 5.10) and, therefore, to better pre-concentration of lipids, which was confirmed by acquired Raman spectra as seen in Figure 5.11.

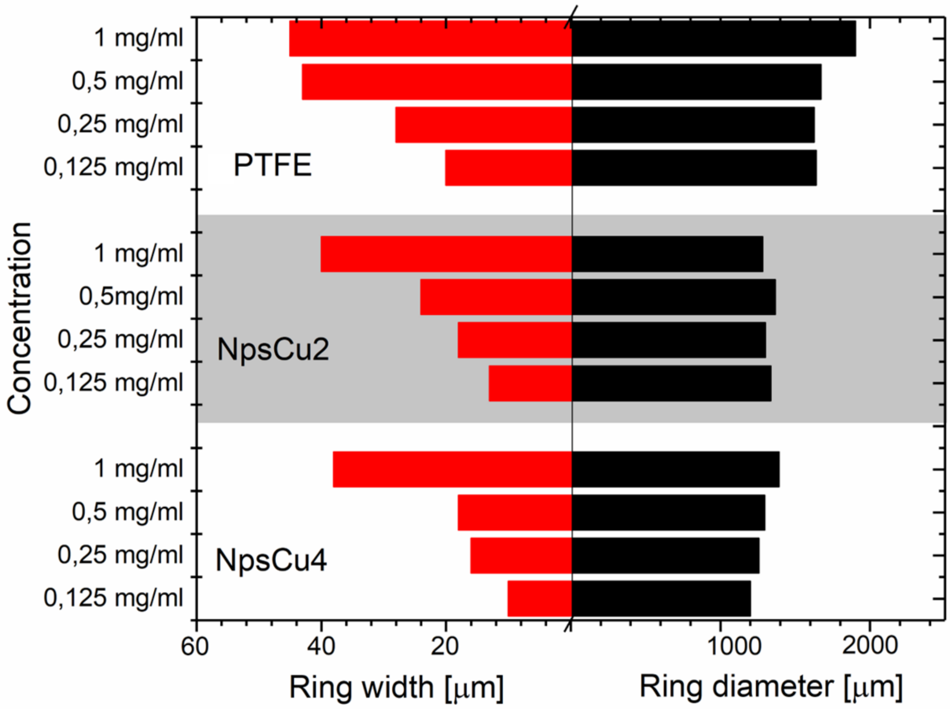

Figure 5.10 Widths and diameters of the ring dried patterns formed after drying of a DPPC unilamellar liposomal suspension droplet.

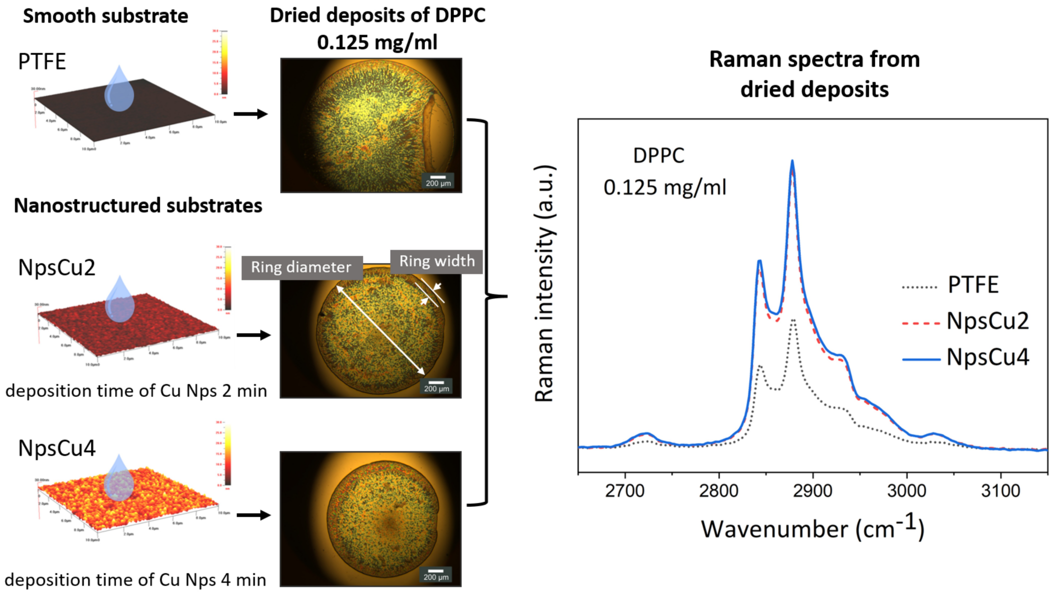

Figure 5.11 DCDR signal improvement for DPPC liposomal suspension by employing nanoroughened substrates NpsCu2 and NpsCu4.

5.2.2 Dried patterns from liposomal suspension

Drying unilamellar liposomal suspension forms a nicely shaped ring pattern known as a coffee-ring pattern. We showed how the chosen substrate and its hydrophobicity linked with roughness can influence drying dynamics and dried patterns, particularly the ring diameter and lateral ring width. Here, we will demonstrate how the liposomal suspension itself can influence the formed dried patterns. Homogeneous unilamellar liposomal suspension (100 nm) and non-homogeneous liposomal suspension (prepared without extrusion) were prepared from DPPC, DMPC and DOPC lipids (1 mg/ml lipid concentration) differing only in hydrocarbon tail (length and saturation).

After deposition of 2 μl droplet of prepared suspension on a smooth substrate (polished stainless steel in this case), we observed distinctive differences between dried patterns from homogeneous and non-homogeneous suspension. Figure 5.12 demonstrates that drying a homogeneous unilamellar liposomal suspension formed coffee-ring patterns for each selected lipid. For fully saturated DPPC and DMPC, the ring surface is smooth when the ring of monounsaturated DOPC expresses irregularities on the outer part of the ring. We assume that this is a result of unsaturated acyl chains, which have higher conformational freedom. Drying of non-homogeneous liposomal suspensions resulted in a fully covered circular dried pattern with no distinctive ring structure as observed for homogeneous unilamellar suspensions. We believe that this is achieved by a mixture of various liposome sizes, lamellarities and weights (as a result of complete hydration and no extrusion), which are influenced differently by the outward and inward flows induced during the droplet evaporation.

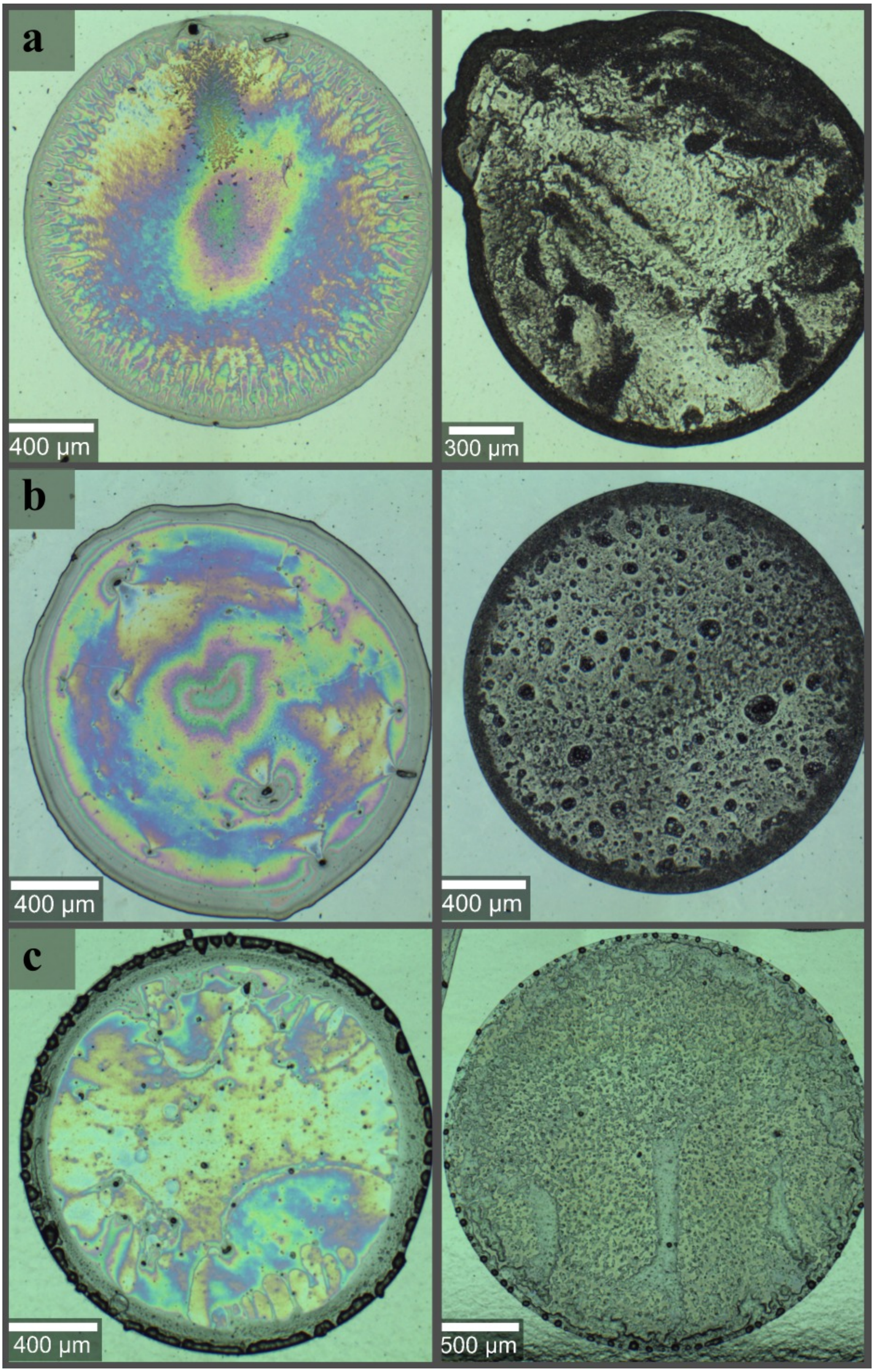

Figure 5.12 White light images of dried patterns of homogeneous unilamellar (on the left) and non-homogeneous (on the right) liposomal suspensions of different lipids: (a) DPPC, 1 mg/ml, (b) DMPC, 1 mg/ml, (c) DOPC, 1 mg/ml.

5.2.3 Comparing Raman spectra measured from liposomal suspension and from dried patterns

Hydration of phospholipids is still being studied using various techniques [85, 86]. It is known that the unsaturation of the hydrocarbon chain increases the chain disorder just as the volume available for the lipid head group, which means an increase in the amount of adsorbed water [87]. In RTM measurements, liposomes are fully hydrated. In DCDR measurements, drying of the suspension from unilamellar liposomes influences the bilayer conformation. It leads to minimizing the volume between the head groups, and the cross-section area for one lipid is smaller. This results in enhancing the lateral packing of the phospholipids with hydrocarbon chains packed tightly together when solvent molecules (mainly water) are fully or partially evaporated [87, 88]. Applying DCDR on unilamellar liposomal suspension, Raman spectra are acquired from the coffee-ring pattern. To determine what changes are distinguished using RS, we compared Raman spectra acquired directly from unilamellar liposomal suspension by RTM with DCDR spectra obtained from coffee-ring patterns dried from unsaturated DOPC and DOPS lipids (1 mg/ml).

Firstly, the Raman signal was acquired from different locations of single dried patterns (25 locations for DOPC and 32 locations for DOPS). To show spectral variations, only a few spectra are presented in Figure 5.13a, together with indicated locations on coffee-ring patterns. These DCDR experiments were done using a laser of 785 nm with a power of cca 25 mW measured prior to the objective (Carl Zeiss 50 × /0.55 LD with a power reduction factor of 0.689). Spectra were recorded with 300 g/mm grating with 1 × 120 s acquisition. Measured Raman spectra were firstly treated with the ”cosmic ray removal” procedure, then baseline corrected by in-house-developed software using the orthogonal-differences baseline correction method [70] and finally smoothed by Savitzky-Golay filter (window width: 5, polynomial order: 2). Spectra were further normalised on $\delta(CH_2)_{\mathrm{sc}}$ at 1440 cm^{-1}. For both lipids, only intensity variations of Raman bands are observed, and no wavenumber shifts. Intensity variations in the region of $800 - 950$ cm^{-1} are characteristic of the change in chain order when higher intensity reflects a disordered chain with higher *gauche* content [89]. Intensity variations of bands in the $1030 - 1130$ cm^{-1} region are also linked to the *trans/gauche* conformation when the relative intensity ratio can be influenced by the position of *gauche* conformer throughout the chain [89]. The band at 1268 cm^{-1} is linked with the unsaturated bonds in the chain, whose intensity depends on the total number of double bonds. Generally, these intensity variations result from different conformations of skeletal $C - C$ and $C = C$ bonds in different locations of dried patterns, subsequently influencing the lipid arrangement and its immediate vicinity. We assume that mutual rearrangement could lead to a different change of polarizability, which is directly linked to the Raman intensity. Interestingly, also choline head group vibration at 716 cm^{-1} shows (for DOPC) intensity variations based on different locations of the dried pattern. Assignment of the specific intensity changes to specific lipid perturbations or different arrangements is the question of more detailed measurements and analysis. However, it shows the heterogeneity of coffee-ring dried patterns of monounsaturated phospholipids.

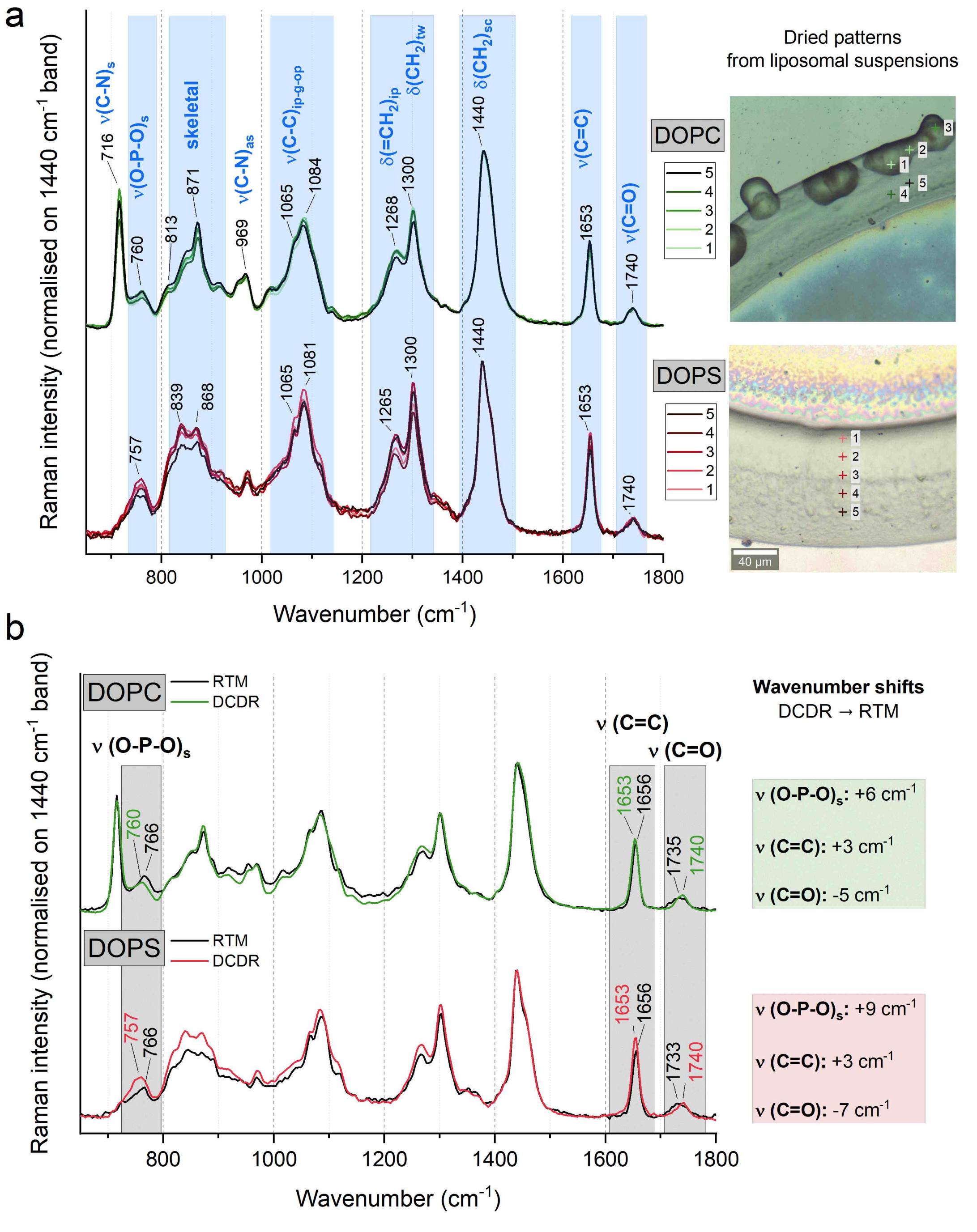

Figure 5.13 a) Comparison of DCDR spectra for lipids DOPC and DOPS from different locations of dried pattern and b) comparison of DCDR (averaged) and RTM spectra of DOPC and DOPS with highlighted wavenumber shifts. Vibrational denotation: ν - stretching vibration, δ - deformation vibration, *ip* - in-plane, *op* - out-of-plane, *g* - *gauche*, *tw* - twisting, *sc* - scissoring, *s* - symmetric, *as* - asymmetric. Band assignments can be seen in [88, 95, 93, 96, 97].

Secondly, DCDR spectra were compared to RTM spectra (measured with the same laser and the same grating covering the same spectral range) for both lipids. We used the averaged DCDR spectrum from different locations (for DOPC calculated from 25 spectra and for DOPS from 32 spectra) to obtain a better signal-to-noise ratio. This means that possible intensity changes between the DCDR and RTM spectrum could not be considered as a relevant indication of lipid state change. All of the recorded raw RTM individual accumulations were first treated with the ”cosmic rays removal” procedure. After that, each accumulation was visually inspected, and spectra without (or very minor) liposome contribution were eliminated from further treatment. The remaining spectra were corrected for water background by subtracting the averaged water signal. Further, baseline correction was applied using in-house-developed software using the orthogonal-differences baseline correction method [70]. The resulting spectra were averaged, smoothed by Savitzky-Golay filter (window width: 5, polynomial order: 2) and normalised on 1440 cm^{-1} band. Figure 5.13b shows a comparison of the RTM spectrum and averaged DCDR spectrum for both lipids. Excluding visible intensity changes, we can distinguish differences in slight wavenumber shifts for several vibrations for both lipids, particularly for $\nu(O-P-O)$, $\nu(C=O)$ and $\nu(C=C)$. The most prominent shifts are observed for symmetric diester stretching vibration $\nu(O-P-O)$, and carbonyl stretch $\nu(C=O)$. Both DOPC and DOPS lipid molecules contain two $C=O$ bonds connecting the head group with two acyl chains and one phosphate group as a part of a polar head group. Non-ester phosphate oxygens and carbonyl oxygens are the primary targets for water molecules to stabilise liposomes by hydrogen bonding [90, 91, 92]. It is well known that hydrogen bonding shifts the wavenumber position of the stretching vibration to the lower frequency. However, the Raman signal of $\nu(P=O)$ vibration is not unequivocally resolved, and it is spectrally overlapped by the vibration of $\rho(=CH_2)$ [93]. On the contrary, infrared (IR) spectroscopy, as a complementary vibrational method to RS spectroscopy, is much more sensitive to polar groups, whose bands are clearly visible and readily distinguished. Thus, the wavenumber shift of PO_2^- due to lipid hydration in IR spectra can be easily monitored and studied [94, 85]. On the other hand, the clearly distinguished Raman band of $\nu(C=O)$ is shifted as expected to lower wavenumbers for the fully hydrated sample, as seen in the RTM spectrum, compared to the dried sample reflected in the DCDR spectrum.

Concerning the phosphate diester group $(O-P-O)$ embedded in a lipid molecule in the hydrophilic part, we can assume that the frequency of the vibration is influenced by tightly packed phospholipid molecules with a lower amount of water. For symmetric diester stretching vibration $\nu(O-P-O)_\mathrm{s}$, there is an evident shift to a lower wavenumber (for DCDR), which is reported in other studies on different anhydrous phospholipids [93, 95]. Calculations of $O-P-O$ rotational isomers for different dihedral angles of both $P-O$ bonds showed that $\nu(O-P-O)$ vibrations are affected not only in intensity variation but also in wavenumber shift [98]. Rotation about both $P-O$ bonds simultaneously has a similar but stronger effect than rotation about one $P-O$ bond. Minimum values for symmetric stretching vibration were assigned to the *cis* conformer about the bond, and the maximum value was assigned to the *trans* arrangement [98]. Furthermore, for both lipids, a slight wavenumber shift between DCDR and RTM spectra is noticed for $\nu(C = C)$ group. This band is significant for unsaturated lipids, as it is assigned to the stretching vibration of the unsaturated olefinic bond. The position of the olefinic stretch is generally affected by various processes, including $(C = C)$ bond isomerization, conjugation of $(C = C)$ bonds or cyclization reaction. These processes are characterised by specific spectral changes (more can be found in [99]), which are not present in our spectra. Moreover, the position of this band can also be affected by the conformation of adjacent bonds, where a slight change can shift the position by a few wavenumbers [96, 100]. From the above-mentioned processes, we assume that a slight wavenumber shift is linked with minor conformational changes of adjacent bonds induced by the drying process of liposomal suspension.

In conclusion, DCDR spectra acquired from different locations from dried patterns express relative intensity variations mainly linked with the $C - C$ and $C = C$ skeleton conformational changes, such as alterations in *gauche* conformer content or its position in the acyl chain, but no wavenumber shifts. However, RTM spectra compared to DCDR spectra exhibited wavenumber shifts, which were assigned to the different levels of lipid hydration and also to the different rotations of the $O - P - O$ bonds in the dried and fully hydrated lipid aggregates.

5.2.4 Thermotropic phase transition of phospholipids

The DCDR method was used to monitor the thermotropic phase behaviour of selected phospholipids. This was done from dried liposomal suspension patterns using 532 nm laser and gratings of 600 g/mm. A substantial study has been performed so far to investigate the conformationally dependent features in Raman spectra of fully hydrated phospholipids. They include monitoring the thermal behaviour through changes in ratios of relevant spectral bands. Less was done on anhydrous of poorly hydrated lipid aggregates (dried). Besides, most studies have been conducted on lyophilized phospholipids and not on the dried aggregates, as here. The conformational order/disorder of hydrocarbon chains has a direct impact on the structure and function of lipids. RS is sensitive to lipid conformational changes occurring during the lipid thermotropic phase transition [61]. Raman spectra obtained from the gel and liquid crystalline phase reflect changes related to the structural alternations during the transition. Upon heating, changes in spectral bands (intensity ratio, wavenumber shift and broadening) can be observed mainly in spectral regions of 2800–3100 cm^{-1} assigned to $C - H$ stretching vibrations or region of 1050–1150 cm^{-1} assigned to $C - C$ stretching vibrations of hydrocarbon chains. Here, we focus on the $C - H$ stretching region, which is the most intense part of the phospholipid spectrum (Figure 5.14).

Three phospholipids that differ in the acyl chain length and the polar head group were selected for temperature-dependent measurements: DPPC, DMPC, and DMPS (Figure 4.1). DCDR spectra from dried patterns were acquired in the temperature range covering the main phase transition from gel-to-liquid crystalline phase as seen in Figure 5.15 (DPPC: 32 - 100 °C, DMPC: 24 - 80 °C, DMPS: 30 - 85 °C). For each measured phospholipid, we observe significant temperature-dependent changes. Factor analysis using the SVD procedure was performed on the acquired spectral sets individually. As already described, this statistical

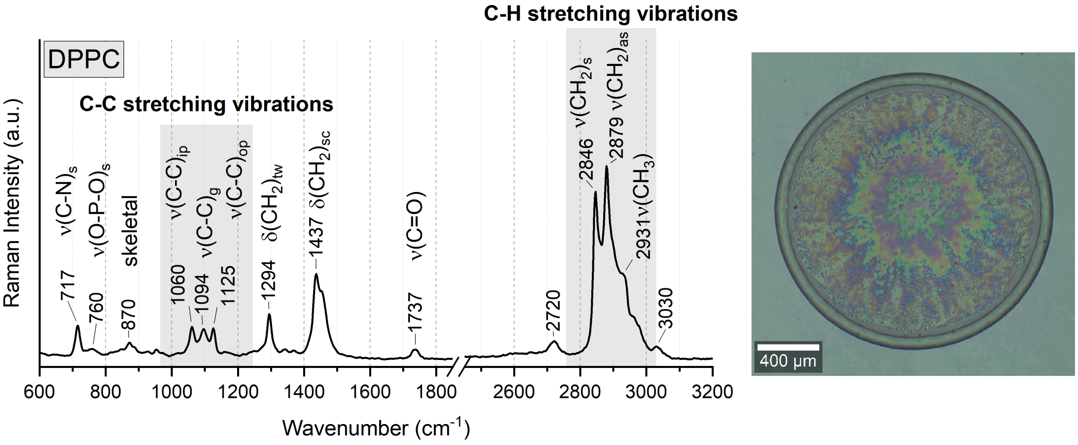

Figure 5.14 White light image of a dried pattern of unilamellar liposomal suspension of DPPC lipid (0.5 mg/ml) with the corresponding DCDR spectrum. Vibrational denotation: ν - stretching vibration, δ - deformation vibration, *ip* - in-plane, *op* - out-of-plane, *g* - *gauche*, *tw* - twisting, *sc* - scisoring, *s* - symmetric, *as* - asymmetric. Band assignments can be seen in [88, 95, 93, 97, 96].

treatment gave us the set of subspectra (S), their statistical weights (W), and normalised coefficients (V), indicating the relative contribution of subspectra in individual spectra, and residual errors (E). Results of factor analysis (Figure 5.16 for DMPC) indicated a factor dimension of 4 for each treated set (factor analysis results for DPPC and DMPS can be seen in the Attachment A.2). The second, third and fourth subspectra show the relevant changes in the spectral shape throughout the measured temperature range, where the second is the most dominant one. The most distinct changes (Figure 5.16 S_2) are wavenumber shifts of the $\nu(CH_2)_{\mathrm{s}}$ and $\nu(CH_2)_{\mathrm{as}}$ together with intensity changes of $\nu(CH_2)_{\mathrm{as}}$ and $\nu(CH_3)_{\mathrm{as}}$ and $\nu(CH_2)_{\mathrm{as}}$ broadening. These changes reflect the general trend of gradually increasing disorder in the acyl chains. Specifically, the wavenumber shift towards higher positions means the increase in decoupling of the chains [97]. Band broadening suggests the existence of several possible conformations through the forming of *gauche* conformers [88].

In order to deduce the T_{m}, the results of factor analysis were described as a simple two-state model. Within the model, the temperature dependence for gel and liquid crystalline phases was approximated by linear behaviour in the analysed region. A least squares method was used to fit the scores from factor analysis results (red line on Figure 5.16). The T_{m} for each lipid was determined as follows, $T_{\mathrm{m}}(DPPC) = 72$ °C, $T_{\mathrm{m}}(DMPC) = 57$ °C, $T_{\mathrm{m}}(DMPS) = 55$ °C . Each T_{m} is higher than for the fully hydrated sample.

Previously published T_{m} for anhydrous or poorly hydrated DPPC are the following: 97.8 °C (differential scanning calorimetry - DSC, lipid sample recrystallised from chloroform/acetone mixture) [101]; $100 - 108$ °C (Raman spectroscopy, lipid sample recrystallised from chloroform) [93]; 75 °C (DSC, mmonohydrated lipid sample) [102]; 97.5 °C (DSC, lyophilized lipid sample) [102]; 95 °C (nanocalorimetry, lipid sample recrystallised from ethanol) [103]; 106 °C (DSC, lyophilized lipid sample) [104]. Published T_{m} values for DMPC are 61 °C (DSC, monohydrated lipid sample) [102]; 87.5 °C (DSC, lyophilized lipid sample) [102]; 97.6 °C (DSC,

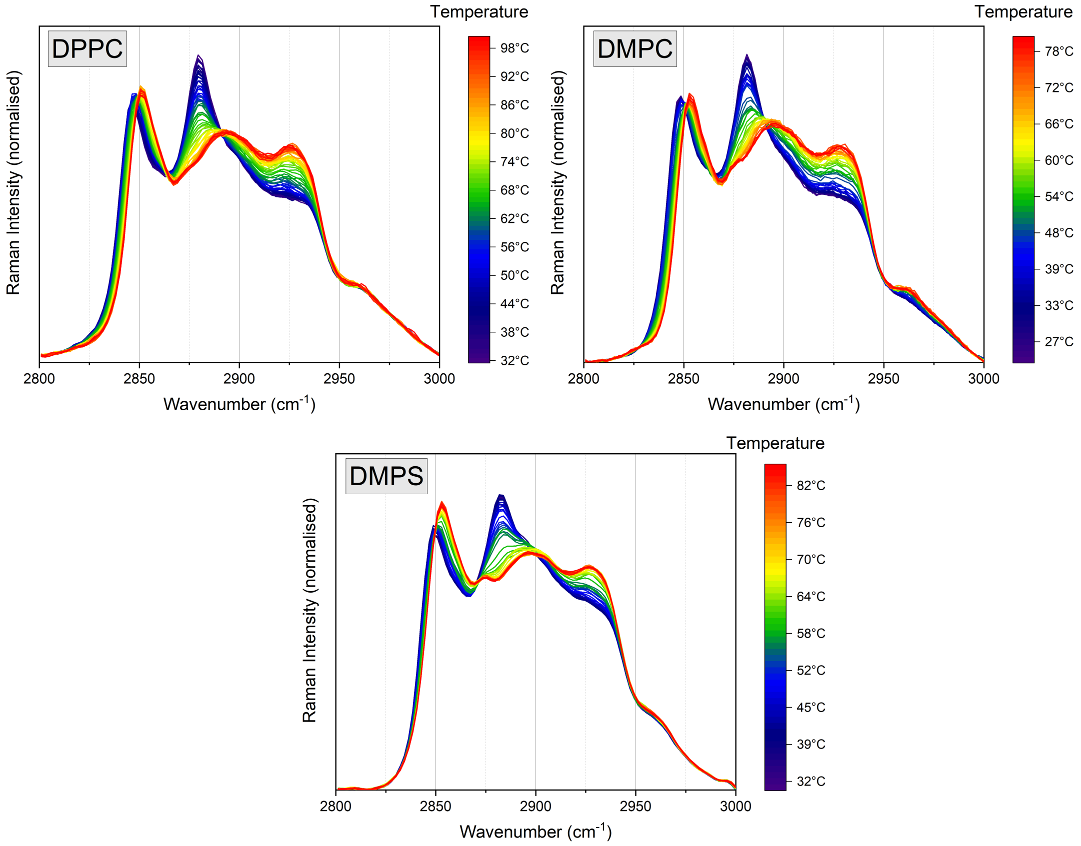

Figure 5.15 Temperature-dependent sets of DCDR spectra in the $C-H$ stretching vibration spectral region for DPPC, DMPC and DMPS covering their phase transition.

dried liposomes) and 84.3 °C (Fourier transform infrared (FTIR) spectroscopy, measured in vacuum, dried liposomes) [94]; 101 °C (DSC, lyophilized lipid sample) [104]. We did not find any information about DMPS. Different experimental approaches were employed to determine the T_m values, mainly for recrystallised or lyophilized lipids, with slightly different results. It is clear, that dried lipids remain in a gel phase towards higher temperatures. And yet, all published temperatures are considerably higher than those determined from our measurements, except monohydrated samples, which indicate that dried lipids are poorly hydrated. The influence of RH on the transition temperature of DPPC was already investigated by nanocalorimetry [103]. It was shown that ambient humidity levels have a profound effect on the transition temperatures. Here, liposomal suspensions were dried and also measured at 55 % RH. Some water molecules were, therefore, still adsorbed in the dried lipid aggregates, and it was not completely anhydrous [105]. We believe, that this is the main source of the difference in the T_m determined by DCDR and already published values. However, we can not forget that we are dealing with dried liposomes. In contrast, most of the studies (except works by Popova) were done on recrystallised or lyophilized samples. For DPPC, it was found that fully hydrated single-shell vesicles and multilamellar dispersion exhibit slightly different T_m and also different cooperativity of phase transition, mainly because of the packing asymmetry by highly curved surfaces [61]. Thus, we cannot exclude the possible influence of sample forms such as dried liposomes and recrystallized or lyophilized lipids on the lipid thermotropic behaviour.

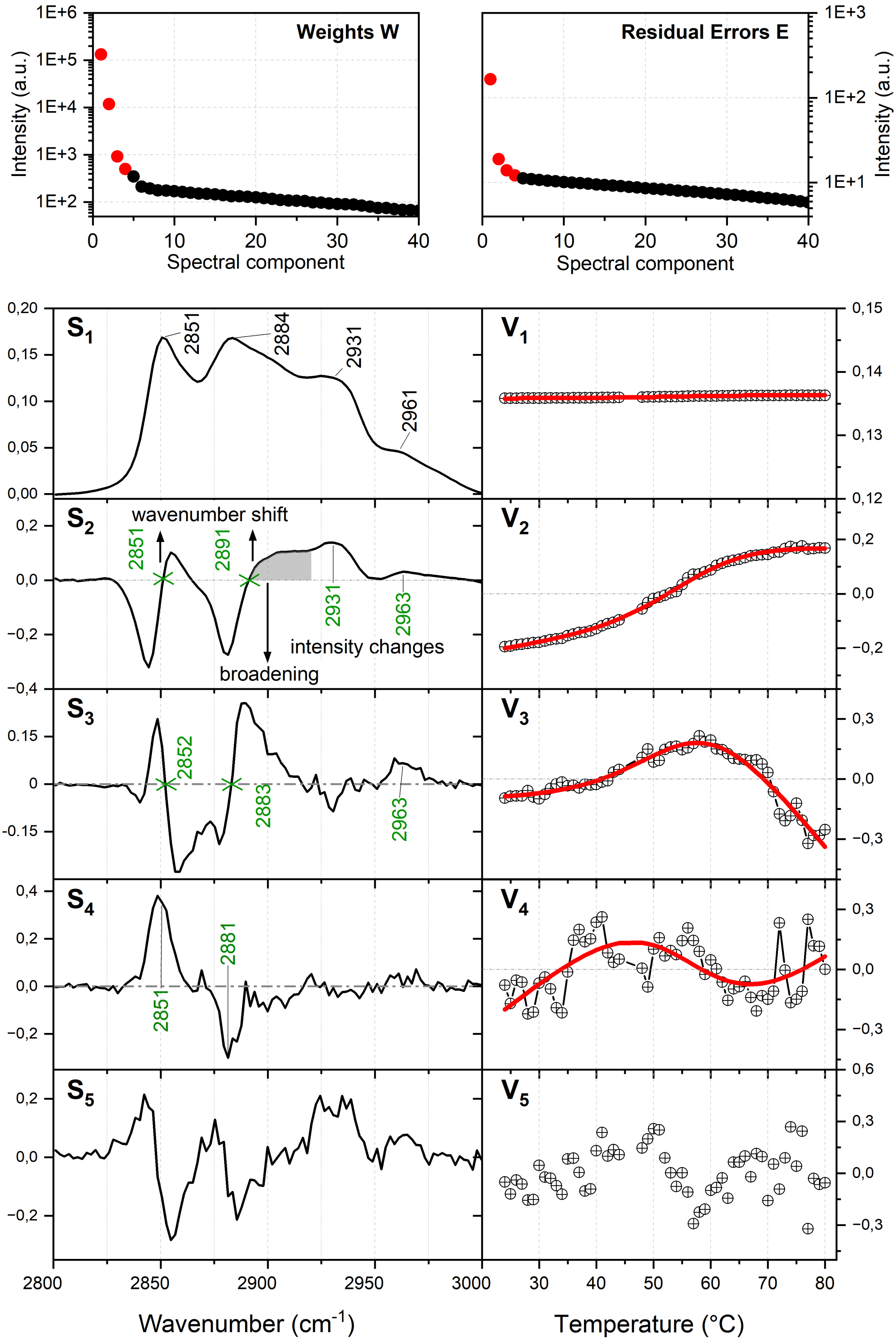

Figure 5.16 Weights (W_j) and residual errors (E_j) together with factor analysis results (first 5 subspectra) applied on temperature-dependant measurements of DMPC homogeneous liposomal suspension dried at 55 % RH monitoring thermotropic phase behaviour. Denotation: S - subspectrum, V - coefficients

Focusing on our results, for choline (DPPC and DMPC), we see an increase of T_{m} about $31 - 33$ °C, whereas, for DMPS, an increase is only about 20 °C. Interestingly, DMPC and DMPS express similar T_{m} if dried but quite different as fully hydrated. These two molecules carry the same acyl chain, but the head groups differ in size, polarity, and charge. Head groups, generally, play an important role in the thermotropic behaviour in fully hydrated lipids, where they are hydrogen-bonded to water, which has an impact on conformational changes induced by heating. Higher T_{m} for hydrated DPPS results from lower hydration compared to DPPC. However, the influence of the poorly hydrated head group on the T_{m} values is lower in the dried aggregates, as can be seen from our results. Further on, we compared theoretical concentration profiles showing the gradual change in phases for each phospholipid (Figure 5.17), calculated from a linear dependence of each phase with temperature (as assumed in the simple two-state model). Focusing on DMPC and DMPS, even though, they express similar T_{m}, we see different progress when heated. Concentration profiles show that phase transition of DMPC is more gradual with temperature and less cooperative than for DMPS, where a change in phases is more abrupt. This suggests that the conformation of the gel phase of dried DMPS liposomal suspension is less sensitive to heating at the beginning than DMPC.

Moreover, we looked into the relative conformational order of dried DMPC and DMPS at temperatures far below (32 °C) and above (80 °C) their phase transition. We compared two intensity ratios (colour-coded in Figure 5.18) in corresponding spectra (calculated from the fit). The ratio of $I[\nu(CH_2)_{\mathrm{s}}]/I[\nu(CH_2)_{\mathrm{as}}]$ is considered to be a sensitive indicator of lateral chain/chain interaction [88], the ratio of $I[\nu(CH_3)_{\mathrm{s}}]/I[\nu(CH_2)_{\mathrm{as}}]$ is correlated to intermolecular chain interactions too, but is also an indication of the mobility of the methyl terminal group of the hydrocarbon chain [106]. These ratios were often used to reflect the conformational order [97, 107, 63]. Generally, the lower the ratios are, the higher the conformational order of hydrocarbon chain is and the lower the mobility of the methyl group. For both temperatures below (32 °C) and above (80 °C) the phase transition, both ratios show that dried DMPC liposomal suspension expresses a higher order of hydrocarbon chain conformation than DMPS. As mentioned before, lipids differ only in the head group region, which clearly has an impact on the different acyl chain packing in dried aggregates. For the PC head group, the diameter of the head group is wider than that of the combined diameters of the two all-*trans* chains. Thus, the chains in fully hydrated bilayer aggregates must be tilted to the extent of the head group to restrict the water access. PS head group is negatively charged and smaller than neutral PC. It results in smaller or no chain tilt whatsoever for the fully hydrated head group. Acyl chains of both lipids are, therefore, packed differently in the liposomal suspension as well. With drying and loss of hydrogen bonds stabilizing liposomes, bilayer thickness generally increases together with a decrease in area per lipid molecule [87]. An increase in bilayer thickness by dehydration was reported before, which is consistent with higher-order conformation [93]. To conclude, the head group region in phospholipids not only plays an important role in stabilizing lipid aggregates in excess water but also has a relevant impact on conformational order in the dried state.

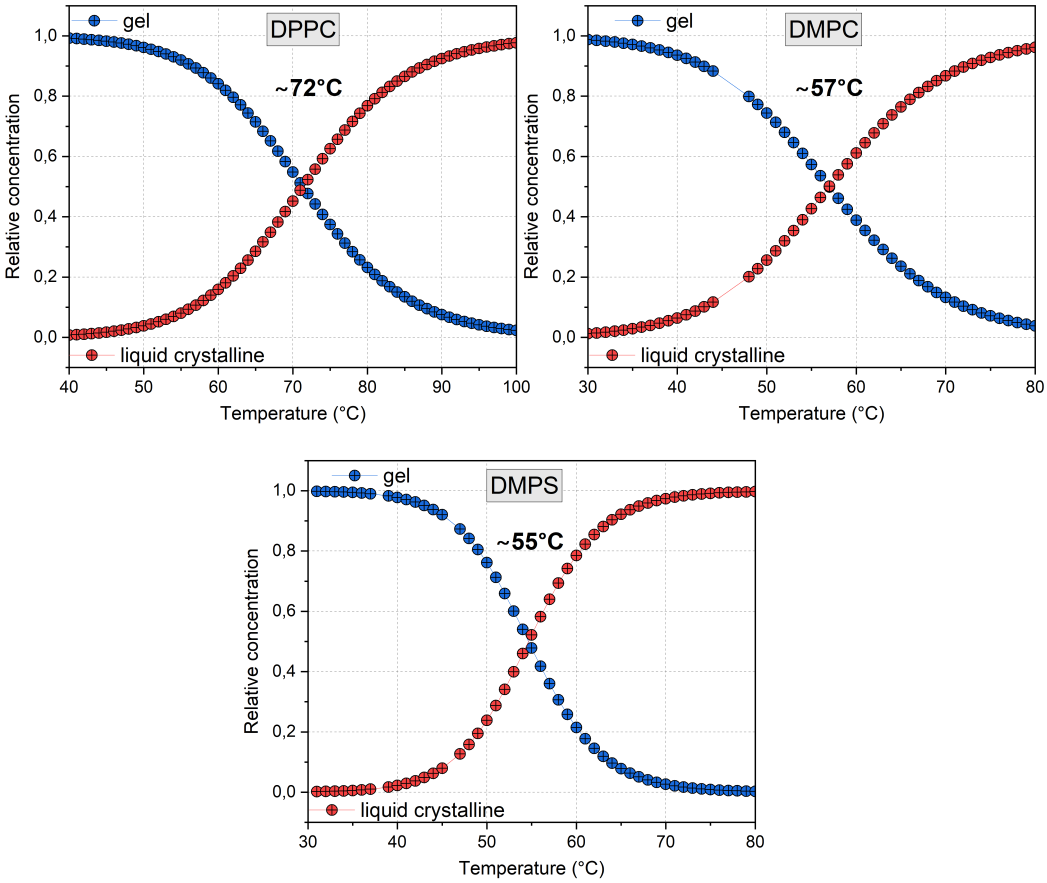

Figure 5.17 Calculated concentration profiles of gel and liquid crystalline phase for DPPC, DMPC and DMPS dried patterns during temperature-dependant measurements.

Finally, we focused on how dried patterns and Raman spectra of DMPC are influenced by the drying of suspension at different RH. Up to now, each drying was held at approximately 55 % RH. Droplets of homogeneous liposomal suspensions of DMPC at the same lipid concentrations of 0.5 mg/ml were left to dry at 55 % and 0.5 % RH. Free drying formed typical coffee-ring dried patterns for both RH, but of different diameters and different structures of the pre-concentrated ring part, as seen in Figure 5.19. The ring formed from DMPC liposomal suspension dried at 55 % RH was wide and consisted of a more pre-concentrated part (r_2 in the Figure 5.19) and less pre-concentrated part (r_1-r_2 in the Figure 5.19 a) in the inner ring side. The dried pattern formed at 0.5 % RH has a bigger diameter by about 0.5 mm and a considerably thinner pre-concentrated ring (r in the Figure 5.19 b) with no sign of non-homogeneous pre-concentrations as for the former pattern. Interestingly, the calculated area covered by pre-concentrated lipids for annulus of r_2 (55 % RH) and r (0.5 % RH) is approximately the same. But, for a pattern formed at 55 % RH, there is an additional less pre-concentrated part in the annulus of (r_1-r_2). Liposomal suspension dried at the lower RH was thus pre-concentrated on the smaller area, which suggests that lipids should be packed more tightly together, presumably with a higher level of conformational order. To compare the conformational order, Raman spectra of $C-H$ stretching vibration were acquired at RT, and respected intensity ratios were calculated as seen in Figure 5.20. These ratios revelead, that liposomal suspension dried at 0.5 % RH

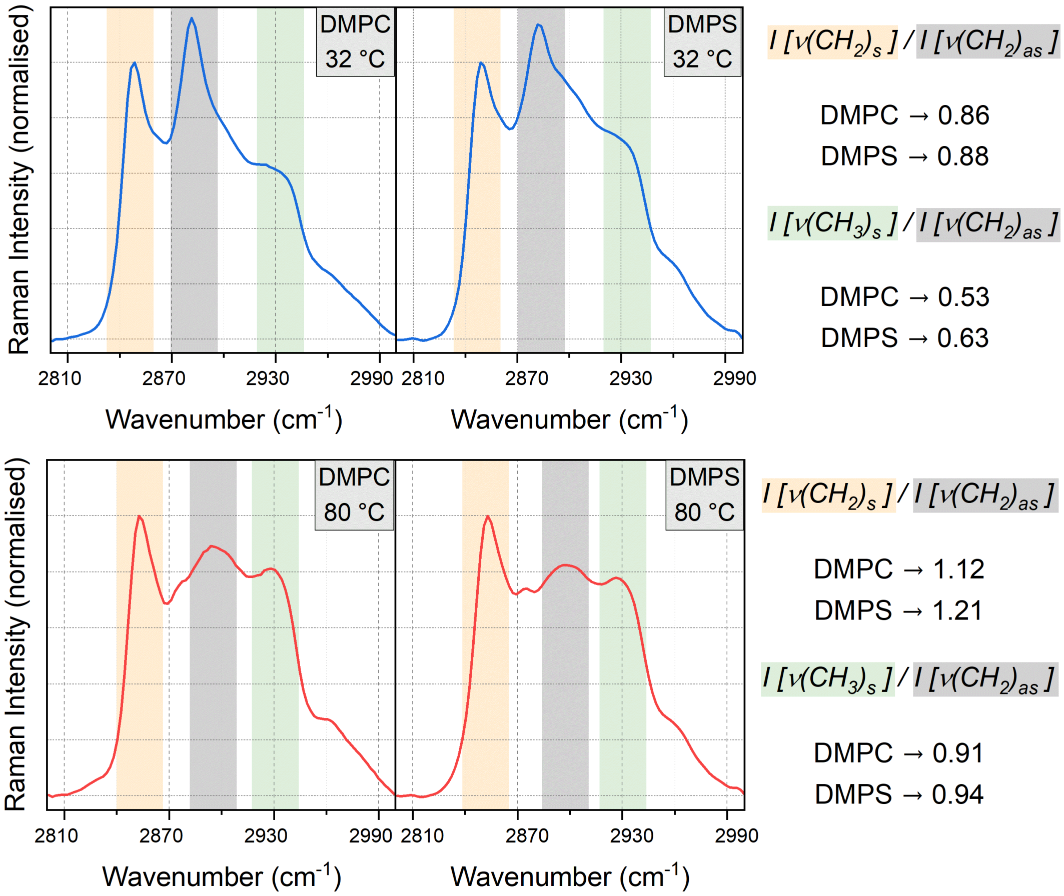

Figure 5.18 Comparison of intensity ratios of bands from $C-H$ stretching vibration region for DMPC and DMPS below (32 °C) and above (80 °C) their phase transition.

at RT is more ordered than liposomal suspension dried at 55 % RH. The results of the observed dried patterns were therefore confirmed. We can conclude that liposomal suspension dried at lower RH expresses a higher conformational order of acyl chains in the gel phase, presumably because lipids are packed tightly together as more water molecules stabilising the structure are evaporated.

To sum up, temperature-dependant measurements showed us the relative importance of the polar head group. Polar head group and, moreover, its hydration directly influences the T_m of fully hydrated lipid aggregates, but it has a lower effect on the value of T_m in the dried state. However, we observed an indirect impact of the head group on the relative conformational order/disorder of hydrocarbon chains for dried liposomal suspension. A smaller PS head group caused a less ordered gel phase together with a less ordered liquid crystalline phase compared to PC. Our results of the T_m values compared to the ones already published showed us the importance of environmental conditions such as RH to the drying process and final dried patterns. Drying of the liposomal suspension at different RH led to different coffee-ring dried patterns. Measuring Raman spectra confirmed that liposomal suspension dried at lower RH is packed more tightly together with higher conformational order for the gel phase.

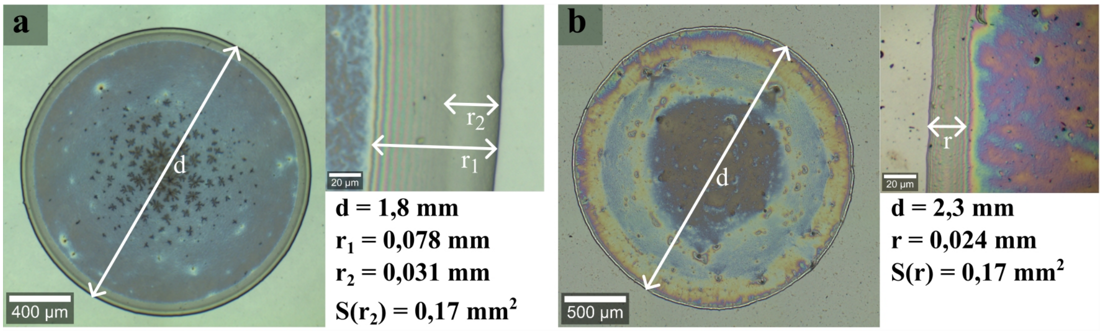

Figure 5.19 White light images of DMPC dried patterns formed a) at 55 % RH and b) at 0.5 % RH, both with their diameters, widths of ring patterns, and the corresponding area of highly pre-concentrated lipids.

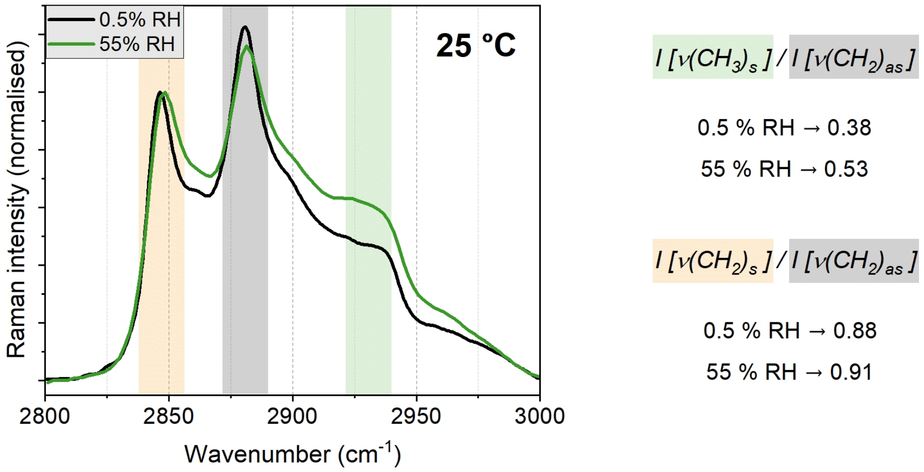

Figure 5.20 Comparison of intensity ratios of bands from $C - H$ stretching vibration region for DMPC dried at 55 % RH and 0.5 % RH.

Conclusion

The thesis focuses on drop coating deposition Raman (DCDR) spectroscopy and the exploration of its potential in the study of biomolecules and biologically important molecules. The first part addresses DCDR's detection capability, where several contaminants were selected. It was shown that pre-concentration in dried patterns was strongly dependent on the deposited concentrations, and for successful detection, the characteristic vibrations of each studied contaminant were assigned. Using commercial substrate, the lowest DCDR detected concentrations in deposited droplets for thiram, bentazone, picloram, and melamine were determined as 0.31 μM, 20 μM and 2 μM, 6.4 μM, respectively. These concentrations represent one or two magnitudes higher concentrations for melamine and thiram than detected by SERS. For bentazone and picloram, no SERS detection limits were reported. DCDR detection of melamine from intentionally blended real infant formula was then investigated. For this purpose, two kinds of powder infant formula were used and tested. Applying DCDR on pure infant formula revealed the spatial segregation of carbohydrates and lipids in circular dried pattern. The ring edge was composed mainly of lipid molecules, and the thin film in the central part was composed mainly of carbohydrates, specifically lactose. From simple melamine-blended model reactions such as melamine mixed with lactose, DOPC and DOPE lipids, lactose was found to be a potent reaction partner for melamine. The DCDR approach applied to the blended infant formula revealed that the melamine compound was present only in the thin film in the central part of the dried patterns together with lactose, confirming its reaction potential even in the mixture. These findings represent a promising utilisation of the DCDR approach as the efficient method for detecting compounds based not only on the successful pre-concentration but also on the spatial distribution throughout the dried pattern, together with the reaction potential between different compounds in the solution mixture.

The next part dealt with the DCDR investigation of liposomal suspensions. Several aspects of the DCDR approach applied to liposomal suspension were discussed, including drying dynamics (smooth/nanoroughened substrate), dried patterns (smooth/nanoroughened substrate, unilamellar homogeneous/non-homogeneous liposome suspension) and its heterogeneity, comparison of DCDR spectra with RTM spectra and lastly the effect of heating (thermotropic phase transition) and RH on the dried pattern. It was discovered that liposomal suspension dried on nanoroughened substrate exhibits a new type of drying dynamics mode, the CR expansion by 10 and 17 % for NpsCu2 and NpsCu4, respectively. CR expansion took place in approximately three-quarters of the complete evaporation time, followed by subsequent shrinking and droplet disappearance. Comparing the coffee-ring patterns formed on smooth and nanoroughened substrates, we observed smaller radii and smaller lateral ring widths and, therefore, better pre-concentration for nanoroughened substrates. Better pre-concentration was confirmed by Raman spectra. Observing dried patterns of different liposomal suspensions, we found that the homogeneity (in liposome size) of suspension and also the saturation of the acyl chain play a role. Monounsaturation caused the formation of small irregularities on the coffee-ring pattern, whether non-homogeneity results in the fully covered circular dried pattern. The formation of dried patterns within the DCDR approach is, therefore, affected by both the selected substrate and the used liposomal suspension. Analyzing the dried patterns by Raman spectroscopy showed us the bands' intensity variations when acquired from different locations. From that, we learnt that the drying process can cause slightly different conformational changes in $C-C$ and $C=C$ bonds throughout the dried pattern. A comparison of DCDR spectra with RTM spectra from fully hydrated liposomes showed us the influence of H-bond loss (on $C=O$ band) and different rotational conformers of $O-P-O$ bonds in a dried and hydrated state.

Finally, by investigating the thermotropic behaviour of dried liposomal suspension monitored by changes in the $C-H$ stretching region, we determined the T_{m} for each studied lipid. We revealed the importance of the headgroup region on the conformational order of lipids and the cooperation of phase transition, even in the dried state. Interestingly, lipids with the smaller PS headgroup had a less ordered acyl chain in the gel phase than PC. Comparing T_{m} with already published values, we supported the importance of external conditions like RH on the final lipid hydration in a dried state, which has a direct impact on T_{m}. We learnt that drying a liposomal suspension at different RH influences the acyl chain packing in the dried pattern. For lower RH, the acyl chain was more tightly packed together, which was confirmed by Raman band intensity ratios.

Bibliography

1. Procházka, M. *Surface-Enhanced Raman Spectroscopy. Bioanalytical, Biomolecular and Medical Applications.* 1st ed. Springer, Cham, 2016. Biological and Medical Physics, Biomedical Engineering. isbn 978-3-319-23992-7. Available from doi: `10.1007/978-3-319-23992-7`.
2. Kočišová, E.; Kuzminova, A.; Kuižová, A.; Hanková, A.; Košutová, T.; Procházka, M.; Kylián, O. V_2O_5 nanoparticle films as a platform for plasmon-free surface-enhanced Raman spectroscopy. *Ceramics International.* 2024, vol. 50, no. 7, Part A, pp. 10026–10033. Available from doi: `10.1016/j.ceramint.2023.12.314`.
3. Itoh, T.; Procházka, M.; Dong, Z.-Ch.; Ji, W.; Yamamoto, Y. S.; Zhang, Y.; Ozaki, Y. Toward a New Era of SERS and TERS at the Nanometer Scale: From Fundamentals to Innovative Applications. *Chemical Reviews.* 2023, vol. 123, no. 4, pp. 1552–1634. Available from doi: `10.1021/acs.chemrev.2c00316`.
4. Kuižová, A.; Kočišová, E. Drop coating deposition Raman (DCDR) spectroscopy of biologically important molecules. *Journal of Raman Spectroscopy.* 2023, vol. 54, no. 7, pp. 694–705. Available from doi: `10.1002/jrs.6524`.
5. Kočišová, E.; Kuižová, A. Drop coating deposition Raman (DCDR) spectroscopy: fundamentals and potential applications. *Applied Spectroscopy Reviews.* 2024, pp. 1–15. Available from doi: `10.1080/05704928.2024.2314534`.
6. Kočišová, E.; Kuižová, A.; Procházka, M. Analytical applications of droplet deposition Raman spectroscopy. *Analyst.* 2024, vol. 149, no. 12, pp. 3276–3287. Available from doi: `10.1039/D4AN00336E`.
7. Zhang, D.; Xie, Y.; Mrozek, M. F.; Ortiz, C.; D., V. J.; Ben-Amotz, D. Raman Detection of Proteomic Analytes. *Analytical Chemistry.* 2003, vol. 75, no. 21, pp. 5703–5709. Available from doi: `10.1021/ac0345087`.
8. Deegan, R. D.; Bakajin, O.; Dupont, T. F.; Huber, G.; Nagel, S. R.; Witten, T. A. Capillary flow as the cause of ring stains from dried liquid drops. *Nature.* 1997, vol. 389, no. 6653, pp. 827–829. Available from doi: `10.1038/39827`.
9. Deegan, R. D.; Bakajin, O.; Dupont, T. F.; Huber, G.; Nagel, S. R.; Witten, T. A. Contact line deposits in an evaporating drop. *Physical Review E.* 2000, vol. 62, no. 1, pp. 756–765. Available from doi: `10.1103/PhysRevE.62.756`.
10. Parsa, M.; Harmand, S.; Sefiane, K. Mechanisms of pattern formation from dried sessile drops. *Advances in Colloid and Interface Science.* 2018, vol. 254, pp. 22–47. Available from doi: `10.1016/j.cis.2018.03.007`.
11. Sefiane, K. Patterns from drying drops. *Advances in Colloid and Interface Science.* 2014, vol. 206, pp. 372–381. Available from doi: `10.1016/j.cis.2013.05.002`.
12. Zhong, X.; Crivoi, A.; Duan, F. Sessile nanofluid droplet drying. *Advances in Colloid and Interface Science.* 2015, vol. 217, pp. 13–30. Available from doi: `10.1016/j.cis.2014.12.003`.

13. Mampallil, D.; Eral, H. B. A review on suppression and utilization of the coffee-ring effect. *Advances in Colloid and Interface Science*. 2018, vol. 252, pp. 38–54. Available from doi: `10.1016/j.cis.2017.12.008`.
14. Kuižová, A.; Přikryl, M.; Procházka, M.; Kočišová, E. Drop coating deposition Raman (DCDR) spectroscopy of contaminants. *Spectrochimica Acta Part A: Molecular and Biomolecular Spectroscopy*. 2021, vol. 262, p. 120109. Available from doi: `10.1016/j.saa.2021.120109`.
15. Kuižová, A.; Kuzminova, A.; Kylián, O.; Kočišová, E. Nanostructured Plasma Polymerized Fluorocarbon Films for Drop Coating Deposition Raman Spectroscopy (DCDRS) of Liposomes. *Polymers*. 2021, vol. 13, no. 22, p. 4023. Available from doi: `10.3390/polym13224023`.
16. Yunker, P. J.; Still, T.; Lohr, M. A.; Yodh, A. G. Suppression of the coffee-ring effect by shape-dependent capillary interactions. *Nature*. 2011, vol. 476, no. 7360, pp. 308–311. Available from doi: `10.1038/nature10344`.
17. Bhardwaj, R.; Fang, X.; Somasundaran, P.; Attinger, D. Self-Assembly of Colloidal Particles from Evaporating Droplets: Role of DLVO Interactions and Proposition of a Phase Diagram. *Langmuir*. 2010, vol. 26, no. 11, pp. 7833–7842. Available from doi: `10.1021/la9047227`.
18. Marin, A.; Liepelt, R.; Rossi, M.; Kähler, Ch. J. Surfactant-driven flow transitions in evaporating droplets. *Soft Matter*. 2016, vol. 12, no. 5, pp. 1593–1600. Available from doi: `10.1039/C5SM02354H`.
19. Zhong, X.; Xie, H.; Duan, F. Deposition patterns from evaporating sessile droplets with suspended mixtures of multi-sized and multi-species hydrophilic and non-adsorbing nanoparticles. *Applied Thermal Engineering*. 2017, vol. 111, pp. 1565–1572. Available from doi: `10.1016/j.applthermaleng.2016.08.040`.
20. Bou Zeid, W.; Brutin, D. Influence of relative humidity on spreading, pattern formation and adhesion of a drying drop of whole blood. *Colloids and Surfaces A: Physicochemical and Engineering Aspects*. 2013, vol. 430, pp. 1–7. Available from doi: `10.1016/j.colsurfa.2013.03.019`.
21. Zurbriggen, L.; Baumgartner, S.; Schaub, N.; Kokornaczyk, M. O. Influence of temperature and relative humidity on patterns formed in dried plasma and serum droplets. *Colloid and Interface Science Communications*. 2022, vol. 49, p. 100645. Available from doi: `10.1016/j.colcom.2022.100645`.
22. Parsa, M.; Harmand, S.; Sefiane, K.; Bigerelle, M.; Deltombe, R. Effect of Substrate Temperature on Pattern Formation of Nanoparticles from Volatile Drops. *Langmuir*. 2015, vol. 31, no. 11, pp. 3354–3367. Available from doi: `10.1021/acs.langmuir.5b00362`.
23. Deegan, R. D. Pattern formation in drying drops. *Physical Review E*. 2000, vol. 61, no. 1, pp. 475–485. Available from doi: `10.1103/PhysRevE.61.475`.
24. Patil, N. D.; Bange, P. G.; Bhardwaj, R.; Sharma, A. Effects of Substrate Heating and Wettability on Evaporation Dynamics and Deposition Patterns for a Sessile Water Droplet Containing Colloidal Particles. *Langmuir*. 2016, vol. 32, no. 45, pp. 11958–11972. Available from doi: `10.1021/acs.langmuir.6b02769`.

25. Still, T.; Yunker, P. J.; Yodh, A. G. Surfactant-Induced Marangoni Eddies Alter the Coffee-Rings of Evaporating Colloidal Drops. *Langmuir*. 2012, vol. 28, no. 11, pp. 4984–4988. Available from DOI: `10.1021/la204928m`.
26. Yildirim Erbil, H. Control of stain geometry by drop evaporation of surfactant containing dispersions. *Advances in Colloid and Interface Science*. 2015, vol. 222, pp. 275–290. Available from DOI: `10.1016/j.cis.2014.08.004`.
27. Thokchom, A. K.; Zhou, Q.; Kim, D.-J.; Ha, D.; Kim, T. Characterizing self-assembly and deposition behavior of nanoparticles in inkjet-printed evaporating droplets. *Sensors and Actuators B: Chemical*. 2017, vol. 252, pp. 1063–1070. Available from DOI: `10.1016/j.snb.2017.06.045`.
28. Zang, D.; Tarafdar, S.; Tarasevich, Y. Y.; Dutta Ch., Moutushi; Dutta, T. Evaporation of a Droplet: From physics to applications. *Physics Reports*. 2019, vol. 804, pp. 1–56. Available from DOI: `10.1016/j.physrep.2019.01.008`.
29. Moffat, J. R.; Sefiane, K.; Shanahan, M. E. R. Effect of TiO2 Nanoparticles on Contact Line Stick−Slip Behavior of Volatile Drops. *The Journal of Physical Chemistry B*. 2009, vol. 113, no. 26, pp. 8860–8866. Available from DOI: `10.1021/jp902062z`.
30. Wong, T.-S.; Chen, T.-H.; Shen, X.; Ho, Ch.-M. Nanochromatography Driven by the Coffee Ring Effect. *Analytical Chemistry*. 2011, vol. 83, no. 6, pp. 1871–1873. Available from DOI: `10.1021/ac102963x`.
31. Kočišová, E.; Petr, M.; Šípová, H.; Kylián, O.; Procházka, M. Drop coating deposition of a liposome suspension on surfaces with different wettabilities: ”coffee ring” formation and suspension preconcentration. *Physical Chemistry Chemical Physics*. 2017, vol. 19, no. 1, pp. 388–393. Available from DOI: `10.1039/c6cp07606h`.
32. Hibshman, J. D.; Clegg, J. S.; Goldstein, B. Mechanisms of Desiccation Tolerance: Themes and Variations in Brine Shrimp, Roundworms, and Tardigrades. *Frontiers in Physiology*. 2020, vol. 11. Available from DOI: `10.3389/fphys.2020.592016`.
33. Lee, Ch.; Bain, C. D. Raman spectra of planar supported lipid bilayers. *Biochimica et Biophysica Acta (BBA) - Biomembranes*. 2005, vol. 1711, no. 1, pp. 59–71. Available from DOI: `10.1016/j.bbamem.2005.02.006`.
34. Czamara, K.; Majzner, K.; Pacia, M. Z.; Kochan, K.; Kaczor, A.; Baranska, M. Raman spectroscopy of lipids: a review. *Journal of Raman Spectroscopy*. 2015, vol. 46, no. 1, pp. 4–20. Available from DOI: `10.1002/jrs.4607`.
35. Uematsu, M.; Shimizu, T. Raman microscopy-based quantification of the physical properties of intracellular lipids. *Communications Biology*. 2021, vol. 4, no. 1, p. 1176. Available from DOI: `10.1038/s42003-021-02679-w`.
36. Rapis, E. A change in the physical state of a nonequilibrium blood plasma protein film in patients with carcinoma. *Technical Physics*. 2002, vol. 47, no. 4, pp. 510–512. Available from DOI: `10.1134/1.1470608`.
37. Gorr, H. M.; Zueger, J. M.; McAdams, D. R.; Barnard, J. A. Salt-induced pattern formation in evaporating droplets of lysozyme solutions. *Colloids and Surfaces B: Biointerfaces*. 2013, vol. 103, pp. 59–66. Available from DOI: `10.1016/j.colsurfb.2012.09.043`.

38. Chen, R.; Zhang, L.; Zang, D.; Shen, W. Blood drop patterns: Formation and applications. *Advances in Colloid and Interface Science*. 2016, vol. 231, pp. 1–14. Available from doi: `10.1016/j.cis.2016.01.008`.
39. Ortiz, C.; Zhang, D.; Xie, Y.; Davisson, V. J.; Ben-Amotz, D. Identification of insulin variants using Raman spectroscopy. *Analytical Biochemistry*. 2004, vol. 332, no. 2, pp. 245–252. Available from doi: `10.1016/j.ab.2004.06.013`.
40. Ortiz, C.; Zhang, D.; Ribbe, A. E.; Xie, Y.; Ben-Amotz, D. Analysis of insulin amyloid fibrils by Raman spectroscopy. *Biophysical Chemistry*. 2007, vol. 128, no. 2, pp. 150–155. Available from doi: `10.1016/j.bpc.2007.03.012`.
41. Filik, J.; Stone, N. Drop coating deposition Raman spectroscopy of protein mixtures. *Analyst*. 2007, vol. 132, no. 6, pp. 544–550. Available from doi: `10.1039/B701541K`.
42. Filik, J.; Stone, N. Analysis of human tear fluid by Raman spectroscopy. *Analytica Chimica Acta*. 2008, vol. 616, no. 2, pp. 177–184. Available from doi: `10.1016/j.aca.2008.04.036`.
43. Filik, J.; Stone, N. Investigation into the protein composition of human tear fluid using centrifugal filters and drop coating deposition Raman spectroscopy. *Journal of Raman Spectroscopy*. 2009, vol. 40, no. 2, pp. 218–224. Available from doi: `10.1002/jrs.2113`.
44. Klener, J.; Hofbauerová, K.; Bartoš, A.; Říčný, J.; Řípová, D.; Kopecký, V. Instability of cerebrospinal fluid after delayed storage and repeated freezing: a holistic study by drop coating deposition Raman spectroscopy. *Clinical Chemistry and Laboratory Medicine*. 2014, vol. 52, no. 5, pp. 657–664. Available from doi: `10.1515/cclm-2013-0800`.
45. Kočišová, E.; Procházka, M.; Štepánek, J.; Mojzeš, P. Interaction of porphyrin/oligonucleotide complex with liposomes studied by drop coating deposition Raman spectroscopy. *Spectroscopy*. 2010, vol. 24, p. 689749. Available from doi: `10.3233/SPE-2010-0452`.
46. Kočišová, E.; Procházka, M. Drop-coating deposition Raman spectroscopy of liposomes. *Journal of Raman Spectroscopy*. 2011, vol. 42, no. 8, pp. 1606–1610. Available from doi: `10.1002/jrs.2915`.
47. Kočišová, E.; Vodáková, A.; Procházka, M. DCDR Spectroscopy as Efficient Tool for Liposome Studies: Aspect of Preparation Procedure Parameters. *Journal of Spectroscopy*. 2012, vol. 27, no. 5-6, p. 182720. Available from doi: `10.1155/2012/182720`.
48. Kočišová, E.; Antalík, A.; Procházka, M. Drop coating deposition Raman spectroscopy of liposomes: role of cholesterol. *Chemistry and Physics of Lipids*. 2013, vol. 172-173, pp. 1–5. Available from doi: `10.1016/j.chemphyslip.2013.04.002`.
49. Šimáková, P.; Kočišová, E.; Procházka, M. Sensitive Raman spectroscopy of lipids based on drop deposition using DCDR and SERS. *Journal of Raman Spectroscopy*. 2013, vol. 44, no. 11, pp. 1479–1482. Available from doi: `10.1002/jrs.4364`.
50. Kočišová, E.; Procházka, M. Drop-coating deposition Raman spectroscopy of porphyrins. *Journal of Raman Spectroscopy*. 2015, vol. 46, no. 2, pp. 280–282. Available from doi: `10.1002/jrs.4637`.

51. Kočišová, E.; Procházka, M.; Vaculčiaková, L. Drop-Coating Deposition Raman (DCDR) Spectroscopy as a Tool for Membrane Interaction Studies: Liposome–Porphyrin Complex. *Applied Spectroscopy.* 2015, vol. 69, no. 8, pp. 939–945. Available from doi: `10.1366/14-07836`.
52. Kočišová, E.; Procházka, M.; Šípová, H. Thiol-modified gold-coated glass as an efficient hydrophobic substrate for drop coating deposition Raman (DCDR) technique. *Journal of Raman Spectroscopy.* 2016, vol. 47, no. 11, pp. 1394–1396. Available from doi: `10.1002/jrs.4961`.
53. Kočišová, E.; Procházka, M. Drop coating deposition Raman spectroscopy of dipicolinic acid. *Journal of Raman Spectroscopy.* 2018, vol. 49, no. 12, pp. 2050–2052. Available from doi: `10.1002/jrs.5493`.
54. Kočišová, E.; Sayedová, S.; Procházka, M. Drop coating deposition Raman scattering of selected small molecules of biological importance. *Journal of Raman Spectroscopy.* 2020, vol. 51, no. 5, pp. 871–874. Available from doi: `10.1002/jrs.5840`.
55. Brown, C. A.; Jeong, K.-S.; Poppenga, R. H.; Puschner, B.; Miller, D. M.; Ellis, A. E.; Kang, K.-I.; Sum, S.; Cistola, A. M.; Brown, S. A. Outbreaks of Renal Failure Associated with Melamine and Cyanuric Acid in Dogs and Cats in 2004 and 2007. *Journal of Veterinary Diagnostic Investigation.* 2007, vol. 19, no. 5, pp. 525–531. Available from doi: `10.1177/104063870701900510`.
56. Ingelfinger, J. R. Melamine and the Global Implications of Food Contamination. *New England Journal of Medicine.* 2008, vol. 359, no. 26, pp. 2745–2748. Available from doi: `10.1056/NEJMp0808410`.
57. Stillwell, W. *Introduction to Biological Membranes: Composition, Structure and Function.* Amsterdam: Elsevier Science, 2016. Second Edition. isbn 978-0-444-63772-7.
58. Haynie, D. T. *Biological Thermodynamics.* Cambridge: Cambridge University Press, 2001. First Edition. isbn 978-0-521-79549-4.
59. Gennis, R. B. *Biomembranes: Molecular Structure and Function.* New York: Springer Science+Business Media, 1989. First Edition. isbn 978-1-4757-2067-9.
60. Cevc, G. *Phospholipids Handbook.* Florida: CRC Press, 1993. First Edition. isbn 978-0-8247-9050-9.
61. Levin, I. W. Vibrational Spectroscopy of membrane assemblies. In: *Advances in Infrared and Raman Spectroscopy.* Ed. by Hester, R. J. H. Clark; E., R. Wiley Heyden, 1984, vol. 11, chap. 1. isbn 0471262676.
62. Fox, Ch. B.; Uibel, R. H.; Harris, J. M. Detecting Phase Transitions in Phosphatidylcholine Vesicles by Raman Microscopy and Self-Modeling Curve Resolution. *Journal of Physical Chemistry B.* 2007, vol. 111, no. 39, pp. 11428–11436. Available from doi: `10.1021/jp0735886`.
63. Sassi, P.; Caponi, S.; Ricci, M.; Morresi, A.; Oldenhof, H.; Wolkers, W. F.; Fioretto, D. Infrared versus light scattering techniques to monitor the gel to liquid crystal phase transition in lipid membranes. *Journal of Raman Spectroscopy.* 2015, vol. 46, no. 7, pp. 644–651. Available from doi: `10.1002/jrs.4702`.
64. Koynova, R.; Caffrey, M. Phases and phase transitions of the phosphatidylcholines. *Biochimica et Biophysica Acta (BBA) - Reviews on*

Biomembranes. 1998, vol. 1376, no. 1, pp. 91–145. Available from DOI: `10.1016/S0304-4157(98)00006-9`.

65. Kučerka, N.; Tristram-Nagle, S.; Nagle, J. F. Closer Look at Structure of Fully Hydrated Fluid Phase DPPC Bilayers. *Biophysical Journal*. 2006, vol. 90, no. 11, pp. L83–L85. Available from DOI: `10.1529/biophysj.106.086017`.
66. Nagle, J. F.; Cognet, P.; Dupuy, F. G.; Tristram-Nagle, S. Structure of gel phase DPPC determined by X-ray diffraction. *Chemistry and Physics of Lipids*. 2019, vol. 218, pp. 168–177. Available from DOI: `10.1016/j.chemphyslip.2018.12.011`.
67. MacDonald, R.; Macdonald, R.; Menco, B.; Takeshita, K.; Subbarao, N.; Hu, L. Small-Volume Extrusion Apparatus for Preparation of Large, Unilamellar Vesicles. *Biochimica et biophysica acta*. 1991, vol. 1061, pp. 297–303. Available from DOI: `10.1016/0005-2736(91)90295-J`.
68. Tatischeff, I.; Larquet, E.; Falcón-Pérez, J. M.; Turpin, P.-Y.; Kruglik, S. G. Fast characterisation of cell-derived extracellular vesicles by nanoparticles tracking analysis, cryo-electron microscopy, and Raman tweezers microspectroscopy. *Journal of Extracellular Vesicles*. 2012, vol. 1, no. 1, p. 19179. Available from DOI: `10.3402/jev.v1i0.19179`.
69. Kruglik, S. G.; Royo, F.; Guigner, J.-M.; Palomo, L.; Seksek, O.; Turpin, P.-Y.; Tatischeff, I.; Falcón-Pérez, J. M. Raman tweezers microspectroscopy of circa 100 nm extracellular vesicles. *Nanoscale*. 2019, vol. 11, no. 4, pp. 1661–1679. Available from DOI: `10.1039/C8NR04677H`.
70. Palacký, J.; Mojzeš, P.; Bok, J. SVD-based method for intensity normalization, background correction and solvent subtraction in Raman spectroscopy exploiting the properties of water stretching vibrations. *Journal of Raman Spectroscopy*. 2011, vol. 42, no. 7, pp. 1528–1539. Available from DOI: `10.1002/jrs.2896`.
71. Malinowski, E. R. *Factor Analysis in Chemistry*. New York: John Wiley and Sons, Inc., 2002. Third Edition. ISBN 0-471-13479-1.
72. Kirchhoff, W. H.; Levin, I. W. Description of the Thermotropic Behavior of the Membrane Bilayers in Terms of Raman Spectral Parameters: A Two-State Model. *Journal of Research of the National Bureau of Standards*. 1987, vol. 92, no. 2, pp. 113–128. Available from DOI: `10.6028/jres.092.012`.
73. Walter, V.; Ruscher, C.; Benzerara, O.; Marques, C. M.; Thalmann, F. A machine learning study of the two states model for lipid bilayer phase transitions. *Physical Chemistry Chemical Physics*. 2020, vol. 22, no. 34, pp. 19147–19154. Available from DOI: `10.1039/D0CP02058C`.
74. Zhu, J.; Chen, Q.; Kutsanedzie, F. Y. H.; Yang, M.; Ouyang, Q.; Jiang, H. Highly sensitive and label-free determination of thiram residue using surface-enhanced Raman spectroscopy (SERS) coupled with paper-based microfluidics. *Analytical Methods*. 2017, vol. 9, no. 43, pp. 6186–6193. Available from DOI: `10.1039/C7AY01637A`.
75. Zheng, J.; He, L. Surface-Enhanced Raman Spectroscopy for the Chemical Analysis of Food. *Comprehensive Reviews in Food Science and Food Safety*. 2014, vol. 13, no. 3, pp. 317–328. Available from DOI: `10.1111/1541-4337.12062`.

76. Ma, J.; Peng, X.; Cheng, K.-W.; Kong, R.; Chu, I. K.; Chen, F.; Wang, M. Effects of melamine on the Maillard reaction between lactose and phenylalanine. *Food Chemistry*. 2010, vol. 119, no. 1, pp. 1–6. Available from DOI: `10.1016/j.foodchem.2009.07.007`.
77. Liu, W.; Cohenford, M. A.; Frost, L.; Seneviratne, C.; Dain, J. A. Non-enzymatic glycation of melamine with sugars and sugar like compounds. *Bioorg Chem*. 2013, vol. 46, pp. 1–9. Available from DOI: `10.1016/j.bioorg.2012.08.004`.
78. Yakes, B. J.; Bergana, M. M.; Scholl, P. F.; Mossoba, M. M.; Karunathilaka, S. R.; Ackerman, L. K.; Holton, J. D.; Gao, B.; Moore, J. C. Effects of Wet-Blending on Detection of Melamine in Spray-Dried Lactose. *Journal of Agricultural and Food Chemistry*. 2017, vol. 65, no. 28, pp. 5789–5798. Available from DOI: `10.1021/acs.jafc.7b00834`.
79. Shanahan, M. E. R.; Bourgès, C. Effects of evaporation on contact angles on polymer surfaces. *International Journal of Adhesion and Adhesives*. 1994, vol. 14, no. 3, pp. 201–205. Available from DOI: `10.1016/0143-7496(94)90031-0`.
80. Bourges-Monnier, C.; Shanahan, M. E. R. Influence of Evaporation on Contact Angle. *Langmuir*. 1995, vol. 11, no. 7, pp. 2820–2829. Available from DOI: `10.1021/la00007a076`.
81. Kratochvíl, J.; Kuzminova, A.; Solař, P.; Hanuš, J.; Kylián, O.; Biederman, H. Wetting and drying on gradient-nanostructured C:F surfaces synthesized using a gas aggregation source of nanoparticles combined with magnetron sputtering of polytetrafluoroethylene. *Vacuum*. 2019, vol. 166, pp. 50–56. Available from DOI: `10.1016/j.vacuum.2019.04.050`.
82. Bai, X.; Xu, L.; Tang, J. Y.; Zuo, Y. Y.; Hu, G. Adsorption of Phospholipids at the Air-Water Surface. *Biophysical Journal*. 2019, vol. 117, no. 7, pp. 1224–1233. Available from DOI: `10.1016/j.bpj.2019.08.022`.
83. Orejon, D.; Sefiane, K.; Shanahan, M. E. R. Stick–Slip of Evaporating Droplets: Substrate Hydrophobicity and Nanoparticle Concentration. *Langmuir*. 2011, vol. 27, no. 21, pp. 12834–12843. Available from DOI: `10.1021/la2026736`.
84. Askounis, A.; Sefiane, K.; Koutsos, V.; Shanahan, M. E. R. The effect of evaporation kinetics on nanoparticle structuring within contact line deposits of volatile drops. *Colloids and Surfaces A: Physicochemical and Engineering Aspects*. 2014, vol. 441, pp. 855–866. Available from DOI: `10.1016/j.colsurfa.2012.10.017`.
85. Rosa, A. S.; Disalvo, E. A.; Frias, M. A. Water Behavior at the Phase Transition of Phospholipid Matrixes Assessed by FTIR Spectroscopy. *The Journal of Physical Chemistry B*. 2020, vol. 124, no. 29, pp. 6236–6244. Available from DOI: `10.1021/acs.jpcb.0c03719`.
86. Chattopadhyay, M.; Krok, E.; Orlikowska, H.; Schwille, P.; Franquelim, H. G.; Piatkowski, L. Hydration Layer of Only a Few Molecules Controls Lipid Mobility in Biomimetic Membranes. *Journal of the American Chemical Society*. 2021, vol. 143, no. 36, pp. 14551–14562. Available from DOI: `10.1021/jacs.1c04314`.

87. Jendrasiak, G. L. The hydration of phospholipids and its biological significance. *The Journal of Nutritional Biochemistry.* 1996, vol. 7, no. 11, pp. 599–609. Available from DOI: `10.1016/S0955-2863(96)00118-0`.

88. Gaber, B. P.; Peticolas, W. L. On the quantitative interpretation of biomembrane structure by Raman spectroscopy. *Biochimica et Biophysica Acta (BBA) - Biomembranes.* 1977, vol. 465, no. 2, pp. 260–274. Available from DOI: `10.1016/0005-2736(77)90078-5`.

89. Meier, R. J.; Csiszár, A.; Klumpp, E. On the Interpretation of the 1100 cm^{-1} Raman Band in Phospholipids and Other Alkyl-Containing Molecular Entities. *The Journal of Physical Chemistry B.* 2006, vol. 110, no. 12, pp. 5842–5844. Available from DOI: `10.1021/jp060420w`.

90. Pasenkiewicz-Gierula, M.; Takaoka, Y.; Miyagawa, H.; Kitamura, K.; Kusumi, A. Hydrogen Bonding of Water to Phosphatidylcholine in the Membrane As Studied by a Molecular Dynamics Simulation: Location, Geometry, and Lipid—Lipid Bridging via Hydrogen-Bonded Water. *The Journal of Physical Chemistry A.* 1997, vol. 101, no. 20, pp. 3677–3691. Available from DOI: `10.1021/jp962099v`.

91. Pasenkiewicz-Gierula, M.; Baczynski, K.; Markiewicz, M.; Murzyn, K. Computer modelling studies of the bilayer/water interface. *Biochimica et Biophysica Acta (BBA) - Biomembranes.* 2016, vol. 1858, no. 10, pp. 2305–2321. Available from DOI: `10.1016/j.bbamem.2016.01.024`.

92. Lee, E.; Kundu, A.; Jeon, J.; Cho, M. Water hydrogen-bonding structure and dynamics near lipid multibilayer surface: Molecular dynamics simulation study with direct experimental comparison. *The Journal of Chemical Physics.* 2019, vol. 151, no. 11. Available from DOI: `10.1063/1.5120456`.

93. O'Leary, T. J.; Levin, I. W. Raman spectroscopic study of the melting behavior of anhydrous dipalmitoylphosphatidylcholine bilayers. *The Journal of Physical Chemistry.* 1984, vol. 88, no. 9, pp. 1790–1796. Available from DOI: `10.1021/j150653a025`.

94. Popova, A. V.; Hincha, D. K. Thermotropic phase behavior and headgroup interactions of the nonbilayer lipids phosphatidylethanolamine and monogalactosyldiacylglycerol in the dry state. *BMC Biophysics.* 2011, vol. 4, no. 1, p. 11. Available from DOI: `10.1186/2046-1682-4-11`.

95. Bicknell-Brown, E.; Brown, K. G.; Person, W. B. Configuration-dependent Raman bands of phospholipid surfaces: 2—Head group and acyl stretching modes in the 800–900 cm^{1} region. *Journal of Raman Spectroscopy.* 1981, vol. 11, no. 5, pp. 356–362. Available from DOI: `10.1002/jrs.1250110513`.

96. Beattie, J. R.; Bell, S. E. J.; Moss, B. W. A critical evaluation of Raman spectroscopy for the analysis of lipids: Fatty acid methyl esters. *Lipids.* 2004, vol. 39, no. 5, pp. 407–419. Available from DOI: `10.1007/s11745-004-1245-z`.

97. Orendorff, Ch. J.; Ducey M. W., Jr.; Pemberton, J. E. Quantitative Correlation of Raman Spectral Indicators in Determining Conformational Order in Alkyl Chains. *The Journal of Physical Chemistry A.* 2002, vol. 106, no. 30, pp. 6991–6998. Available from DOI: `10.1021/jp014311n`.

98. Bicknell-Brown, E.; Brown, K. G.; Person, W. B. Conformation-dependent Raman bands of phospholipid surfaces. 3—head group Ortho-

phosphate stretching vibrations. *Journal of Raman Spectroscopy*. 1982, vol. 12, no. 2, pp. 180–189. Available from DOI: `10.1002/jrs.1250120218`.

99. BOUR, A.; KRUGLIK, S. G.; CHABANON, M.; RANGAMANI, P.; PUFF, N.; BONNEAU, S. Lipid Unsaturation Properties Govern the Sensitivity of Membranes to Photoinduced Oxidative Stress. *Biophysical Journal*. 2019, vol. 116, no. 5, pp. 910–920. Available from DOI: `10.1016/j.bpj.2019.01.033`.
100. KOYAMA, Y.; IKEDA, K. Raman spectra and conformations of the cis-unsaturated fatty-acid chains. *Chemistry and Physics of Lipids*. 1980, vol. 26, no. 2, pp. 149–172. Available from DOI: `10.1016/0009-3084(80)90004-3`.
101. KODAMA, M.; KUWABARA, M.; SEKI, S. Successive phase-transition phenomena and phase diagram of the phosphatidylcholine-water system as revealed by differential scanning calorimetry. *Biochimica et Biophysica Acta (BBA) - Biomembranes*. 1982, vol. 689, no. 3, pp. 567–570. Available from DOI: `10.1016/0005-2736(82)90315-7`.
102. HANDA, T.; ICHIHASHI, C.; NAKAGAKI, M. Polymorphic phase transition and monomolecular spreading of synthetic phospholipids. In: WILKE, W. (ed.). *Frontiers in Polymer Science*. Steinkopff, 1985, pp. 26–31. ISBN 978-3-7985-1698-4.
103. YI, F.; KIM, I. K.; LI, S.; LAVAN, D. A. Hydrated/Dehydrated Lipid Phase Transitions Measured Using Nanocalorimetry. *Journal of Pharmaceutical Sciences*. 2014, vol. 103, no. 11, pp. 3442–3447. Available from DOI: `10.1002/jps.24187`.
104. OWUSU-WARE, S. K.; CHOWDHRY, B. Z.; LEHARNE, S. A.; ANTONIJEVIĆ, M. D. Phase behaviour of dehydrated phosphatidylcholines. *Journal of Thermal Analysis and Calorimetry*. 2017, vol. 127, no. 1, pp. 415–421. Available from DOI: `10.1007/s10973-016-5957-x`.
105. MANSOUR, H. M.; ZOGRAFI, G. The relationship between water vapor absorption and desorption by phospholipids and bilayer phase transitions. *Journal of Pharmaceutical Sciences*. 2007, vol. 96, no. 2, pp. 377–396. Available from DOI: `10.1002/jps.20810`.
106. YELLIN, N.; LEVIN, I. W. Hydrocarbon chain disorder in lipid bilayers: Temperature dependent ram an spectra of 1,2-diacyl phosphatidylcholine-water gels. *Biochimica et Biophysica Acta (BBA) - Lipids and Lipid Metabolism*. 1977, vol. 489, no. 2, pp. 177–190. Available from DOI: `10.1016/0005-2760(77)90137-0`.
107. BISTA, R. K.; BRUCH, R. F.; COVINGTON, A. M. Variable-temperature Raman spectro-microscopy for a comprehensive analysis of the conformational order in PEGylated lipids. *Journal of Raman Spectroscopy*. 2009, vol. 40, no. 4, pp. 463–471. Available from DOI: `10.1002/jrs.2156`.
108. DIEING, T.; HOLLRICHER, O.; TOPORSKI, J. *Confocal Raman Microscopy*. Berlin, Heidelberg: Springer, 2011. First Edition. ISBN 978-3-642-12521-8.

List of Figures

List of Tables

List of Abbreviations

CA	Contact angle
CCA	Constant contact angle
CCR	Constant contact radius
CR	Contact radius
Cryo-Tem	Cryogenic transmission electron microscopy
DCDR	Drop coating deposition Raman
DMPC	1,2-dimyristoyl-sn-glycero-3-phosphocholine
DMPS	1,2-dimyristoyl-sn-glycero-3-phospho-L-serine
DOPC	1,2-dioleoyl-sn-glycero-3-phosphocholine
DOPE	1,2-dioleoyl-sn-glycero-3-phosphoethanolamine
DOPS	1,2-dioleoyl-sn-glycero-3-phospho-L-serine
DPPC	1,2-dipalmitoyl-sn-glycero-3-phosphocholine
DSC	diiferential scanning calorimetry
FAs	Fatty acids
FTIR	Furier transform infrared
IR	Infrared
Mel	Melamine
Nps	Nanoparticles
Nut	Nutrilon
PC	Phosphocholine
PN	Product number
PS	Phosphoserine
PTFE	Polytetrafluoroethylene
RH	Relative humidity
RS	Raman scattering
RT	Room temperature
RTM	Raman tweezer microspectroscopy
SERS	Surface-enhanced Raman scattering
Sun	Sunar
SVD	Singular value decomposition

List of Publications

1. KUIŽOVÁ, A.; PŘIKRYL, M.; PROCHÁZKA, M.; KOČIŠOVÁ, E. Drop coating deposition Raman (DCDR) spectroscopy of contaminants. *Spectrochimica Acta Part A: Molecular and Biomolecular Spectroscopy.* **2021**, vol. 262, pp. 120109. IF 4.3, 13 times cited (by August 22, 2024)
   Author´s contribution: the majority of experimental work, data treatment and analysis and writing the paper
2. KUIŽOVÁ, A.; KUZMINOVA, A.; KYLIÁN, O.; KOČIŠOVÁ, E. Nanostructured Plasma Polymerized Fluorocarbon Films for Drop Coating Deposition Raman Spectroscopy (DCDRS) of Liposomes. *Polymers.* **2021**, vol. 13, no. 22, pp. 4023. IF 4.7, 6 times cited (by August 22, 2024)
   Author´s contribution: the majority of experimental work, data treatment and analysis and writing the paper
3. KUIŽOVÁ, A.; KOČIŠOVÁ, E. Drop coating deposition Raman (DCDR) spectroscopy of biologically important molecules. *Journal of Raman spectroscopy.* **2023**, vol. 54, no. 7, pp. 694-705. IF 2.4, 4 times cited (by August 22, 2024)
   Author´s contribution: part of writing the paper
4. VALÁŠKOVÁ, M., KUIŽOVÁ, A.; KOČIŠOVÁ, E.; PROFANT, V. Insights into thiram fungicide: A comparative study of solution and solid phases through Raman, DCDR, and SERS measurements and DFT simulations. *Journal of Raman Spectroscopy.* **2023**, vol. 54, no. 9, pp. 950-965. IF 2.4, 1 time cited (by August 22, 2024)
   Author´s contribution: part of experimental work, part of data treatment and part of writing the paper
5. KOČIŠOVÁ, E.; KUZMINOVA, A.; KUIŽOVÁ, A.; HANKOVÁ A.; KOŠUTOVÁ T.; PROCHÁZKA, M.; KYLIÁN, O. V_2O_5 nanoparticle films as a platform for plasmon-free surface-enhanced Raman spectroscopy. Ceramics International, **2024**, vol. 50, p. 10026-10033. IF 5.1
   Author´s contribution: part of data treatment
6. KUIŽOVÁ, A.; KOČIŠOVÁ, E. Exploring drying-induced separation of main constituents in melamine-blended milk infant formula using DCDR spectroscopy. *Microchemical Journal.* **2024**, vol. 199, pp. 110206. IF 4.9, 1 time cited (by August 22, 2024)
   Author´s contribution: the majority of experimental work, data treatment, writing the paper
7. KOČIŠOVÁ, E.; KUIŽOVÁ, A. Drop coating deposition Raman (DCDR) spectroscopy: fundamentals and potential applications. *Applied Spectroscopy Reviews.* **2024**, pp. 1-15. IF 5.4, 1 time cited (by August 22, 2024)
   Author´s contribution: part of writing the paper

8. KOČIŠOVÁ, E.; KUIŽOVÁ, A.; PROCHÁZKA, M. Analytical applications of the droplet deposition Raman spectroscopy. *Analyst.* **2024**, pp. 1-15. IF 3.6
   Author´s contribution: part of writing the paper

List of conference abstracts

1. KUIŽOVÁ, A.; KUZMINOVA, A.; KYLIÁN, O.; KOČIŠOVÁ, E.: Drop Coating Deposition Raman Spectroscopy of Liposomes on Substrates with Different Roughness, poster, 27th International Conference on Raman Spectroscopy (ICORS), Long Beach, California, USA, August 14 - 19, 2022
2. KUIŽOVÁ, A.; PŘIKRYL, M.; PROFANT, V.; PROCHÁZKA, M.; KOČIŠOVÁ, E.: Drop coating deposition Raman spectroscopy of contaminants, oral presentation, 19th European Conference on The Spectroscopy of the Biological Molecules (ECSBM), Reims, France, August 29 - September 1, 2022
3. KUIŽOVÁ, A.; KUZMINOVA, A.; KYLIÁN, O.; KOČIŠOVÁ, E.: Drop coating deposition Raman spectroscopy of liposomes, poster, European Symposium on Analytical Spectrometry and 17th Czech - Slovak Spectroscopic Conference (ESAS-CSSC), Brno, Czech Republic, September 4 - 9, 2022
4. KUIŽOVÁ, A.; KUZMINOVA, A.; KYLIÁN, O.; KOČIŠOVÁ, E. Drop Coating Deposition Raman Spectroscopy of Liposomes, flash poster presentation + poster, MKE, 4th Nemzeti Konferencia, Eger, Hungary, July 10 - 12, 2023
5. KUIŽOVÁ, A.; PROFANT, V.; KOČIŠOVÁ, E.: Thermotropic phase transition of dehydrated glycerophospholipids monitored by drop coating deposition Raman spectroscopy (DCDRS), oral presentation, The XXXV European Congress on Molecular Spectroscopy (EUCMOS), Jyväskylä, Finland, August 14 - 17, 2023
6. KUIŽOVÁ, A.; KOČIŠOVÁ, E.: Drop coating deposition Raman spectroscopy (DCDRS) as a tool for rapid determination and identification of contaminants and food additives, flash poster presentation + poster, 12th International Conference on Advanced Vibrational Spectroscopy (ICAVS), Krakow, Poland, August 27 - September 1, 2023
7. KUIŽOVÁ, A.; PROFANT, V.; KOČIŠOVÁ, E.: Thermotropic phase transition of dehydrated phospholipids monitored by drop coating deposition Raman (DCDR) spectroscopy, oral presentation, 18th Czech - Slovak Spectroscopic Conference (CSSC), Kurdějov, Czech Republic, May 27 - 31, 2024
8. KUIŽOVÁ, A.; PROFANT, V.; KOČIŠOVÁ, E.: Exploring thermotropic phase transition of dried phospholipids by droplet deposition Raman spectroscopy, oral presentation, 28th International Conference on Raman Spectroscopy (ICORS), Rome, Italy, July 28 - August 2, 2024

A Attachments

A.1 Confocality - Raman microspectrometer Alpha 300 from WiTec

Here, the confocality of the WITec Raman micro-spectrometer is presented for different combinations of available objectives and laser wavelengths. The nature of confocality in a microscope lies in the limitation of detected light only to the focal plane by placing the pinhole to the image plane. In this manner, the fluorescent background from areas above and below the focal plane is diminished, and the axial resolution is improved. A combination of different objectives and laser wavelengths or gratings adjusts the resulting confocality for a particular Raman microspectrometer [108]. To find out the confocality using Raman microspectrometer Alpha 300 from WiTec, we performed a series of measurements with a thin silicon (Si) slide. Three laser wavelengths (785 nm, 633 nm, 532 nm) were tested with a combination of two objectives (Carl Zeiss 100×/0.9, Carl Zeiss 50×/0.55 LD). For each combination, the series of spectra were acquired with stepwise change in the Z-axis (0.2 μm) linked with the spectral intensity alteration. A distinct Si Raman band at 520 cm^{-1} was used for integral intensity calculation, which was plotted depending on the Z-axis position as pictured on Figure A.1. Individual dependencies were subsequently fitted with peak function to obtain confocality for each measured combination. The measured confocality for each combination can be found in the table A.1.

Table A.1 Experimentally obtained values of confocality

Laser wavelength and used grating	Objectives	
	100×	50× **LD**
785 nm (300 g/mm)	(2.33 ± 0.05) μm	(5.42 ± 0.03) μm
633 nm (300 g/mm)	(1.29 ± 0.01) μm	(3.50 ± 0.02) μm
532 nm (600 g/mm)	(0.82 ± 0.01) μm	(2.66 ± 0.01) μm

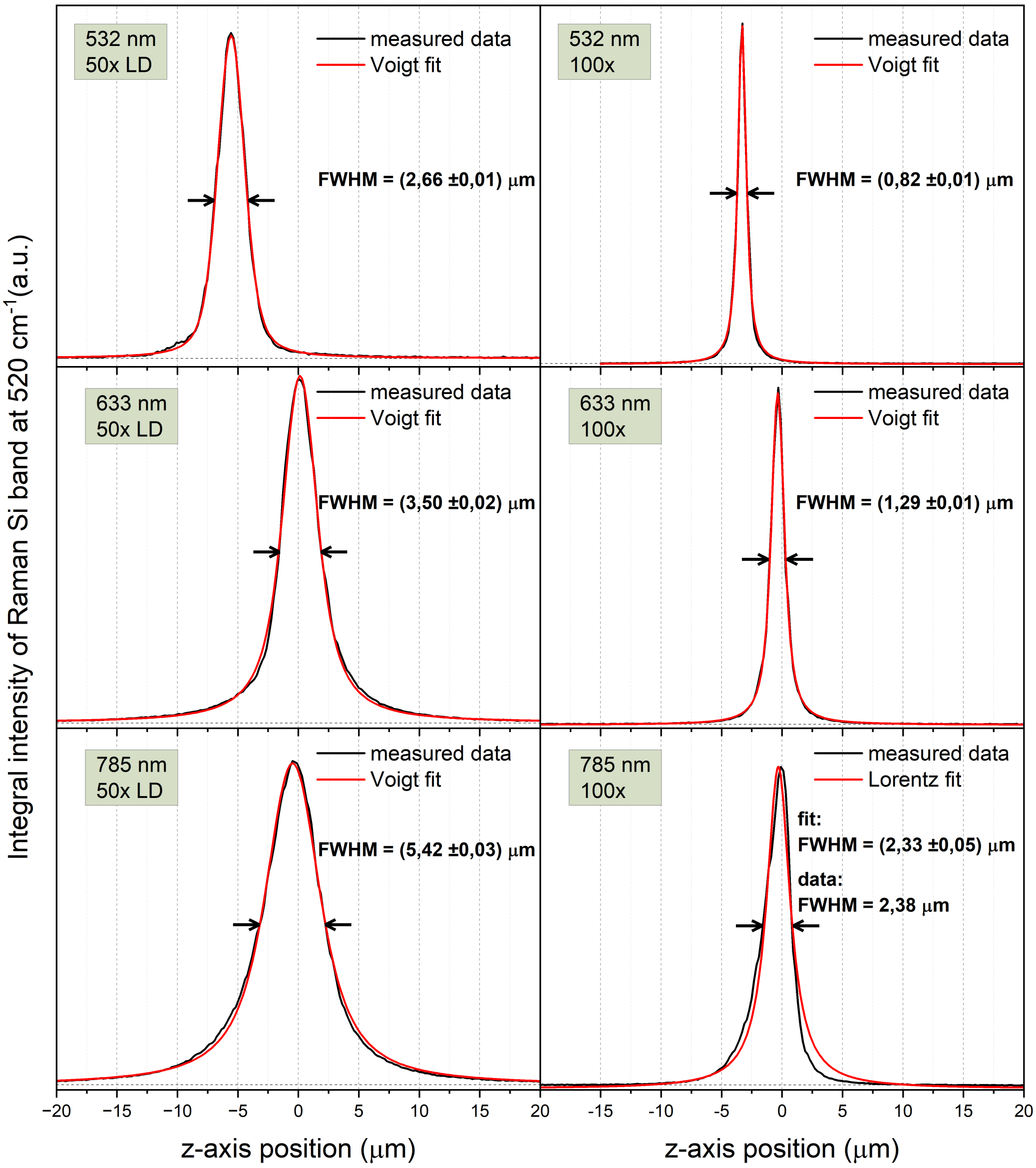

Figure A.1 Confocality for different combinations of used objectives and laser wavelengths employed in Alpha300 Raman microspectrometer from WiTec.

A.2 Supplementary results: factor analysis of DPPC and DMPS

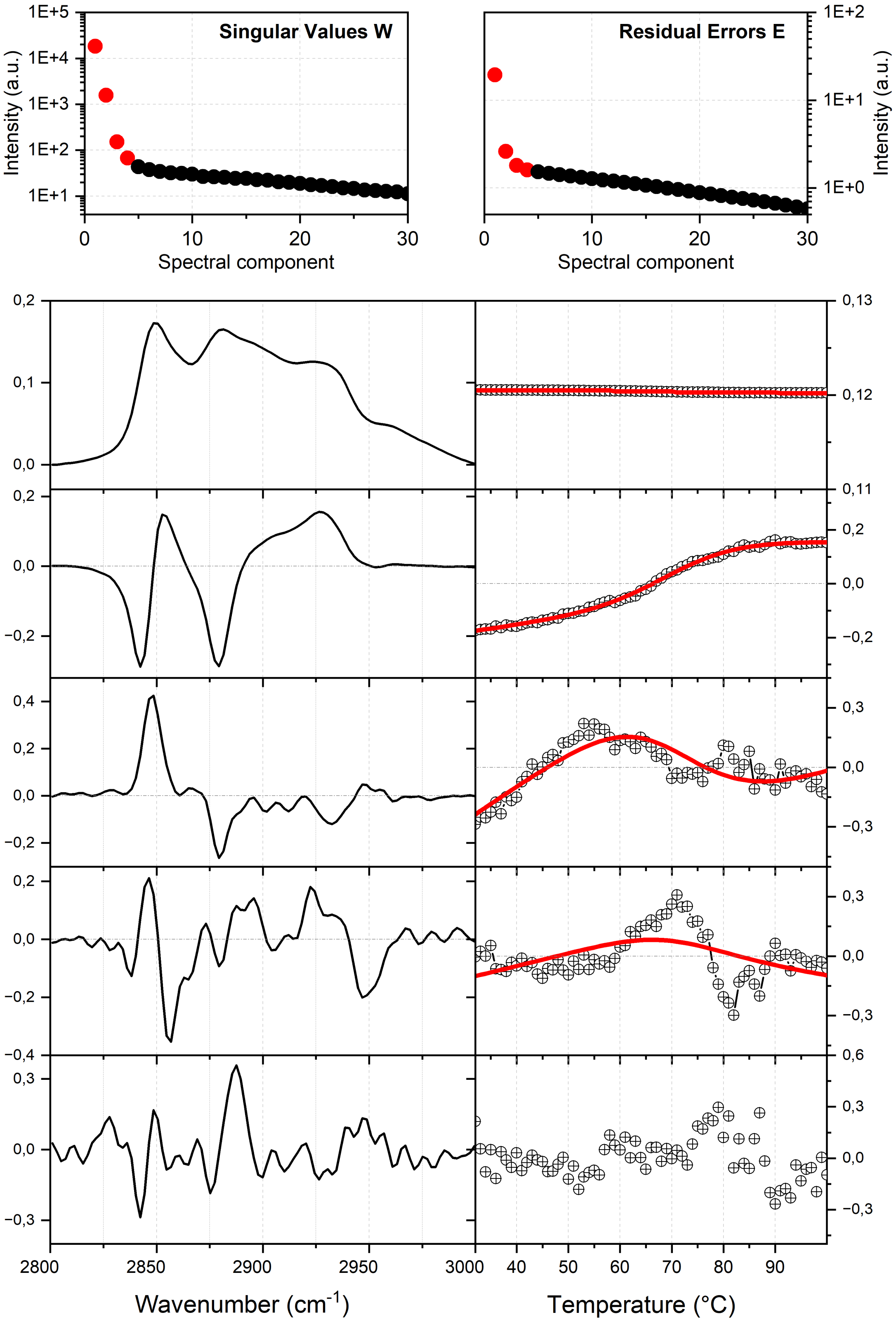

Figure A.2 Weights (W_j) and residual errors (E_j) together with factor analysis results (first 5 subspectra) applied on temperature-dependant measurements of DPPC homogeneous liposomal suspension dried at 55 % RH monitoring thermotropic phase behaviour. Denotation: S - subspectrum, V - coefficients.

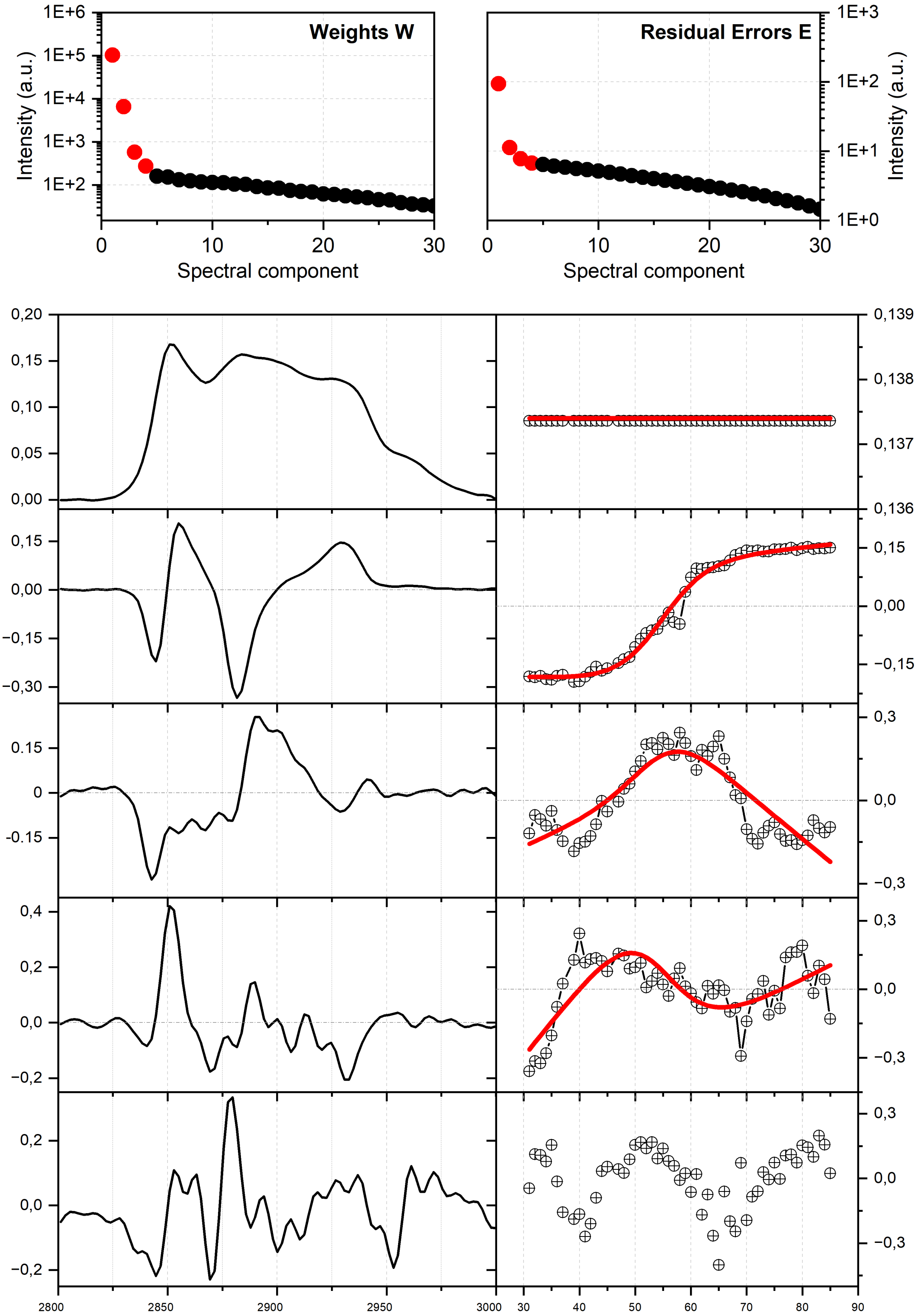

Figure A.3 Weights (W_j) and residual errors (E_j) together with factor analysis results (first 5 subspectra) applied on temperature-dependant measurements of DMPS homogeneous liposomal suspension dried at 55 % RH monitoring thermotropic phase behaviour. Denotation: S - subspectrum, V - coefficients.

A.3 Drop coating deposition Raman (DCDR) spectroscopy of biologically important molecules

KUIŽOVÁ, Alžbeta; KOČIŠOVÁ, Eva. Drop coating deposition Raman (DCDR) spectroscopy of biologically important molecules. *Journal of Raman spectroscopy.* **2023**, vol. 54, no. 7, pp. 694-705.

Available from doi: 10.1002/jrs.6524

Received: 17 January 2023 | Revised: 27 March 2023 | Accepted: 28 March 2023

DOI: 10.1002/jrs.6524

MINI REVIEW

Journal of RAMAN SPECTROSCOPY WILEY

Drop coating deposition Raman (DCDR) spectroscopy of biologically important molecules

Alžbeta Kuižová | **Eva Kočišová**

Faculty of Mathematics and Physics, Institute of Physics, Charles University, Prague 2, Czech Republic

Correspondence
Eva Kočišová, Charles University, Faculty of Mathematics and Physics, Institute of Physics, Ke Karlovu 5, 121 16, Prague 2, Czech Republic.
Email: kocisova@karlov.mff.cuni.cz

Funding information
Charles University, Grant/Award Number: UNCE/SCI/010; Grantová Agentura, Univerzita Karlova, Grant/Award Number: 290120

Abstract

Drop coating deposition Raman (DCDR) spectroscopy introduces a simple and easily accessible approach to studying biologically important molecules and their mixtures. The method is based on drying a small drop of solution or suspension of studied molecules deposited on a special hydrophobic surface. The drying process efficiently accumulates the molecules in the 'coffee-ring' or any small pattern from which the Raman spectrum can be measured. In this way, a significant (several orders of magnitude) improvement of the Raman detection sensitivity compared with Raman measurement from solution can be reached. Therefore, a small sample volume (several microliters), as well as a low initial concentration of studied molecules in deposited droplets, are important advantages of the DCDR method over the normal Raman one. Recently, many relevant DCDR applications on biomolecules and related molecules have been reported. The mini-review covers a brief overview of the DCDR method (principle, short history, suitable hydrophobic surfaces and state-of-the-art). It will be followed by a summary of the studies over the last 15–20 years on different biologically important molecules, including proteins, lipids (in the form of liposomes) and small molecules (e.g., porphyrins, anthrax marker dipicolinic acid and food and environmental contaminants). Finally, the application potential and further perspectives of the DCDR method for biomolecular studies will be discussed.

KEYWORDS

biomolecule, DCDR, drop coating deposition Raman, hydrophobic substrate

1 | INTRODUCTION

Raman spectroscopy, since the period of its intensive development, has been a powerful tool in the study of the structure and function of various molecules and their mixtures. However, this capability is obviously hampered by a weak Raman scattering cross-section related to a demand for relatively highly concentrated samples (>1 mM) and large quantities of analyte (>1 μg). Moreover, in the case of biological molecules, these high concentrations do not correspond to physiological conditions. The intensity of Raman scattering may be increased by resonance and/or surface-enhancement techniques. The surface-enhanced Raman spectroscopy (SERS) is an efficient possibility to overcome this disadvantage, which provides enhancement over 10^5 for molecules adsorbed on nanostructural metal (such as gold or silver) surfaces.[1] The properties of the 'SERS-active' substrates affect both Raman enhancement and spectral reproducibility. Although this method is nowadays widely and fruitfully applied in various studies and applications, its use is often not straightforward and generally not possible for any molecule. Moreover, both resonance Raman and SERS techniques have more restricted applicability because of the problems with spectral variations, increased background and the possibility of photochemical damage. Therefore, there is a need to develop a different approach to obtain their normal Raman spectra from low-concentrated samples, such as the drop coating deposition Raman (DCDR) method.

A potential inspiration trigger for the development of the DCDR method was the paper by Deegan et al. published in the journal *Nature* in 1997.[2] This study was focused on a commonly known phenomenon (and physics background as well) about the formation of a ring-like deposit known as 'coffee-ring' when a spilt drop of coffee is evaporated on a solid surface. They stated that the necessary condition for such kind of deposit is a surface with a non-zero contact angle for a deposited liquid sample and the subsequent creation of a drop contact line that is pinned to its initial position. Despite the fact that the evaporation process does not always lead to the 'coffee-ring' formation, this work pointed out the phenomenon of a sample preconcentration, which was later applied in the DCDR method.

2 | PRINCIPLE OF THE DCDR METHOD

The DCDR method is based on a simple idea of a deposition of a small volume (drop or droplet) of solution or suspension containing molecules of interest on a solvophobic (hydrophobic for aqueous solution) surface (in the following text referred to as a substrate) (Figure 1A). Due to the drying process and subsequent preconcentration of the analyte, the dried samples form a pattern of different forms: (i) a 'coffee-ring', (ii) small (somewhat spherical) spots. The formed pattern can contain amorphous parts as well as small crystals (Figure 1B). The 'coffee-ring' is formed if the evaporating droplet has a pinned contact line, which causes that liquid evaporated from the periphery of the droplet to be replenished by the liquid from the interior.[2] The resulting flow can virtually carry all dispersed material to the edge, where a ring of sample molecules is formed. In contrast, the small spots are observed when deposited drops have less tendency to pin to the surface, so the droplets will remain almost spherical as they shrink during evaporation.[3] The most commonly used solvent is water or some organic substances such as ethanol. After the droplet deposition and completion of the evaporation, the formed

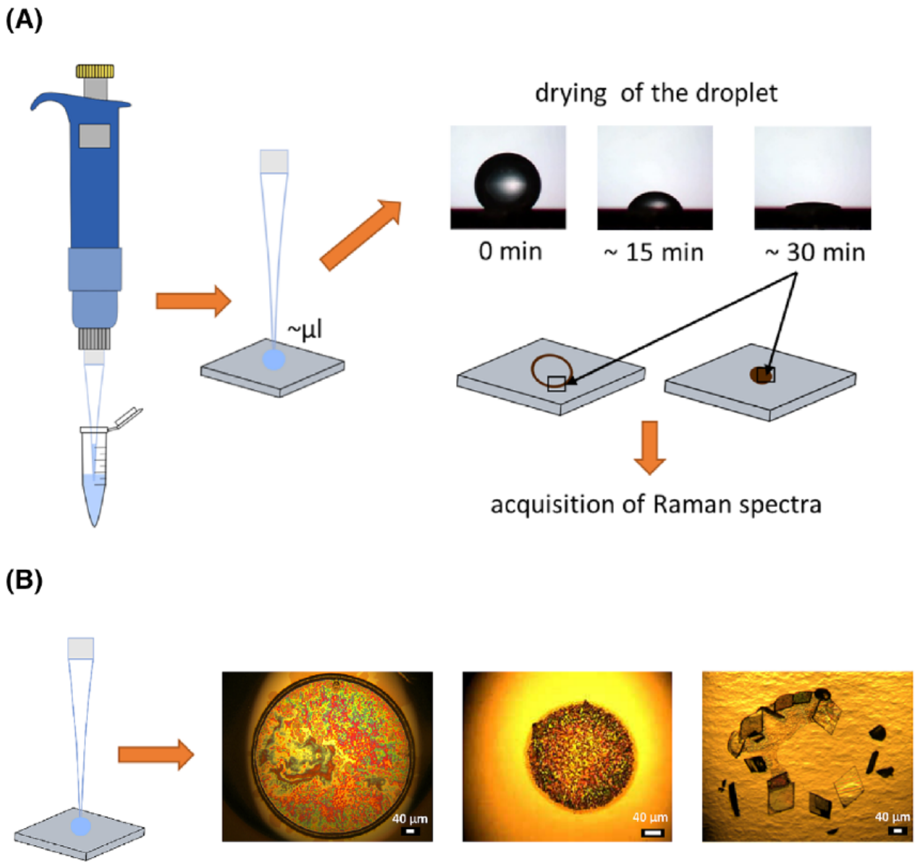

FIGURE 1 (A) The scheme of the drop coating deposition Raman (DCDR) experiment: taking of a small sample volume (a droplet) by micropipette, the droplet deposition on the substrate and drying, followed by the Raman spectrum acquisition, and (B) examples of patterns formed after completion of the evaporation, from left to right: a 'coffee-ring', small homogenous spot and a set of small crystals. [Colour figure can be viewed at wileyonlinelibrary.com]

dried deposit is solvent free. When placed under a microscope objective, a normal Raman spectrum is measured from the preconcentrated dried parts in the deposit. This way, high quality spectra can be obtained from low concentrated samples at small initial volumes (a few microliters are sufficient), which improves the sensitivity several times when compared with normal Raman measurement from a solution or suspension.

3 | DIFFERENT TYPES OF DCDR SUBSTRATES

Choosing a suitable substrate is an integral part of the DCDR experiment. Substrate wettability, that is, the extent to which a drop of deposited sample covers its surface, affects the drying process and so the final appearance of the pattern. Generally, the formed pattern is always the result of the interplay among more factors, such as the type of molecular solution or suspension (analyte), the sample concentration and the chosen substrate. The substrate wettability is characterised by a contact angle and influences the size of the formed pattern and thus the analyte preconcentration (Figure 2). Smaller patterns with more preconcentrated samples give rise to Raman spectra of higher intensity. In this way, we can reduce the detection limit, significantly improve (several orders of magnitude) the detection sensitivity and consequently extend the usefulness of Raman spectroscopy for biomolecules in biologically relevant concentrations.

One of the most frequently mentioned and experimentally used substrates is a commercial SpectRIM™ Slide (Tienta Sciences; see Figure 2B, a). It consists of a 3 × 1 × 0.1 in. plastic carrier with an optically flat stainless steel plate coated with an ultra-thin (50 nm) hydrophobic layer providing a contact angle of 122° for a drop of water. The substrate is chemically inert and highly solvophobic, making them ideal for DCDR spectroscopy from dilute solutions in polar solvents. However, the SpectRIM™ Slide substrate is no longer commercially

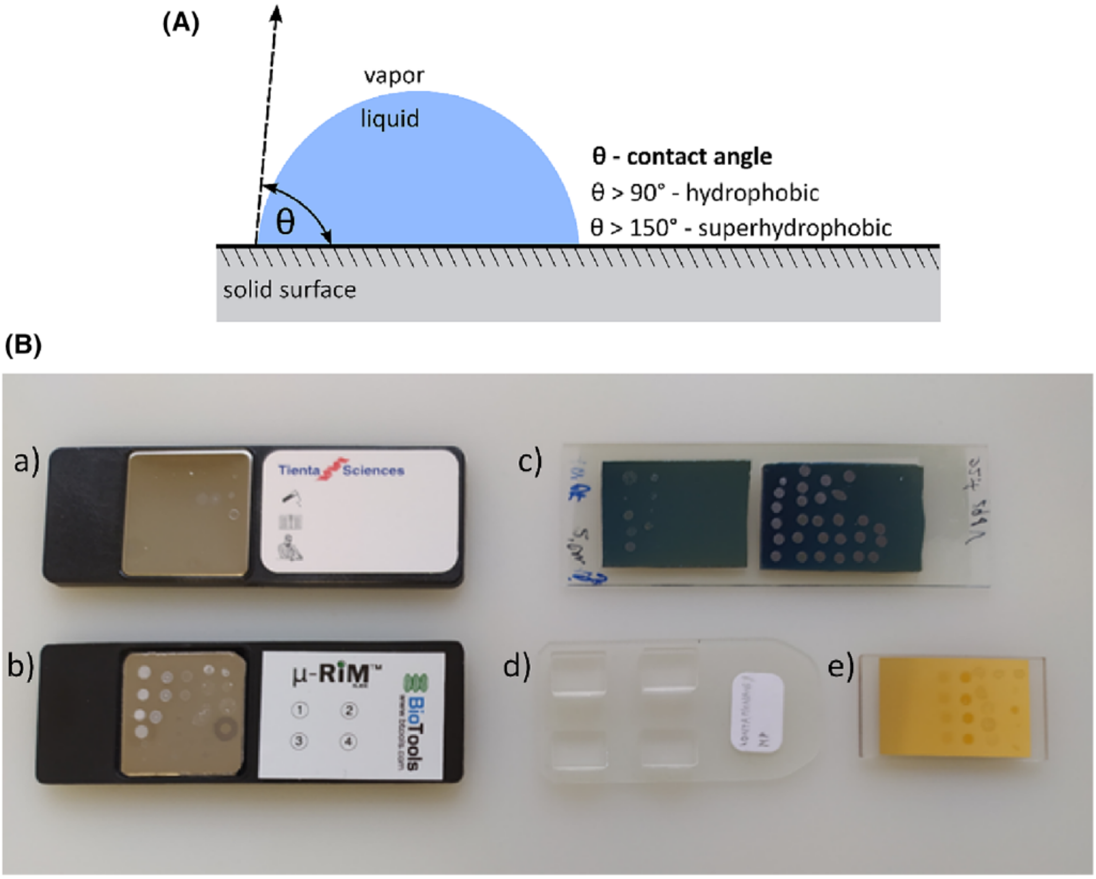

FIGURE 2 (A) The scheme of the deposited droplet and its contact angle and (B) examples of drop coating deposition Raman (DCDR) substrates (with corresponding contact angles for a drop of water): commercial (a) SpectRIM™ (122°) and (b) μRIM™ (108°) and non-commercial (c) nanostructured platform with metal nanoparticles overcoated with plasma polymerised fluorocarbon films prepared by magnetron sputtering (can be tailored in the range from hydrophobic to superhydrophobic), (d) polished CaF$_2$ plate (90°) and (e) thiol-modified gold coated glass (110°). [Colour figure can be viewed at wileyonlinelibrary.com]

available. Another one currently at disposal is a μRIM™ from BioTools (see Figure 2B, b), which is less hydrophobic with a contact angle of 108°.

The non-commercial home-made substrates profiting from the hydrophobic character of smooth fluorocarbon coating (with a contact angle of ~108°) represent a promising platform for DCDR spectroscopy. The modification of this class of hydrophobic substrates is represented by nanostructured platforms with metal nanoparticles that are sandwiched in plasma polymerised fluorocarbon films prepared by magnetron sputtering (Figure 2B, c). The presence of nanoparticles, depending on their type (copper or silver), size and amount significantly increases the roughness of the surface and thus the contact angle of the deposited droplet. It was demonstrated that surface roughness is a key parameter that governs higher wettability. In this way, highly hydrophobic as well as superhydrophobic substrates can be fabricated.[4,5]

The other non-commercial DCDR substrates include polished CaF_2 plates, silanised glass surfaces, quartz slides, gold foil, thiol-modified gold-coated glass and so forth (Figure 2B, d, e) or polytetrafluorethylene tape as a law-cost hydrophobic substrate.[6–8] Their contact angles for water droplets vary in the range of 80–120°. With a higher contact angle, the preconcentration of the analyte is more efficient.[6]

From the point of view of the Raman spectra acquisition, it is important that the substrate itself has minimal background signal in the desired spectral region. The thin fluorocarbon layer displays no apparent Raman or fluorescence signal and so ensures that the analyte spectra are of good quality. Moreover, the presence of polished stainless steel acts as a mirror and significantly increases the acquired signal. According to our experiences, the substrates based on stainless steel plate coated with a fluorocarbon hydrophobic layer are the best ones for DCDR spectroscopy. Concerning other substrates, the Raman background from the glass surfaces can be substantially reduced by gold coating, and for CaF_2 plates with a Raman band at 322 cm^{-1}, subtraction methods can be used.

4 | DCDR STUDIES OF BIOMOLECULES AND BIOLOGICALLY IMPORTANT MOLECULES

The group of Dor Ben-Amotz from Purdue University was the first to start DCDR experiments with a focus on biologically important molecules, especially on amino acids, peptides and proteins. This work resulted in several exciting pivotal papers published in the years 2003–2010. The strong motivation was to show that non-enhanced Raman scattering spectra of high quality can also be obtained from the samples in low concentrations. They described the main features and advantages of the DCDR experiment in the context of normal Raman measurements from solution or SERS as well. The potential of DCDR detection, thus the measurement under conditions compatible with chromatographic and mass spectroscopic proteomic separation and sensing methods were successfully introduced.[9]

The pioneering work of Zhang et al. in 2003[9] on the protein samples of lysozyme and human insulin demonstrated the possibility of measuring reproducible, high-quality normal Raman spectra from femtomole quantities of only micromolar concentrations. It represents over a 1000-fold increase in the sensitivity of normal Raman spectroscopy from protein solutions. Moreover, the measured DCDR spectra were practically identical to those measured from protein solutions in higher concentrations. Therefore, it seems that proteins maintain their structure from solution when drying. Another work of Zhang et al.[10] discussed the DCDR approach as a physical segregation method enabling the reduction of fluorescence interference from the spectra of impure solids and liquid mixtures. DCDR can serve as a method for separating proteins from other solution components, such as buffers and impurities (mainly fluorescent ones).[10] The effectiveness of the method derives from the fact that components in the deposited solution tend to precipitate in different regions on the DCDR substrate. A possible kinetic contribution to segregation is the ‘coffee-ring’ effect induced by convecting streaming during the evaporation of deposited liquid droplet. This was presumed to be an important driving force for the observed tendency of protein accumulation in the edge ring of the pattern. The formation of crystals may also contribute to spatial segregation, as the substances with different crystallisation rates tend to deposit separately. The dissimilar solubilities of solution components play another important role in a segregation process. Proteins that are relatively insoluble precipitate earlier during the evaporation process, and highly soluble components of buffers (almost salts) remain in the evaporating droplet much longer. These components deposit inside the formed pattern around its central part.[10] However, it seems that described chemical segregation during the drying process is not universal. For example, compounds having a strong chemical affinity for each other are assumed not to segregate into different substrate regions. Similarly, systems that do not crystallise easily, such as sugars, tend to retain fluorescent impurities even after drying.[10] These studies include lysozyme, insulin, myoglobin, O-phospho-L-serine and glycan isomers.[9–11]

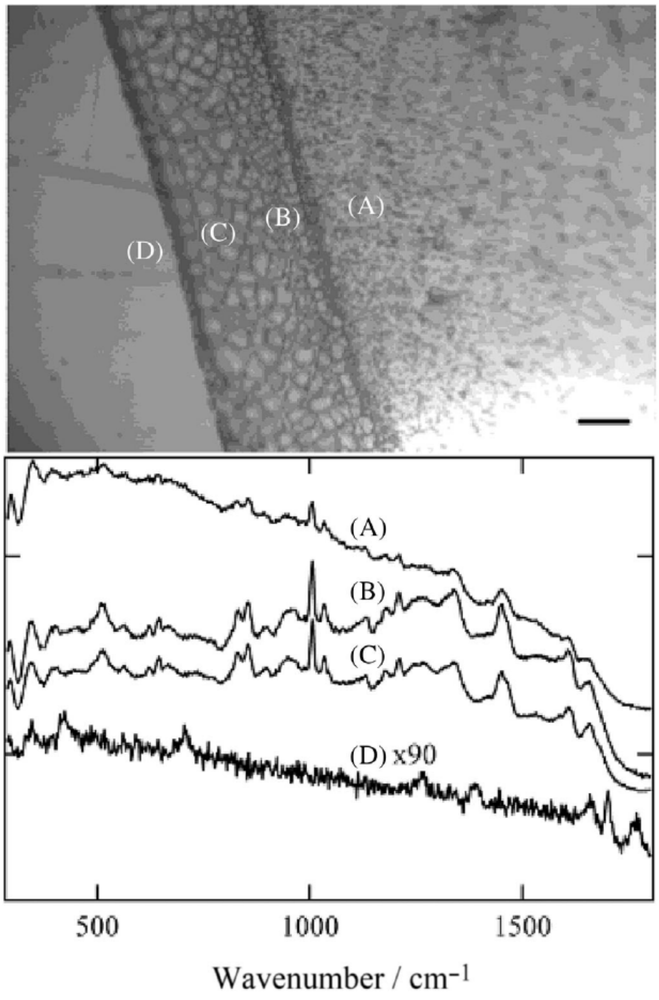

FIGURE 3 An example of drop coating deposition Raman (DCDR) study on human insulin sample. Upper part represents the white light image of human insulin (10 μL of 100 μM solution) deposited on a nominally flat gold substrate. Bottom part is a DCDR spectra (a–d) acquired from the corresponding positions shown in the above image (with an integration time of 50 s, and the bar represents 50 μm). Reproduced with permission from Zhang et al.[9]

Formation of the 'coffee-ring' pattern is typically observed for proteins and liposomes (will be mentioned later). A representative example of such a pattern is in the upper part of Figure 3.[9] The white light image shows 'coffee-ring' in detail originating from the sample of human serum albumin deposited on a flat gold substrate. The bottom part of Figure 3 depicts DCDR spectra obtained from the ring deposit and positions outside and inside the ring structure. Acquired spectra profiles confirm the preconcentration of the analyte in the ring structure. However, the Raman spectrum measured from the inner part of the ring indicates that the thin layer of material also remains inside the drying pattern. The spectrum obtained from the bare substrate (the outer part of the ring) shows no Raman signal from the protein. The structure of the dried ring itself was also the subject of interest. Kopecký and Baumruk[12] studied ring patterns formed from deposited protein (albumin) solution. They concluded that reproducible DCDR spectra should be collected from central or slightly inner parts of the ring structure.

Ortiz et al. worked on three insulin variants (human, bovine and porcine) that differed by one to three amino acid residues,[13] lysozyme, ovalbumin, b-lactoglobulin,[14] and insulin amyloid fibrils.[15] Results showed the usefulness of the DCDR method in the identification of proteins of slightly different amino acid composition. This spectroscopic identification and the classification of the close molecular variants were made after using suitable data treatment. A normalised second derivative preprocessing and a multivariate partial least squares classification algorithm were successfully employed in the case of insulin variants.[13] Moreover, the authors emphasised (i) the high quality and the reproducibility of the DCDR spectra, (ii) the absence of photochemical and thermal sample damage induced by the laser excitation under typical DCDR data collection conditions and (iii) the similarities between DCDR spectra and Raman spectra from solution.[14]

DCDR method was further used to detect spectral changes induced by the phosphorylation of tyrosine amino acid residues in four peptides with sequences derived from the human protein-tyrosine kinase p60c-src.[11,16] The degree of tyrosine phosphorylation in peptide mixtures was determined using DCDR spectra combined with partial least squares multivariate calibration treatment. Following pH-dependent DCDR measurements of peptide confirmed that this method can be employed to obtain information on conformational changes induced by changes in pH in both the phosphorylated and unphosphorylated states.[17] DCDR approach can also be a part of the screening and the characterisation of protein-ligand binding detection.[18]

An important part of published papers includes DCDR experiments on mixtures and complex (real) samples, which have been published since 2007. Filik and Stone analysed changes in the relative protein concentrations of protein mixtures composed of lysozyme, lactoferrin and albumin.[19] They showed that the combination of the DCDR method and principal components analysis is sensitive and suitable for the detection of small changes in the relative protein concentrations. The same authors published other DCDR studies on the analysis of human tear fluid (Figure 4), which is a complex solution containing proteins, metabolites, electrolytes and lipids as well.[20,21] This work confirmed that the DCDR method could provide a fingerprint of the tear protein and lipid

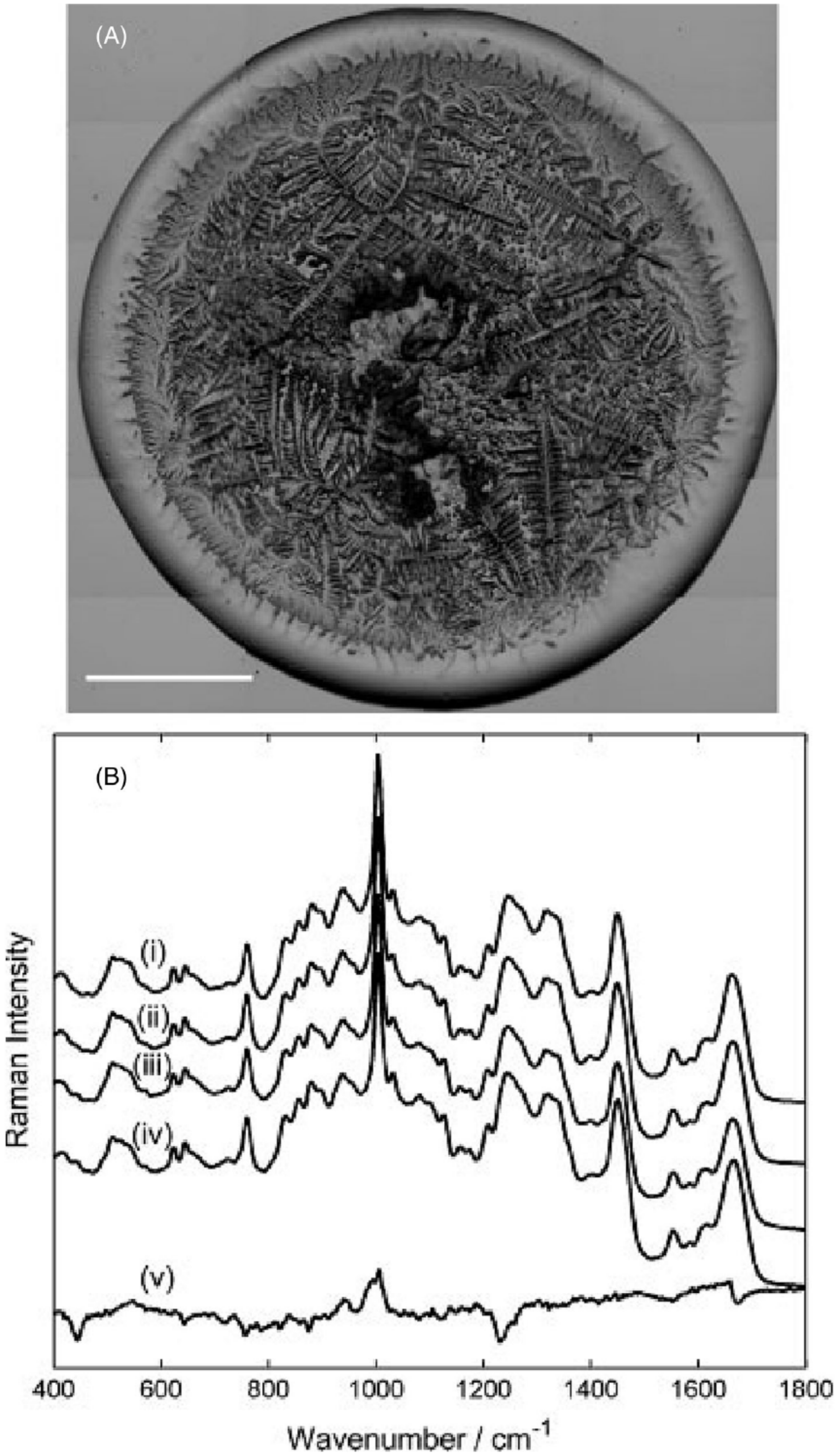

FIGURE 4 An example of drop coating deposition Raman (DCDR) study of human tear fluid; (a) white light transmission image of a dried 1.5-μL tear drop deposited on CaF_2 plate (scale bar shows 500 μm), and (b) mean tear protein DCDR spectra, (i)–(iv) volunteers 1–4, (v) difference between spectra i and iv, intensity ×3. Reproduced with permission from Filik and Stone.[21]

composition, and it is worth pursuing as a possible diagnostic technique. Following this work, Hu et al., in the study of human tear fluid, employed both DCDR and SERS methods.[22] They demonstrated that both approaches could be used to analyse the samples without any sample pretreatment or separation. Moreover, both methods can provide complementary information about whole human tears. Another example of a DCDR study of a real complex sample is cerebrospinal fluid.[23] In this work, it was revealed that the stability of the real sample

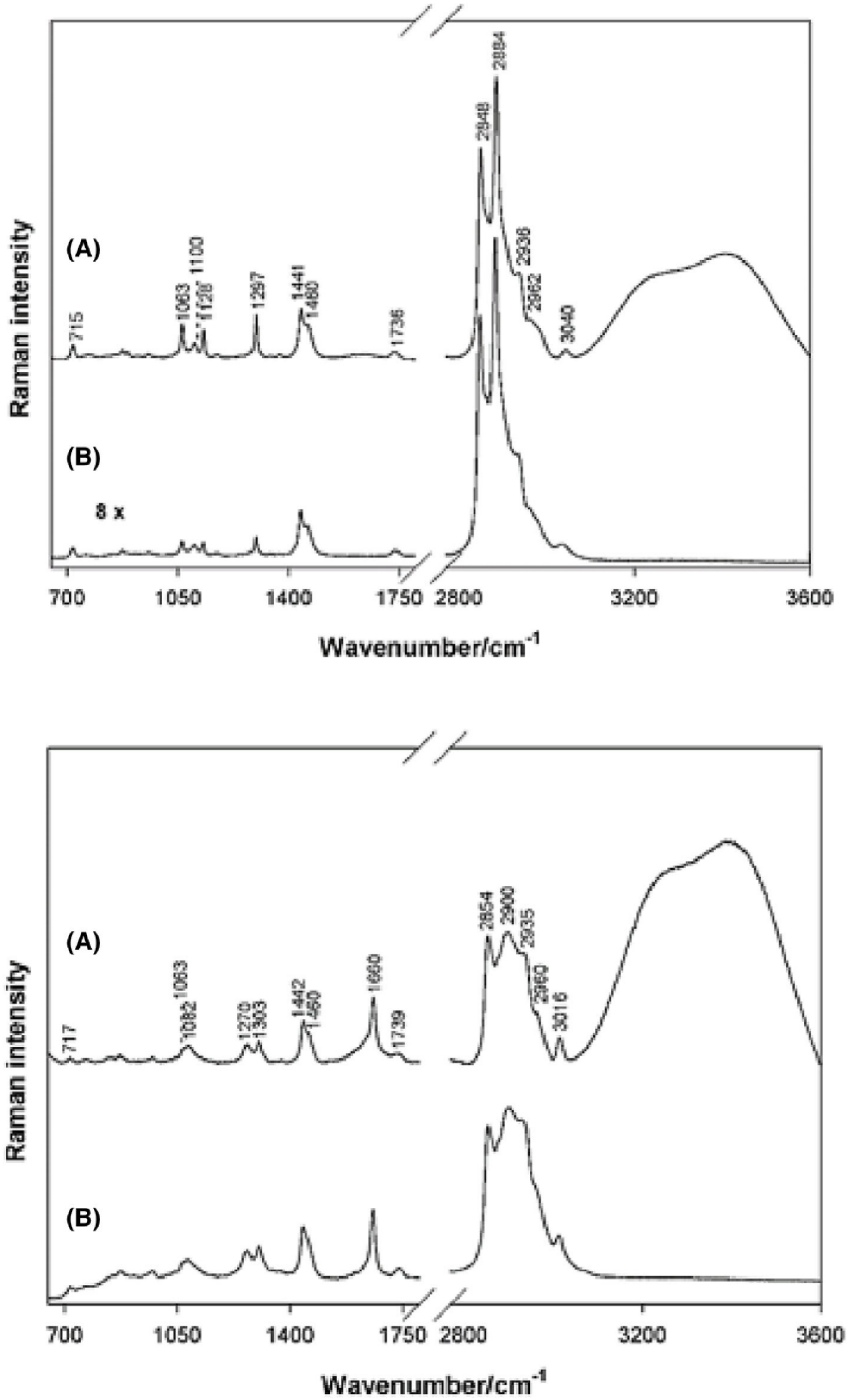

FIGURE 5 Upper part is Raman spectra of 1,2-distearoyl-sn-glycero-3-phospocholine (DSPC) liposomes measured from (A) aqueous suspension and (B) the ring of the pattern on drop coating deposition Raman (DCDR) substrate (SpectRIM™, Tienta Sciences). Spectra are baseline-corrected. Bottom part is Raman spectra of asolectin liposomes measured from (A) aqueous suspension and (B) the ring of dried drop on DCDR substrate (SpectRIM™, Tienta Sciences). Spectra are baseline-corrected. Reproduced with permission from Kočišová and Procházka.[27] [Colour figure can be viewed at wileyonlinelibrary.com]

is limited, and it is necessary to process the sample for DCDR measurement as soon as possible after collection. Another employment of the DCDR method was an examination of chemical changes in synovial fluid of patients with clinical evidence of knee osteoarthritis, which can have diagnostic and/or prognostic value.[24]

DCDR method was also employed to analyse microcystin (MC) samples, an ubiquitous and potent hepatotoxin produced by cyanobacteria. The aim was to unequivocally identify MC-LR toxin from aqueous solution in trace concentrations by DCDR, as it can cause the contamination of freshwaters used for drinking water supply. For the differentiation of more MC variants and nodularin (another toxin produced by a specific cyanobacterium), principal component analysis and peak ratio analysis were used as mathematical approaches for the collected DCDR spectra.[25,26]

The DCDR studies on lipids organised mainly in the liposomes in the liposomal suspension have been started by our group since 2010. Lipids, as an important group of biological molecules, are the principal structural components of the living cell membrane. The liposomes—spherical self-closed structures composed of curved lipid bilayers in the aqueous environment—are often used as suitable model membrane systems. The homogeneous liposomal suspension (in lipid composition and size) deposited on the substrate dries similarly to proteins, forming the 'coffee-ring' pattern with a circular shape and the edge ring (see Figure 1B, left image). Generally, the diameter of the pattern and the width of the edge ring varies depending on the lipid composition of the liposomes and the concentration, as observed in the case of 1,2-distearoyl-sn-glycero-3-phospocholine (DSPC) and asolectin samples.[27] Normal Raman spectroscopy from aqueous liposomal suspension demands high initial concentrations of lipids several times higher than is needed for DCDR. For instance, the Raman measurement of the DSPC liposomal sample in suspension had 120 times higher concentration than that used for the DCDR measurement (0.3 mg mL^{-1}). It was found that this concentration is optimal for the acquisition of reproducible DCDR spectra of good quality.[27,28] Thus, DCDR spectroscopy provided Raman spectra using initial sample concentrations of at least two orders of magnitude lower than those needed for normal Raman spectroscopy in aqueous suspensions. Spectra in Figure 5 compare the normal Raman spectra from aqueous suspension and the DCDR spectra for DSPC and asolectin samples. The spectral features of lipids are the same in both cases, which means that the liposomes maintained their phase even after drying, liquid-crystalline and gel one for asolectin and DSPC, respectively. The excellent reproducibility of the liposomal spectra was confirmed by spectral mapping from the edge ring area (consecutively measured spectra) scanned at particular chosen points in precisely defined locations, as can be seen in Figure 6.[27]

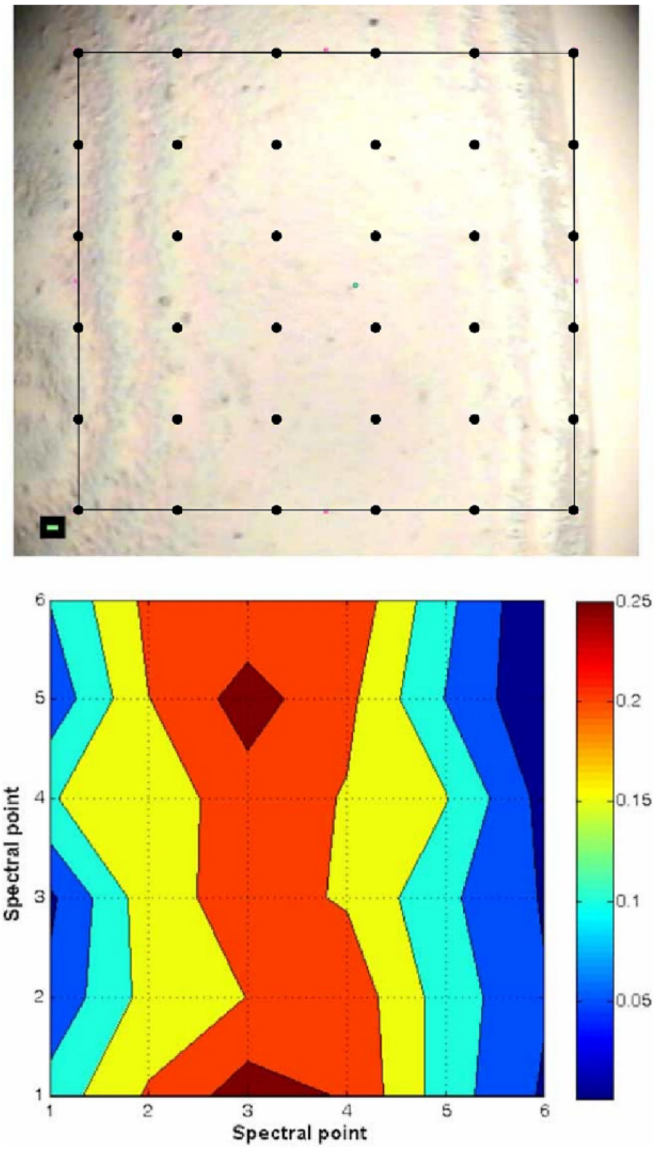

FIGURE 6 Upper part represents a typical white-light micro-image. Bottom part is the corresponding spectral map of a ring section of a dried drop of dipalmitoylphosphatidylcholine. The bar corresponds to 2 μm. Reproduced and adapted from Kočišová and Procházka.[27] [Colour figure can be viewed at wileyonlinelibrary.com]

In addition to homogeneous liposomes themselves, we also investigated liposomes with increasing content of cholesterol. Cholesterol, as an important component of the animal plasma membrane, was inserted between the phospholipid molecules in liposomes, which significantly affects the membrane structure and fluidity. The presence of cholesterol in a liposome causes a diminishment of the dried pattern size and an increase in the diameter of the ring.[29] However, a higher amount of cholesterol (20% of cholesterol for liposomes composed of 1,2-dipalmitoyl-sn-glycero-3-phosphocholine) causes the formation of the compact pattern without the formation of the ring. Acquired DCDR spectra contained characteristics of both phospholipids and cholesterol. Moreover, liposomes did not change their initial phase state after drying. Spectral mapping demonstrated that maximum Raman intensity originated from the central part of the ring structure.

A comparison of DCDR and SERS methods in sensitive lipid detection was made for synthetic 1,2-dimyristoyl-3-trimethylammonium-propane

(DMTAP).[30] DCDR method provided reproducible DMTAP spectra without considerable loss of its solution properties if measured from the 'coffee-ring' pattern dried on a SpectRIM™ substrate. DMTAP was detected from ~10 μM initial solution concentration, which is about three orders of magnitude lower than that for normal Raman spectroscopy. SERS spectra from the dried ring of Ag hydrosol/DMTAP system deposited on a clean glass slide were obtained down to ~0.3 μM DMTAP concentration, which means that the sensitivity of SERS is about five orders of magnitude higher than that of normal Raman spectroscopy. However, in contrast to the DCDR technique, SERS spectra of DMTAP of good quality were obtained only from the ring locations containing big nanoparticle aggregates. Moreover, the structural properties of DMTAP were significantly perturbed by adsorption on the Ag nanoparticles.[30]

DCDR method was then employed to investigate the interaction of the complexed cationic copper 5,10,15,20-tetrakis(1-methyl-4-pyridyl) porphyrin (CuP) and phosphorothioate modified oligonucleotide with liposomes.[31] The drying process on the SpectRIM™ substrate produced a separation of liposomes with bound CuP/oligonucleotide complexes forming a ring at the edge part of the pattern. The complex itself remained in the central part of the ring. High-quality spectra measured from the ring revealed an unperturbed arrangement of lipid chains, partial binding of the CuP/oligonucleotide complexes to liposomes, and a certain reorientation of lipid chains as a consequence of the interaction. The main advantage was a perfect accumulation of liposomes in the 'coffee-ring' without remarkable loss of the lipid structural arrangement and a complete separation of smaller molecules or molecular complexes not bound to liposomes. This permits the DCDR method to observe interacting molecular systems present at low percentages in the original liposome suspension.[32]

To improve DCDR performance even more, we performed substantial studies concerning new substrates for DCDR. In addition to the available commercial and non-commercial substrates, attempts to prepare novel hydrophobic substrates in an easy and low cost way were made. The thiol-modified Au-coated glass substrate, prepared by vacuum evaporation of adhesion promoting titanium film and a gold film on a glass slide, showed only a weak background signal.[7] Gold coating similar to the polished stainless steel in the SpectRIM™ or μRIM™ substrates served as a highly refractive layer, strongly increasing the Raman signal. The substrate was tested with albumin solution and liposomal suspension and showed similar behaviour when compared to the commercial SpectRIM™ where the DCDR spectra were in good agreement with our previously published paper.[7] Another attempt included glass substrates modified by different silanes (with different wettabilities corresponding to different contact angles) fabricated and tested by a liposomal suspension. An efficient preconcentration was evident from a sufficiently high DCDR signal, although it was smaller than for SpectRIM™.[6] As the DCDR performance strongly depends on the wetting properties of substrates, novel fluorocarbon nanostructured coatings were introduced.[5] These substrates were prepared by a novel method based on the deposition of arrays of nanoparticles (copper or silver) fusing a gas aggregation source and subsequent overcoating by sputter-deposited thin fluorocarbon film. The nanoroughness and, with it, connected wettability of produced coatings was controlled by the number of nanoparticles in the base layer. For the liposomal suspension, two times higher Raman signal intensity was observed compared with smooth fluorocarbon films without change in the profile of recorded Raman spectra. This was assumed because of a better preconcentration of liposomes in the edge of the ring structure.

In addition to large molecules, molecular systems and more complex samples (including real body fluid samples), small molecules were also the subject of the DCDR study of our group. The solutions of these molecules dry obviously dissimilar to proteins and liposomes and often do not form the pattern with a 'coffee-ring'. The observed patterns can be composed of small crystals and/or non-uniform spots that are more or less homogenous. Small molecules include a broad set of substances, such as amino acids, porphyrins, dipicolinic acid, acetylsalicylic acid, riboflavin, methylene blue, contaminants (food and environmental) and so forth.[33–37] We reported the improvement of detection sensitivity for cationic (copper (II) 5,10,15,20-tetrakis(1-methyl-4-pyridyl)porphyrin) and anionic (copper(II) 5,10,15,20-tetrakis(4-sulfonatophenyl) porphyrin) porphyrins by a factor of 10^5 when the DCDR spectra from ~20 nM deposited concentrations were acquired. Moreover, we measured the DCDR spectrum of protoporphyrin IX known as a marker in clinical diagnostics of cancer, even from 10 nM deposited concentration. We demonstrated that the DCDR detection limit is comparable with or even better than that of SERS using Ag nanoparticles.[34] Dipicolinic acid, an important spore biomarker for *Bacillus anthracis* (anthrax), was detected at 5×10^{-7} M deposited concentration that is equivalent to approximately 90 bacterial spores, which is significantly below the infective dose (Figure 7).[35] The DCDR detection limits for riboflavin, acetylsalicylic acid and methylene blue were 10^{-6}, 10^{-7} and 10^{-8} M for deposited concentrations, respectively. These detection limits are comparable to or even better than those of SERS using

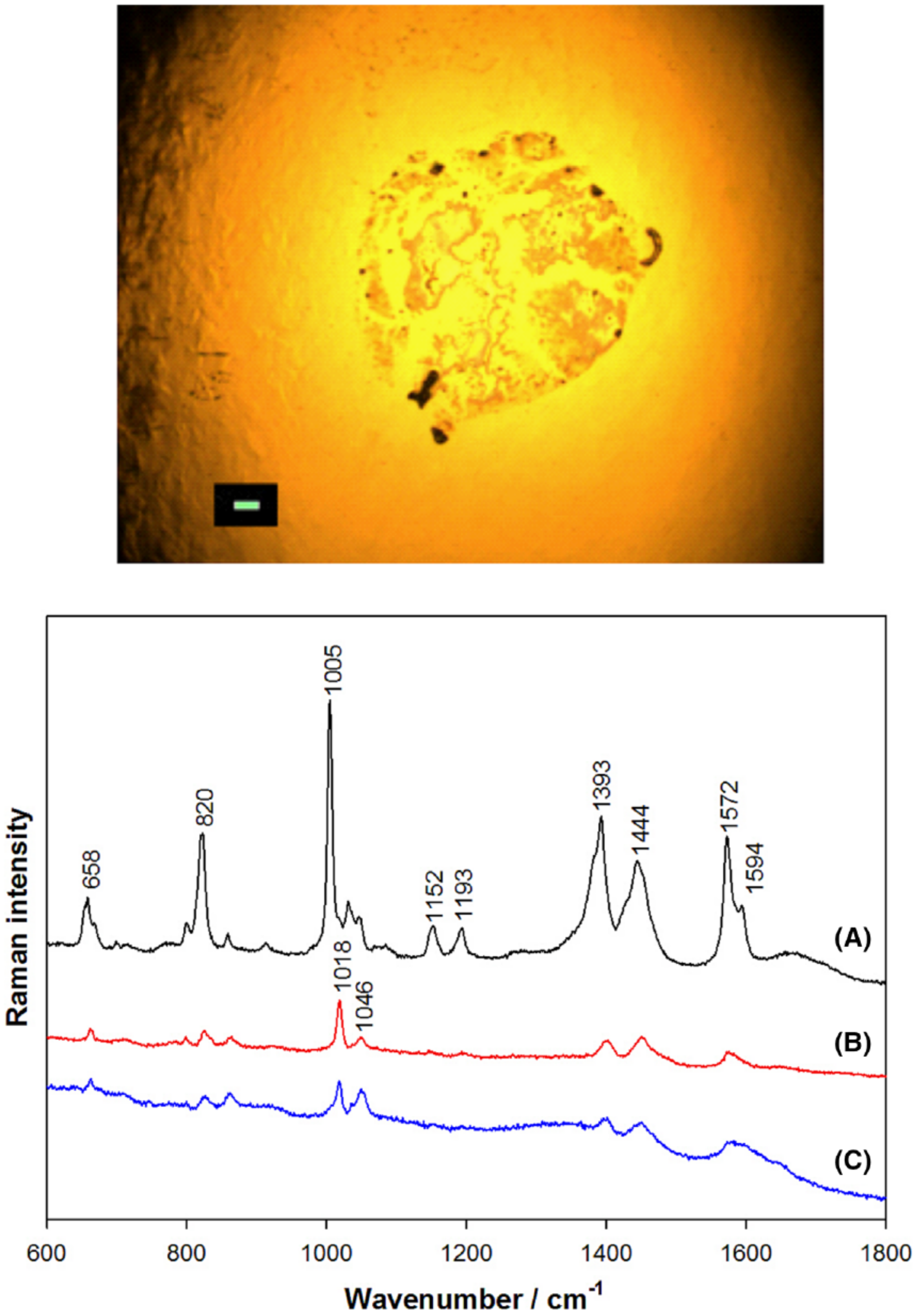

FIGURE 7 Upper part represents a white-light microimage of the pattern of dipicolinic acid on SpectRIM™ substrate at a concentration of 5 × 10^{-7} M, bar corresponds to 20 μm. Bottom part is an example of drop coating deposition Raman (DCDR) spectra of dipicolinic acid measured from patterns in deposited concentrations (a) 1 × 10^{-5} M, (b) 1 × 10^{-6} M and (c) 5 × 10^{-7} M. Reproduced from Kočišová and Procházka.[35] [Colour figure can be viewed at wileyonlinelibrary.com]

commercial Ag substrate.[36] The DCDR spectra of selected contaminants (food contaminant melamine, fungicide thiram and herbicides bentazon and picloram) were detected in concentrations relevant to food and groundwater contaminations. Moreover, normal Raman spectra from stock solutions of these substances were impossible to obtain under the same experimental conditions. The lowest DCDR detected concentrations were determined as 6.4, 0.31, 20 and 2 mM in deposited concentrations for melamine, thiram, bentazon and picloram, respectively.[37]

5 | CONCLUSIONS AND FURTHER PERSPECTIVES

The DCDR method is a very suitable tool for the detection and study of biomolecules and biologically important molecules, their mixtures, as well as more complex samples, such as real body fluids. The possibility of measuring from small volumes (up to units of μL) of low-concentrated (~μM) initial solutions and suspensions that are close to physiological concentrations or relevant in food and groundwater contaminations represents the main advantages. Several orders of magnitude improvement (obviously ~10^3 to 10^5) in Raman detection sensitivity is often achieved compared with normal Raman measurement from a solution. Moreover, the DCDR method can be useful when the normal Raman spectra from the solution or SERS spectra are impossible to acquire. The potential importance of DCDR also comes from the fact that Raman spectroscopy offers additional information not readily obtainable from current detection methods (such as fluorescence or mass spectroscopy).

The DCDR spectra are obviously well reproducible and of high quality with a very good signal to noise ratio, and what is important, they mostly maintain the properties from solutions and the phases for lipids. In the case of small molecules, their DCDR spectra are often similar to the Raman spectra of powder. It was shown that the hydrophobic substrate and its characteristics are important in the DCDR experiment as the formed pattern has been the result of the interplay among not only the type of molecular solutions or suspensions and the sample concentration but also a chosen substrate. From the point of view of DCDR sensitivity, the DCDR substrate should be optimised to provide a formation of the highly concentrated pattern of the studied analyte. Therefore, further research and development of optimal DCDR substrates would be a significant challenge for additional improvement, thanks to which even more efficient signal collection would be possible. Nanostructured substrates with tailored wettability appear to be very promising in this direction.

Optimised substrates would be helpful in planning and designing of the experiments for the necessity to monitor the presence of various substances and contaminants and/or their mutual interaction. This, together with the segregation potential, can cause the important progress of the DCDR method, including proteomic separation and pharmaceutical detection. The challenge is the examination of body fluid samples for diagnosis and identification of ongoing processes with the potential to treat diseases, which could be of great benefit.

ACKNOWLEDGEMENTS

Financial support from the Charles University Research Centre program UNCE/SCI/010 and Grantová Agentura, Univerzita Karlova (GA UK) (290120) is gratefully acknowledged.

ORCID

Alžbeta Kuižová https://orcid.org/0000-0002-2184-6537
Eva Kočišová https://orcid.org/0000-0001-5758-595X

REFERENCES

[1] M. Procházka, *Surface-Enhanced Raman Spectroscopy. Bioanalytical, Biomolecular and Medical Applications*, 1st ed., Springer, Cham **2016**.

[2] R. D. Deegan, O. Bakajin, T. F. Dupont, G. Huber, S. R. Nagel, T. A. Witten, *Nature* **1997**, *389*, 827.

[3] I. A. Larmour, J. P. E. D. Gray, S. E. J. Bell, *Spectrosc. Eur/-World* **2009**, *21*, 6.

[4] O. Kylián, M. Petr, A. Serov, P. Solař, O. Polonskyi, J. Hanuš, A. Choukourov, H. Biederman, *Vacuum* **2014**, *100*, 57.

[5] A. Kuižová, A. Kuzminova, O. Kylián, E. Kočišová, *Polymers* **2021**, *13*, 4023.

[6] E. Kočišová, M. Petr, H. Šípová, O. Kylián, M. Procházka, *Phys. Chem. Chem. Phys.* **2017**, *19*, 388.

[7] E. Kočišová, M. Procházka, H. Šípová, *J. Raman Spectrosc.* **2016**, *47*, 1394.

[8] J. Smith, H. Arnolds, *J. Raman Spectrosc.* **2018**, *49*, 1236.

[9] D. Zhang, Y. Xie, M. F. Mrozek, C. Ortiz, V. J. Davisson, D. Ben-Amotz, *Anal. Chem.* **2003**, *75*, 5703.

[10] D. Zhang, M. F. Mrozek, Y. Xie, D. Ben-Amotz, *Appl. Spectrosc.* **2004**, *58*, 929.

[11] D. Zhang, C. Ortiz, Y. Xie, V. J. Davisson, D. Ben-Amotz, *Spectrochim. Acta, Part a* **2005**, *61*, 471.

[12] V. Kopecký, V. Baumruk, *Vib. Spectrosc.* **2006**, *42*, 184.

[13] C. Ortiz, D. Zhang, Y. Xie, V. J. Davisson, D. Ben-Amotz, *Anal. Biochem.* **2004**, *332*, 245.

[14] C. Ortiz, D. Zhang, Y. Xie, A. E. Ribbe, D. Ben-Amotz, *Anal. Biochem.* **2006**, *353*, 157.

[15] C. Ortiz, D. Zhang, A. E. Ribbe, Y. Xie, D. Ben-Amotz, *Biophys. Chem.* **2007**, *128*, 150.

[16] Y. Xie, D. Zhang, G. K. Jarori, V. J. Davisson, D. Ben-Amotz, *Anal. Biochem.* **2004**, *332*, 116.

[17] Y. Xie, Y. Jiang, D. Ben-Amotz, *Anal. Biochem.* **2005**, *343*, 223.

[18] Y. Xie, D. Zhang, D. Ben-Amotz, *Anal. Biochem.* **2008**, *373*, 154.

[19] J. Filik, N. Stone, *Analyst* **2007**, *132*, 544.

[20] J. Filik, N. Stone, *Anal. Chim. Acta* **2008**, *616*, 177.

[21] J. Filik, N. Stone, *J. Raman Spectrosc.* **2009**, *40*, 218.

[22] P. Hu, X.-S. Zheng, C. Zong, M.-H. Li, L.-Y. Zhang, W. Li, B. Ren, *J. Raman Spectrosc.* **2014**, *45*, 565.

[23] J. Klener, K. Hofbauerová, A. Bartoš, J. Říčný, D. Řípová, V. Kopecký, *Clin. Chem. Lab. Med.* **2014**, *52*, 657.

[24] K. Esmonde-White, G. Mandair, F. Raaii, J. Jacobson, B. Miller, A. Urquhart, B. Roessler, M. Morris, *J. Biomed. Opt.* **2009**, *14*, 034013.

[25] R. A. Halvorson, P. J. Vikesland, *Environ. Sci. Technol.* **2011**, *45*, 5644.

[26] R. A. Halvorson, W. Leng, P. J. Vikesland, *Anal. Chem.* **2011**, *83*, 9273.

[27] E. Kočišová, M. Procházka, *J. Raman Spectrosc.* **2011**, *42*, 1606.

[28] E. Kočišová, A. Vodáková, M. Procházka, *Spectroscopy* **2012**, *27*, 182720.

[29] E. Kočišová, A. Antalík, M. Procházka, *Chem. Phys. Lipids* **2013**, *172-173*, 1.

[30] P. Šimáková, E. Kočišová, M. Procházka, *J. Raman Spectrosc.* **2013**, *44*, 1479.

[31] E. Kočišová, M. Procházka, J. Štěpánek, P. Mojzeš, *Spectroscopy* **2010**, *24*, 689749.

[32] E. Kočišová, M. Procházka, L. Vaculčiaková, *Appl. Spectrosc.* **2015**, *69*, 939.
[33] T. Pazderka, V. Kopecký, *Spectrochim. Acta, Part a* **2017**, *185*, 207.
[34] E. Kočišová, M. Procházka, *J. Raman Spectrosc.* **2015**, *46*, 280.
[35] E. Kočišová, M. Procházka, *J. Raman Spectrosc.* **2018**, *49*, 2050.
[36] E. Kočišová, S. Sayedová, M. Procházka, *J. Raman Spectrosc.* **2020**, *51*, 871.
[37] A. Kuižová, M. Přikryl, M. Procházka, E. Kočišová, *Spectrochim. Acta, Part a* **2021**, *262*, 120109.

How to cite this article: A. Kuižová, E. Kočišová, *J Raman Spectrosc* **2023**, 1. https://doi.org/10.1002/jrs.6524

A.4 Drop coating deposition Raman (DCDR) spectroscopy: fundamentals and potential applications

KOČIŠOVÁ, Eva; KUIŽOVÁ, Alžbeta. Drop coating deposition Raman (DCDR) spectroscopy: fundamentals and potential applications. *Applied Spectroscopy Reviews*. **2024**, pp. 1-15.

Available from doi: 10.1080/05704928.2024.2314534

APPLIED SPECTROSCOPY REVIEWS
https://doi.org/10.1080/05704928.2024.2314534

REVIEW ARTICLE

OPEN ACCESS

Drop coating deposition Raman (DCDR) spectroscopy: fundamentals and potential applications

Eva Kočišová and Alžbeta Kuižová

Institute of Physics, Faculty of Mathematics and Physics, Charles University, Prague, Czech Republic

ABSTRACT

Raman spectroscopy has developed significantly since its discovery and has become an important analytical vibrational technique for investigating the sample's chemical and structural properties. Today, great emphasis is placed on detecting low-concentrated samples of small volumes, which is a problematic task considering the weak intensity of the Raman signal. To improve the sensitivity significantly, resonance Raman spectroscopy and surface-enhanced Raman spectroscopy were employed. However, they face certain limitations and cannot generally be applied to any molecule. Here, we focus on drop coating deposition Raman (DCDR) spectroscopy that offers a general solution. DCDR lies in a droplet deposition of a liquid sample on an ideally solvophobic substrate where the subsequent drying process results in a preconcentrated deposit. After focusing on the preconcentrated dried parts in the deposit under the Raman microspectrometer, this offers high-quality classical Raman spectra even from a low-concentrated sample. Besides the overview of the method, its potential and the applications to biomolecules, biologically significant molecules and contaminants will be discussed.

KEYWORDS

Drop coating deposition Raman; DCDR; hydrophobic substrate; biomolecule; contaminant

1. Introduction

The Raman scattering phenomenon was discovered in 1928 and named after the physicist Sir Chandrasekhara Venkata Raman, who made the first recorded observation.[1,2] Raman was awarded the Nobel Prize for Physics in 1930 for this first experimental evidence. The phenomenon occurs when a sample is irradiated by incident light that is immediately scattered by molecules. Generally, the majority of the scattered light is elastic scattering (Rayleigh), which occurs at the same wavelength as the incident light. The Raman scattering is inelastic, shifting the frequency/wavelength of scattered radiation due to molecular vibrational motion. The Raman signal is very weak, at about a million times less intense than Rayleigh scattering (only one of 10^5-10^7 photons is scattered inelastically). Moreover, at the time of the first Raman experiments, only rudimentary instruments were available, and it was truly remarkable that such a weak phenomenon

CONTACT Eva Kočišová kocisova@karlov.mff.cuni.cz Institute of Physics, Faculty of Mathematics and Physics, Charles University, Prague, Czech Republic.

was detected. Nevertheless, the instrumentation gradually developed over time, making it possible to record Raman spectra of various compounds in liquid and solid phases.

However, despite the technical developments (e.g. using laser excitation sources and sensitive detectors), the maximal conversion of the incident laser photons into Raman signal is only about 10^8 due to the weak Raman scattering cross-section.[3] It is challenging to record Raman spectra from poor scatterers or low-concentrated materials, where relatively highly concentrated samples (more than 1 mM) and large amounts of analyte (more than 1 µg) are necessary. Concerning biological samples/molecules and contaminants (e.g. food and environmental contaminants), such high amounts do not correspond to physiological conditions and environmentally relevant concentrations.[3,4] Therefore, their detection is complicated.

To overcome the aforementioned obstacles, the Raman intensity is often increased using non-classical (enhanced) Raman spectroscopy such as resonance Raman spectroscopy (RRS) and surface-enhanced Raman spectroscopy (SERS) methods. RRS occurs when the incident laser light is near resonance with an electronic transition of the molecule and thus amplifies Raman scattering from a specific vibrational mode of the molecule in resonance with the excitation. It can enhance the Raman scattering cross-section by orders of magnitude. SERS is based on the presence of metal nanoparticles in colloid or in the form of roughened/nanostructured metal (plasmonic), very often silver and gold surface/platform, called "SERS-active" providing the electromagnetic enhancement due to the excitation of localized surface plasmons. For the molecule of interest adsorbed on such a platform (due to chemisorption or physisorption), the enhancement of the Raman signal over 10^5 can be achieved.[5] Used surfaces have an important influence on both Raman enhancement and spectral reproducibility. It has been widely and successfully employed in various applications over the past few decades. Even though the SERS method has brought many important discoveries, its use is often not straightforward and generally not applicable to any molecule. Moreover, both RRS and SERS have more restricted validity due to the problems with spectral alteration, increased background, strong fluorescence signal, and the propensity for photochemical damage.

Besides the above-mentioned enhanced methods, it would be advantageous to have another approach at one's disposal to increase the intensity of the Raman scattering when measuring classical (non-enhanced) Raman spectra. The drop coating deposition Raman (DCDR) method meets these requirements and overcomes the above-mentioned obstacles. As discussed further, the method benefits from a simple deposition of a small volume of liquid sample, which, when dried, creates a deposit suitable for measuring high-quality classical Raman spectra from the preconcentrated dried parts under the Raman micro-spectrometer. This review summarizes the state of the art of DCDR spectroscopy and demonstrates its potential and current applications on biomolecules and biologically significant molecules in relevant concentration ranges.

2. Methods

2.1. Inspiration for the DCDR method

The development of the DCDR method was very likely inspired by the simple observation of drying a spilled liquid drop, such as a drop of coffee. Basic physical principles of drying were elaborated in the paper by Deegan et al.[6] published in the journal Nature in 1997. It described the phenomenon of the formation of an annular (ring-like) deposit known as a "coffee-ring" when a spilled drop of coffee evaporated on a solid surface. The authors stated the necessary conditions which had to be fulfilled for the formation of a "coffee-ring" deposit. These included a surface with a non-zero contact angle for the deposited liquid sample and the subsequent formation of a droplet contact line (at the air-liquid-solid interface) that is pinned to its initial position when dropped and dried. Although the evaporation process does not always result in the formation of a "coffee-ring" for each deposited droplet, this study emphasizes the effect of sample pre-concentration in the edge ring, which was later successfully applied in the DCDR method.[7]

In 2009, the paper by Larmour et al.[8] reminded and pointed out an idea about solvent removal that could be a universal mode for signal enhancement from dilute solutions. Solvent removal influences the increasing concentration of the solute. When the concentration of the solution increases, more molecules of interest (causing the inelastically scattered photons) enter the laser beam, and a higher signal is detected. As Raman scattering is proportional to concentration, the signal is expected to increase linearly with concentration. The authors calculated that if a 2-μl drop with a diameter of 1.56 mm shrinks by evaporation into the drop with a diameter of 100 μm, the signal will increase more than by a factor of 3000 ×. Further evaporation of the solvent to a 10 μm drop diameter will increase the concentration, and so will the Raman signal by at least a factor of 3×10^6 times. This approach is generally suitable for any solution and does not depend on the properties of diluted molecules or the surface used for deposition. Nevertheless, some types of surfaces could be more beneficial because they give rise to smaller, more compact deposits that provide higher signal.[9]

2.2. The principle of the DCDR method and fundamental features

The principle of the DCDR method (Figure 1) is straightforward and simple. It lies in the deposition of a small volume – a droplet – of solution or suspension of molecules of interest on a surface, later in the text, mentioned as substrate. The optimal substrate should be highly solvophobic in the range of used solvents. Since the studied sample is in an aqueous solution, in most cases, the preferred substrate is hydrophobic. Another commonly used solvent is ethanol. The deposition is then followed by the drying process, usually at room temperature. The sample deposited on the substrate is protected from dust by covering it with a Petri dish. A final preconcentration of the analyte occurs as a result of the complete drying process. The resulting dried samples create a pattern of different forms. Sessile droplets very often dry with the "coffee-ring" effect when the evaporating droplet has a pinned contact line, and the solvent that is evaporated from the periphery of the droplet is replenished by solvent from the interior. The resulting flow (streaming) can virtually carry all dispersed material to the edge, where a ring of sample molecules is formed. After the droplet deposition and its subsequent evaporation, the formed dried deposit is solvent-free. After putting the substrate under the Raman micro-spectrometer and focusing on the preconcentrated dried parts in the deposit, classical Raman spectra are measured. Besides dried deposits with the "coffee-

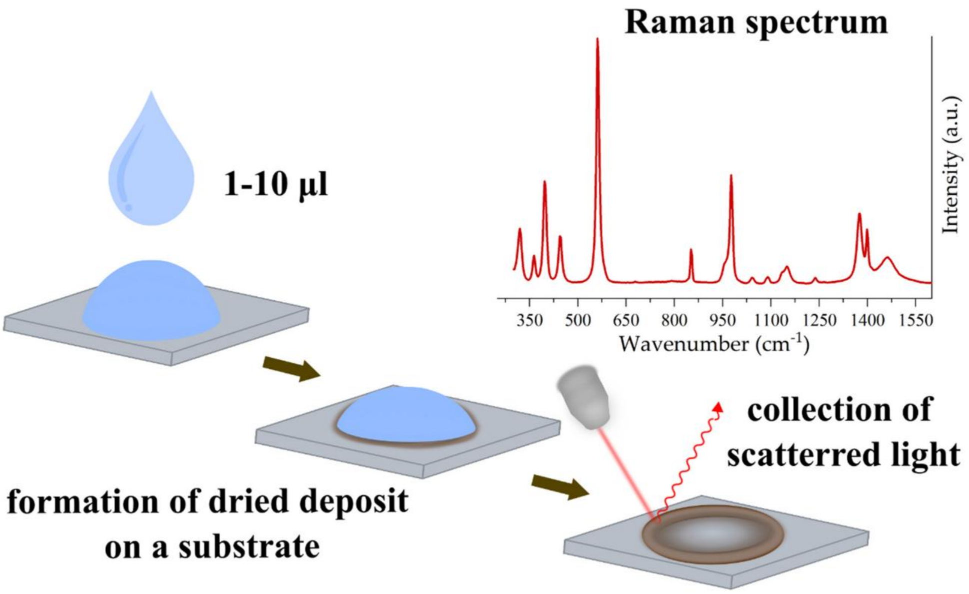

Figure 1. The principle of the DCDR method: the deposition of a droplet of solution or suspension on a solvophobic substrate followed by the drying process and the measurement of classical Raman spectra from the created deposit pattern.

ring" effect, other types of patterns formed after drying can be observed (Figure 2). Small spots with often spherical form are observed when sessile drops have less tendency to pin to the substrate during drying. Thus, the droplets will remain almost spherical as they shrink during evaporation. In addition, the formed pattern may be nonuniform and non-compact (composed of several parts, such as small isles). It can contain some amorphous parts, as well as tiny crystals, formed when the molecules in the drop tend to form self-assembling complexes *via* crystalizing.

DCDR approach, due to the significant preconcentration during drying, usually leads to the acquisition of high-quality classical spectra. In addition, strong preconcentration permits the measurement from initially low-concentrated samples (lower than for classical Raman measurement measured directly from solution). It is enough to drop only a small initial volume, a droplet of a few microliters. This enables a several-fold improvement of the sensitivity when compared to classical Raman measurement from solution or suspension.[7,10–12]

Choosing a suitable substrate is crucial for optimizing a DCDR experiment. Hydrophobic substrates are preferred because the studied molecules are mostly in aqueous solution. Therefore, the substrate wettability, i.e. the extent to which a drop of deposited sample covers the surface, is relevant and affects both the drying process and the resulting appearance of the pattern. The wettability is described by a contact angle, the angle between liquid-solid and liquid-air interfaces. Generally, the pattern formed by the drying process is a result of the interplay among more factors, such as the type of molecular solution (or analyte), i.e. its chemical composition, concentration, molecular or particle size, charge, as well as the used solvent, and the selected substrate. All of these strongly influence the ability of sessile droplets to pin to the substrate and subsequently keep the contact line during drying. The resulting pattern is always a combination of both the properties of the analyte and the properties of the substrate. As presumed in the work of Larmour et al.[8], the smaller dried patterns with more

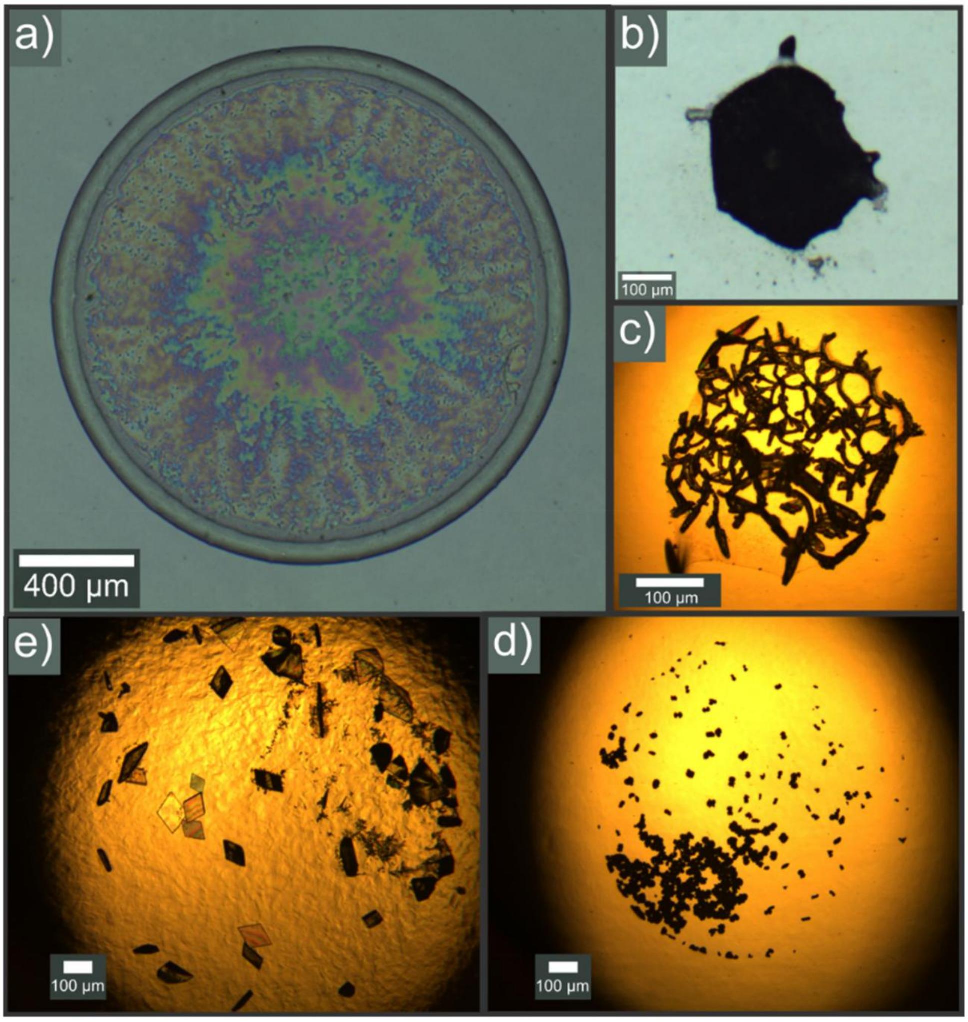

Figure 2. White-light microimages of dried deposit patterns. (a) DPPC, 1 mg/ml, (b) lactose, 1.2 mg/ml, (c) bentazone, 0.5 mg/ml, (d) picloram – 0.5 mg/ml, (e) melamine, 2 mg/ml.

preconcentrated samples give rise to a Raman signal of higher intensity. In this way, we can reduce the detection limit and significantly (several orders of magnitude) improve the detection sensitivity. At the same time, it is possible to extend the attractiveness and usefulness of Raman spectroscopy for any analyte, biomolecules and contaminants (at physiological conditions and environmentally relevant concentrations) that we are interested in.

Different substrates were continuously tested from the beginning of the DCDR experiments. More experimental results showed that a polished stainless steel overlaying with a hydrophobic layer was the most promising. SpectRIM^{TM} substrate, commercially produced by Tienta Sciences, was successfully employed in many published works. It consisted of a $3 \times 1 \times 0.1$ inch plastic pad in which an optically flat stainless steel plate coated with an ultra-thin (50 nm) hydrophobic layer was placed. It provided a contact angle of 122° for a drop of water. The substrate was chemically inert and appeared ideal for DCDR spectroscopy for dilute solutions in polar solvents. However, the SpectRIM^{TM} Slide is no longer commercially available. Another substrate that is currently at disposal is a µRIM^{TM} from BioTools. This substrate is less hydrophobic than SpectRIM^{TM} Slide, with a contact angle of 108°.

Another big group of substrates are the noncommercial home-made ones profiting from the hydrophobic character of smooth fluorocarbon coating with contact angle in the range of 108°-120°. They represent a very promising platform for DCDR spectroscopy. This class of hydrophobic substrates can be additionally improved to create nanostructured platforms with metal nanoparticles to increase the hydrophobicity even more.[9,13,14] Metal nanoparticles are sandwiched in plasma polymerized fluorocarbon films and prepared by magnetron sputtering. The presence of nanoparticles, depending on the type of metal (copper or silver), their size and amount, leads to a significant increase in the roughness of the surface and so in the contact angle of the deposited droplet. It was shown that surface roughness is a key parameter adjusting the wettability.[14] In this way, not only highly hydrophobic but also super-hydrophobic substrates with a contact angle of at least 150° can be produced.[13] Super-hydrophobic substrates thus can cause the formation of smaller dried patterns with better preconcentration.[15] Despite the use of metal nanostructures, the enhancement of the Raman signal from deposited molecules is caused only by a better preconcentration on the roughened surface, and the contribution of the SERS enhancement to the resulting signal is excluded due to the long distance from the metal nanostructures.

The other noncommercial and often used DCDR substrates include polished CaF_2 plates, silanized glass surfaces, quartz slides, gold foil, aluminum foil, thiol-modified gold-coated glass etc.[16–18] A polytetrafluoroethylene tape as a low-cost hydrophobic substrate was also tested.[19] The contact angles of these substrates vary in the range of 80°-120°. With a higher contact angle, the preconcentration of the analyte is generally more efficient.[9,17]

As for the Raman spectra measurement, there are several crucial points regarding substrates and measurement conditions. Any used substrate should have a minimal background signal in the spectral region of interest, otherwise, the subsequent signal subtraction of this signal may not be straightforward. It is also necessary to properly adjust the intensity of the incident laser beam, as the sample may be photodamaged, especially when the sample layer is very thin. The presence of the fluorocarbon layer is advantageous because when thin, it shows no apparent Raman or fluorescence signal and thus provides the spectra from dried deposits of good quality. Furthermore, the polished stainless steel performs as a mirror and significantly increases the incoming signal by reflecting it to the objective. Similarly, all the substrates with mirror-like surface (e.g. gold and aluminum foils) profit from its presence. For substrates with the background signal from glass surfaces, a gold coating can be used to reduce it efficiently. For polished CaF_2 plates, the single Raman band at $322\,cm^{-1}$ can be easily removed by subtraction methods. Although, CaF_2 band is mostly outside the spectral region of interest. Based on experience to date, a stainless steel plate coated with a thin hydrophobic fluorocarbon layer appears to be the most suitable substrate for DCDR spectroscopy.

3. Results and discussion: Beginnings, first results and our work

In the first DCDR experiments, emphasis was placed on the research of important biological molecules, such as amino acids, peptides and proteins.[7,18,20–25] Later, due to the promising results, the studies were extended to investigate other molecules, molecular mixtures and complex solutions.[10,11,26–31]

The first encouraging results were published by Zhang et al.[7] in 2003 on samples of lysozyme and human insulin proteins. Their work combined Raman measurements with chromatography and mass spectrometry to demonstrate proteomic sensing. The authors were driven by an effort to detect the proteins derived from a chromatographic (HPLC) fraction by classical Raman or by following the Raman acquisition by mass spectroscopic techniques (MALDI-TOF). Since the concentrations needed for the classical Raman spectroscopy from solutions are higher than those issued from chromatography and needed for mass spectroscopy, the possibility of following up on it was challenging. However, the work of Zhang et al.[7] reported the potential to reproducibly measure high-quality classical Raman spectra from femtomole amounts of only micromolar concentrations of protein samples when deposited and dried on a hydrophobic substrate. The observed results showed a more than 1000-fold increase in the sensitivity of classical Raman spectroscopy from protein solutions. An important aspect of the DCDR experiments was the observation that the DCDR spectra were virtually identical to those measured from protein solutions at higher concentrations. In addition, it turned out that proteins maintain their structure from solution after the drying process so their native structure is not disrupted. All this indicated a potential benefit of DCDR spectroscopy in proteomic diagnostics.

Moreover, the capacity of the DCDR to act as a segregation method was also shown by the effective separation of proteins from the other components, such as some impurities (mostly fluorescent ones) and buffer compounds (obviously salts).[32] The segregation effect is produced by convective streaming occurring during the evaporation and subsequent precipitation of components in different regions on the substrate. The streaming is a prominent driving force for the observed tendency of proteins and lipids (in the form of liposomes) to accumulate in an edge ring of dried patterns. In addition, crystallization may also contribute to segregation, as compounds with higher nucleation and crystal growth rates tend to deposit separately from compounds with lower crystallization rates. Different solubility of the solution's components also plays an important role in the segregation process. However, for example, components with a strong affinity for each other will not tend to segregate, and thus, the segregation process does not work universally for every two- or multi-component analyte. As mentioned later, the potential profit from the segregation of individual components can be useful for understanding the interactions in complex samples.

In addition to proteins, lipids were another group of biologically important molecules that were studied by the DCDR method.[33–38] Since 2010, these studies have been carried out mainly in our laboratory. Lipids perform several functions in the cell, but in particular, they are the main structural components of living membranes (cell and organelle). This task is provided mainly by phospholipids. We studied lipids organized in liposomes (spherical self-enclosed structures formed by curved lipid bilayers) as a liposomal suspension. Due to their structure, liposomes are often used as suitable model membrane systems. The homogeneous liposomal suspension (in liposome dimension as well as lipid composition), when deposited on a hydrophobic substrate, dries to similar patterns as proteins studied so far. It has an overall round shape form with a "coffee-ring" edge ring.[37] The size of the formed pattern, the diameter, as well as the width of the edge ring varies depending on the type of lipid, its concentration in the deposited drop and the lipid composition, i.e. whether they consist of only one type of lipid or a lipid mixture. The differences in patterns were observed for 1,2-distearoyl-sn-glycero-3-phospocholine (DSPC) (pure) compared to asolectin (mixture) samples.[37] At the same initial deposited concentrations, the diameter of the DSPC dried pattern was higher than that for the asolectin sample. The formed edge rings had a width of about 65-70 µm. Moreover, when comparing DSPC and asolectin dried patterns, less asolectin is transported to the edge during the drying as the formed ring is less distinct. In the case of DSPC liposomes, the membrane is composed of lipids with fully saturated carbohydrate chains (with 18 carbons), so it is rigid. Since the phase transition temperature of DSPC is 54 °C, the DSPC suspension is in an ordered gel phase at room temperature. The studied asolectin is a natural lipid extract from soybeans and is composed of various types of lipids with approximately equal proportions of lecithin, cephalin and phosphatidylinositol and other phospholipids, as well as polar lipids in small amounts. As it is a mixture of various lipids, the phase transition is broad, and the temperature cannot be precisely determined. Moreover, liposomes formed by asolectin differ from those formed by only one type of lipid, as that is a model system closer to and mimics natural/real membranes.

As for Raman measurement, the classical Raman spectroscopy directly from liposomal suspension is possible only with high initial concentrations of lipids, obviously more than tenfold higher than are needed for DCDR. For the classical Raman measurement of DSPC liposomes from suspension, it had about 120 times higher concentration than the one found to be optimal for the DCDR measurement (0.3 mg/ml).[37] Such a low concentration is sufficient to form a thin layer pattern and obtain high-quality and highly reproducible DCDR spectra, which was confirmed by Raman mapping. Moreover, comparing the classical Raman spectra from aqueous suspension of liposomes and their DCDR spectra, the spectral features were the same in both cases. This demonstrates that the measured samples maintained their phase even after drying, liquid crystalline and gel one for asolectin and DSPC, respectively. As a result, DCDR spectroscopy provides Raman spectra of lipids using initial concentrations of at least two orders of magnitude lower than those needed for classical Raman spectroscopy in aqueous suspensions.[37]

Besides the liposomes composed of pure phospholipids or their mixtures, we have also studied the changes in liposomes containing cholesterol.[35] Cholesterol is a sterol-ringed lipid important in biosynthetic pathways, especially in mammalian organisms, as it acts as a precursor for the biosynthesis of steroid hormones. Although it does not form the membrane itself, it is an important structural component. Cholesterol helps to maintain the proper membrane heterogeneity in both membrane leaflets, its overall stability and the necessary permeability. When mixed with phospholipids, molecules of cholesterol insert between the phospholipid molecules so that their polar hydroxyl group is close to the head group of phospholipids and thus significantly affect the membrane structure and fluidity. The presence of cholesterol in the liposomes influences the dried patterns and induces changes in the dimension and thickness of the edge ring. The growing amount of cholesterol leads to a diminishing of pattern size as well as the increase of the edge ring thickness. This was confirmed for both homogenous liposomes composed of pure 1,2-dipalmitoyl-sn-glycero-3-phosphocholine (DPPC) and mixed asolectin liposomes. Moreover, a higher amount of cholesterol (20%) in DPPC liposomes caused the formation of a compact flat pattern without the edge ring. Measured DCDR spectra contained characteristics of both, phospholipid and cholesterol. The presence of cholesterol in the liposomes can be revealed in the DCDR spectra already at 5% amount. As the proportion of cholesterol increases in liposomes, so does its signal in the spectra. The measured Raman spectra showed that both liposomes without cholesterol and with an increasing proportion of cholesterol after drying retain their initial phase from a liquid suspension, i.e. gel phase for DPPC and liquid crystalline for asolectin samples. Additionally, spectral mapping was also used to examine the edge ring of the lipid dried patterns, and it demonstrated the formation of homogenous rings providing reproducible DCDR spectra with maximum intensity originating from the central part of the ring structure.

We[9] then utilize homogeneous DPPC liposomal suspensions to quantify the DCDR signal improvement by comparing the smooth fluorocarbon (C:F) surfaces and nanostructured ones with increased hydrophobicity but identical surface chemical composition. The smooth C:F thin films were prepared by magnetron sputter deposition of 40 nm thick polytetrafluoroethylene (PTFE) on the polished Si wafers. Nanostructured surfaces were prepared by embedding a controlled number of nanoparticles between two 20 nm thick C:F layers. The resulting surface roughness and increased hydrophobicity were reached by adjusting the size and the number of nanoparticles embedded in the C:F film. Drying the liposomal suspension on nanostructured surfaces led to a well-defined "coffee-ring" pattern with a lower diameter of the resulting rings when compared to the pattern on the smooth C:F coating (pictured in Figure 3), which means a

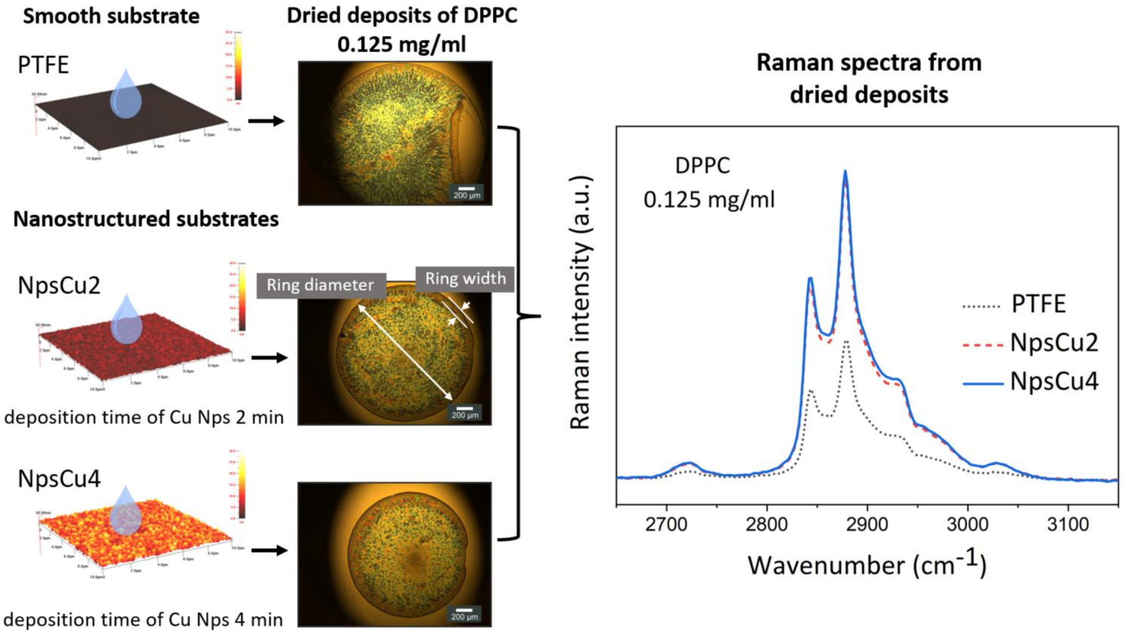

Figure 3. DCDR signal improvement for DPPC liposomal suspension by employing nanostructured substrates with embedded Cu nanoparticles in the PTFE layer. The deposition time set to deposit Cu nanoparticles was 2 min and 4 min. The longer deposition of nanoparticles leads to higher roughness and thus more hydrophobic substrate.

better accumulation of lipid molecules in the ring. After measuring DCDR spectra, two times higher Raman signal intensity was acquired from a sample dried on a nanostructured substrate than from a dried pattern on smooth fluorocarbon film, without compromising the profile of recorded Raman spectra. It was shown that the intensity in DCDR spectra could be significantly increased only by changing and adjusting a substrate roughness.

We[33,38] also did the DCDR study on the interaction of the complex of the cationic copper(II) 5,10,15,20-tetrakis(1-methyl-4-pyridyl) porphyrin (CuTMPyP) and phosphorothioate modified oligonucleotide with DPPC liposomes. In the first experiment, we prepared a suspension composed of CuTMPyP and liposomes. The DCDR spectra contained both the lipid and porphyrin spectral features, but upon the treatment by factor analysis, it was demonstrated that the distribution of CuTMPyP throughout the dried pattern was not homogenous. In the next experiment porphyrin/oligonucleotide complex was added to the liposome suspension. The drying process caused a separation of liposomes with bound complex CuTMPyP/oligonucleotide in the formed edge ring, and the complex remained in the pattern's central part. Moreover, it was possible to distinguish the spectral changes caused by the drying process from the changes caused by the interaction of CuTMPyP with the DPPC liposomes. These were attributed to the perturbation of lipid chain order as well as porphyrin interaction with the lipid head.

Much work was then devoted to the study of smaller molecules of different origin, character and properties. Djaoued et al.[39] focused on a domoic acid (tribasic amino acid containing a proline ring, structurally related to glutamic acid, with a side chain having a conjugated double bond moiety and a hind carboxylic acid) that is naturally present in the marine ecosystem in different locations in the world and recognized as a neurotoxin. Poisoning can cause short-term memory loss, nausea, breathing difficulty and coma. The study demonstrated that DCDR spectroscopy can be applied for rapid detection down to 25 ng of domoic acid per ml (0.025 ppm).[39] Dingari et al.[29] demonstrated an application of DCDR spectroscopy on the detection and quantification of glycated albumin, an important glycemic marker for long-term diabetes monitoring. Using this approach, it was possible to accurately discriminate glycated albumin from the unglycated variant, even at low µM concentrations. The reached limit of the detection for glycated albumin is nearly 4 times lower than the minimum physiological concentrations encountered in practice.[29]

Dipicolinic acid, another interesting small molecule, was studied in our laboratory.[11] It is a component of bacterial spores of Bacillus species and represents ∼10% of their dry weight. The spores are dormant and extremely resistant to different environmental stresses. Dipicolinic acid is a crucial component of the spore core responsible for this resistance. Using the DCDR approach, it was possible to detect dipicolinic acid from a 2-µl drop of 5×10^{-7} M deposited concentration, which is equivalent to approximately 90 Bacillus anthracis spores.[11] Other molecules with biological importance studied by the DCDR approach include acetylsalicylic acid (a substance with antipyretic, anti-inflammatory and cardioprotective properties), riboflavin (vitamin B2, important in the living cell functioning) and methylene blue (used in different areas of biology and medicine for therapeutic and diagnostic purposes) [31]. The found DCDR detection limits are 10^{-6}, 10^{-7}, and 10^{-8} M of deposited concentrations for riboflavin, acetylsalicylic acid, and methylene blue, respectively. These detection limits are comparable to or even better than those attained by the SERS method by means of commercial silver SILMECO substrate. For example, for acetylsalicylic acid, no SERS spectra were obtained from the concentrations used for the DCDR approach, probably due to weak adsorption on the silver surface. For riboflavin, a concentration of 10^{-5} M was the last concentration providing a SERS spectrum, and this is one order of magnitude lower than in the case of DCDR measurements. The SERS spectrum of methylene blue can be obtained from 5×10^{-9} M concentration, which is only twice lower than the DCDR approach. Thus, it can be concluded that the sensitivity of DCDR could be comparable to or even better than that of SERS spectroscopy.[31] Using the DCDR approach, it was possible to improve the Raman detection sensitivity of porphyrins by a factor of 10^5 and thus, the spectra from ∼20 nM initial (deposited) concentrations of cationic CuTMPyP and anionic copper(II) 5,10,15,20-tetrakis(4-sulfonatophenyl) porphyrin were obtained. Protoporphyrin IX, known as a marker in the clinical diagnosis of cancer, was also detected from a deposited concentration of 10 nM, and although a fluorescence background also appeared, clear Raman bands of this molecule were observed in the spectra.

The relevant group of studied molecules represented food and agricultural contaminants. In our study[30] selected contaminants such as food contaminant melamine (known as an illegal food additive of infant formula in China in 2008 and pet food in 2004 and 2007), fungicide thiram (an animal repellent to protect fruit trees and used as well to prevent deterioration from harvested crops in storage or transport from fungal diseases), and herbicides bentazon (detected in groundwater as well as in surface water, applied aerially on food crops to control the spread of weeds occurring amongst the food crops) and picloram (systemic herbicide used for broadleaf weed control in pasture and rangeland, wheat, barley, oats, and woody plant species, can contaminate groundwater and surface water) were detected by DCDR approach whereas classical Raman spectra directly from stock solutions of these substances were impossible to obtain under the same experimental conditions.[30] In addition to that, no reported SERS study for bentazone and picloram was found in the literature for comparison. The lowest detected concentrations were determined as 6.4 μM, 0.31, 20 and 2 μM for deposited concentrations of melamine, thiram, bentazon and picloram aqueous solutions, respectively. DCDR approach was shown to be a powerful tool for the detection of these contaminants at concentrations relevant to food/groundwater contamination.

Furthermore, concerning melamine contamination, our laboratory also focused on melamine detection from intentionally adulterated infant formula. Firstly, we applied the DCDR approach to pure milk infant formula to discover that the drying process induced the spatial separation of main milk constituents like carbohydrates and lipids (Figure 4). Lipids tended to accumulate in the ring structure, as discussed before, for liposomal suspensions, and the carbohydrates formed the thin film layer in the central part of the ring pattern. Spatial separation was confirmed by the acquired classical Raman spectra from the dried pattern. We observed the same spatial separation of lipids and carbohydrates even for the melamine-blended infant formula, detecting melamine only in the central thin layer with the sugars. Melamine detection was possible due to the distinct Raman band belonging to the breathing vibration of melamine at the position of 681 cm^{-1}. We assumed that melamine glycation by carbohydrates in the

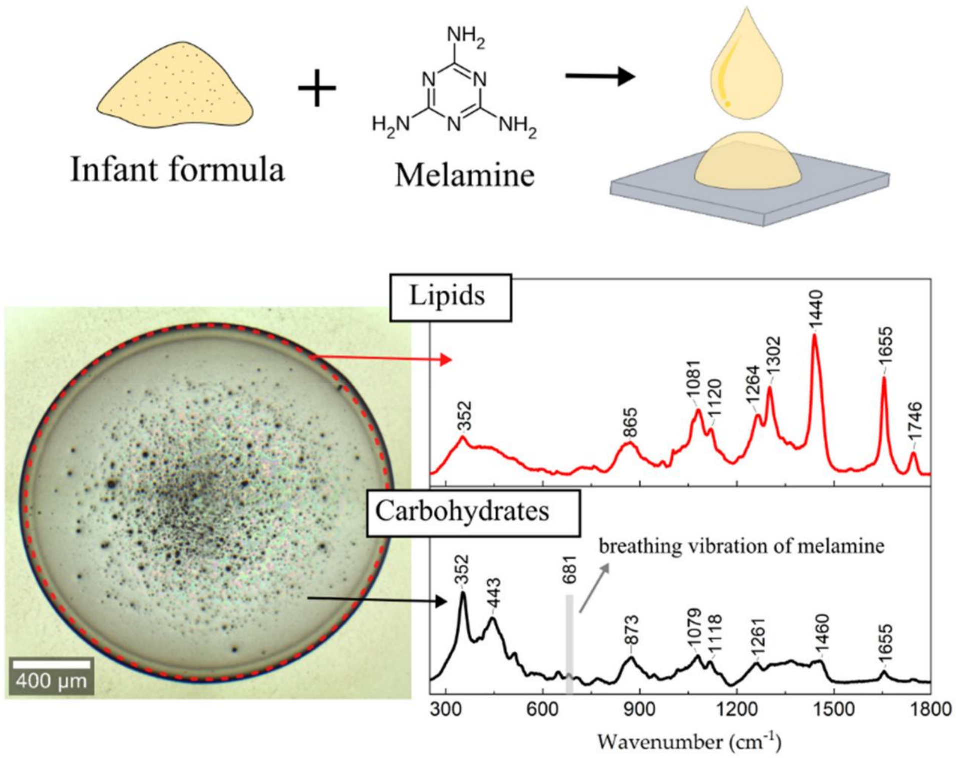

Figure 4. The spatial separation of lipids and carbohydrates in the dried deposit pattern of melamine adulterated milk solution by using the DCDR method with melamine detection only from lipid ring structure.

formula played a crucial role in accumulating melamine molecules inside the ring, making its detection possible even for relevantly low concentrations for melamine contamination. These findings are relevant for the future utilization of DCDR spectroscopy, which can profit not only from analyte preconcentration but also from the chemical reaction potential of molecules of interest and their drying-induced spatial separation in the deposit.

4. Conclusion

Raman spectroscopy, based on the phenomenon of inelastic light scattering, has undergone significant development and has become an important analytical vibrational technique. Nowadays, it is well-established for investigating the chemical and structural properties of a sample in both liquid and solid phases. From the beginning, it has gradually branched out so much that currently, it includes several special methods that are successfully used in many different applications. Today, a strong emphasis is placed on high-quality detection of samples with small volumes and low concentrations. Resonance Raman spectroscopy and surface-enhanced Raman spectroscopy meet this requirement, although they face certain limitations, like spectral alteration, increased spectral background, propensity to photochemical damage, etc. Moreover, neither of the mentioned methods is generally applicable to any molecule.

This review focuses on drop coating deposition Raman (DCDR) spectroscopy that aspires to overcome these problems and increases the intensity of the Raman scattering when measuring classical (non-enhanced) Raman spectra. This is ensured by the deposition of a small volume – a droplet – of liquid of interest on a solvophobic substrate, leading after the evaporation process to the preconcentration of the analyte into the dried deposit. Measuring spectra from selected positions throughout the deposit provides high-quality and reproducible classical Raman spectra, even from small volumes of low-concentrated samples.

The DCDR method has already been applied for the detection and studies of properties of biomolecules, biologically significant molecules, and various food and environmental contaminants at relevant concentrations, both physiological and environmental. The principal advantages of this method are the analyte preconcentration, the chemical reaction potential of the monitored molecules in the droplet, and the subsequent spatial separation (segregation) of interacting/non-interacting components induced by drying. In addition, the optimization of hydrophobicity of used substrates, for example, by tuning surface roughness using nanoparticles of various numbers and sizes deposited in the PTFE film, is promising for its implementation in routine sensing applications.

Acknowledgements

This work was supported by Charles University under Grant SVV-2023-260716.

Disclosure statement

The authors declare no conflict of interest.

ORCID

Eva Kočišová http://orcid.org/0000-0001-5758-595X
Alžbeta Kuižová http://orcid.org/0000-0002-2184-6537

References

1. Raman, C. V.; Krishnan, K. S. A New Type of Secondary Radiation. *Nature* 1928, *121*, 501–502. DOI: 10.1038/121501c0.
2. Raman, C. V. A New Radiation. *Indian J. Phys.* 1928, *2*, 387–398.
3. Long, D. A. *Raman Spectroscopy*; New York City, United States: McGraw-Hill International Book Company, 1977.
4. Schrader, B. *Infrared and Raman Spectroscopy*; Weinheim: Wiley - VCH; 1995.
5. Procházka, M. *Surface-Enhanced Raman Spectroscopy. Bioanalytical, Biomolecular and Medical Applications;* Springer, Cham, 2016.
6. Deegan, R. D.; Bakajin, O.; Dupont, T. F.; Huber, G.; Nagel, S. R.; Witten, T. A. Capillary Flow as the Cause of Ring Stains from Dried Liquid Drops. *Nature* 1997, *389*, 827–829. DOI: 10.1038/39827.
7. Zhang, D.; Xie, Y.; Mrozek, M. F.; Ortiz, C.; Davisson, V. J.; Ben-Amotz, D. Raman Detection of Proteomic Analytes. *Anal. Chem.* 2003, *75*, 5703–5709. DOI: 10.1021/ac0345087.
8. Larmour, I. A.; Gray, J. P. E. D.; Bell, S. E. J. Universal Raman Enhancement by Solvent Removal. *Spectrosc. Eur. World* 2009, *21*, 3.

9. Kuižová, A.; Kuzminova, A.; Kylián, O.; Kočišová, E. Nanostructured Plasma Polymerized Fluorocarbon Films for Drop Coating Deposition Raman Spectroscopy (DCDR) of Liposomes. *Polymers (Basel)* 2021, *13*, 4023. DOI: 10.3390/polym13224023.
10. Kočišová, E.; Procházka, M. Drop-Coating Deposition Raman Spectroscopy of Porphyrins. *J. Raman Spectrosc.* 2015, *46*, 280–282. DOI: 10.1002/jrs.4637.
11. Kočišová, E.; Procházka, M. Drop Coating Deposition Raman Spectroscopy of Dipicolinic Acid. *J. Raman Spectrosc.* 2018, *49*, 2050–2052. DOI: 10.1002/jrs.5493.
12. Kuižová, A.; Kočišová, E. Drop Coating Deposition Raman (DCDR) Spectroscopy of Biologically Important Molecules. *J. Raman Spectrosc.* 2023, *54*, 694–705. DOI: 10.1002/jrs.6524.
13. Kylián, O.; Petr, M.; Serov, A.; Solař, P.; Polonskyi, O.; Hanuš, J.; Choukourov, A.; Biederman, H. Hydrophobic and Super-Hydrophobic Coatings Based on Nanoparticles Overcoated by Fluorocarbon Plasma Polymer. *Vacuum* 2014, *100*, 57–60. DOI: 10.1016/j.vacuum.2013.07.014.
14. Kratochvíl, J.; Kuzminova, A.; Solař, P.; Hanuš, J.; Kylián, O.; Biederman, H. Wetting and Drying on Gradient-Nanostructured C:F Surfaces Synthesized Using a Gas Aggregation Source of Nanoparticles Combined with Magnetron Sputtering of Polytetrafluoroethylene. *Vacuum* 2019, *166*, 50–56. DOI: 10.1016/j.vacuum.2019.04.050.
15. Parsa, M.; Harmand, S.; Sefiane, K. Mechanisms of Pattern Formation from Dried Sessile Drops. *Adv. Colloid Interface Sci.* 2018, *254*, 22–47. DOI: 10.1016/j.cis.2018.03.007.
16. Kočišová, E.; Procházka, M.; Šípová, H. Thiol-Modified Gold-Coated Glass as an Efficient Hydrophobic Substrate for Drop Coating Deposition Raman (DCDR) Technique. *J. Raman Spectrosc.* 2016, *47*, 1394–1396. DOI: 10.1002/jrs.4961.
17. Kočišová, E.; Petr, M.; Šípová, H.; Kylián, O.; Procházka, M. Drop Coating Deposition of a Liposome Suspension on Surfaces with Different Wettabilities: "Coffee Ring” Formation and Suspension Preconcentration. *Phys. Chem. Chem. Phys.* 2017, *19*, 388–393. DOI: 10.1039/c6cp07606h.
18. Filik, J.; Stone, N. Drop Coating Deposition Raman Spectroscopy of Protein Mixtures. *Analyst* 2007, *132*, 544–550. DOI: 10.1039/b701541k.
19. Smith, J.; Arnolds, H. Polytetrafluoroethylene Tape as a Low-Cost Hydrophobic Substrate for Drop-Coating Deposition Raman Spectroscopy of Proteins. *J. Raman Spectrosc.* 2018, *49*, 1236–1239. DOI: 10.1002/jrs.5371.
20. Xie, Y.; Jiang, Y.; Ben-Amotz, D. Detection of Amino Acid and Peptide Phosphate Protonation Using Raman Spectroscopy. *Anal. Biochem.* 2005, *343*, 223–230. DOI: 10.1016/j.ab.2005.05.038.
21. Pazderka, T.; Kopecký, V. Drop Coating Deposition Raman Spectroscopy of Proteinogenic Amino Acids Compared with Their Solution and Crystalline State. *Spectrochim. Acta A Mol. Biomol. Spectrosc.* 2017, *185*, 207–216. DOI: 10.1016/j.saa.2017.05.043.
22. Zhang, D.; Ortiz, C.; Xie, Y.; Davisson, V. J.; Ben-Amotz, D. Detection of the Site of Phosphorylation in a Peptide Using Raman Spectroscopy and Partial Least Squares Discriminant Analysis. *Spectrochim. Acta A Mol. Biomol. Spectrosc.* 2005, *61*, 471–475. DOI: 10.1016/j.saa.2004.04.019.
23. Xie, Y.; Zhang, D.; Jarori, G. K.; Davisson, V. J.; Ben-Amotz, D. The Raman Detection of Peptide Tyrosine Phosphorylation. *Anal. Biochem.* 2004, *332*, 116–121. DOI: 10.1016/j.ab.2004.05.052.
24. Ortiz, C.; Zhang, D.; Xie, Y.; Ribbe, A. E.; Ben-Amotz, D. Validation of the Drop Coating Deposition Raman Method for Protein Analysis. *Anal. Biochem.* 2006, *353*, 157–166. DOI: 10.1016/j.ab.2006.03.025.
25. Kopecký, V.; Baumruk, V. Structure of the Ring in Drop Coating Deposited Proteins and Its Implication for Raman Spectroscopy of Biomolecules. *Vib. Spectrosc.* 2006, *42*, 184–187. DOI: 10.1016/j.vibspec.2006.04.019.
26. Filik, J.; Stone, N. Investigation into the Protein Composition of Human Tear Fluid Using Centrifugal Filters and Drop Coating Deposition Raman Spectroscopy. *J. Raman Spectrosc.* 2009, *40*, 218–224. DOI: 10.1002/jrs.2113.

27. Filik, J.; Stone, N. Analysis of Human Tear Fluid by Raman Spectroscopy. *Anal. Chim Acta* 2008, *616*, 177–184. DOI: 10.1016/j.aca.2008.04.036.
28. Hu, P.; Zheng, X.-S.; Zong, C.; Li, M.-H.; Zhang, L.-Y.; Li, W.; Ren, B. Drop-Coating Deposition and Surface-Enhanced Raman Spectroscopies (DCDR and SERS) Provide Complementary Information of Whole Human Tears. *J. Raman Spectrosc.* 2014, *45*, 565–573. DOI: 10.1002/jrs.4499.
29. Dingari, N. C.; Horowitz, G. L.; Kang, J. W.; Dasari, R. R.; Barman, I. Raman Spectroscopy Provides a Powerful Diagnostic Tool for Accurate Determination of Albumin Glycation. *PLoS One* 2012, *7*, e32406. DOI: 10.1371/journal.pone.0032406.
30. Kuižová, A.; Přikryl, M.; Procházka, M.; Kočišová, E. Drop Coating Deposition Raman (DCDR) Spectroscopy of Contaminants. *Spectrochim. Acta A Mol. Biomol. Spectrosc.* 2021, *262*, 120109. DOI: 10.1016/j.saa.2021.120109.
31. Kočišová, E.; Sayedová, S.; Procházka, M. Drop Coating Deposition Raman Scattering of Selected Small Molecules of Biological Importance. *J. Raman Spectrosc.* 2020, *51*, 871–874. DOI: 10.1002/jrs.5840.
32. Zhang, D.; Mrozek, M. F.; Xie, Y.; Ben-Amotz, D. Chemical Segregation and Reduction of Raman Background Interference Using Drop Coating Deposition. *Appl. Spectrosc.* 2004, *58*, 929–933. DOI: 10.1366/0003702041655430.
33. Kočišová, E.; Procházka, M.; Vaculčiaková, L. Drop-Coating Deposition Raman (DCDR) Spectroscopy as a Tool for Membrane Interaction Studies: Liposome–Porphyrin Complex. *Appl. Spectrosc.* 2015, *69*, 939–945. DOI: 10.1366/14-07836.
34. Šimáková, P.; Kočišová, E.; Procházka, M. Sensitive Raman Spectroscopy of Lipids Based on Drop Deposition Using DCDR and SERS. *J. Raman Spectrosc.* 2013, *44*, 1479–1482. DOI: 10.1002/jrs.4364.
35. Kočišová, E.; Antalík, A.; Procházka, M. Drop Coating Deposition Raman Spectroscopy of Liposomes: Role of Cholesterol. *Chem. Phys. Lipids* 2013, *172-173*, 1–5. DOI: 10.1016/j.chemphyslip.2013.04.002.
36. Kočišová, E.; Vodáková, A.; Procházka, M. DCDR Spectroscopy as Efficient Tool for Liposome Studies: Aspect of Preparation Procedure Parameters. *J. Spectrosc. (Hindawi)* 2012, *27*, 182720.
37. Kočišová, E.; Procházka, M. Drop-Coating Deposition Raman Spectroscopy of Liposomes. *J. Raman Spectrosc.* 2011, *42*, 1606–1610. DOI: 10.1002/jrs.2915.
38. Kocišová, E.; Procházka, M.; Štepánek, J.; Mojzeš, P. Interaction of Porphyrin/Oligonucleotide Complex with Liposomes Studied by Drop Coating Deposition Raman Spectroscopy. *Spectroscopy* 2010, *24*, 197–200. DOI: 10.1155/2010/689749.
39. Djaoued, Y.; Balaji, S.; Priya, S. Non-Resonance Micro-Raman Spectroscopic Studies on Crystalline Domoic Acid and Its Aqueous Solutions. *Spectrochim. Acta A Mol. Biomol. Spectrosc.* 2007, *67*, 1362–1369. DOI: 10.1016/j.saa.2006.10.025.

A.5 Analytical applications of the droplet deposition Raman spectroscopy

KOČIŠOVÁ, Eva; KUIŽOVÁ, Alžbeta; PROCHÁZKA, Marek. Analytical applications of the droplet deposition Raman spectroscopy. *Analyst*. **2024**, pp. 1-15.

Available from doi: 10.1039/D4AN00336E

Analyst

MINIREVIEW

View Article Online
View Journal | View Issue

Cite this: *Analyst*, 2024, **149**, 3276

Analytical applications of droplet deposition Raman spectroscopy

Eva Kočišová, Alžbeta Kuižová and Marek Procházka*

Received 1st March 2024,
Accepted 4th May 2024

DOI: 10.1039/d4an00336e

rsc.li/analyst

The droplet deposition methods in Raman spectroscopy have received considerable attention in the field of analytical sensing focusing on effective pre-concentration of the studied analyte (coffee-ring effect or small spots). This review covers different analytical applications of drop-coating deposition Raman scattering (DCDRS) and droplet deposition surface-enhanced Raman scattering (SERS) spectroscopy. Two main advantages of droplet deposition Raman techniques are considered: the drying-induced segregation of the components from the mixtures (such as body fluids) and the sensitivity of detection of various analytically important molecules. Some recent advanced applications, including clinical cancer diagnosis, are discussed and summarized. Finally, the potential and further perspectives of the droplet deposition Raman methods for analytical studies are introduced.

1. Introduction

Modern analytical techniques should be highly specific and sufficiently sensitive to detect, identify, and quantify an analyte of interest with minimal requirements for sample pre-treatment and preparation. Raman scattering (RS) spectroscopy is an essential analytical technique for chemical and biological analyses based on the fingerprint chemical/structural information extracted from Raman spectra.[1] The relevant advantages are generally low spectral interference from water as a solvent, minimal need for sample pre-treatment, and non-invasive rapid measurement. However, its serious drawback arises from the inherently weak Raman cross-section of a normal RS (*ca.* 10^{-29} cm^2 per molecule), so relatively high concentrations (>1 mM) and/or large quantities of analyte (>1 μg) are typically required. Surmounting this weakness/difficulty and thus amplifying the Raman cross-section are of utmost importance for the trace detection of abundant analytes in biological samples, contaminants, or pollutants. This can be achieved by surface-enhanced techniques or by an analyte drying-induced pre-concentration effect.

Surface-enhanced Raman scattering (SERS) spectroscopy is an efficient method to obtain enhancement of RS on the order of 10^5–10^{10} for molecules adsorbed on plasmonic (such as gold or silver) nanoparticles (NPs) or nanostructures. In this case, electromagnetic enhancement takes place due to the localised surface plasmon resonance (LSPR) on metal nanostructures. Although SERS has become one of the most sensitive analytical tools with a wide range of applications,[2] it is often not straightforward and generally not applicable for any analyte detection. Another enhancement mechanism, a so-called chemical mechanism (CM), is explained as a charge-transfer between the adsorbed molecule and the surface. This is, for instance, a case involving an analyte dried on a hydrophobic graphene-based substrate known as graphene-enhanced Raman scattering (GERS).[3]

An alternative method for improving the Raman sensitivity is drying-induced pre-concentration of the analyte dropped on a suitable (generally hydrophobic) solid surface. The radially outward flow of a liquid in the evaporating droplet carries the dispersed material of the sample to the edge of the droplet, where it is pre-concentrated in a coffee-ring pattern. An original inspiration for the development of the methods based on the coffee-ring effect was the work by Deegan *et al.* published in the journal *Nature* in 1997.[4] This study brought to mind a commonly known phenomenon when a spilled drop of coffee is evaporated on a solid surface. The process was described based on a capillary flow mechanism and showed that it is due to a geometrical constraint where the free surface, constrained by a pinned contact line, pushes the fluid (with the dispersed material) outwards to compensate for evaporative losses. The edge rings of the pre-concentrated analyte are formed for a wide variety of substrates, dispersed materials (solutes), and carrier liquids (solvents), as long as (1) the solvent meets the surface at a non-zero contact angle, (2) the contact line is pinned to its initial position as is commonly the case, and (3) the solvent evaporates. Moreover, they found that mechanisms typically responsible for solute transport such as surface-tension gradients, solute diffusion, and electrostatic as well as

---

*Charles University, Faculty of Mathematics and Physics, Institute of Physics, Ke Karlovu 5, 121 16 Prague 2, Czech Republic.
E-mail: marek.prochazka@matfyz.cuni.cz*

gravity effects are negligible for the ring formation.[4,5] More details on the drying and formation of coffee-ring patterns can be found elsewhere.[6,7]

Combining the coffee-ring effect with detection techniques such as chromatography,[8] colorimetry,[9] mass spectrometry,[10] fluorescence spectroscopy,[11] and Raman spectroscopy brought about various powerful analytical applications.[12] Drop-coating deposition Raman scattering (DCDRS) spectroscopy uses a droplet deposition and evaporation of the target analyte when the Raman spectra are usually measured from the edge of this ring.[13] This way, high-quality Raman spectra can be obtained from samples at small initial volumes (a few μL are sufficient) and several orders of magnitude lower concentrations than in the case of Raman measurement directly from solution or suspension.[13–16]

Although evaporation does not always lead to a coffee-ring pattern, and sometimes small (somewhat spherical) spots are formed, we can benefit from an efficiently pre-concentrated analyte, which is a main prerequisite of the DCDRS approach. Generally, the formed pattern and so the analyte pre-concentration are always the result of the interplay of several factors, such as the type of molecular solution/suspension (analyte), sample concentration and physicochemical properties (contact angles, wettability, and roughness) of the used substrate.[17,18] Various substrates based on hydrophobic top layers such as Teflon-coated stainless steel, polished metals, calcium fluoride (CaF_2), silanised glass, quartz, thiol-modified gold-coated glass or polytetrafluoroethylene tape are successfully used in DCDRS spectroscopy to efficiently pre-concentrate the analyte.[15,16] From the point of view of Raman spectrum acquisition, the substrate itself must have low optical absorbance, the highest possible optical reflectance, and a minimal Raman background signal in the desired spectral region, which is well-ensured in the case of fluorocarbon coatings or polished stainless steel.

The combination of drop-coating deposition with SERS can significantly improve detection sensitivity, benefitting from the synergy of two distinct effects: analyte pre-concentration in a dried pattern (coffee-ring or small spot) and LSPR on the SERS-active surface. Two possible approaches should be taken into consideration: (1) the coffee-ring is formed by dropping and drying the analyte solution on the solid SERS substrate, which ensures SERS enhancement, and (2) the coffee-ring is formed by dropping and drying of the SERS-active NP/analyte mixture on glass/silicon or a similar substrate, so SERS enhancement is ensured by SERS-active NPs. The schematics of DCDRS and both combinations of DCDRS and SERS are depicted in Fig. 1.

This review covers the analytical applications of DCDRS and droplet deposition SERS spectroscopy. Two main advantages of droplet deposition Raman techniques will be considered: the segregation of the components in the mixtures (such as body fluids) and the sensitivity of detection of various analytically important molecules. Some recent advanced applications, including clinical cancer diagnosis, will be summarized. Finally, the potential and further perspectives of the droplet deposition Raman methods for analytical studies will be discussed.

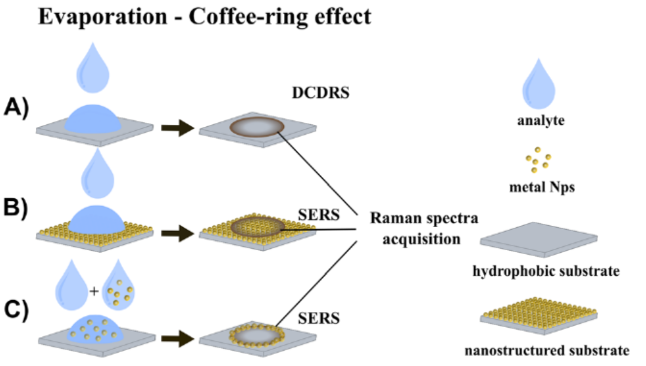

Fig. 1 Schematic figure of (A) DCDRS and (B, C) a combination of droplet deposition with SERS spectroscopy benefitting from the coffee-ring effect where the analyte is dropped on the solid SERS substrate (B) and SERS-active NPs mixed with analyte solution are dropped on the glass/silicon substrate (C).

2. Analytical applications of DCDRS spectroscopy

In the pioneering work of Benz-Amotz *et al.*[13,19] DCDRS was used for the very first time to obtain high-quality Raman spectra of proteins, lysozyme, and insulin, with up to 1000 times higher sensitivity than Raman spectra from solution. Moreover, the authors found that DCDRS spectroscopy benefits from facilitating possible segregation during drying and subsequently enables independent spectral characterisation of the components in the mixture. It was shown to be useful as an efficient approach for separating proteins from other solution components, including fluorescent impurities and buffers.[19] The strength of this method comes from the fact that components in a deposited solution tend to precipitate at different locations on the substrate as a result of a convective streaming during the drying of liquid droplets. This was assumed to be essential for protein accumulation in the edge ring of the dried pattern.[19] In our opinion, the benefits resulting from the segregation capability linked with the coffee-ring effect are still challenging to achieve, and only a few promising studies successfully benefiting from it have been reported.[19–22]

First tests were conducted on single protein and protein/buffer solutions and subsequently on simple protein mixtures. In their first study, Filik and Stone focused on mixtures of three proteins: lysozyme, lactoferrin, and albumin, all of which are commonly found in human body fluids.[20] The aim was to assess the effectiveness of the DCDRS method for determining relative protein concentrations. The study proved that the method is suitable for the compositional analysis of low-concentration protein mixtures and made it possible to assess changes in the relative protein concentrations when subjected to principal component analysis (PCA). This was done with protein levels similar to those in human tear fluid. Moreover, inhomogeneous deposition of the different proteins during the drying process was also observed. For example, lactoferrin–albumin mixtures were regularly spaced compared to spots from mixtures containing lysozyme, which separated from the other proteins.

The following study was performed on human tears, focusing on determining the components in the tear fluid of healthy volunteers and using Raman point mapping to resolve the spatial distribution of these components in the tear's drying pattern.[23] The DCDRS technique produced good-quality spectra (very high signal-to-noise ratio) collected with short acquisition times and small sample volumes. Raman mapping on the dried deposits revealed the presence of protein, lipid, urea, and bicarbonate, which were inhomogeneously distributed throughout the drying pattern. The positioning of the protein, urea and bicarbonate deposits was related to their relative solubility and concentration. The lipid component was found to never be in solution but visible as debris within the drop.

In the next step, an evaluation of tear fluid analysis by the DCDRS method was developed to determine its potential use as a future medical diagnostic technique.[24] The measured spectra of the tear samples of four volunteers were similar, with only subtle differences between them. Fig. 2 shows a white light image of a section of the tear ring with variation in the concentrations of the proteins separated by filtering urea and CaF_2 across the ring determined by least-squares fitting. The three retentate filtrates from the 100 kDa filter (Ret100), 50 kDa filter (Ret50) and 3 kDa filter (Ret3) were analysed. From the outer edge into the middle of the ring, there is a sharp decrease in the relative contributions of Ret100 and Ret3 compared to that of Ret50. The largest spectral variation from Ret50 shown in Ret3 and Ret100 is the large tryptophan and amide III signal, respectively. In the outer ring mean spectrum, both these features are markedly stronger than those in the inner ring mean spectrum. It is obvious that this approach if combined with determining the tear protein compositions of samples by other techniques (gel electrophoresis or colorimetry) and subsequent advanced data processing by partial least squares (PLS) regression can serve as a possible diagnostic tool.

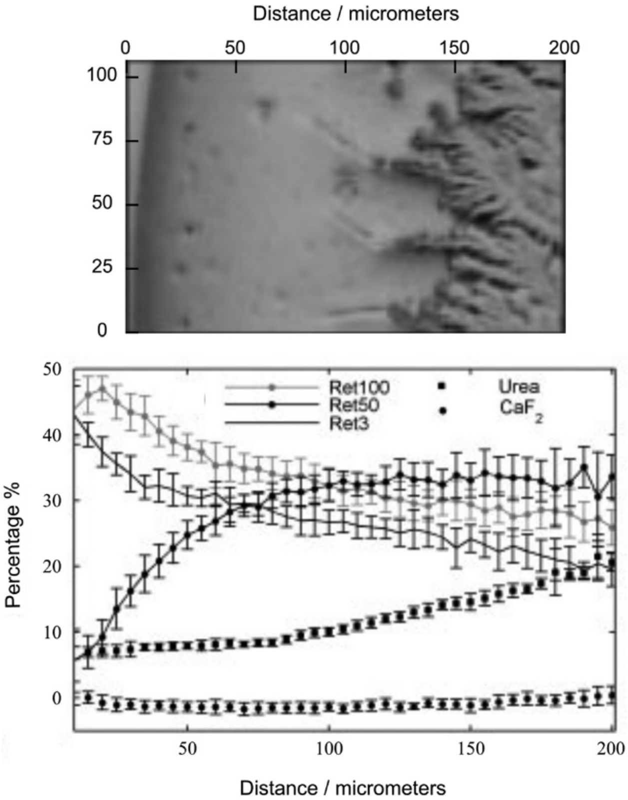

Fig. 2 White light image of the section of the tear ring (top) with variation in the concentrations of the proteins separated by filtering urea and CaF_2 across the ring determined by least-squares fitting (bottom). Adapted from ref. 24 with permission from John Wiley & Sons, Ltd, copyright 2009.

Furthermore, Hu *et al.* employed both DCDRS and SERS spectroscopy to study human tear fluid.[25] They demonstrated that both could be successfully used to analyse the samples without any pretreatment or separation and can provide complementary information about the whole human tear sample. Their results prove that DCDRS is advantageous for the detection of some high-abundance components and SERS for some low-abundance components in the whole tears. They proposed potential further extension also to the analysis of other body fluids.

We employed DCDRS spectroscopy to examine the complex of the cationic copper(II) 5,10,15,20-tetrakis(1-methyl-4-pyridyl) porphyrin (CuTMPyP) and liposomes as a model membrane system, composed of 1,2-dipalmitoyl-*sn*-glycero-3-phosphocholine (DPPC).[26] The measured spectra consisted of the spectral features of DPPC and porphyrins, although the distribution of CuTMPyP in the sample was non-homogeneous. The DCDRS method made it possible to segregate complexed parts from the non-complexed parts of the sample. In addition, the study of the spectra by factor analysis made it possible to distinguish the spectral changes caused by the drying process from the changes caused by the interaction of CuTMPyP with the DPPC liposomes. These spectral changes were attributed to the perturbation of the lipid chain order and porphyrin interaction with the lipid head.

Another experiment in which the CuTMPyP porphyrin/oligonucleotide complex was added to the liposome suspension showed that the drying process caused separation; the liposomes with the bound CuTMPyP porphyrin/oligonucleotide complex were pre-concentrated in the formed edge ring, while the complex itself remained in the central part of the dried pattern. The DCDRS approach also allowed us to reveal that the complexation of oligonucleotides with cationic porphyrin caused its possible binding to the liposome and that this interaction led to certain reorientation of lipid chains.[21]

In addition, DCDRS spectroscopy has been successfully used for the detection of different substances in analytically interesting low concentrations. Djaoued *et al.* studied a domoic acid–tribasic amino acid containing a proline ring, structurally related to glutamic acid, with a side chain having a conjugated double bond moiety and a hind carboxylic acid.[27] It is naturally present in the marine ecosystem in different locations in the world and is recognised as a neurotoxin. Poisoning can cause short-term memory loss, nausea, difficulty breathing, and coma. The study showed that DCDRS spectroscopy can be applied for the rapid detection of domoic acid down to 25 ng of domoic acid per mL (0.025 ppm). The next study by Dingari *et al.* demonstrated an application of DCDRS spectroscopy to the detection and quantification of the concentration of glycated albumin, which is an important glycaemic marker for long-term diabetes monitoring.[28] Moreover, they were able to accurately discriminate glycated albumin from the unglycated variant, even at low µM concentrations. The reached limit of detection (LOD) for glycated albumin is nearly 4 times lower than the lowest physiological concentrations encountered in practice.

Other important analytes detected by DCDRS spectroscopy were food and agricultural contaminants. In our study, selected contaminants formed small dried spots on a hydrophobic surface making it impossible to obtain Raman spectra from stock solutions under the same experimental conditions.[29] The food contaminant melamine (known as an illegal food additive), fungicide thiram (an animal repellent to protect fruit trees), and herbicides bentazone (applied aerially on food crops to control the spread of weeds occurring amongst the food crops) and picloram (a systemic herbicide used for broadleaf weed control in pasture and rangeland, wheat, barley, oats, and woody plant species) have been studied. DCDRS spectroscopy has shown to be a powerful method for the detection of these molecules at concentrations relevant to food/groundwater contamination. The lowest detected concentrations were determined as 6.4 µM, 0.31 µM, 20 µM, and 2 µM in deposited concentrations for melamine, thiram, bentazone, and picloram, respectively. Fig. 3A shows the detection of the herbicide bentazone as an example. Although SERS provided better sensitivity for melamine[30] and thiram,[31] no reported SERS study for bentazone and picloram was found in the literature.

We then used the DCDRS approach to explore the drying-induced separation of the main constituents in a melamine-blended milk infant formula.[22] The spatial segregation of lipids and carbohydrates from pure infant formula into a dried pattern was confirmed by Raman spectral mapping. Lipids tended to accumulate in the coffee-ring, and carbohydrates formed a thin layer in the central part of the ring. The same separation in the dried pattern was also observed for the melamine-blended infant formula, where melamine was detected only from the thin central layer together with carbohydrates due to the melamine glycation by lactose depicted in Fig. 3C. We could benefit not only from the efficient pre-concentration and drying-induced spatial separation but also from the chemical reaction potential of molecules of interest present in a complex solution or suspension.

Regarding bacterial studies, dipicolinic acid is an important component of the bacterial spores of the *Bacillus species* and represents ~10% of their dry weight. The spores are dormant and extremely resistant to different environmental stresses. Dipicolinic acid is a principal component of the spore core responsible for this resistance. Using the DCDRS approach, it is possible to detect dipicolinic acid from a 2 µl drop of 5 × 10^{-7} M deposited concentration as shown in Fig. 3B, which is equivalent to approximately 90 *Bacillus anthracis* spores.[32]

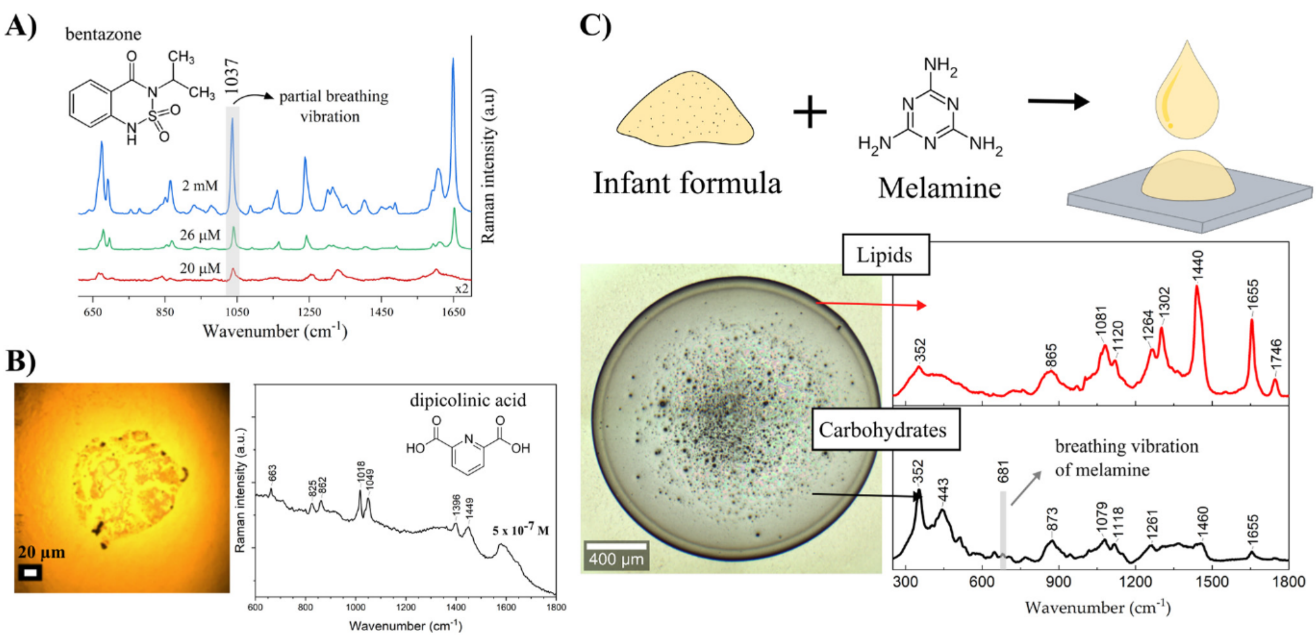

Fig. 3 (A) Detection of the herbicide bentazone by DCDRS spectroscopy. (B) White light image of a dried deposit of dipicolinic acid with the corresponding spectrum. (C) Segregation of lipids and carbohydrates in the dried deposit pattern with the detection of the melamine contaminant only from the layer together with carbohydrates. Inset: chemical structures.

We also used the DCDRS approach to study small molecules with biological importance – acetylsalicylic acid (a substance with antipyretic, anti-inflammatory, and cardio-protective properties), riboflavin (vitamin B2, important in the living cell functioning), and methylene blue (used in different areas of biology and medicine for therapeutic and diagnostic purposes, *e.g.* treatment of methemoglobinemia).[33] The DCDRS detection limits found are 10^{-6}, 10^{-7}, and 10^{-8} M of deposited concentrations for riboflavin, acetylsalicylic acid, and methylene blue, respectively. These detection limits are comparable to or even better than those of the SERS method using the commercial Ag substrate. As for acetylsalicylic acid, no spectra were obtained from concentrations used for the DCDRS approach, probably due to weak adsorption to the silver surface. Moreover, using the DCDRS approach, it was possible to improve the Raman detection sensitivity of porphyrins by a factor of 10^5, and thus, the spectra from ~20 nM deposited concentrations of cationic copper(II) 5,10,15,20-tetrakis(1-methyl-4-pyridyl) porphyrin and anionic copper(II) 5,10,15,20-tetrakis(4-sulfonatophenyl) porphyrin were acquired.[34] Protoporphyrin IX, known as a marker in the clinical diagnosis of cancer, was also detected from a deposited concentration of 10 nM, and although a fluorescence background also appeared, clear Raman bands assigned to the molecule were observed in the spectra.

To profit from DCDRS even more, some studies combined this approach with additional analytical techniques such as chromatography or mass spectrometry. Zhang *et al.* demonstrated the possible compatibility of non-enhanced Raman spectroscopy with chromatographic and mass spectroscopic proteomic sensing on examples of proteomic analytes.[13] They proposed a combined DCDRS/MALDI-TOF approach, providing a mechanism for correlating Raman and mass spectral information. Thus, genetic, environmental, or disease-induced variations in peptides derived from a given protein (with or without posttranslational modifications) could be detected by enzymatic digestion and chromatographic separation followed by DCDRS detection.

Abdolahzadeh *et al.* combined DCDRS spectroscopy with offline monitoring of the reaction's progress.[35] They examined catalysed oxidation of alkenes to epoxides in aqueous solutions at concentrations <10 mM and demonstrated that reproducible spectra can be obtained routinely with relatively little variance, with short acquisition times and sample volumes of 2–10 μL and as little as 1 μg of analyte. The benefit of the DCDRS approach was compared with that of on-line reaction monitoring by ^{1}H NMR and Raman spectroscopy. The authors affirmed the excellent correlation between data obtained from offline and online approaches.

3. Analytical applications of droplet deposition SERS spectroscopy

3.1. Approach 1: analytes dried on a SERS-active substrate

This approach includes all cases where the coffee-ring is formed by dropping and drying the analyte solution on a solid SERS substrate, which ensures SERS enhancement.

Huang *et al.* reported a simple platform, a hydrophobic Ag ink-based plasmonic paper substrate, for simultaneous drop-coating deposition-based pre-concentration and SERS detection of analytes.[36] The hydrophobicity of the plasmonic Ag paper was tuned by Ag-ink concentration to achieve the best pre-concentration of the rhodamine 6G (R6G) analyte in the coffee-ring. Compared with the Raman spectra obtained from conventional DCDRS substrates (such as aluminium), the plasmonic Ag paper offered a much higher Raman signal. From our perspective, dyes like R6G are extensively used in SERS spectroscopy due to their high Raman cross-section value but do not demonstrate the feasibility of the method for real samples with low Raman cross-section value. Although this study did not realise any proof of concept on relevant analytes, it seems that their approach could potentially be a sensitive and label-free detection technique.

Recently, Wi *et al.* introduced a similar platform for the efficient detection of TiO_2 NPs. TiO_2 NPs are widely used as cosmetic additives for blocking UV light and as food additives for artificial colorants.[37] However, there is concern over TiO_2's toxicity. The sensor platform was formed by inkjet-printed porous Ag disks placed on a hydrophobic substrate, such as a hydrogen-terminated Si surface or a fluorosilane-coated glass slide or plastic film (by vapour coating of fluorosilane). A commercial sunscreen lotion (Degussa P25) was dispersed in distilled water and dropped onto the sensor platform. Raman spectra measured from the coffee-ring pattern formed on the Ag disk showed a clear Raman band of TiO_2 at 143 cm^{-1} even at a 0.1 ppb concentration which corresponds to 500 fg of TiO_2. Raman bands belonging to TiO_2 were also identified from the tested chocolate sample, reaching the sensitivity of approximately 200–2000 ppm of TiO_2 (verified by coupled plasma-mass spectroscopy). Since the proposed Raman sensor can be readily prepared by the ink-jet printing of additive-free Ag ion ink, degradation of the Ag nanostructures during storage is avoided.

A distinguished approach is using lithographically fabricated silicon pillar arrays functionalized by Ag NPs for sensitive detection. A dual enhancement of the Raman signals from microdroplets of low-concentration analytes was ensured by combining analyte enrichment through solvent evaporation and plasmonic SERS enhancement. A ≥100-fold concentration of analyte was estimated, with the LOD of 2.9×10^{-12} M for mitoxantrone dihydrochloride.[38] Similar ideas employed superhydrophobic metal needles precoated with SERS-active Ag or Au NPs.[39] This coating step was carried out by pushing the tips through a layer of the NPs confined at a water–oil interface, which resulted in the deposition of a monolayer of NPs on the surface. The NPs were capped with polyvinylpyrrolidone (PVP) to prevent them from jamming together. Then, the small (μL) droplets were dropped to the tip of the needles where they were pinned in place and evaporated, leaving a solid deposit in contact with the SERS enhancing NPs from which the Raman signal is measured. This approach was proved to be extremely sensitive achieving a detection of 2 pg of crystal violet (CV) and 2.5 ng of trinitrotoluene (TNT).[39]

Juneja and Bhattacharya proposed a diagnostic tool to identify low concentrations of noxious pathogens (*Staphylococcus aureus*) from spiked drinking water.[40] They used small pockets of SERS enhancers formed by a 3D Au nanoflower structure on a silicon wafer, providing strong SERS enhancement. To enhance the signal intensities even further, they benefitted from the coffee-ring effect for the pre-concentration of the analytes (water containing *S. aureus*) on such a nanostructure surface. The methodology provided reproducible SERS spectra and the LOD of *S. aureus* in spiked drinking water of 10^3 CFU mL^{-1}. This simple, low-cost, robust, and reproducible method could be useful for increasing the sensitivity of SERS-based detection devices with the capability to be developed into a micro total analysis system.

Liamtsau *et al.* employed the combination of the coffee-ring effect and SERS measurement to study thioarsenicals, such as dimethylmonothioarsinic acid ($DMMTA^V$) and dimethyldithioarsinic acid ($DMDTA^V$), which are important unstable arsenic metabolities.[41,42] The aim was to develop a novel analytical method for the speciation of thiolated arsenicals with minimal sample preparation. They used a Ag nanofilm platform to not only produce the SERS enhancement but to promote the separation of thioarsenic species (Fig. 4). Optimization of the chemical environment (varying pH) resulted in different migration distances of individual species that were together influenced by the radially outward flow of the solute, the thio-arsenical–Ag nanofilm interactions and a thermally induced Marangoni flow. The spatial separation of $DMMTA^V$ to the centre and $DMDTA^V$ to the ring edge of the coffee-ring during the drying process enabled subsequent identification of the species using fingerprint SERS spectra. This work shows how the coffee-ring effect could enable not only the pre-concentration of the studied analyte but also drying-induced spatial separation of different species, which can be further analysed using Raman fingerprint signals. The authors also developed a theoretical framework that adopts a unified approach for both the conventional chromatographic techniques (*e.g.*, GC and HPLC) and coffee-ring-based nanochromatography which employs a stationary phase on the nanometer scale to enable separation at a very short distance (~5 mm). This analysis requires minimal sample pretreatment and allows for nondestructive and simultaneous detection of multiple analytes.[43]

de la O-Cuevas *et al.* combined GERS with DCDRS for sensitive Raman detection of human recombinant interleukin-6 (IL-6) in PBS solution.[44] They successfully used a hybrid platform prepared from a reduced graphene oxide (rGO) thin film deposited on a silicon wafer. The measured signal from the coffee-ring reached a detection limit below 1 pg mL^{-1} with an absolute mass of 1 fg of IL-6. Raman bands acquired from the coffee-ring indicated that IL-6 remains in a solution-like state. In their next study, a combination of DCDRS and GERS was used for specific recognition of the human IL-6 based on the coffee-ring pre-concentration of monoclonal antibodies of IL-6 (mabIL-6) onto an amine functionalized graphene substrate.[45] The formed coffee-ring from the solution of mabIL-6 determined where the selective interaction of the antigen/antibody took place, and IL-6 could be detected and identified by Raman imaging. Fig. 5 (top) shows a scheme of the formation of the substrate: (i) Langmuir–Blodgett (LB) assembly of graphene oxide (GO) substrates ($rGO–NH_2$ and GO) on a solid support, (ii) drop-coating deposition of mabIL-6 (coffee-ring

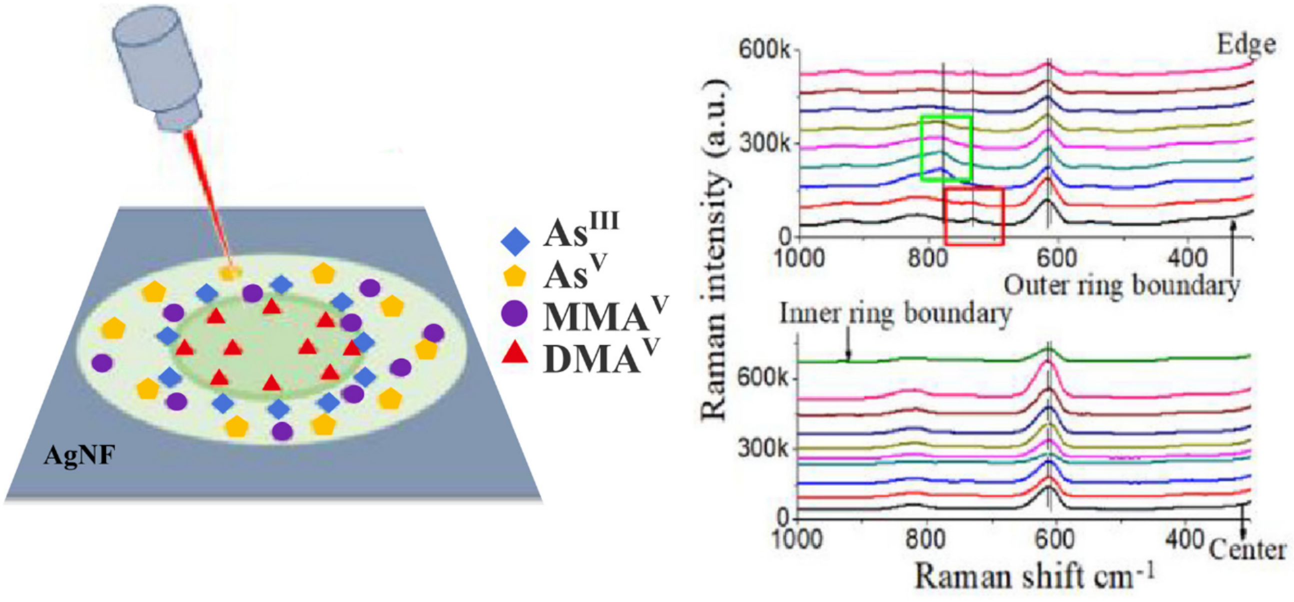

Fig. 4 SERS method for arsenic speciation by using the separation potential of the coffee-ring effect on negatively charged silver nanofilms. (Left) Four arsenic species formed the coffee-ring and (right) the fingerprint SERS signal in solution and on the films. Adapted from ref. 42 with permission from American Chemical Society, copyright 2019.

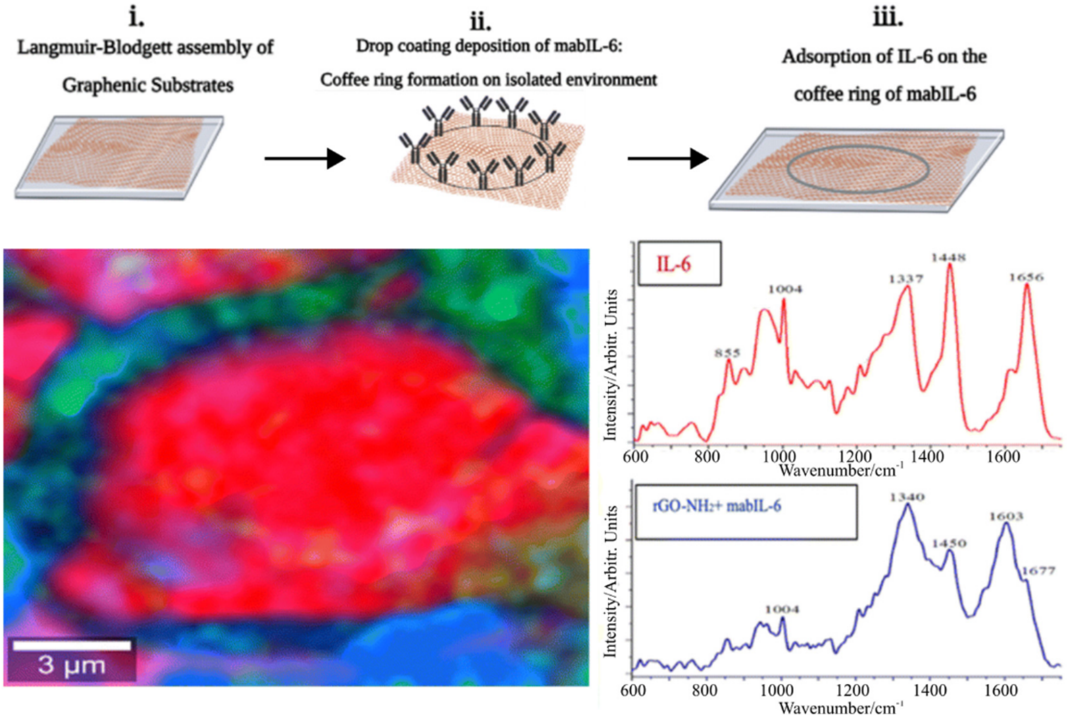

Fig. 5 (Top) Scheme showing (i) the Langmuir–Blodgett (LB) assembly of graphene substrates (rGO–NH_2 and GO) on a solid support, (ii) drop-coating deposition of mabIL-6 (coffee-ring formation) on LB thin films of graphenic substrates and (iii) adsorption of IL-6 on the coffee-ring of mabIL-6. (Bottom) Raman image of the formed coffee-ring and corresponding Raman spectra when the red Raman spectrum is coincident with pure IL-6 and the blue Raman spectrum presents a combination of mabIL-6 and rGO–NH_2 signals. Adapted from ref. 45 with permission from Royal Society of Chemistry, copyright 2023.

formation) on LB thin films of the graphene substrates and (iii) adsorption of IL-6 on the coffee-ring of mabIL-6. Fig. 5 (bottom) shows a Raman image of the formed coffee-ring with Raman spectra when the red Raman spectrum is coincident with pure IL-6 and mabIL-6 and the blue Raman spectrum presents a combination of mabIL-6 and rGO–NH_2 signals. Graphene, prepared by using the chemical vapor deposition technique, served as a substrate where dried drops of the studied amino acids formed coffee-ring patterns.[46] GERS spectra of tryptophan, leucine, phenylalanine, and 3,4-hydroxy-phenylalanine were measured from the ring with the LOD of tens of ng mL^{-1}. Unfortunately, GERS suffers from a low enhancement factor (on the order of 10–20) and in our opinion will not become a routine analytical technique.

3.2. Approach 2: SERS-active NPs/analyte drying on a solid substrate

It is well known that drying of colloidal NPs also forms coffee-ring patterns on certain solid surfaces such as glass/silicon or similar ones.[47] The second approach, the combination of the coffee-ring effect of colloidal metallic NPs and SERS, has received considerable attention thanks to its important applications in the field of analytical sensing.

Our results demonstrated that dried drops of Ag colloid/analyte systems on glass slides formed compact coffee-rings after drying on glass slides.[48–50] We used borohydride-reduced (b.-r.) and hydroxylamine-reduced (h.-r.) Ag NPs with maximum particle size distribution of about 16.8 nm and 38 nm for b.-r. and h.-r. NPs, respectively. The drying process efficiently led to the pre-concentration of the analyte in the ring deposit and promoted the adsorption of the studied analytes to the NPs, as well as creating highly SERS-enhancing sites ('hot-spots'). Thus, by measuring from the ring, SERS spectra that cannot be acquired directly from Ag colloidal solutions (*e.g.* 2×10^{-7} M 1,2-distearoyl-*sn*-glycero-3-phosphocholine – DSPC phospholipid) were obtained.[31] Citrate-reduced (c.-r.) Ag NPs were also tested for the same purpose, allowing the detection of uric acid in solutions down to a 10^{-6} M concentration.[51]

Xu *et al.* developed a SERS sensor for the detection and identification of the environmental pollutants polycyclic aromatic hydrocarbons (PAHs) using bare c.-r. Au NPs (20 nm in size).[52] PAHs are environmental pollutants without any functional group attached to metallic NPs, so direct detection from Ag NPs is impossible. In their tested sensor, a Au NP/PAH mixture dried on a silicon wafer formed the coffee-ring pattern containing closely packed but not aggregated arrays of Au NPs and pre-concentrated PAHs. The SERS spectra of six PAHs, namely, naphthalene, anthracene, pyrene, benzo[*a*]pyrene, benzo[*g*,*h*,*i*]perylene, and indeno[1,2,3-*cd*]pyrene in concentrations down to 5×10^{-6}–2.5×10^{-7} M were obtained by measurement from this coffee-ring pattern. SERS signals collected from 40 spots randomly chosen along each ring demonstrated that the ring provides reproducible and uniform SERS spectra. To prove the feasibility of detection, the SERS spectra of a sample containing six PAHs in river water matrices were collected using a portable Raman spectrometer, and particular PAHs were identified. This portable SERS sensor provided a robust and versatile approach for simple and direct PAH detection and identification from the environment.

Guo *et al.* introduced an approach combining SERS, chemometrics, and coffee-ring effect to detect patulin (PAT) and alternariol (AOH).[53] PAT and AOH are the main mycotoxin contaminants in fruits and their products, which have great toxic effects on the human body due to their teratogenicity and carcinogenicity. Au nanorods (Au NRs) were mixed with standard PAT and AOH solution and dropped and dried on a silicon wafer to form the coffee-ring pattern (Fig. 6). A stable coffee-ring structure was obtained by optimising the drying temperature and droplet volume. The smoothed and baseline-corrected SERS spectra were analysed using the PLS models to predict the content of PAT and AOH. The best performance was obtained by using the synergy interval and genetic algorithm. The LOD values for PAT and AOH were as low as 1 μg L^{-1}, and the relative standard deviation (RSD) $\leq$ 4.86 for PAT and $\leq$2.28% for AOH. To verify the applicability of their approach, the detection of PAT and AOH in actual apple samples was carried out. Since the number of broken apple cells, soluble polysaccharides, and other substances in apple juice may seriously interfere with signal collection, it was difficult to collect SERS spectra directly from apple juice. Therefore, PAT and AOH were extracted from apple juice samples and detected by SERS and HPLC. The lowest detection concentrations of spiked juice samples were 6.49×10^{-5} mol L^{-1} (PAT) and 3.87×10^{-5} mol L^{-1} (AOH), indicating that SERS combined with the coffee-ring effect had the potential to detect PAT and AOH in real samples quickly and effectively. The SERS technology combined with chemometrics and the coffee-ring effect holds promise for high-throughput label-free detection of PAT and AOH in fruits and their products.

Pan *et al.* prepared a β-cyclodextrin-coated Ag NP to form a coffee-ring for the SERS detection of aromatic compounds such as *o*-phenylenediamine with the LOD of 10^{-10} M.[54] Ag NPs were fabricated, and β-cyclodextrins (β-CD) were physically absorbed on the surface of the Ag NPs as capturing layers of aromatic compounds for enriching the analytes at the interface of the Ag NPs in solution. After the analyte was captured, a mixture of Ag NPs and aromatic compounds was dropped on a silicon wafer to form the coffee-ring from which SERS spectra were acquired.

Ni *et al.* used SiO_2@Ag NPs for SERS-based detection and degradation of target species, including the herbicides paraquat and diquat, and their free radicals.[55] The enhanced Raman signals of these target analytes were achieved through the 'hot-spot' region formed by the self-aggregation of SiO_2@Ag NPs due to the coffee-ring effect. The SERS sensor allowed the detection of the analytes down to 10^{-9} M in the aqueous solution. Recently, Yan *et al.* detected aflatoxin B1 down to 5×10^{-7} M using c.-r. Au NPs.[56]

Wang *et al.* reported the sensitive detection of toxic malachite green (MG) and arsenate based on the Ag NPs and coffee-ring effect.[57] Samples with analytes (from environmental water), Ag NPs, and polyvinyl alcohol (PVA) were vortex mixed, and then the mixture was dripped onto the silicon wafer, where it dried to the coffee-ring pattern. The SERS spectra measured from the ring provided the LOD values of 0.1 ng L^{-1} and 0.03 μg L^{-1} for MG and arsenate, respectively. Since the SERS spectrum is still discriminable even in the MG concentration down to 10^{-12} mol L^{-1} (which corresponds to 25 MG molecules at the laser spot), the authors suggested that this SERS sensor might be applicable for single-molecule detection of MG. Lu *et al.* detected 10^{-15} mol L^{-1} R6G (which also corres-

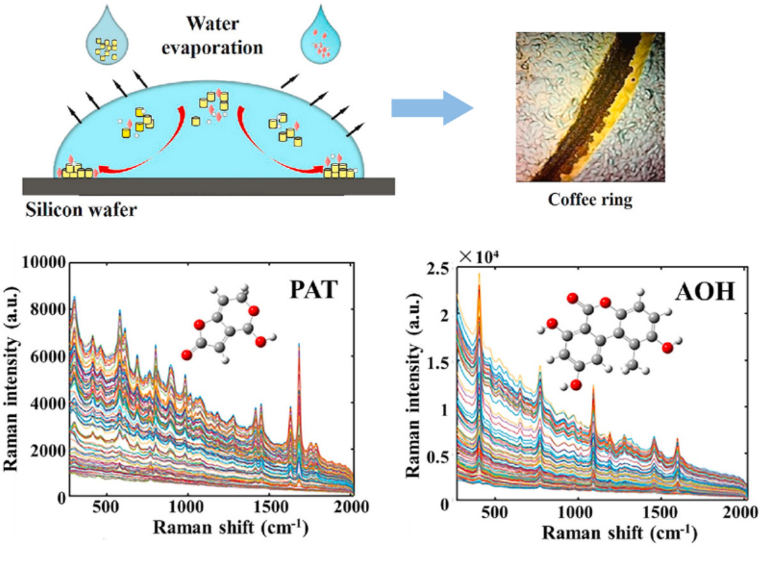

Fig. 6 The high-throughput label-free detection of PAT and AOH using SERS technology based on the coffee-ring effect. Adapted from ref. 53 with permission from Elsevier, copyright 2021.

ponds to the single-molecule level) from Ag NPs dried on a Teflon film.[58] They concluded that Ag NPs dried on the Teflon films exhibit a higher SERS enhancement and better spectral reproducibility compared with that on glass slides.

Wu *et al.* used Ag NPs as the SERS substrate and further employed the coffee-ring effect to detect the illegal adulteration of the chemicals vardenafil and rosiglitazone maleate in healthcare products upto the μg mL^{-1} level.[59] Sodium alginate used as a reduction agent for Ag NP synthesis also protects Ag NPs from aggregation. SERS spectra were measured from the coffee-ring formed by drying the Ag NP/analyte mixture. The method displays a linear response for the determination of vardenafil and rosiglitazone maleate in the 4.88–488 μg mL^{-1} and 4.74–94.7 μg mL^{-1} concentration ranges, and the LOD was as low as 1.63 μg mL^{-1} and 2.20 μg mL^{-1}, respectively. The method was successfully applied to the detection of both analytes in healthcare products, with recoveries higher than 91.52% and RSDs of less than 4.31%.

Regarding medical applications, Hussain *et al.* used Au NPs and Au@Ag NPs with a coffee-ring effect on a gold-coated slide for detecting urea and ammonium sulphate in milk at concentrations down to 5 mg dL^{-1}.[60] This method required a small sample volume and minimal sample treatment. High reproducibility was achieved, confirming that the combination of SERS with coffee-ring effects had the potential to screen other banned and health-hazardous adulterants in milk products simultaneously.

Villa and co-workers reported the pioneering analysis of cancer-relevant biomarkers using the coffee-ring effect of Au NPs.[61,62] The direct deposition of monodisperse Au NPs and *in situ* synthesis of Au NPs on filter paper were used. After that, the analyte adsorption was promoted *via* simple immersion of the SERS substrate in the analyte solution for 30 min. The method displayed in Fig. 7A was successfully applied to the quantitative SERS detection of adenine and guanine in calf thymus DNA after pre-concentration in ring deposit with a calculated value of (G + C)/(A + T) close to the literature value.[61] Later, using this approach, they quantified adenosine (a potential cancer biomarker) in human urine samples.[62] Resolution-alternating least squares (MCR-ALS) were applied to address overlapping bands in the analysis of SERS spectra. The method was shown to be sensitive (the LOD values varying between 3.8 and 4.9 μmol L^{-1}), reproducible (RSD less than ±15%), and selective over other nucleosides (guanosine, cytidine, thymidine, and uridine). This was the first report of a SERS-chemometric method applied to urinary adenosine sensing at physiologically relevant concentrations with minimal sample preparation. Murugesan and Yang used PVP-stabilised Ag NPs mixed with a sample solution.[63] Following the deposition and drying of the mixture solution on a solid substrate, a coffee-ring was formed. When applying the proposed method to determine the phenylalanine level in urine for rapid screening of the phenylketonuria disorder, strong chemical interference from uric acid was observed. To minimise this interference, ZnO powder was applied to the urine sample to adsorb uric acid before SERS detection. Then, SERS signals of phenylalanine were recorded for quantitative purposes. Under the optimised conditions, both the sensitivity and reproducibility of SERS measurement were considerably improved. Quantitative analyses revealed that the developed method is highly feasible for the rapid determination of phenylalanine in real samples. Since adenosine and phenylalanine molecules exhibit high Raman cross-section values, we believe that these approaches are very promising as valuable methods in cancer detection from urine samples.

Hong *et al.* developed a sensor for the rapid diagnosis of colorectal cancer (CRC) through SERS measurements of blood serum.[64] The droplet of a Au NP–serum mixture formed a coffee-ring-like region, providing strong and stable SERS signals. The obtained spectra from cancer patients and healthy volunteers were analysed using unsupervised principal component analysis (PCA) and a supervised machine learning

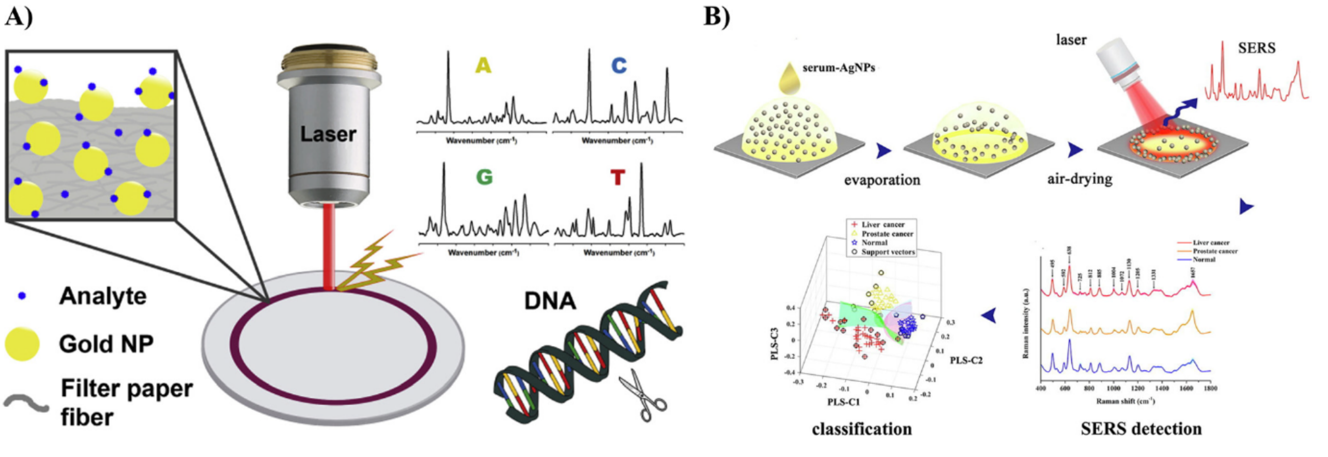

Fig. 7 (A) Quantitative SERS detection of adenine and guanine in calf thymus DNA after pre-concentration due to the coffee-ring effect using the SERS substrate fabricated by *in situ* synthesis of Au NPs on filter paper. Adapted from ref. 61 with permission from Elsevier, copyright 2017. (B) Blood serum analysis strategy using coffee-ring assisted label-free SERS for different types of cancer screening with the corresponding spectra and PLS results for SERS spectral data. Adapted from ref. 65 with permission from Elsevier, copyright 2022.

model, such as support-vector machine (SVM), respectively. The results demonstrate that the SVM model achieves an accuracy and sensitivity of 80% for CRC screening better than that of PCA. Gao *et al.* first used Ag NPs as the SERS substrate combined with a coffee-ring effect for direct label-free blood serum analysis for accurate cancer screening.[65] The unmodified Ag NPs were mixed with the serum from liver cancer patients (n = 40), prostate cancer patients (n = 32) and healthy volunteers (n = 30). The droplets of the Ag NP–serum mixture formed the coffee-ring on the peripheral region after air-drying, providing a stable and reliable SERS signal. Fig. 7B shows typical SERS spectra from the blood serum of liver cancer patients, prostate cancer patients, and healthy volunteers. PLS and SVM algorithms were utilised to establish the diagnosis model for SERS spectral data classification, yielding a high diagnostic accuracy of 98.04% for the healthy group and two types of cancers simultaneously distinguished (Fig. 7B). More importantly, for the unknown testing set, an ideal diagnostic accuracy of 100% could be achieved using the PLS-SVM algorithm for differentiating cancers from the healthy group. The authors stated that the SERS analysis of blood samples combined with the coffee-ring effect and PLS-SVM diagnostic algorithm has the potential for the non-invasive and label-free detection of cancer. Nevertheless, from our point of view, label-free detection of disease markers from blood serum is challenging and may often suffer from low specificity and sensitivity.

3.3. Comparison of both approaches for analytical applications

Two approaches were introduced along with a description of their successful use and application. A comparison of these approaches reveals the advantages and disadvantages of each of them from the point of view of analytical applications.

In approach 1, the dried pattern is formed by dropping and drying the analyte solution on a solid SERS (or GERS) platform, which ensures enhancement of the Raman signal. SERS activity is derived from the SERS-active substrate itself. For the solid, regular, homogeneous SERS-active nanostructure, the signal fluctuation is caused only by the variations of pre-concentration of the analyte in the dry pattern. SERS sensitivity is not as high as in approach 2, but better spectral reproducibility can be achieved. Moreover, in the case of complex analytes and mixtures, approach 1 provides good separation of individual components. Since the SERS effect, in some cases, may be mistaken for a mere coffee-ring effect, a careful evaluation of the measured raw data is necessary.

In approach 2, the dried pattern is formed by dropping and drying the SERS-active NP/analyte mixture on glass/silicon or a similar substrate, so SERS enhancement is ensured by SERS-active NPs. The drying efficiently pre-concentrates the analyte in the ring and promotes adsorption of the studied analyte components to NPs as well as creates 'hot-spots'. The inherent limitation of the drying of NPs is inhomogeneity in sizes of NPs and their aggregates and consequently 'hot-spot' distribution leading to SERS signal alteration and fluctuation. Therefore, this approach offers a high sensitivity but, in some cases, may lack spectral reproducibility. Although some authors reported a stable and reliable SERS signal from dried metal NP/analytes, it seems that achieving satisfactory quantification with this approach remains challenging.

4. Conclusion and further prospects

The droplet deposition Raman spectroscopy considerably improves the Raman sensitivity by drying-induced pre-concentration of the analyte dropped on a suitable (generally hydrophobic) solid surface. The significant advantage is the simplicity and straightforwardness of the technique: only a small sample volume (~μL) and no or minimal sample pre-treatment are needed. The non-enhanced Raman spectrum of the dried analyte deposit provides direct molecular information. Due to segregation capability, the quality of the Raman spectra can be significantly improved as a result of reduced spectral interference from fluorescent impurities and buffer compounds. On the other hand, the separation capability might be limited by the size of molecules and will not work for too small molecules and molecules with high mutual affinity. Moreover, benefitting from the synergy of two distinct effects – analyte pre-concentration in a dried pattern (coffee-ring or small spot) and LSPR in the SERS-active surface – the Raman signal of the analyte can be enhanced even more. In that case, an enhanced SERS spectrum can suffer from signal alteration and fluctuation. Owing to the low enhancement factor (on the order of 10–20), GERS is not suitable for routine analytical applications.

Droplet deposition Raman spectroscopy and its combination with SERS have received considerable attention in the field of analytical sensing. The fundamental applications of droplet deposition Raman techniques include sensitive detection of various analytically important molecules and biomolecules. Moreover, the drying-induced segregation of the components from the mixtures (such as body fluids) represents an important advantage. Chemometric profiting from advanced mathematical tools, *i.e.* PLS regression, should be used to distinguish individual components. There are some exciting advances in body fluid detection combining the coffee-ring effect and SERS technology, where some of such studies focus on the application of the coffee-ring effect-based SERS method to accurately screen cancer in clinical diagnosis. However, the sensitivity and accuracy of simultaneous screening of multiple types of cancer still need to be improved, and further analysed for specific spectral markers linked with individual types of diseases.

The implementation of droplet deposition Raman techniques as routine commercial applications is still challenging. The formation of dried deposits of the target analyte on specific surfaces is generally a complex process and its control is still under investigation. The evaporation of a droplet at room temperature takes around 30 min which brings some limitations, *i.e.* for monitoring fast chemical processes. Moreover, the problematic quantification of the obtained results is a serious drawback for analytical applications. The outcome should be validated *via* other independent techniques (such as chromatography, colorimetry, or mass spectrometry), not only for quantification but also to prevent potential false positives, especially in the case of disease marker detection. Point-of-care or on-site analysis of droplet deposition Raman spectroscopy could be successfully performed *via* combination with the microarray techniques allowing simple and rapid analysis with high throughput.

Author contributions

Eva Kočišová: writing review/editing and resources; Alžbeta Kuižová: writing review/editing, resources, and visualization; Marek Procházka: writing original draft, resources, supervision, conceptualization, and project administration.

Conflicts of interest

There are no conflicts to declare.

Acknowledgements

Financial support from the Czech Science Foundation (grant GAČR 24-12197S) and Charles University (grant SVV-2023-260716) is acknowledged.

References

1 A. Kudelski, *Talanta*, 2008, **76**, 1–8.
2 M. Procházka, *Surface-Enhanced Raman Spectroscopy. Bioanalytical, Biomolecular and Medical Applications*, Springer, Cham, 1st edn, 2016.
3 X. Ling, L. Xie, Y. Fang, H. Xu, H. Zhang, J. Kong, M. S. Dresselhaus, J. Zhang and Z. Liu, *Nano Lett.*, 2010, **10**, 553–561.
4 R. D. Deegan, O. Bakajin, T. F. Dupont, G. Huber, S. R. Nagel and T. A. Witten, *Nature*, 1997, **389**, 827–829.
5 R. D. Deegan, *Phys. Rev. E: Stat., Nonlinear, Soft Matter Phys.*, 2000, **61**, 475–485.
6 D. Mampallil and H. B. Eral, *Adv. Colloid Interface Sci.*, 2018, **252**, 38–54.
7 M. Parsa, S. Harmand and K. Sefiane, *Adv. Colloid Interface Sci.*, 2018, **254**, 22–47.
8 T.-S. Wong, T.-H. Chen, X. Shen and C.-M. Ho, *Anal. Chem.*, 2011, **83**, 1871–1873.
9 R. Hernandez-Perez, Z. H. Fan and J. L. Garcia-Cordero, *Anal. Chem.*, 2016, **88**, 7312–7317.
10 A. L. M. Marsico, B. Duncan, R. F. Landis, G. Y. Tonga, V. M. Rotello and R. W. Vachet, *Anal. Chem.*, 2017, **89**, 3009–3014.
11 M. K. Fan, C. Z. Huang and Y. F. Li, *Anal. Chim. Acta*, 2002, **453**, 97–104.
12 M. Yang, D. Chen, J. Hu, X. Zheng, Z.-J. Lin and H. Zhu, *Trends Anal. Chem.*, 2022, **157**, 116752.
13 D. Zhang, Y. Xie, M. F. Mrozek, C. Ortiz, V. J. Davisson and D. Ben-Amotz, *Anal. Chem.*, 2003, **75**, 5703–5709.
14 E. Kočišová and M. Procházka, *J. Raman Spectrosc.*, 2011, **42**, 1606–1610.
15 A. Kuižová and E. Kočišová, *J. Raman Spectrosc.*, 2023, **54**, 694–705.
16 E. Kočišová and A. Kuižová, *Appl. Spectrosc. Rev.*, 2024, DOI: **10.1080/05704928.2024.2314534**.
17 E. Kočišová, M. Petr, H. Šípová, O. Kylián and M. Procházka, *Phys. Chem. Chem. Phys.*, 2017, **19**, 388–393.
18 A. Kuižová, A. Kuzminova, O. Kylián and E. Kočišová, *Polymers*, 2021, **13**, 4023.
19 D. Zhang, M. F. Mrozek, Y. Xie and D. Ben-Amotz, *Appl. Spectrosc.*, 2004, **58**, 929–933.
20 J. Filik and N. Stone, *Analyst*, 2007, **132**, 544–550.
21 E. Kočišová, M. Procházka, J. Štepánek and P. Mojzeš, *Spectroscopy*, 2010, **24**, 689749.
22 A. Kuižová and E. Kočišová, *Microchem. J.*, 2024, **199**, 110206.
23 J. Filik and N. Stone, *Anal. Chim. Acta*, 2008, **616**, 177–184.
24 J. Filik and N. Stone, *J. Raman Spectrosc.*, 2009, **40**, 218–224.
25 P. Hu, X.-S. Zheng, C. Zong, M.-H. Li, L.-Y. Zhang, W. Li and B. Ren, *J. Raman Spectrosc.*, 2014, **45**, 565–573.
26 E. Kočišová, M. Procházka and L. Vaculčiaková, *Appl. Spectrosc.*, 2015, **69**, 939–945.
27 Y. Djaoued, S. Balaji and S. Priya, *Spectrochim. Acta, Part A*, 2007, **67**, 1362–1369.
28 N. C. Dingari, G. L. Horowitz, J. W. Kang, R. R. Dasari and I. Barman, *PLoS One*, 2012, **7**, e32406.
29 A. Kuižová, M. Přikryl, M. Procházka and E. Kočišová, *Spectrochim. Acta, Part A*, 2021, **262**, 120109.
30 J. Zheng and L. He, *Compr. Rev. Food Sci. Food Saf.*, 2014, **13**, 317–328.
31 J. Zhu, Q. Chen, F. Y. H. Kutsanedzie, M. Yang, Q. Ouyang and H. Jiang, *Anal. Methods*, 2017, **9**, 6186–6193.
32 E. Kočišová and M. Procházka, *J. Raman Spectrosc.*, 2018, **49**, 2050–2052.
33 E. Kočišová, S. Sayedová and M. Procházka, *J. Raman Spectrosc.*, 2020, **51**, 871–874.
34 E. Kočišová and M. Procházka, *J. Raman Spectrosc.*, 2015, **46**, 280–282.
35 S. Abdolahzadeh, N. M. Boyle, A. Draksharapu, A. C. Dennis, R. Hage, J. W. de Boer and W. R. Browne, *Analyst*, 2013, **138**, 3163–3171.
36 Z. Huang, A. Nagpal, S. Siddhanta and I. Barman, *J. Raman Spectrosc.*, 2018, **49**, 1552–1558.
37 J.-S. Wi, J. D. Kim, W. Lee, H. Choi, M. Kwak, J. Song, T. G. Lee and J. G. Ok, *Int. J. Precis. Eng. Manuf. - Green Technol.*, 2022, **9**, 421–429.
38 R. A. Wallace, J. J. Charlton, T. B. Kirchner, N. V. Lavrik, P. G. Datskos and M. J. Sepaniak, *Anal. Chem.*, 2014, **86**, 11819–11825.

39 C. Li, L. Chai, Q. Chen, Z. Ye, Y. Xu and S. E. J. Bell, *J. Raman Spectrosc.*, 2021, **52**, 386–393.

40 S. Juneja and J. Bhattacharya, *Colloids Surf., B*, 2019, **182**, 110349.

41 V. Liamtsau, C. Fan, G. Liu, A. J. McGoron and Y. Cai, *Anal. Chim. Acta*, 2020, **1106**, 88–95.

42 M. Yang, V. Liamtsau, C. Fan, K. L. Sylvers, A. J. McGoron, G. Liu, F. Fu and Y. Cai, *Anal. Chem.*, 2019, **91**, 8280–8288.

43 V. Liamtsau, G. Liu, A. N. Morozov, A. M. Mebel and Y. Cai, *Talanta*, 2022, **250**, 123688.

44 E. de la O-Cuevas, I. Badillo-Ramírez, S. R. Islas, C. Araujo-Andrade and J. M. Saniger, *RSC Adv.*, 2019, **9**, 12269–12275.

45 E. de la O-Cuevas, S. R. Islas, P. Gallegos-Flores, E. L. Esparza-Ibarra, H. Tototzintle-Huitle and J. M. Saniger, *RSC Adv.*, 2023, **13**, 15114–15120.

46 V. Ranc and Z. Chaloupková, *Analyst*, 2020, **145**, 7701–7708.

47 A. F. Routh, *Rep. Prog. Phys.*, 2013, **76**, 046603.

48 P. Šimáková, M. Procházka and E. Kočišová, *Spectrosc. Int. J.*, 2012, **27**, 393847.

49 P. Šimáková, E. Kocisová and M. Procházka, *J. Raman Spectrosc.*, 2013, **44**, 1479–1482.

50 P. Šimáková, E. Kočišová and M. Procházka, *J. Nanomater.*, 2021, **2021**, 4009352.

51 M. Pucetaite, M. Velicka, J. Pilipavicius, A. Beganskiene, J. Ceponkus and V. Sablinskas, *J. Raman Spectrosc.*, 2016, **47**, 681–686.

52 J. Xu, J. Du, C. Jing, Y. Zhang and J. Cui, *ACS Appl. Mater. Interfaces*, 2014, **6**, 6891–6897.

53 Z. Guo, P. Chen, M. Wang, M. Zuo, H. R. El-Seedi, Q. Chen, J. Shi and X. Zou, *LWT–Food Sci. Technol.*, 2021, **152**, 112333.

54 X. Pan, J. Dong, Y. Li, X. Sun, C. Yuan and W. Qian, *RSC Adv.*, 2016, **6**, 29586–29591.

55 C. Ni, J. Zhao, X. Xia, Z. Wang, X. Zhao, J. Yang, N. Zhang, Y. Yang, H. Zhang and D. Gao, *J. Agric. Food Chem.*, 2022, **70**, 15296–15310.

56 X. Yan, W. Zhu, Y. Wang, Y. Wang, D. Kong and M. Li, *Chemosensors*, 2023, **11**, 22.

57 W. Wang, Y. Yin, Z. Tan and J. Liu, *Nanoscale*, 2014, **6**, 9588–9593.

58 L.-Q. Lu, Y. Zheng, W.-G. Qu, H.-Q. Yu and A.-W. Xu, *J. Mater. Chem.*, 2012, **22**, 20986–20990.

59 J. Wu, L. Zhang, X. Bu, P. Li, B. Zhao and Y. Tian, *Analyst*, 2018, **143**, 5202–5209.

60 A. Hussain, D.-W. Sun and H. Pu, *Food Addit. Contam.: Part A*, 2019, **36**, 851–862.

61 J. E. L. Villa, C. Pasquini and R. J. Poppi, *Anal. Chim. Acta*, 2017, **991**, 95–103.

62 J. E. L. Villa, C. Pasquini and R. J. Poppi, *Talanta*, 2018, **187**, 99–105.

63 B. Murugesan and J. Yang, *ACS Omega*, 2019, **4**, 14928–14936.

64 Y. Hong, Y. Li, L. Huang, W. He, S. Wang, C. Wang, G. Zhou, Y. Chen, X. Zhou, Y. Huang, W. Huang, T. Gong and Z. Zhou, *J. Biophotonics*, 2020, **13**, e201960176.

65 S. Gao, Y. Lin, X. Zhao, J. Gao, S. Xie, W. Gong, Y. Yu and J. Lin, *Spectrochim. Acta, Part A*, 2022, **267**, 120605.

A.6 Nanostructured Plasma Polymerized Fluorocarbon Films for Drop Coating Deposition Raman Spectroscopy (DCDRS) of Liposomes

KUIŽOVÁ, Alžbeta; KUZMINOVA, Anna; KYLIÁN, Ondřej; KOČIŠOVÁ, Eva. Nanostructured Plasma Polymerized Fluorocarbon Films for Drop Coating Deposition Raman Spectroscopy (DCDRS) of Liposomes. *Polymers.* **2021**, vol. 13, no. 22, pp. 4023.

Available from doi: 10.3390/polym13224023 polymers

MDPI

Article

Nanostructured Plasma Polymerized Fluorocarbon Films for Drop Coating Deposition Raman Spectroscopy (DCDRS) of Liposomes

Alžbeta Kuižová [1], Anna Kuzminova [2], Ondřej Kylián [2,*] and Eva Kočišová [1,*]

[1] Faculty of Mathematics and Physics, Institute of Physics, Charles University, Ke Karlovu 5, 121 16 Prague, Czech Republic; betka.kuizova@gmail.com
[2] Department of Macromolecular Physics, Faculty of Mathematics and Physics, Charles University, V Holešovičkách 2, 180 00 Prague, Czech Republic; annakuzminova84@gmail.com
* Correspondence: Ondrej.Kylian@mff.cuni.cz (O.K.); Eva.Kocisova@mff.cuni.cz (E.K.); Tel.: +420-951552258 (O.K.); +420-951551349 (E.K.)

Abstract: Raman spectroscopy is one of the most used biodetection techniques. However, its usability is hampered in the case of low concentrated substances because of the weak intensity of the Raman signal. To overcome this limitation, the use of drop coating deposition Raman spectroscopy (DCDRS), in which the liquid samples are allowed to dry into well-defined patterns where the non-volatile solutes are highly concentrated, is appropriate. This significantly improves the Raman sensitivity when compared to the conventional Raman signal from solution/suspension. As DCDRS performance strongly depends on the wetting properties of substrates, we demonstrate here that the smooth hydrophobic plasma polymerized fluorocarbon films prepared by magnetron sputtering (contact angle 108°) are well-suited for the DCDRS detection of liposomes. Furthermore, it was proved that even better improvement of the Raman signal might be achieved if the plasma polymer surfaces are roughened. In this case, 100% higher intensities of Raman signal are observed in comparison with smooth fluorocarbon films. As it is shown, this effect, which has no influence on the profile of Raman spectra, is connected with the increased hydrophobicity of nanostructured fluorocarbon films. This results in the formation of dried liposomal deposits with smaller diameters and higher preconcentration of liposomes.

Keywords: drop coating deposition Raman spectroscopy; DCDRS; plasma polymers; liposomes; nanostructured surfaces; wettability

Citation: Kuižová, A.; Kuzminova, A.; Kylián, O.; Kočišová, E. Nanostructured Plasma Polymerized Fluorocarbon Films for Drop Coating Deposition Raman Spectroscopy (DCDRS) of Liposomes. *Polymers* **2021**, *13*, 4023. https://doi.org/10.3390/polym13224023

Academic Editor: Johannes Carolus (John) Jansen

Received: 15 October 2021
Accepted: 15 November 2021
Published: 21 November 2021

1. Introduction

The wetting of polymeric surfaces plays a crucial role in different sectors such as the textile industry [1], ink-jet printing [2], metallization of polymers [3], and last but not least in biomedical applications [4,5]. The latter is connected with the fact that the surface wettability governs the interaction of polymers with surrounding media, including the biological suspensions or solutions. This, in turn, influences the attachment, adhesion, or the proliferation of cells or adsorption of biomolecules on polymeric surfaces [6–9]. In addition, in some situations, the wettability per-se is not the only parameter to be considered. Equally, and in some cases an even more important parameter, is the way in which a liquid drop dries on a surface. As demonstrated in numerous studies, the droplet drying dynamics have a strong impact on the formation of stains after the complete evaporation of droplets that contain non-volatile solutes [10–12]. A prominent example of this is the formation of the so-called "coffee-ring", i.e., the ring-shaped pattern where the edge part comprises accumulated non-volatile solutes [13]. Such structures are highly advantageous, especially for biodetection, as the substances to be detected are highly preconcentrated in well-defined surface locations. One of the biodetection techniques that benefit from the "coffee-ring" formation is the drop coating deposition Raman spectroscopy (DCDRS). In this technique, the Raman signal is acquired from a dried ring pattern where the analyte is highly preconcentrated, which allows the detection and identification of molecules in small volumes (a drop of several µL) and at low concentrations (mM–µM). Furthermore, the great advantage of this approach is the possibility of detecting biological samples at biologically relevant concentrations, which is not possible by conventional Raman spectroscopy (measurement from solutions or suspensions at a standard concentration from cuvette). Previous works showed improvement by 10^3–10^5 orders of magnitude as compared to the detection sensitivity of conventional Raman spectroscopy from solutions of proteins [14,15], porphyrins [16] or suspensions of liposomes [17,18]. The DCDRS method was also successfully employed in the detection of dipicolinic acid [19], oligosaccharides [20], food and environmental contaminants [21] and also in a study of real body samples as human tears [22–24]. These past studies were concerned about determining the lowest possible detected concentration and finding the spectral fingerprint of protein composition for the tear samples. In addition, the DCDRS technique was shown to be applicable to monitor processes such as albumin glycation [25], catalyzed oxidation [26], and amino acid and peptide phosphate protonation [27] or segregation of impurities and components in mixed solutions [28–30]. As for using Raman spectroscopy to study biological samples, it is inevitable to employ a method that can be sensitive even in low concentrations and small volumes. This makes the DCDRS technique an interesting alternative to the more often employed surface-enhanced Raman spectroscopy (SERS) that relies on substrates with precisely designed metal or metal oxide nanostructures (e.g., [31–33]).

DCDRS technique proved itself a versatile tool for a broad range of applications, mainly because of its sensitivity to low concentrated samples compared to conventional Raman spectroscopy. Nevertheless, we believe that this sensitivity could be further improved because, despite its simplicity, the applicability of DCDRS is strongly dependent on the used substrate material. It has to be highly hydrophobic to provide as low a diameter of the formed stain as possible to reach the highest preconcentration of the analyte and assure the reliable formation of well-defined rings needed for the DCDRS measurements. For instance, three types of smooth substrates (commercial Teflon-coated stainless steel surface SpecTRIM from Tienta Sciences (Indianapolis, IN, USA), non-commercial polished CaF_2, and silanized glass surfaces) were tested and compared in a recent study [34]. This comparison revealed significant variation in the Raman signal enhancement in dependence on the wettability of employed surfaces (the hydrophobicity was different because of the different chemical composition/used materials): the highest signal enhancement was observed for fluorocarbon surfaces that exhibited the highest water contact angle. Therefore, we have focused our attention on the fluorocarbon (C:F) surfaces.

The aim of this study is to demonstrate the possibility to enhance further the DCDRS detection capability of fluorocarbon surfaces by their nanostructuring that results in the increase in the surface hydrophobicity. The nanostructured surfaces were used here for the first time since all the previous DCDRS works employed only the smooth ones [14–30]. To meet this general aim, smooth C:F and nanoroughened C:F surfaces with invariant chemical composition were produced using a fully solvent-free plasma-based deposition strategy that combines radio frequency magnetron sputtering of polytetrafluoroethylene target and gas-phase synthesis of Cu nanoparticles. As will be shown, this allows to precisely tailor the roughness and wettability of produced coatings. The DCDRS performance of produced surfaces was subsequently compared using liposome suspension selected as a model biological system.

2. Materials and Methods

2.1. Fabrication of DCDRS Substrates and Their Characterization

To evaluate the role of surface roughness of fluorocarbon (C:F) thin films on the DCDRS performance, two types of surfaces with identical surface chemical composition were produced—(i) smooth and (ii) roughened. The smooth C:F films were produced by magnetron sputter deposition of 40 nm thick polytetrafluoroethylene (PTFE) layer onto the base platform—one side polished Si wafers (ON Semiconductor, cleaned in ethanol and water) in our case. These substrates are denoted as pPTFE in the subsequent text. The tailor-made roughness of C:F coatings was achieved following a procedure introduced in [35]. This strategy, which is schematically depicted in Figure 1, relies on the additional deposition step, in which the controlled number of nanoparticles (Nps) are sandwiched between two C:F layers (both 20 nm thick in this study). The required surface roughness of resulting coatings is then reached simply by adjusting the size [36] and the number of Nps embedded in the C:F layer [37]. The Cu Nps were deposited in this study utilizing a Haberland-type gas aggregation source (GAS) [38]. It was based on the direct current (DC), water-cooled, 3-inch planar magnetron equipped with a Cu target, which was placed into the water-cooled aggregation chamber (inner diameter of 100 mm) and terminated by a conical output orifice (diameter of 1.5 mm). The GAS was attached to the main deposition chamber, which was pumped by rotary and diffusion pumps. The Cu Nps are produced using Ar as a working gas at the pressure of 40 Pa in the aggregation chamber and using the magnetron current of 400 mA. The deposition time of Cu Nps was 2 and 4 min, and the corresponding samples are denoted as NpsCu2 and NpsCu4, respectively.

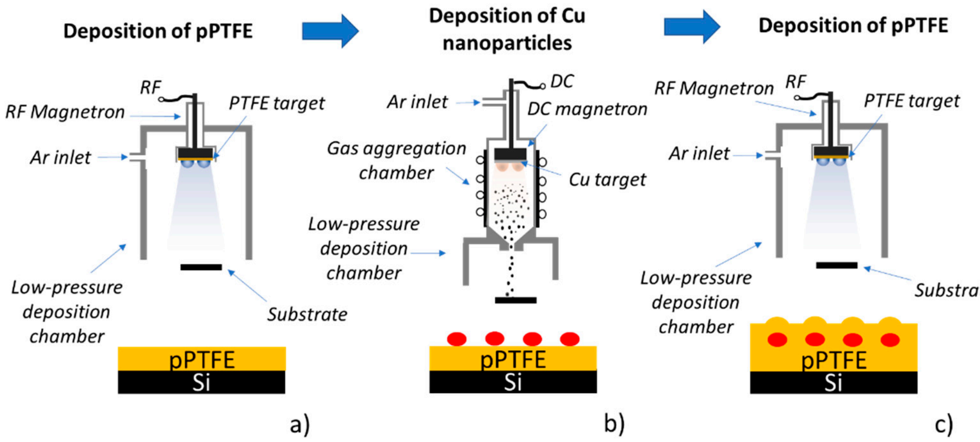

Figure 1. (**a**) Deposition of pPTFE layer. (**b**) Deposition of Cu nanoparticles. (**c**) Overcoating Cu Nps with pPTFE film.

The surface morphology of fabricated coatings was determined by means of atomic force microscopy (AFM) and scanning electron microscopy (SEM). The AFM measurements (scanned area 10 µm × 10 µm) were performed using a QuesantQ-Scope 350 AFM. The AFM scans were acquired in the semi-contact mode (scan rate 2 s) using ACLA–10 Si probes (tip radius < 10 nm, AppNano, Mountain View, CA, USA). The AFM images were subsequently analyzed by open-source Gwyddion software. SEM analysis of the produced coatings was done employing the scanning electron microscope JSM 7200F (JEOL, Akišima, Japan). The SEM images were measured in both secondary electron (SE) and back-scattered electron (BE) modes using an accelerating voltage of 15 kV and a working distance of 10 mm. The wettability of produced smooth and nano-roughened fluorocarbon DCDRS substrates was determined by a home-built goniometer. It consisted of a syringe with testing liquid (liposomal suspensions), substrate holder and camera connected to a computer.

2.2. DCDRS Measurements

To test and compare the DCDRS performance of produced fluorocarbon-based films, the liposomal suspensions were used. These were prepared from 1,2-dipalmitoyl-sn-glycero-3-phosphocholine (DPPC) powder purchased from Avanti Polar Lipids. After the complete dissolution of lipid in pure chloroform in a glass flask, a stream of nitrogen gas was used to remove the solvent to form a thin layer of lipid spread on a glass surface. Subsequently, deionized water (18 MΩ, Millipore-Q, Darmstadt, Germany) was added to the flask and mixed for lipid hydration and spontaneous vesicles formation. Complete hydration to cloudy liposome suspension was achieved by applying an ultrasonic bath and maintaining the suspension at a temperature of 10–15 °C above the main phase transition of DPPC (41 °C) for about half an hour. Apparatus LiposoFast-BasicTM (Avestin, Inc., Mannheim, Germany) with polycarbonate membrane filter with 100 nm pores was used to obtain a unilamellar suspension. The liposomal suspension was extruded through a membrane filter approximately thirty-five times at a temperature of 50 °C. The detailed standard preparation procedure can be seen elsewhere [39]. The final concentration of liposomal suspension was 1 mg/mL (1.36 mM). This stock suspension was subsequently diluted to 0.5 mg/mL, 0.25 mg/mL and 0.125 mg/mL (0.68 mM, 0.34 mM and 0.17 mM, respectively) and all four concentrations were finally used for DCDRS measurements on smooth and nanostructured fluorocarbon substrates.

Liposome suspensions at all concentrations were deposited on substrates as 2 µL droplets and left to dry at room temperature for about half an hour. All DCDRS spectra from ring patterns were recorded by Raman microspectrometer LabRAM HR800 (Horiba Jobin Yvon, Longjumeau, France) in the back-scattering arrangement. The Microspectrometer was equipped with 300 grooves/mm grating and a nitrogen-cooled charged coupled device (CCD) for collecting the scattered light. Irradiation by He-Ne laser with excitation line at 632.8 nm was employed with final power on samples set to 6.4 mW. All spectra were recorded with 400 µm pinhole diameter, 100 µm entrance slit width and 50× ULWD (ultra-long working distance) objective with the spectral acquisition of 60 × 1 s. White light images of formed, dried rings patterns were taken by using objective 5×. Lateral parameters as widths and diameters of rings deposits were determined from white light images using ImageJ software. The lateral widths of the formed rings were measured at 10 randomly selected positions on the ring and the presented values correspond to the average of these measurements.

2.3. Treatment of Measured Spectra by Factor Analysis (FA)

The measured spectra were treated with background corrections and factor analysis by the in-house software developed by J. Palacký [40]. Factor analysis as a multivariate mathematical technique uses a singular value decomposition algorithm for reducing matrices of data to their lowest dimension [41]. The procedure consists of solving the eigenvalue equation that provides orthonormal subspectra $\mathrm{S_j}(\upsilon)$, orthonormal matrix of corresponding scores $\mathrm{V_{ij}}$ and a set of singular values $\mathrm{W_j}$ (weights). A linear combination of computed subspectra can express each original measured spectrum $\mathrm{Y_i}(\upsilon)$ as:

$$\mathrm{Y_i}(\upsilon) = \sum_{j=1}^{m} \mathrm{W_j V_{ij} S_j}(\upsilon) \tag{1}$$

The number *m*, factor dimension, is a minimal number of subspectra that are needed for the best approximation and reconstruction of measured (original) spectra. The output of FA is a set of subspectra, their statistical weights (singular values), residuals errors and normalized coefficients (scores), which indicate the relative presence of subspectra in individual spectra. To analyze measured Raman spectra, the 1st subspectrum is a weighted average of experimental spectra, and all other (second and each subsequent) subspectra reflect various spectral changes. The information from individual subspectra is independent because of their orthogonality. To obtain the factor dimension, singular values assigned to the subspectra can be used, where the significant drop in the value (several orders) is crucial. The number of values before the critical drop indicates the dimension.

3. Results

3.1. Characterization of C:F Substrates

The first step of this study was the characterization of fabricated fluorocarbon-based DCDRS platforms. As mentioned, two distinct types of surfaces for the DCDRS measurements were investigated: smooth pPTFE coatings and C:F coatings with nano-roughness induced by the presence of Cu Nps. The corresponding AFM images of these materials are depicted in Figure 2, where the typical height profiles of all samples and their height histograms are plotted, too. As can be seen, the pPTFE is indeed smooth with a root mean square roughness (Rms) of 0.1 nm, while the increasing number of Cu Nps in the coatings results in more nanostructured character of the coatings and in a gradual increase in their roughness with the growing number of Cu Nps in the films. According to the AFM measurements, the values of Rms were found to be 1.3 nm in the case of NpsCu2 sample and 2 nm in the case of sample NpsCu4. These values are comparable with previously reported values for systems with Ag nanoparticles having similar size (diameter 14 nm) deposited for several minutes and overcoated with pPTFE layer (Rms ~ 2 nm for 2 min deposition time of Ag Nps) [38].

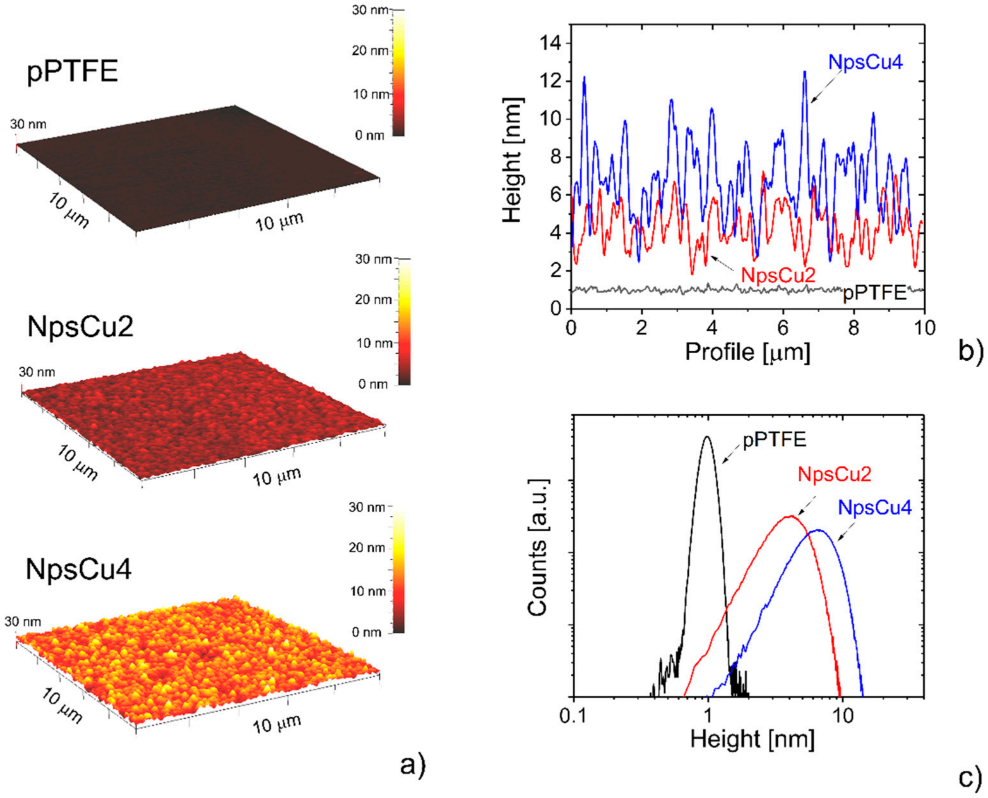

Figure 2. (**a**) AFM images of substrates used for the DCDRS measurements together with their (**b**) height profiles and (**c**) height histograms. The height profiles and height histograms were determined from the AFM images using standard procedures in the program Gwyddion.

The nanostructured character of the samples that contain Cu Nps was also confirmed by SEM with clearly distinguishable Cu Nps (see Figure 3a). The investigation of surface nanostructures using both SE and BE modes of the scanning electron microscope revealed that the Cu Nps are fully coated by a C:F layer (Figure 3b). According to the measured radial profile of intensity of BE signal (false red) that highlights the material contrast (the higher intensity may be ascribed to the presence of Cu Nps in our case), the size of individual Nps is around 14 nm. Such value corresponds to the value reported in the previous work for the Cu Nps prepared under similar conditions [38]. Furthermore, the thickness of the C:F overcoat deduced for the radial profile of nanostructures visualized in the SE mode (false green), i.e., in the mode that is primarily sensitive to the morphology of the samples, was found to be around 6 nm. This value is markedly lower than the thickness of the C:F overcoat that was 20 nm. Such difference is most likely connected with a partial penetration of pPTFE below the copper Nps due to the favored downhill current of the plasma polymer-forming species from the outmost surface of the Nps down to the substrate or into the inter-particle voids [42].

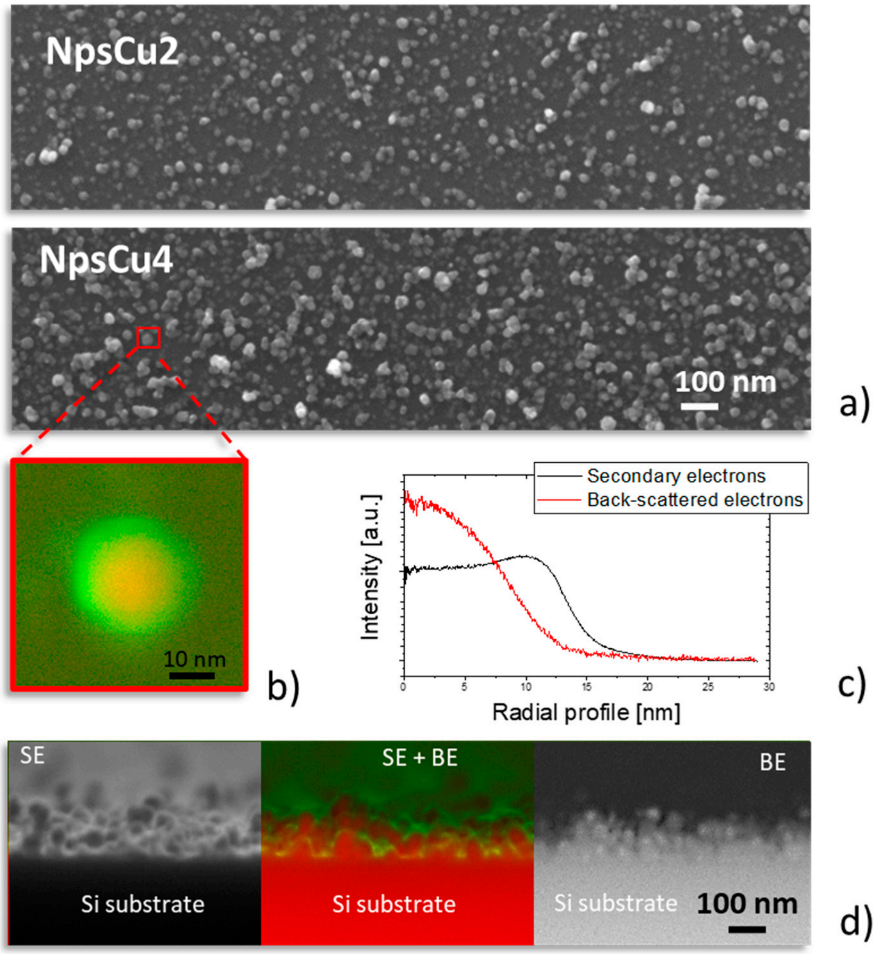

Figure 3. (**a**) Top-view SEM images of samples NpsCu2 and NpsCu4 measured in SE mode. (**b**) Composite SE (false green) and BE (false red) image of detail of surface nanostructure of sample NpsCu4 and (**c**) corresponding radial profiles. (**d**) Cross-section of NpsCu4 coatings measured in SE mode (**left**), BE mode (**right**) and composite SE and BE SEM image (**middle**).

3.2. *Wettability and Drying of Liposome Suspension*

A model dipalmitoylphosphatidylcholine (DPPC) was chosen to prepare a liposome suspension and subsequently to study the influence of smooth and nano-roughened substrates on the wetting/drying process of deposited samples. 2-µL droplets of DPPC suspension at four concentrations (1, 0.5, 0.25 and 0.125 mg/mL) were deposited on the above-mentioned substrates and left to dry at room temperature.

The first important observation is a significant increase in the initial contact angle value of deposited droplets observed with the change of smooth pPTFE substrate to the C:F substrate with deposited nanoparticles: the static contact angle increased from 108° measured on smooth C:F films to 130° and 135° in the case of NpsCu2 and NpsCu4 samples, respectively. Such changes in surface wettability are in qualitative agreement with Wenzel's wetting model, which predicts the enhancement of hydrophobicity of hydrophobic materials upon their roughening [43]. This behavior was found to be independent of the concentration of freshly deposited suspension as the differences of the contact angles for the same substrate were always in the range ±3°.

Next, representative white light images of the liposomal deposits after the complete evaporation of the liquid phase of the suspension presented in Figure 4 demonstrate the typical "coffee-ring" formation after an evaporation process for each deposited droplet on each substrate. As for smooth substrate, the evaporation process led to the formation of compact rings only for concentrations of 1 mg/mL and 0.5 mg/mL (as already observed for commercial smooth substrate SpecTRIM (Tienta Sciences, Indianapolis, IN, USA) in the study [15]). A tendency to form a ring in case of lower concentrations could also be observed. However, this had failed, and a pattern with an incomplete ring was created. This is connected with the presence of the constant contact angle (CCA) drying phase during the droplet evaporation [44] in which the triple line of the drying droplet slides on the smooth pPTFE substrate, as shown in our previous study [37]. In contrast, the heterogeneities in the C:F surface topography induced by the presence of Cu Nps lead to the suppression of the CCA drying phase. Thus, the droplet stays pinned on the surface during its evaporation. The droplet pinning, in turn, allows for the formation of complete and well-defined rings after the complete droplet evaporation also for the lower concentrations.

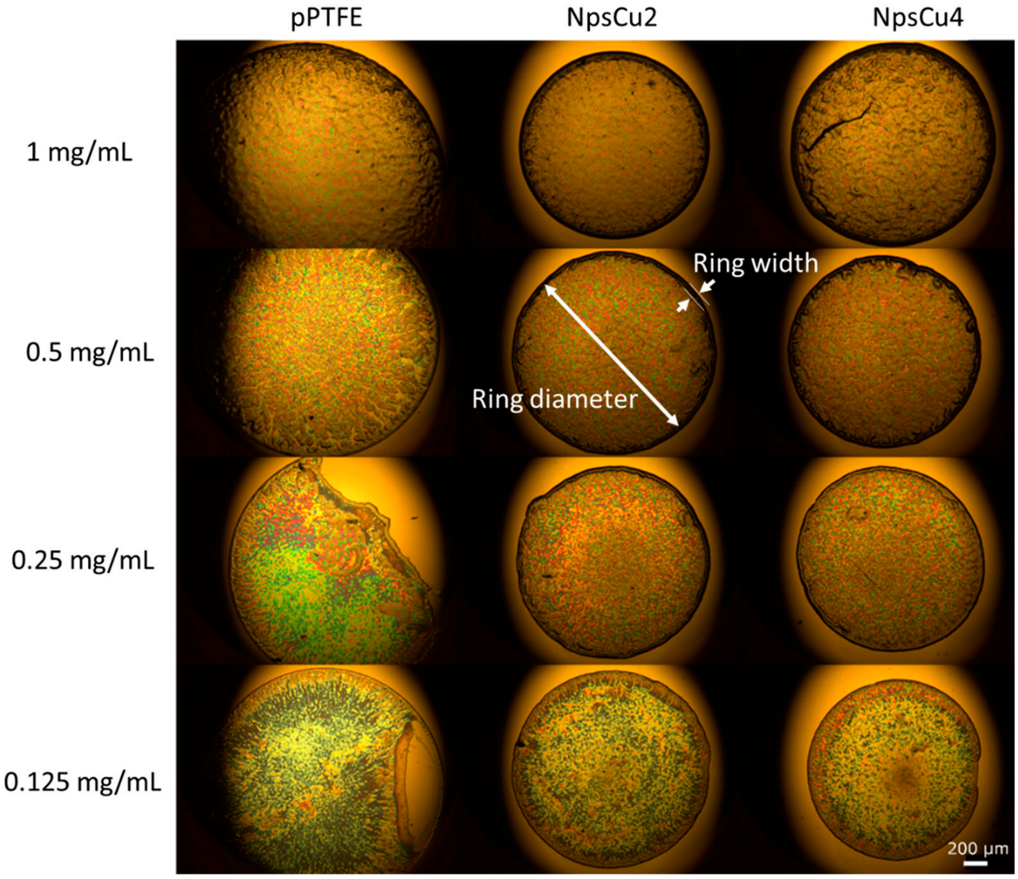

Figure 4. White light images of formed patterns after evaporation of DPPC liposome suspension at four concentrations on three different substrates.

Another effect visible in Figure 4 and quantitatively summarized in Figure 5 is a decrease in the mean diameters and widths of rings formed after the droplet evaporation. As the hydrophobicity and thus also the contact angle increased, the initial contact radius for the droplets with the same volume had to decrease. Because of this, the diameter of the dried DPPC ring decreased in all cases as the wettability decreased. Furthermore, it was found that the initial concentration of the deposited droplet influenced the final structure of the dried pattern, namely the width of the formed ring: deposited drops of lower concentrations dried out into the patterns with a narrower width of the final ring, as shown in Figure 5. This phenomenon is supposed to be connected with the lower number of liposomes that may form the ring. It was also observed that greater roughening (in the case of NpsCu4) did not cause a more pronounced decrease in the diameters and widths of the formed rings, which is consistent with similar wettability of both samples.

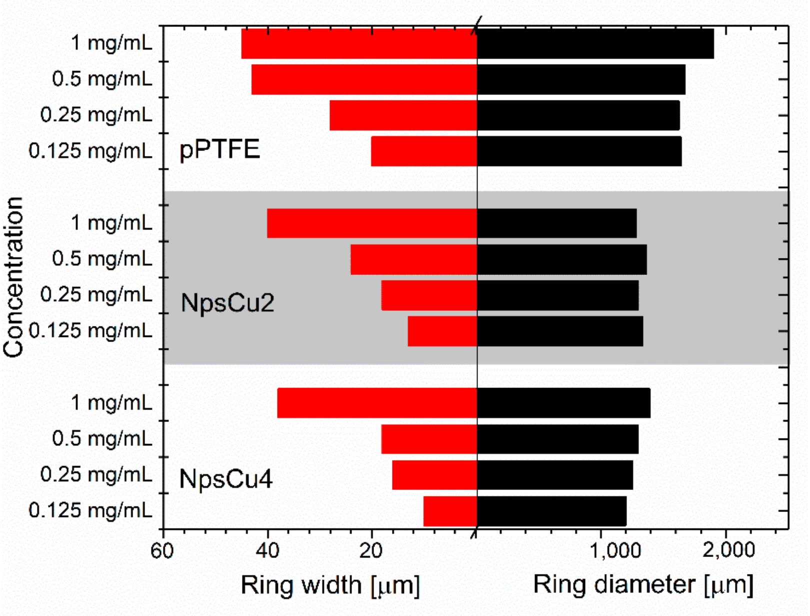

Figure 5. Lateral widths and diameters of the rings formed after the DPPC liposome suspension evaporation.

3.3. DCDRS Performance

Polymeric fluorocarbon smooth surface (pPTFE) was used for testing DCDRS performance of dropped samples of liposomal suspension at different concentrations. For each dried deposit, 25 Raman spectra over the whole ring were accumulated. Acquired spectra for each concentration were treated by baseline adjustment procedure using in-house software to eliminate background signal variations [40]. A typical example of the whole measured spectral interval 550–3300 cm^{-1} for DPPC liposomes by DCDRS on pPTFE substrate is presented in Figure 6a. The upper region 2600–3200 cm^{-1} shown in Figure 6b represents the dominant, more intense part corresponding to the C–H stretching vibrations. Specifically, the spectral band of 2850 cm^{-1} is assigned to the C–H symmetric stretching, 2885 cm^{-1} to the C–H antisymmetric stretching, and the shoulder at 2936 cm^{-1} corresponds to terminal CH_3 symmetric stretching vibrations. The lower part 550–1800 cm^{-1} is less intense and can be more affected by the background signal during the measurement. The three spectral bands in the 1000–1150 cm^{-1} region are assigned to C–C stretching, the band 1299 cm^{-1} is assigned to the CH_2 twisting and the signal at 1441 cm^{-1} corresponds to CH_2 bending [17,45,46]. To compare the signal for different concentrations, the dominant part of spectra sensitive to the phase transitions changes or conceivable interaction with the substrate was used [46]. After the background correction, the averaged spectra for each concentration were compared as shown in Figure 6b, where a decrease of the signal with concentration is clearly demonstrated. This confirms that polymeric fluorocarbon smooth substrate can serve as a suitable hydrophobic DCDRS substrate for liposomal suspension.

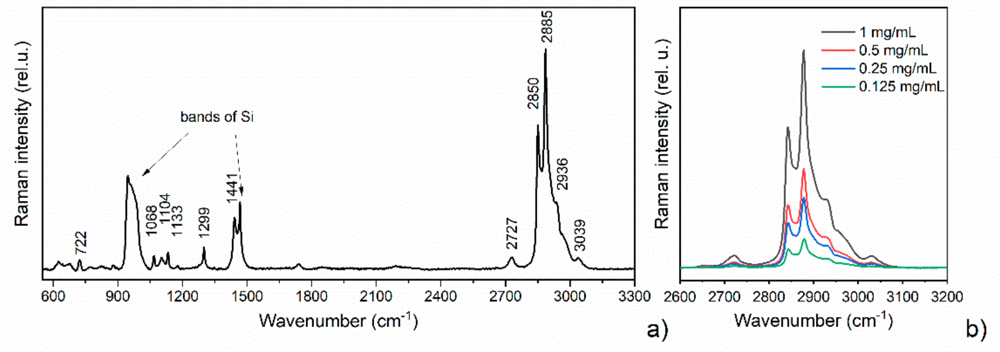

Figure 6. DCDRS spectra of dried liposome suspension from ring-shaped pattern on smooth pPTFE substrate (**a**) at DPPC concentration of 1 mg/mL in the spectral interval 550–3300 cm^{-1}. Marked bands of Si originate from the base layer of the substrate; and (**b**) comparison for the upper dominant region at four different concentrations.

Afterwards, the DCDRS performance of nano-roughened hydrophobic surfaces (NpsCu2 and NpsCu4) for the same samples of liposomal suspension was studied and compared to the performance of the smooth pPTFE substrate. In total, 5 DCDRS spectra were accumulated similarly as for the pPTFE substrate focusing on the dominant part of spectra 2600–3200 cm^{-1}. The baseline-corrected spectra were averaged for each concentration and substrate and compared to each other, as shown in Figure 7. Obtained results showed that the intensity of DPPC spectral bands for each concentration varied in the case of the nanostructured substrates with Cu Nps. For lower concentrations (0.5 mg/mL and 0.125 mg/mL) only a minor intensity difference is present for both nanostructured substrates. At 1 mg/mL, the averaged spectrum from NpsCu4 is more intense than from NpsCu2, but at 0.25 mg/mL the performance from NpsCu2 is better.

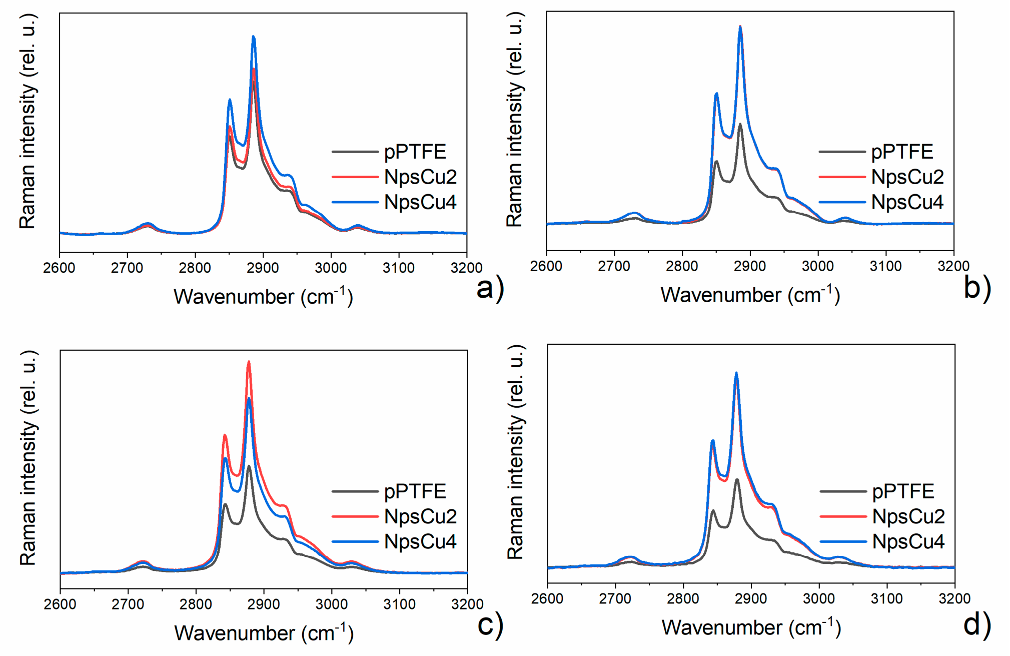

Figure 7. Averaged spectra (baseline corrected) for (**a**) 1 mg/mL, (**b**) 0.5 mg /mL, (**c**) 0.25 mg/mL and (**d**) 0.125 mg/mL deposited concentration of DPPC in the form of liposome suspension.

To demonstrate the DCDRS performance of smooth versus nanostructured substrates, integral intensities in the region 2780–3020 cm^{-1} were calculated. These values, as well as the increase in intensity (in %), are summarized in Figure 8. The significant about twofold increase in integral intensity for nanostructured NpsCu2 substrate relative to the pPTFE one at a concentration of 0.5, 0.25 and 0.125 mg/mL when increased by 105, 97 and 114%, respectively, is clearly seen. Unlike in the case of the concentration 1 mg/mL this increase is only by 10%. Moreover, these results show that the relevant improvement is achieved when the smooth pPTFE substrate is replaced by the nano-roughened NpsCu2, but the additional increase in deposited nanoparticles (NpsCu4) does not guarantee even better performance. The mechanism is based on a more efficient preconcentration of the liposomes from suspension into the dried ring deposit due to the nano-roughened substrate.

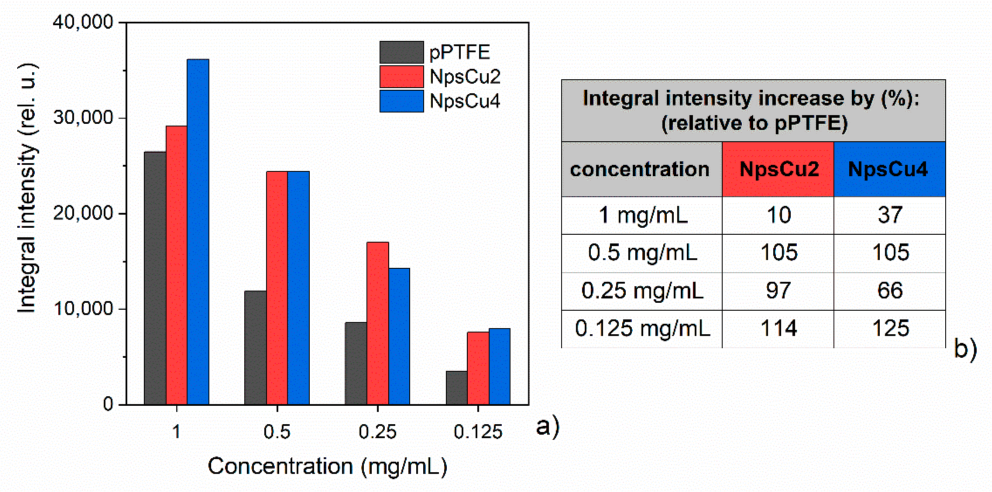

Integral intensity increase by (%): (relative to pPTFE)		
concentration	**NpsCu2**	**NpsCu4**
1 mg/mL	10	37
0.5 mg/mL	105	105
0.25 mg/mL	97	66
0.125 mg/mL	114	125

Figure 8. (**a**) Comparison of the integral intensity of averaged DPPC spectra in the region 2780–3020 cm^{-1} for smooth pPTFE and nanorough NpsCu2, NpsCu4 substrates with (**b**) the integral intensity increase (in %) for nanostructured substrates relative to the smooth pPTFE substrate.

The previous comparison of averaged spectra illustrates only the intensity difference but does not give any information of possible changes in spectral shape due to the side effects, such as an interaction of DPPC with the substrate. A factor analysis (FA) was therefore used as a suitable tool for better determination of the performance for employed hydrophobic substrates. This robust treatment can show (across the different substrates) if any other than intensity changes are present in measured spectral sets. One spectral set for FA consisted of 75 spectra in total, 25 spectra for each substrate.

Due to the nature of the studied system, we expected that the factor dimension would be one. In this case, no change in spectral shape caused by phase transition or interaction between DPPC and substrate would be present, and only intensity variations could be observable. The FA results (seen in Figure 9 for an example of FA performed for the concentration of 0.5 mg/mL) showed that the factor dimension is indeed equal to 1 as the singular values (W) representing the statistical weight of the spectral component decreased significantly for the second and higher components. Furthermore, the residual errors do not have any significant drop, which implies that the first subspectrum with its scores is sufficient to describe our original set of spectra, and including the second or higher subspectrum does not lower the overall residual error significantly.

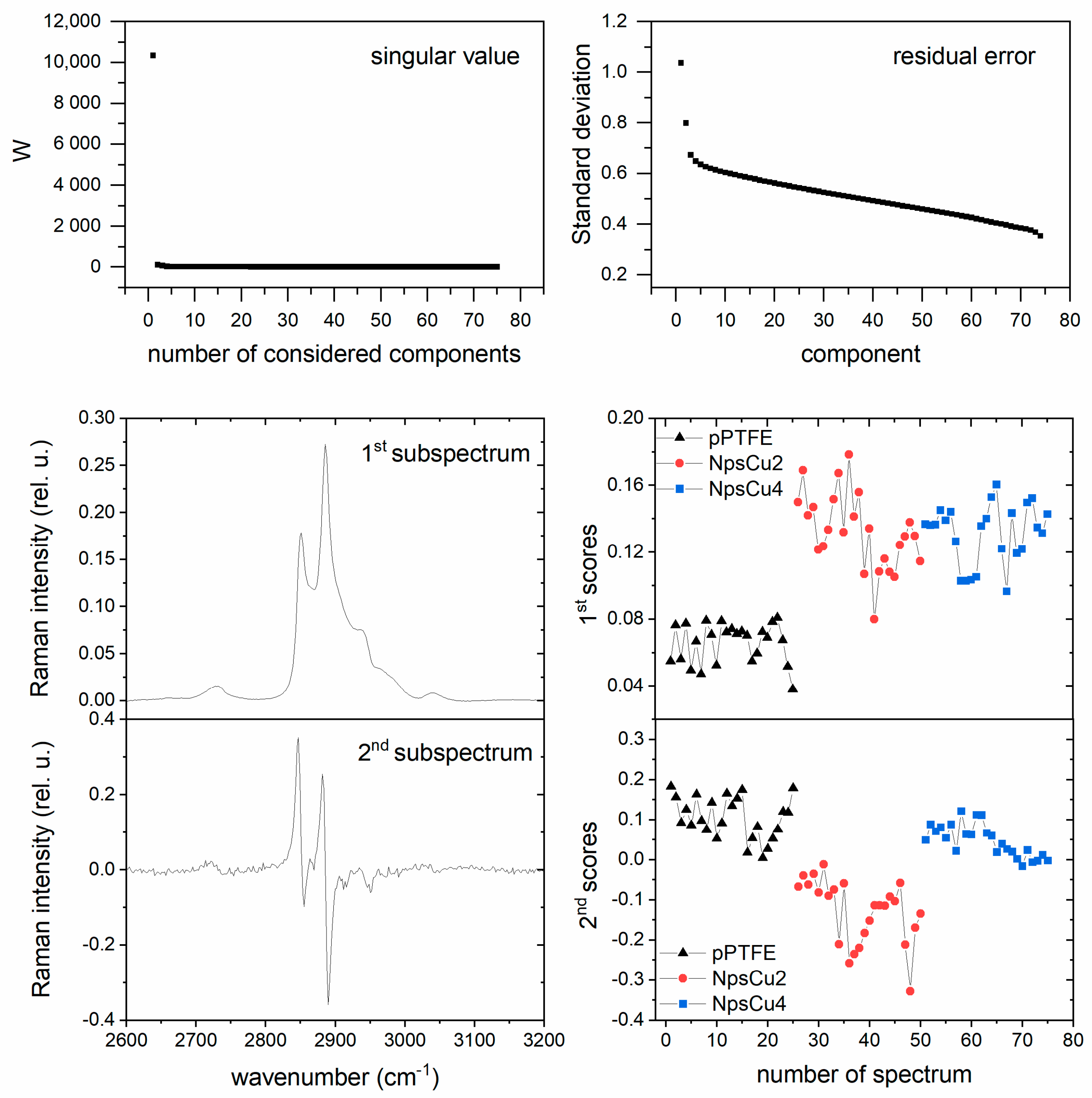

Figure 9. Results of FA for deposited liposome suspension at concentration of 0.5 mg/mL of DPPC, in the particular singular value assigned as W, standard deviation, first and second subspectrum and their belonging scores.

The first subspectrum represents the spectral shape of the DPPC liposome spectrum for the selected spectral interval, and sets of coefficients (scores) belonging to it represent the overall Raman intensity for each baseline-corrected spectrum. From the scores belonging to the first subspectrum concentration, it can be seen that coefficients increase when changing the smooth pPTFE substrate to the nanostructured substrates. As for the second subspectrum, its peculiar shape can be produced by the external effect of calibration due to the laser line shifting during the measurements and by the background signal. Similar results, i.e., the shape of the first and second subspectra, relevant statistical weights and residual errors were also achieved for other studied concentrations. Thus, we can conclude that we observe only changes in the intensities of the Raman signal due to the preconcentration and the interaction of the liposomes with the surface does not occur.

4. Conclusions

DCDRS appeared recently to be a highly promising tool for biodetection. The main advantages of this technique are its simplicity and the possibility to analyze samples at biologically relevant concentrations. However, further improvement of the detection capabilities of DCDRS is still needed. While previous studies employed smooth DCDRS substrates, in this study, we propose and investigate for the first time a novel platform for DCDRS measurements based on the nanostructured C:F plasma polymer coatings fabricated by means of the vacuum-based and fully solvent-free procedure. This technique was found to enable the fabrication of C:F films with tailor-made surface properties relevant for the DCDRS (roughness and wettability). In order to highlight the advantages of nanostructuring, the performance of nanostructured C:F films are compared with smooth C:F films with the same surface chemical composition. The main results may be summarized as follows:

- The smooth C:F surfaces deposited by magnetron sputtering were found to be suitable for the DCDRS detection of liposomes. This is due to the hydrophobic character of C:F coatings that forces liquid liposome suspensions to form coffee-ring structures after the complete evaporation of the liquid phase, at least at a higher DPPC concentration.
- As it is shown, the DCDRS measurements might be significantly improved when the fluorocarbon coatings are nanostructured. This led not only to the pinning of the drying droplet that allowed for the formation of well-defined rings also in the case of lower DPPC concentration but also to the lowering the diameter of the resulting rings. The latter, in turn, made it possible to reach a higher concentration of liposomes in the rings and, hence, to get two times higher Raman signal intensity as compared to smooth fluorocarbon films without compromising the profile of recorded Raman spectra.
- These findings may pave the way for the development of cheap and disposable platforms for efficient DCDRS-based biodetection.

Author Contributions: Conceptualization, A.K. (Alžbeta Kuižová) and E.K.; investigation, A.K. (Alžbeta Kuižová), A.K. (Anna Kuzminova), E.K. and O.K.; writing—original draft preparation, A.K. (Alžbeta Kuižová); writing—review and editing, O.K.; supervision, E.K. All authors have read and agreed to the published version of the manuscript.

Funding: This research was funded by the Czech Science Foundation, grant number 18-10897S, Charles University Research Centre program UNCE/SCI/01 and Grant Agency of Charles University, grant number GA UK (290120).

Institutional Review Board Statement: Not applicable.

Informed Consent Statement: Not applicable.

Data Availability Statement: The data presented in this study are available on request from the corresponding authors.

Conflicts of Interest: The authors declare no conflict of interest.

References

1. Li, S.; Huang, J.; Chen, Z.; Chen, G.; Lai, Y. A review on special wettability textiles: Theoretical models, fabrication technologies and multifunctional applications. *J. Mater. Chem. A* **2017**, *5*, 31–55. [CrossRef]
2. van Osch, T.H.J.; Perelaer, J.; de Laat, A.W.M.; Schubert, U.S. Inkjet Printing of Narrow Conductive Tracks on Untreated Polymeric Substrates. *Adv. Mater.* **2008**, *20*, 343–345. [CrossRef]
3. Su, X.; Li, X.; Ong, C.Y.A.; Herng, T.S.; Wang, Y.; Peng, E.; Ding, J. Metallization of 3D Printed Polymers and Their Application as a Fully Functional Water-Splitting System. *Adv. Sci.* **2019**, *6*, 1801670. [CrossRef]
4. Ferreira, P.; Alves, P.; Coimbra, P.; Gil, M.H. Improving polymeric surfaces for biomedical applications: A review. *J. Coat. Technol. Res.* **2015**, *12*, 463–475. [CrossRef]

5. Kim, M.S.; Khang, G.; Lee, H.B. Gradient polymer surfaces for biomedical applications. *Prog. Polym. Sci.* **2008**, *33*, 138–164. [CrossRef]
6. van Wachem, P.B.; Beugeling, T.; Feijen, J.; Bantjes, A.; Detmers, J.P.; van Aken, W.G. Interaction of cultured human endothelial cells with polymeric surfaces of different wettabilities. *Biomaterials* **1985**, *6*, 403–408. [CrossRef]
7. Lee, J.H.; Khang, G.; Lee, J.W.; Lee, H.B. Interaction of Different Types of Cells on Polymer Surfaces with Wettability Gradient. *J. Colloid Interface Sci.* **1998**, *205*, 323–330. [CrossRef]
8. Bacakova, L.; Filova, E.; Parizek, M.; Ruml, T.; Svorcik, V. Modulation of cell adhesion, proliferation and differentiation on materials designed for body implants. *Biotechnol. Adv.* **2011**, *29*, 739–767. [CrossRef]
9. Cai, S.; Wu, C.; Yang, W.; Liang, W.; Yu, H.; Liu, L. Recent advance in surface modification for regulating cell adhesion and behaviors. *Nanotechnol. Rev.* **2020**, *9*, 971–989. [CrossRef]
10. Mampallil, D.; Eral, H.B. A review on suppression and utilization of the coffee-ring effect. *Adv. Colloid Interface Sci.* **2018**, *252*, 38–54. [CrossRef]
11. Parsa, M.; Harmand, S.; Sefiane, K. Mechanisms of pattern formation from dried sessile drops. *Adv. Colloid Interface Sci.* **2018**, *254*, 22–47. [CrossRef] [PubMed]
12. Zang, D.; Tarafdar, S.; Tarasevich, Y.Y.; Dutta Choudhury, M.; Dutta, T. Evaporation of a Droplet: From physics to applications. *Phys. Rep.* **2019**, *804*, 1–56. [CrossRef]
13. Deegan, R.D.; Bakajin, O.; Dupont, T.F.; Huber, G.; Nagel, S.R.; Witten, T.A. Capillary flow as the cause of ring stains from dried liquid drops. *Nature* **1997**, *389*, 827–829. [CrossRef]
14. Zhang, D.; Xie, Y.; Mrozek, M.F.; Ortiz, C.; Davisson, V.J.; Ben-Amotz, D. Raman Detection of Proteomic Analytes. *Anal. Chem.* **2003**, *75*, 5703–5709. [CrossRef]
15. Kopecký, V.; Baumruk, V. Structure of the ring in drop coating deposited proteins and its implication for Raman spectroscopy of biomolecules. *Vib. Spectrosc.* **2006**, *42*, 184–187. [CrossRef]
16. Kočišová, E.; Procházka, M. Drop-coating deposition Raman spectroscopy of porphyrins. *J. Raman Spectrosc.* **2015**, *46*, 280–282. [CrossRef]
17. Kočišová, E.; Procházka, M. Drop-coating deposition Raman spectroscopy of liposomes. *J. Raman Spectrosc.* **2011**, *42*, 1606–1610. [CrossRef]
18. Šimáková, P.; Kocisová, E.; Procházka, M. Sensitive Raman spectroscopy of lipids based on drop deposition using DCDR and SERS. *J. Raman Spectrosc.* **2013**, *44*, 1479–1482. [CrossRef]
19. Kočišová, E.; Procházka, M. Drop coating deposition Raman spectroscopy of dipicolinic acid. *J. Raman Spectrosc.* **2018**, *49*, 2050–2052. [CrossRef]
20. Mrozek, M.F.; Zhang, D.; Ben-Amotz, D. Oligosaccharide identification and mixture quantification using Raman spectroscopy and chemometric analysis. *Carbohydr. Res.* **2004**, *339*, 141–145. [CrossRef]
21. Kuižová, A.; Přikryl, M.; Procházka, M.; Kočišová, E. Drop coating deposition Raman (DCDR) spectroscopy of contaminants. *Spectrochim. Acta Part A Mol. Biomol. Spectrosc.* **2021**, *262*, 120109. [CrossRef] [PubMed]
22. Filik, J.; Stone, N. Analysis of human tear fluid by Raman spectroscopy. *Anal. Chim. Acta* **2008**, *616*, 177–184. [CrossRef]
23. Filik, J.; Stone, N. Investigation into the protein composition of human tear fluid using centrifugal filters and drop coating deposition Raman spectroscopy. *J. Raman Spectrosc.* **2009**, *40*, 218–224. [CrossRef]
24. Hu, P.; Zheng, X.-S.; Zong, C.; Li, M.-H.; Zhang, L.-Y.; Li, W.; Ren, B. Drop-coating deposition and surface-enhanced Raman spectroscopies (DCDRS and SERS) provide complementary information of whole human tears. *J. Raman Spectrosc.* **2014**, *45*, 565–573. [CrossRef]
25. Dingari, N.C.; Horowitz, G.L.; Kang, J.W.; Dasari, R.R.; Barman, I. Raman Spectroscopy Provides a Powerful Diagnostic Tool for Accurate Determination of Albumin Glycation. *PLoS ONE* **2012**, *7*, e32406. [CrossRef]
26. Abdolahzadeh, S.; Boyle, N.M.; Draksharapu, A.; Dennis, A.C.; Hage, R.; de Boer, J.W.; Browne, W.R. Off-line reaction monitoring of the oxidation of alkenes in water using drop coating deposition Raman (DCDR) spectroscopy. *Analyst* **2013**, *138*, 3163–3171. [CrossRef] [PubMed]
27. Xie, Y.; Jiang, Y.; Ben-Amotz, D. Detection of amino acid and peptide phosphate protonation using Raman spectroscopy. *Anal. Biochem.* **2005**, *343*, 223–230. [CrossRef]
28. Kočišová, E.; Procházka, M.; Vaculčiaková, L. Drop-Coating Deposition Raman (DCDR) Spectroscopy as a Tool for Membrane Interaction Studies: Liposome–Porphyrin Complex. *Appl. Spectrosc.* **2015**, *69*, 939–945. [CrossRef]
29. Zhang, D.; Mrozek, M.F.; Xie, Y.; Ben-Amotz, D. Chemical Segregation and Reduction of Raman Background Interference Using Drop Coating Deposition. *Appl. Spectrosc.* **2004**, *58*, 929–933. [CrossRef]
30. Filik, J.; Stone, N. Drop coating deposition Raman spectroscopy of protein mixtures. *Analyst* **2007**, *132*, 544–550. [CrossRef]
31. Prochazka, M. *Surface-Enhanced Raman Spectroscopy. Bioanalytical, Biomolecular and Medical Applications*, 1st ed.; Springer: Cham, Switzerland, 2016; pp. 1–221.
32. Mosier-Boss, P.A. Review of SERS Substrates for Chemical Sensing. *Nanomaterials* **2017**, *7*, 142. [CrossRef] [PubMed]
33. Pilot, R.; Signorini, R.; Durante, C.; Orian, L.; Bhamidipati, M.; Fabris, L. A Review on Surface-Enhanced Raman Scattering. *Biosensors* **2019**, *9*, 57. [CrossRef] [PubMed]

34. Kocisova, E.; Petr, M.; Sipova, H.; Kylian, O.; Prochazka, M. Drop coating deposition of a liposome suspension on surfaces with different wettabilities: "Coffee ring" formation and suspension preconcentration. *Phys. Chem. Chem. Phys.* **2017**, *19*, 388–393. [CrossRef] [PubMed]
35. Kylián, O.; Polonskyi, O.; Kratochvíl, J.; Artemenko, A.; Choukourov, A.; Drábik, M.; Solař, P.; Slavínská, D.; Biederman, H. Control of Wettability of Plasma Polymers by Application of Ti Nano-Clusters. *Plasma Process. Polym.* **2012**, *9*, 180–187. [CrossRef]
36. Kylián, O.; Petr, M.; Serov, A.; Solař, P.; Polonskyi, O.; Hanuš, J.; Choukourov, A.; Biederman, H. Hydrophobic and super-hydrophobic coatings based on nanoparticles overcoated by fluorocarbon plasma polymer. *Vacuum* **2014**, *100*, 57–60. [CrossRef]
37. Kratochvíl, J.; Kuzminova, A.; Solař, P.; Hanuš, J.; Kylián, O.; Biederman, H. Wetting and drying on gradient-nanostructured C:F surfaces synthesized using a gas aggregation source of nanoparticles combined with magnetron sputtering of polytetrafluoroethylene. *Vacuum* **2019**, *166*, 50–56. [CrossRef]
38. Haberland, H.; Karrais, M.; Mall, M.; Thurner, Y. Thin films from energetic cluster impact: A feasibility study. *J. Vac. Sci. Technol. A* **1992**, *10*, 3266–3271. [CrossRef]
39. MacDonald, R.; Macdonald, R.; Menco, B.; Takeshita, K.; Subbarao, N.; Hu, L.-r. Small-Volume Extrusion Apparatus for Preparation of Large, Unilamellar Vesicles. *Biochim. Biophys. Acta* **1991**, *1061*, 297–303. [CrossRef]
40. Palacký, J.; Mojzeš, P.; Bok, J. SVD-based method for intensity normalization, background correction and solvent subtraction in Raman spectroscopy exploiting the properties of water stretching vibrations. *J. Raman Spectrosc.* **2011**, *42*, 1528–1539. [CrossRef]
41. Malinowski, E.R. *Factor Analysis in Chemistry*, 3rd ed.; Wiley: New York, NY, USA, 2002.
42. Choukourov, A.; Kylian, O.; Petr, M.; Vaidulych, M.; Nikitin, D.; Hanus, J.; Artemenko, A.; Shelemin, A.; Gordeev, I.; Kolska, Z.; et al. RMS roughness-independent tuning of surface wettability by tailoring silver nanoparticles with a fluorocarbon plasma polymer. *Nanoscale* **2017**, *9*, 2616–2625. [CrossRef]
43. Wenzel, R.N. Resistance of Solid Surfaces to Wetting by Water. *Ind. Eng. Chem.* **1936**, *28*, 988–994. [CrossRef]
44. Pittoni, P.G.; Chang, C.-C.; Yu, T.-S.; Lin, S.-Y. Evaporation of water drops on polymer surfaces: Pinning, depinning and dynamics of the triple line. *Colloids Surf. A Physicochem. Eng. Asp.* **2013**, *432*, 89–98. [CrossRef]
45. Czamara, K.; Majzner, K.; Pacia, M.Z.; Kochan, K.; Kaczor, A.; Baranska, M. Raman spectroscopy of lipids: A review. *J. Raman Spectrosc.* **2015**, *46*, 4–20. [CrossRef]
46. Levin, I.W. Vibrational spectroscopy of membrane assemblies. In *Advances in Infrared and Raman Sepctroscopy*, 1st ed.; Clark, R.J.H., Hester, R.E., Eds.; Wiley: New York, NY, USA, 1984; Volume 12, p. 48.

A.7 Drop coating deposition Raman (DCDR) spectroscopy of contaminants

KUIŽOVÁ, Alžbeta; PŘIKRYL, Mikuláš; PROCHÁZKA, Marek; KOČIŠOVÁ, Eva. Drop coating deposition Raman (DCDR) spectroscopy of contaminants. *Spectrochimica Acta Part A: Molecular and Biomolecular Spectroscopy.* **2021**, vol. 262, pp. 120109.

Available from doi: 10.1016/j.saa.2021.120109

Spectrochimica Acta Part A: Molecular and Biomolecular Spectroscopy 262 (2021) 120109

Contents lists available at ScienceDirect

Spectrochimica Acta Part A: Molecular and Biomolecular Spectroscopy

journal homepage: www.elsevier.com/locate/saa

Drop coating deposition Raman (DCDR) spectroscopy of contaminants

Alžbeta Kuižová, Mikuláš Přikryl, Marek Procházka, Eva Kočišová *

Charles University, Faculty of Mathematics and Physics, Institute of Physics, Ke Karlovu 5, 121 16 Prague 2, Czech Republic

HIGHLIGHTS

- DCDR detection of contaminants at biologically/environmentally relevant amounts.
- The lowest DCDR detected concentrations close to SERS limits.
- Two different DCDR spectra of picloram (powder *versus* crystal)

GRAPHICAL ABSTRACT

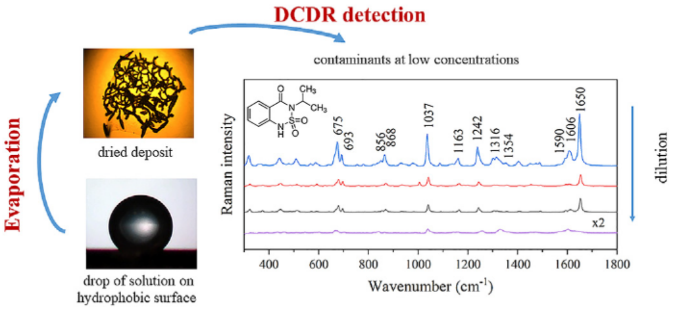

ARTICLE INFO

Article history:
Received 25 January 2021
Received in revised form 2 June 2021
Accepted 21 June 2021
Available online 24 June 2021

Keywords:
Drop coating deposition Raman
DCDR
Contaminant
Melamine
Picloram
Thiram
Bentazon

ABSTRACT

Raman spectroscopy is a useful technique to identify small organic molecules, including contaminants. The drop coating deposition Raman (DCDR) is more sensitive than conventional Raman spectroscopy from solution. It is based on Raman measurement from a small drop dried on a hydrophobic surface where studied molecules are preconcentrated. In this paper, DCDR spectra of dried drops of selected contaminants (food contaminant melamine, fungicide thiram, herbicides bentazon and picloram) on the hydrophobic substrate were acquired for the first time, whereas Raman spectra from stock solutions were impossible to obtain under the same experimental conditions. The lowest DCDR detected concentrations were determined as 6.4 μM, 0.31 μM, 20 μM and 2 μM in deposited concentrations for melamine, thiram, bentazon and picloram, respectively. Therefore, DCDR spectroscopy can serve to detect these molecules in concentrations relevant in food/groundwater contaminations.

1. Introduction

Raman spectroscopy, as a vibrational spectroscopic technique, serves as a powerful analytical tool providing unique information about molecules and their interactions. However, the application of conventional Raman spectroscopy to solutions is generally limited to highly concentrated samples. To study solutions or suspensions in low concentration, a special method – a drop coating deposition Raman (DCDR) spectroscopy – was introduced. It has been a widely used technique to study biological molecules and molecular mixtures in recent years [1–5]. DCDR technique is based on the deposition of a small volume of analyte solution (several μl) on a suitable hydrophobic substrate. Due to the surface hydrophobicity, evaporation of the solvent may lead to preconcentration of studied analyte in ring-shaped drying pattern (known as “coffee-ring”) or into small spots, from which Raman spectra are acquired [6–7]. Compared to conventional Raman spectra from solution, the sensitivity of DCDR can be significantly improved, often by several orders of magnitude [8]. Thus, DCDR represents a special technique of Raman spectroscopy that enables the measurement of solutions at very low concentrations and small volumes which is required for the detection and identification of substances at trace concentrations [9]. Important examples of such substances are various food

---

* Corresponding author.
E-mail address: kocisova@karlov.mff.cuni.cz (E. Kočišová).

https://doi.org/10.1016/j.saa.2021.120109
1386-1425/

additives or pesticides for controlling pests and weeds, which can be both life and environment threatening. We have selected for our study melamine as a food contaminant, thiram as a fungicide and herbicides bentazon and picloram.

Melamine (2,4,6-triamino-1,3,5-triazine) is known as a food additive for apparent elevation of protein content due to its high content of nitrogen. Excessive consumption can lead to the formation of kidney stones. This substance became infamous for its negative health effect established by contamination of infant formula in China in 2008 and pet food in 2004 and 2007. A tolerance level for infant formula was set to 1 mg/l and for other food products to 2.5 mg/l (20 μM) [10].

Thiram (bis(dimethylthiocarbamyl) disulphide) is an example of a fungicide that serves as an animal repellent to protect fruit trees as well. As a fungicide, it is used to prevent deterioration from harvested crops in storage or transport from a variety of fungal diseases. This compound is toxic to the liver due to its breakdown to the form of the carbon disulfide in the body [11]. Thiram is not expected to contaminate groundwater because of its slight water solubility and strong adsorption tendency to soil particles. The maximum residue limit for thiram in EU is 2–7 mg/kg (8–30 μM in solution) [12].

Bentazon (3-isopropyl-2,1,3-benzothiadiazin-4-one 2,2-dioxide) is a herbicide applied aerially on food crops to control the spread of weeds occurring amongst the food crops. It has been detected in groundwater and also in surface water throughout various countries [13–14], which can be dangerous due to its toxicity and mutagenic effects [15–16]. Picloram (4-amino-3,5,6-trichloro pyridine-2-carboxylic acid) is a systemic herbicide used for broadleaf weed control in pasture and rangeland, wheat, barley, oats, and woody plant species [17]. It causes uncontrolled growth of the plant cells leading subsequently to the death of the plant. This substance is relatively water-soluble and can contaminate groundwater and surface water due to its high half-life in soil, where its main degradation pathway is by microbial action [18]. The toxicity of bentazon and picloram in the case of oral exposure is in the order of 50 mg/kg (0.2 mM in solution) and 0.03 mg/kg (0.1 μM in solution) according to the United States Environmental Protection Agency and European Commission, respectively.

This work is focused on the detection of selected contaminants by the DCDR method. We followed the measurements down to concentrations as low as possible to determine their lowest DCDR detected concentrations. They will be compared with previously reported detected concentrations by surface-enhanced Raman spectroscopy (SERS), known as the most sensitive Raman technique.

2. Material and methods

All studied contaminants were purchased from Sigma-Aldrich, Inc. at the highest possible purity as crystalline powders: melamine (product number M2659) and thiram (product number 43966) with 99% purity, bentazon with 99.9% purity (product number 32052) and an amorphous powder picloram with 99,6% purity (product number 36774). Their chemical structure is demonstrated in Fig. 1. All purchased powders were dissolved in deionized water (Millipore-Q, 18 MΩ) and prepared at the highest achievable concentrations. To prepare these stock solutions, data on the highest aqueous solubility published by Yalkowski were used [19]. They are summarized in Table 1. Stock solutions were subsequently diluted into a series of concentrations independently for each contaminant according to its Raman spectra sensitivity.

These initial solutions were further diluted (as will be mentioned in results) and deposited by micropipette as 2-μl drops on hydrophobic substrate SpectRIM™ (Tienta Sciences). This substrate is formed by a polished stainless steel plate with an ultrathin hydrophobic coating (<50 nm) of Teflon. The substrate with deposited drops was covered by a Petri dish to avoid dust contamination and left to dry at room temperature for approximately 30 min. DCDR spectra from formed deposits were measured by a confocal Raman microspectrometer LabRAM HR800 (Horiba Jobin Yvon) equipped with 300 grooves/mm grating, a nitrogen-cooled CCD detector and an internal He-Ne laser with excitation line 632.8 nm. All spectra (DCDR, powders and solutions as well) were recorded with 400 μm pinhole diameter, 100 μm entrance slit width and 50 × ULWD objective. The final laser power on the sample was set to 3 mW. Spectra were accumulated in 300 – 1800 cm^{-1} spectral range with the acquisition of 60 × 1 s.

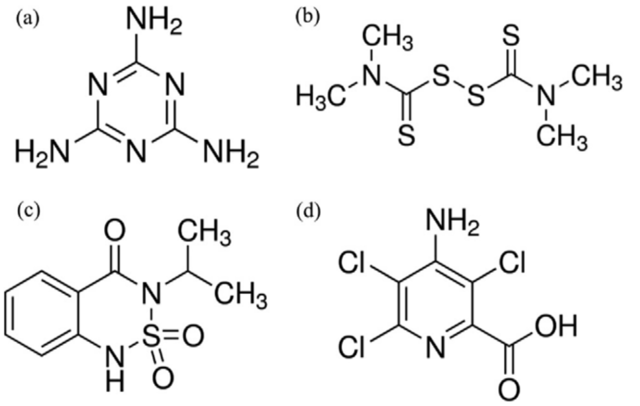

Fig. 1. Chemical structure of (a) melamine, (b) thiram, (c) bentazon and (d) picloram.

Table 1
Aqueous solubility and concentrations of prepared stock solutions.

Contaminant	Maximum solubility (20 °C)	Concentration of prepared stock solution
Melamine	2.69 mg/ml (21.35 mM)	16 mM
Thiram	0.03 mg/ml (0.12 mM)	0.062 mM
Bentazon	0.5 mg/ml (2.08 mM)	2 mM
Picloram	0.55 mg/ml (2.28 mM)	2 mM

For DCDR measurement, we have always monitored 2–3 dried drops and accumulated a minimum of 10 spectra per deposit. Presented DCDR spectra correspond to the average of three spectra of the highest quality. To check the signal from different spots of the dried drop, we measured a spectral map of the bentazon (Figure S1). The signal fluctuation was up to 40%. Spectra of stock solutions as reference measured under the same experimental conditions from drops on a microscope slide are presented in Figure S2. They do not show any spectral features of studied molecules, except for the weak band at 676 cm^{-1} that appeared in the spectrum of melamine.

White light images of dried patterns were taken by using objectives 5 ×, 10 × and 50 × .

3. Results and discussion

Droplets of aqueous solutions of all studied contaminants were deposited on commercial SpectRIM™ hydrophobic surface (contact angle for a drop of water is 122°) at various concentrations, starting with the highest one and gradually decreasing. We observed the dried deposits at different forms and measured DCDR spectra from them in every case.

3.1. Melamine

Droplets of aqueous solutions of melamine after an evaporation process demonstrated different dried patterns according to initial deposited concentration, as seen in Fig. 2. A droplet of the prepared stock solution (1.6 × 10^{-2} M) led to the formation of small sharply shaped crystals, which were still observable for 10^{-3} M concentration (not shown). Gradual dilution to lower concentrations led to the dried deposits that change from the homogenous amorphous form (0.16 mM) (Fig. 2b) to small non-homogenously distributed spots (32 μM – not shown and 6.4 μM) (Fig. 2c).

Afterwards, Raman spectra for each concentration were acquired from preconcentrated spots on the substrate. The characteristic spectral bands of melamine appeared in the lower wavenumber spectral region. Fig. 3 shows that detected bands from dried deposits are in good agreement with reference Raman spectrum of melamine acquired from crystalline powder. We assessed that the lowest initial concentration from which we are able to obtain a Raman spectrum of good quality for melamine is 6.4 μM. This lowest DCDR detected concentrations is one or two orders of magnitude higher than those reported by the SERS technique on common Ag or Au nanoparticles or solid nanostructures (10^{-7}–10^{-8} M) [20].

3.2. Thiram

Dried deposit from a drop of stock solution of thiram (62 μM), as next examined contaminant, led to the formation of a bulk pattern situated in the centre of the initially placed droplet (Fig. 4a). The final dried deposit possessed a rough height profile without any signs of visible microcrystals. Subsequent dilution of the stock solution caused a change in the dried residue, and for 0.62 μM and lower concentration 0.31 μM, we observed nonhomogenous deposits varying in total size and final pattern (Fig. 4b,c). Another dilution to lower concentrations (0.1 μM and 62 nM – not shown) led to the formation of similar dried deposits, but we no longer were able to obtain Raman spectra. Fig. 5 compares the acquired Raman spectra from each deposit of detectable thiram solution

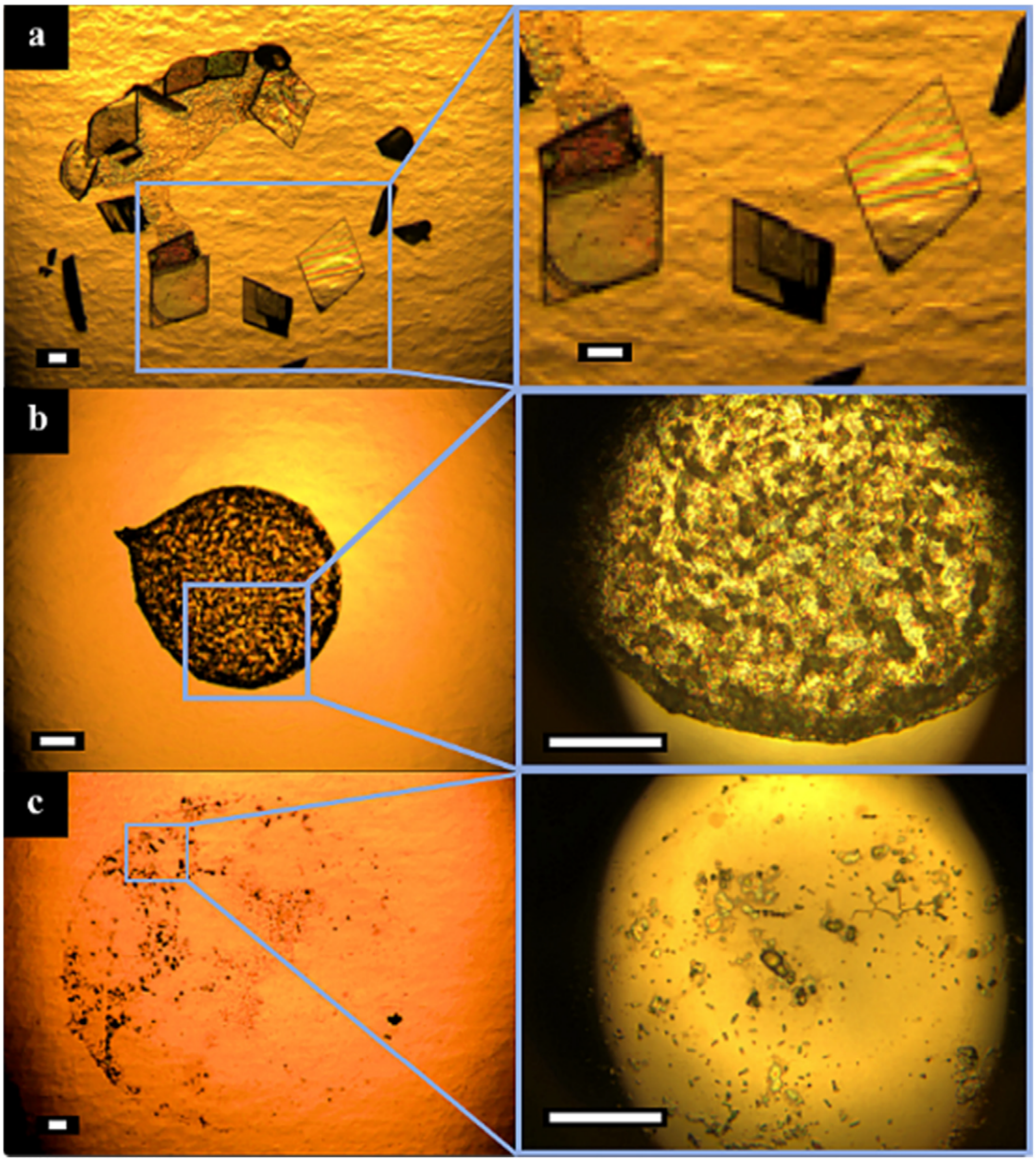

Fig. 2. White light images of dried drops of melamine a) 1.6 × 10^{-2} M, b) 0.16 mM and c) 6.4 μM concentration (1 white bar = 40 μm).

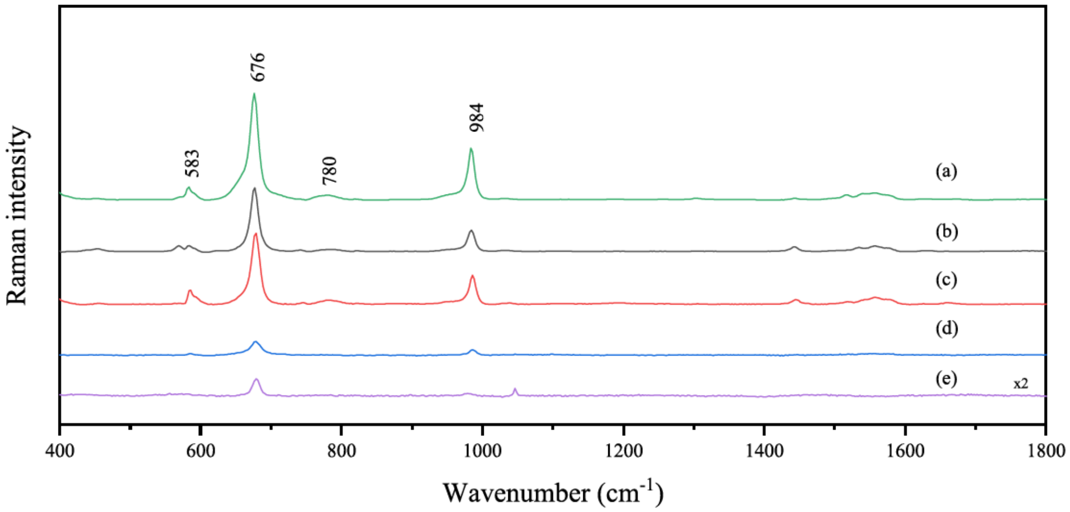

Fig. 3. Raman spectra of melamine from a) crystalline powder, and dried drop in deposited concentration b) 16 mM, c) 1.6 mM d) 0.16 mM and e) 6.4 μM.

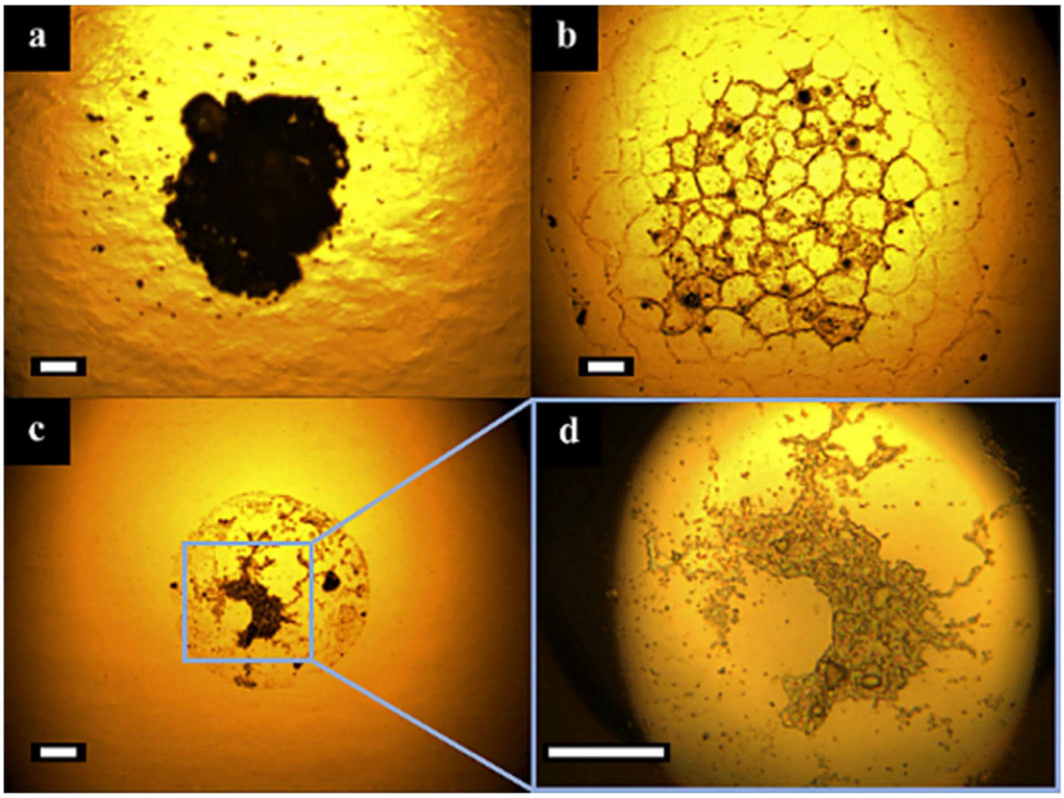

Fig. 4. White light images of dried drops of thiram a) 62 μM, b) 0.62 μM and c,d) 0.31 μM concentration (1 white bar = 40 μm).

and crystalline powder sample as a reference. DCDR spectra were similar to the spectrum of the powder; only slight changes in intensity ratios were observed, specifically at 320/396 cm^{-1}, 976/851 cm^{-1} and at 1398/1374 cm^{-1}.

We estimated the lowest DCDR detected concentration of thiram as 0.31 μM. It is close to the detected concentration obtained by SERS from Au nanorods (10^{-7} M) [21]. Again, the more sophisticated SERS detection using Au@Ag nanoparticles and paper-based microfluidic allowed SERS detection of thiram at 10^{-9} M concentration [22].

3.3. Bentazon

Deposition and subsequent evaporation of small droplets of bentazon solutions led to different final dried patterns depending on the initial concentration. A stock solution with the initial concentration of 2 mM resulted in a deposit of crystalline character that had the form of thin, tangled stripes (Fig. 6a). After dilution to 0.2 mM, a significant change in the dried deposit was noticed where the evaporation led to the round shape pattern, and the sample was homogeneously distributed (Fig. 6c). Reaching 20 μM

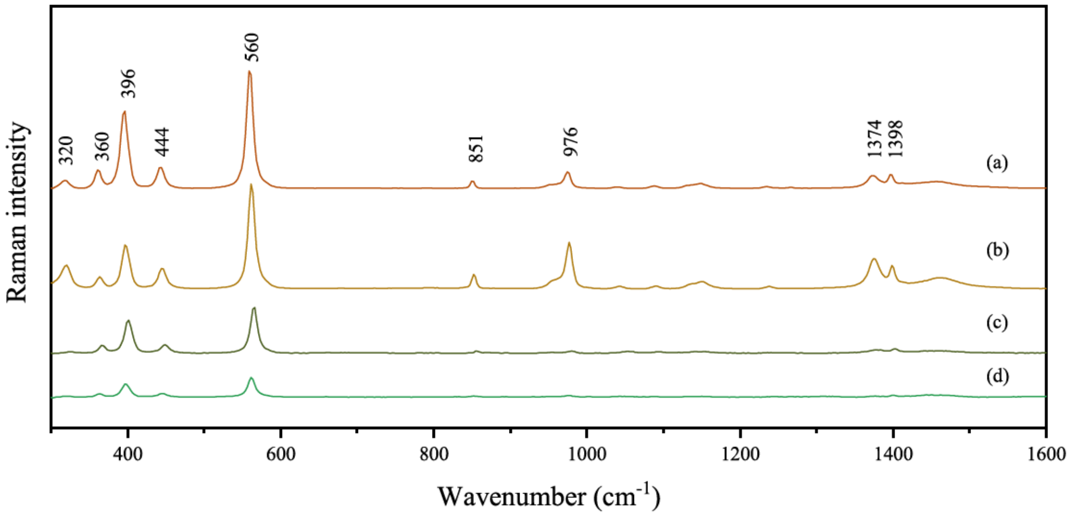

Fig. 5. Raman spectra of thiram from a) crystalline powder, and dried drop in deposited concentration b) 62 μM, c) 0.62 μM, and d) 0.31 μM.

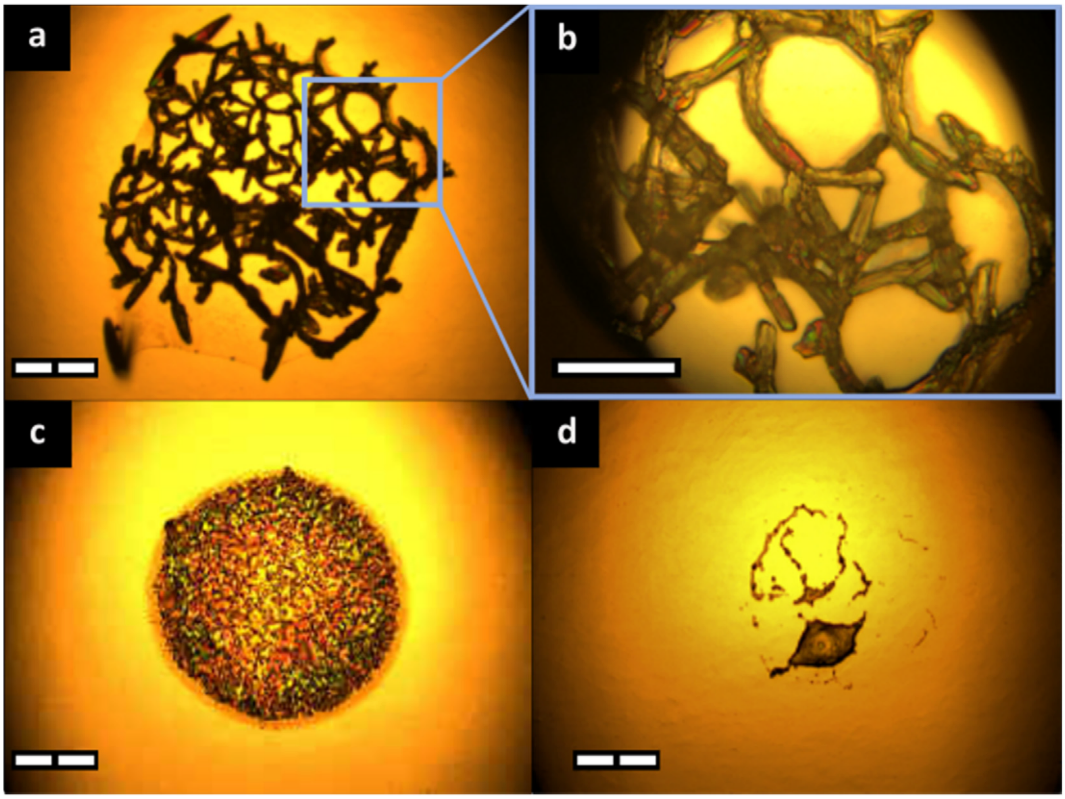

Fig. 6. White light images of dried drops of bentazon a,b) 2 mM, c) 0.2 mM and d) 20 μM concentration (1 white bar = 40 μm).

concentration, a final deposit composed of small non-homogeneously spread dried residue was formed (Fig. 6d).

We measured DCDR spectra for a series of concentrations, and due to bentazon molecular structure, it exhibited a rich Raman spectrum (Fig. 7). The spectrum from a crystalline powder possessed similar spectral features as DCDR spectrum from a stock solution; only slight changes in intensity ratios were observed, specifically at 675/693 cm^{-1}, 856/868 cm^{-1} and 1606/1650 cm^{-1}. Deposition of a drop with an initial concentration lower than 20 μM led to dried deposit from which we were not able to acquire a Raman spectrum with distinguishable spectral bands of bentazon. Therefore, we estimated the lowest DCDR detected concentration of bentazon as 20 μM in the deposited concentration. We did not find any SERS study of bentazon in literature.

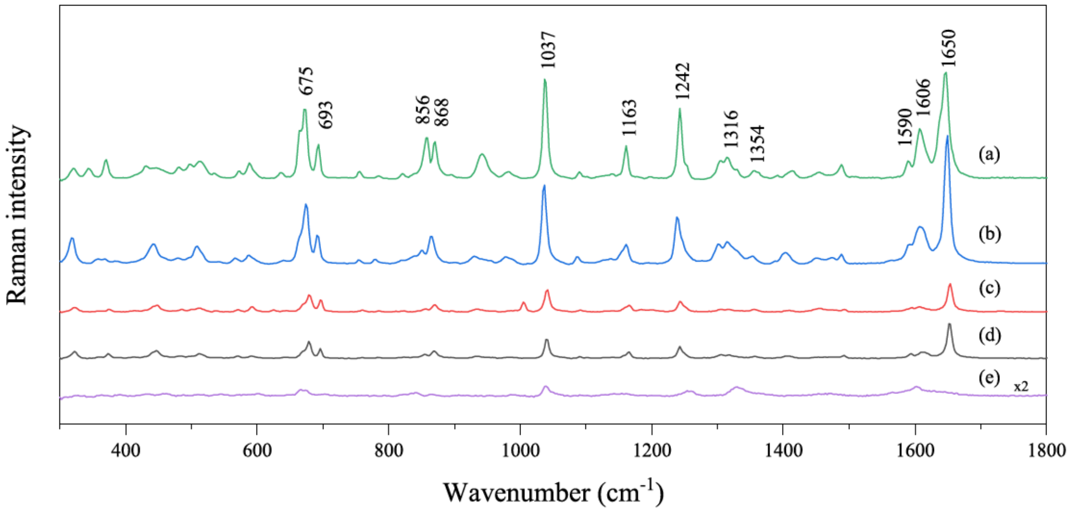

Fig. 7. Raman spectra of bentazon from: a) crystalline powder, and from a dried drop in deposited concentration b) 2 mM, c) 0.2 mM, d) 26 μM and e) 20 μM.

3.4. Picloram

In the case of another herbicide picloram, after the evaporation process, we observed changes in the shape of a dried pattern depending on initial concentration. For a stock solution with an initial concentration of 2 mM we observed uneven distribution of small picloram spots (Fig. 8a). The dilution to 0.2 mM led to intermittent coverage of substrate with visible preconcetrated locations (Fig. 8b). A similar pattern was also observable for lower concentrations as 40 μM (Fig. 8c) and 20 μM (not shown), but preconcentrated places and spots were less distinct. After the evaporation for the concentration of 2 μM (Fig. 8d), a thin layer of nonhomogenously distributed material was present, where a few preconcentrated spots were visible and measurable.

Fig. 9 and 10 show Raman spectra from the dried deposits and the reference spectrum from a powder as well. Two sets of Raman spectra are present (Fig. 9 for 2 mM and 0.2 mM, Fig. 10 for 0.2 mM and lower), where the first one has the same spectral features as the powder reference and the second one differed significantly. Dried deposits from initial concentrations 40 μM and lower exhibited solely the second type of spectrum (Fig. 9). The deposit formed by the initial concentration of 2 mM was composed of small spots, and it exhibited the same spectrum as in the case of amorphous powder (Fig. 9). The threshold concentration for this change was a 0.2 mM one, from a deposit of which we obtained both types of spectra due to the specific focused sites. Visible bulk locations exhibited the first type, whereas the spectrum acquired from the rest of the deposit possessed the same spectral features as spectra from lower concentrations. The first set of spectra was quite rich in bands (Fig. 9). We can observe strong spectral bands in the lower wavenumber spectral region at 343, 361 and 593 cm^{-1} and at several positions in the higher wavenumber region, 1110, 1285, 1395, 1535, 1662 cm^{-1}. The second type of spectra (Fig. 10) from lower concentrations (0.2 mM and lower) exhibited strong bands at 353, 605 and 1110 cm^{-1}, which were well distinguishable even for the deposited concentration of 10^{-6} M. There was only one evident common feature for both sets of spectra, which was a spectral band at 1110 cm^{-1}. To understand the origin of the sites providing the second type of spectrum, we imaged them in polarized light that revealed picloram crystals. We estimated the lowest DCDR detected concentration of picloram as 2 μM. We did not find any reported SERS study for comparison.

4. Conclusions

DCDR spectra of dried drops of selected contaminants (food contaminant melamine, fungicide thiram, herbicides picloram and bentazon) on the commercial hydrophobic substrate SpectRIM^{TM} (Tienta Sciences) were acquired. The Raman spectra of powders and stock solutions were accumulated as a reference under the same experimental conditions. Spectra of solutions showed only spectral bands of water as a solvent except for one weak band for melamine at 676 cm^{-1}. Thus, they could not have been used as reference spectra.

For DCDR measurements, in all cases, the dried drops formed patterns composed of small crystals or preconcentrated dried spots often depending on the deposited concentration. No dried pattern with a "coffee-ring" effect was noticed. The DCDR spectra were generally similar to Raman spectra of powder except for picloram. In this case, two types of spectra were measured with the threshold concentration of 0.2 mM as a border at which the change occurred. The first type of spectrum for higher concentrations possesses the same spectral features as an amorphous powder. The second type of spectrum was assigned to picloram crystals proved by imaging in polarized light. The lowest DCDR detected concentrations were assessed as 6.4 μM, 0.31 μM, 20 μM and 2 μM in deposited concentrations of solutions for melamine, thiram, bentazon and picloram, respectively. The detected

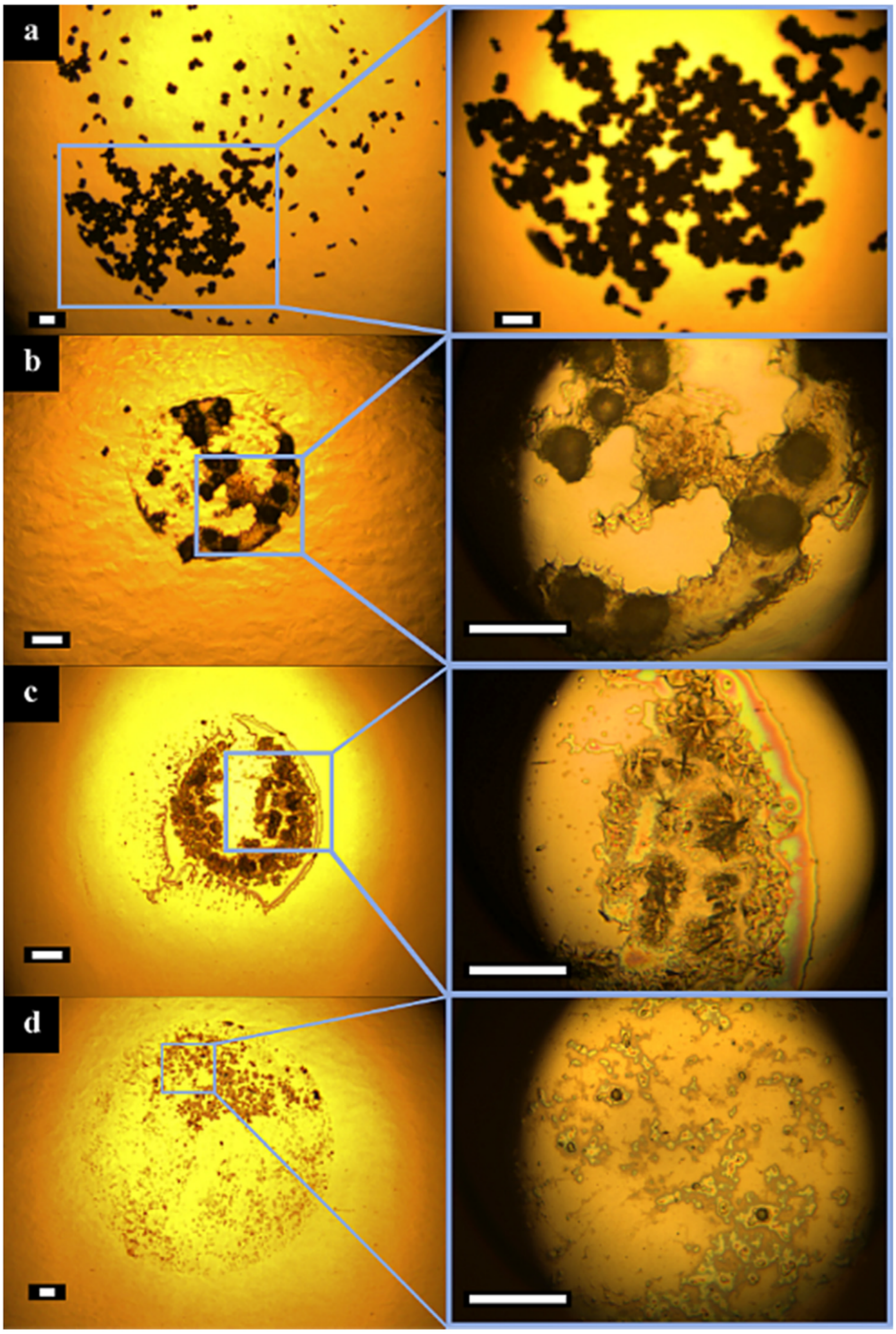

Fig. 8. White light images of dried drops of picloram a) 2 mM, b) 0.2 mM, c) 40 μM and d) 2 μM concentration (1 white bar = 40 μm).

concentrations for melamine and thiram were one or two magnitudes higher than in the case of common SERS detection, but it still represents the concentrations relevant in food/groundwater contaminations.

Our study proved that the DCDR is a powerful method to detect the studied contaminants at small volumes at biologically and environmentally relevant concentrations, which is impossible by Raman measurements from solutions.

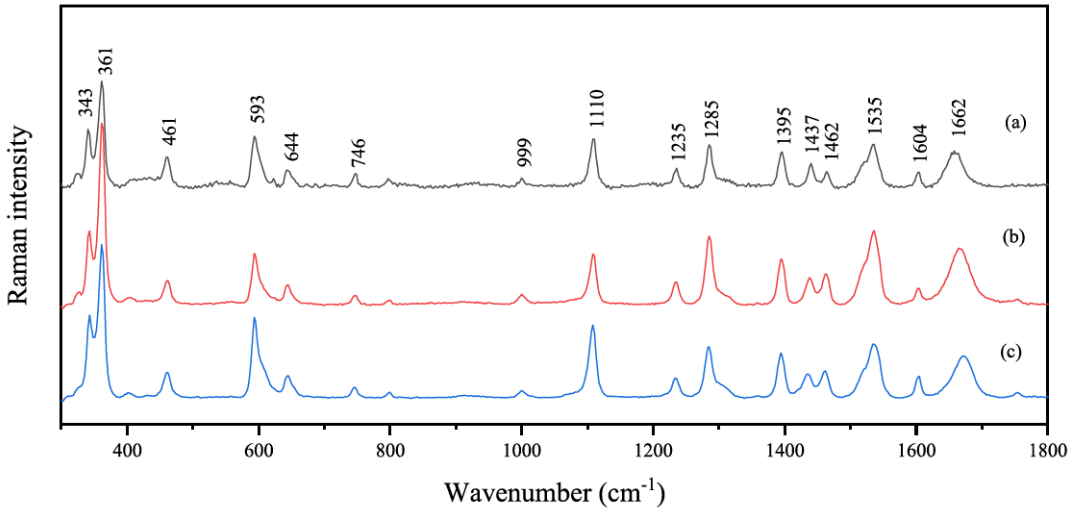

Fig. 9. Raman spectra of picloram from a) powder, and dried drop in deposited concentration b) 2 mM and c) 0.2 mM.

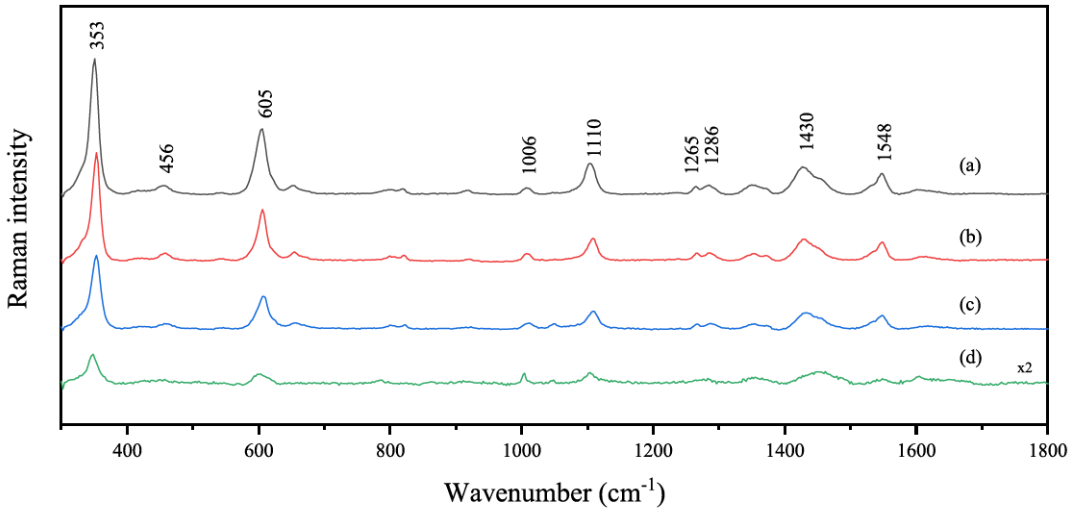

Fig. 10. Raman spectra of picloram from a dried drop in deposited concentration a) 0.2 mM, b) 40 μM, c) 20 μM and d) 2 μM.

Funding

Financial support from the Czech Science Foundation (18-10897S) and Charles University Research Centre program UNCE/SCI/010 and GA UK (290120) is gratefully acknowledged.

CRediT authorship contribution statement

Alžbeta Kuižová: Data curation, Formal analysis, Writing - original draft, Funding acquisition. **Mikuláš Přikryl:** Data curation, Formal analysis. **Marek Procházka:** Writing - review & editing, Funding acquisition, Project administration. **Eva Kočišová:** Writing - review & editing, Conceptualization, Supervision.

Declaration of Competing Interest

The authors declare that they have no known competing financial interests or personal relationships that could have appeared to influence the work reported in this paper.

Appendix A. Supplementary material

Supplementary data to this article can be found online at https://doi.org/10.1016/j.saa.2021.120109.

References

[1] D. Zhang, Y. Xie, M.F. Mrozek, C. Ortiz, V.J. Davisson, D. Ben-Amotz, Raman Detection of Proteomic Analytes, Anal. Chem. 75 (21) (2003) 5703–5709, https://doi.org/10.1021/ac0345087.

[2] C. Ortiz, D. Zhang, Y. Xie, V.J. Davisson, D. Ben-Amotz, Identification of insulin variants using Raman spectroscopy, Anal. Biochem. 332 (2) (2004) 245–252, https://doi.org/10.1016/j.ab.2004.06.013.

[3] J. Filik, N. Stone, Drop Coating deposition Raman spectroscopy of protein mixtures, Analyst. 132 (2007) 544–550, https://doi.org/10.1039/b701541k.

[4] E. Kočišová, M. Procházka, Drop-coating deposition Raman spectroscopy of liposomes, J. Raman Spectrosc. 42 (8) (2011) 1606–1610, https://doi.org/10.1002/jrs.2915.

[5] E. Kočišová, M. Petr, H. Šípová, O. Kylián, M. Procházka, Drop coating deposition of liposome suspension on surface with different wettabilities: “coffee ring” formation and suspension preconcentration, Phys. Chem. Chem. Phys. 19 (2017) 388–393, https://doi.org/10.1039/C6CP07606H.

[6] R.D. Deegan, O. Bakajin, T.F. Dupont, G. Huber, S.R. Nagel, T.A. Witten, Capillary flow as the cause of ring stains from dried liquid drops, Nature. 389 (6653) (1997) 827–829, https://doi.org/10.1038/39827.

[7] I.A. Larmour, J.P.E.D. Gray, S.E.J. Bell, Universal Raman enhancement by solvent removal, Spectrosc. Eur. 21 (2009) 6–8, www.spectroscopyeurope.com.

[8] E. Kočišová, M. Procházka, Drop-coating deposition Raman spectroscopy of porphyrins, J. Raman Spectrosc. 46 (2) (2015) 280–282, https://doi.org/10.1002/jrs.4637.

[9] E. Kočišová, M. Procházka, Drop-coating deposition Raman spectroscopy of dipicolinic acid, J. Raman Spectrosc. 49 (12) (2018) 2050–2052, https://doi.org/10.1002/jrs.5493.

[10] C.G. Skinner, J.D. Thomas, J.D. Osterloh, Melamine toxicity, J. Med. Toxicol. 6 (1) (2010) 50–55, https://doi.org/10.1007/s13181-010-0038-1.

[11] I.R. Edwards, D.G. Ferry, W.A. Temple, Handbook of Pesticide Toxicology, Academic Press, New York, 1991.

[12] V.K. Sharma, J.S. Aulakh, A.K. Malik, Thiram: degradation, applications and analytical methods, J. Environ. Monit. 5 (2003) 717–723, https://doi.org/10.1039/b304710e.

[13] M. Köck-Schulmeyer, A. Ginebreda, C. Postigo, T. Garrido, J. Fraile, M. López de Alda, D. Barceló, Four-year advanced monitoring program of polar pesticides in groundwater of Catalonia (NE-Spain), Sci. Total Environ. 470–471 (2014) 1087–1098, https://doi.org/10.1016/j.scitotenv.2013.10.079.

[14] E.T. Rodrigues, M.F. Alpendurada, F. Ramos, M.Â. Pardal, Environmental and human health risk indicators for agricultural pesticides in estuaries, Ecotoxicol. Environ. Saf. 150 (2018) 224–231, https://doi.org/10.1016/j.ecoenv.2017.12.047.

[15] V. Galhano, F. Peixoto, J. Gomes-Laranjo, Bentazon Triggers the Promotion of Oxidative Damage in the Portuguese Ricefield Cyanobacterium Anabaena cylindrical: Response of the Antioxidant Systém, Environ. Toxicol. 25 (2010) 517–526, https://doi.org/10.1002/tox.20597.

[16] J.M.M. Oliveira, V. Galhano, I. Henriques, A.M.V.M. Soares, S. Loureiro, Basagran® induces developmental malformations and changes the bacterial community of zebrafish embryos, Environ. Pollut. 221 (2017) 52–63, https://doi.org/10.1016/j.envpol.2016.10.028.

[17] D.-J. Lee, S.A. Senseman, A.S. Sciumbato, S.-C. Jung, L.J. Krutz, The Effect of Titanium Dioxide Alumina Beads on the Photocatalytic Degradation of Picloram in Water, J. Agric. Food Chem. 51 (9) (2003) 2659–2664, https://doi.org/10.1021/jf026232u.

[18] M.J. Sadowsky, W.C. Koskinen, M. Bischoff, B.L. Barber, J.M. Becker, R.F. Turco, Rapid and Complete Degradation of the Herbicide Picloram by Lipomyces kononenkoae, J. Agric. Food Chem. 57 (11) (2009) 4878–4882, https://doi.org/10.1021/jf900067f.

[19] S.H. Yalkowsky, Y. He, P. Jain, Handbook of Aqueous Solubility Data, second ed., CRC Press, New York, 2010.

[20] J. Zheng, L. He, Surface-Enhanced Raman Spectroscopy for the Chemical Analysis of Food, Compr. Rev. Food Sci. Food Saf. 13 (3) (2014) 317–328, https://doi.org/10.1111/1541-4337.12062.

[21] X. Tang, R. Dong, L. Yang, J. Liu, Fabrication of Au nanorod-coated Fe_3O_4 microspheres as SERS substrate for pesticide analysis by near-infrared excitation, J. Raman Spectrosc. 46 (5) (2015) 470–475, https://doi.org/10.1002/jrs.4658.

[22] J. Zhu, Q. Chen, F.Y.H. Kutsanedzie, M. Yang, Q. Ouyang, H. Jiang, Highly sensitive and label-free determination of thiram residue using surface-enhanced Raman spectroscopy (SERS) coupled with paper-based microfluidics, Anal. Methods. 9 (43) (2017) 6186–6193, https://doi.org/10.1039/C7AY01637A.

Supplementary Information file

Drop coating deposition Raman (DCDR) spectroscopy of contaminants

Alžbeta Kuižová, Mikuláš Přikryl, Marek Procházka and Eva Kočišová*

Charles University, Faculty of Mathematics and Physics, Institute of Physics, Ke Karlovu 5, 121 16, Prague 2, Czech Republic.

**Corresponding author: kocisova@karlov.mff.cuni.cz (E.K.)*

Grid points as a map (red points in figure S2) were selected in the dried deposit of bentazon. The set of 25 spectra were accumulated from these points. Obtained spectra were treated by factor analysis, the map of coefficients of the first subspectrum reflects the overall signal intensity for each point.

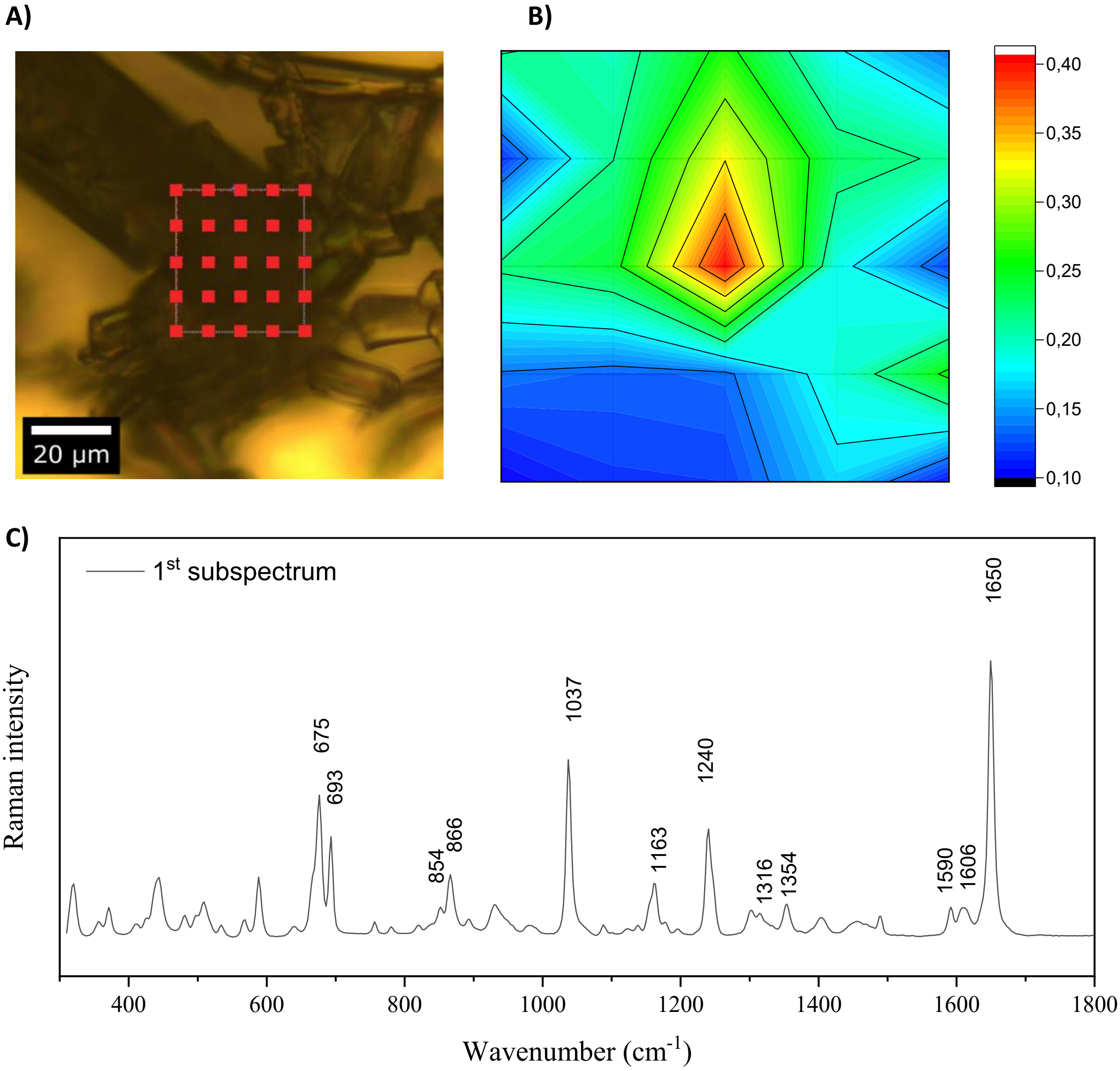

Figure S1: A) 25 selected grid points for a map measurement from bentazon deposit, B) the final map of coefficients of the first subspectrum from factor analysis, C) the first subspectrum for the accumulated set of spectra.

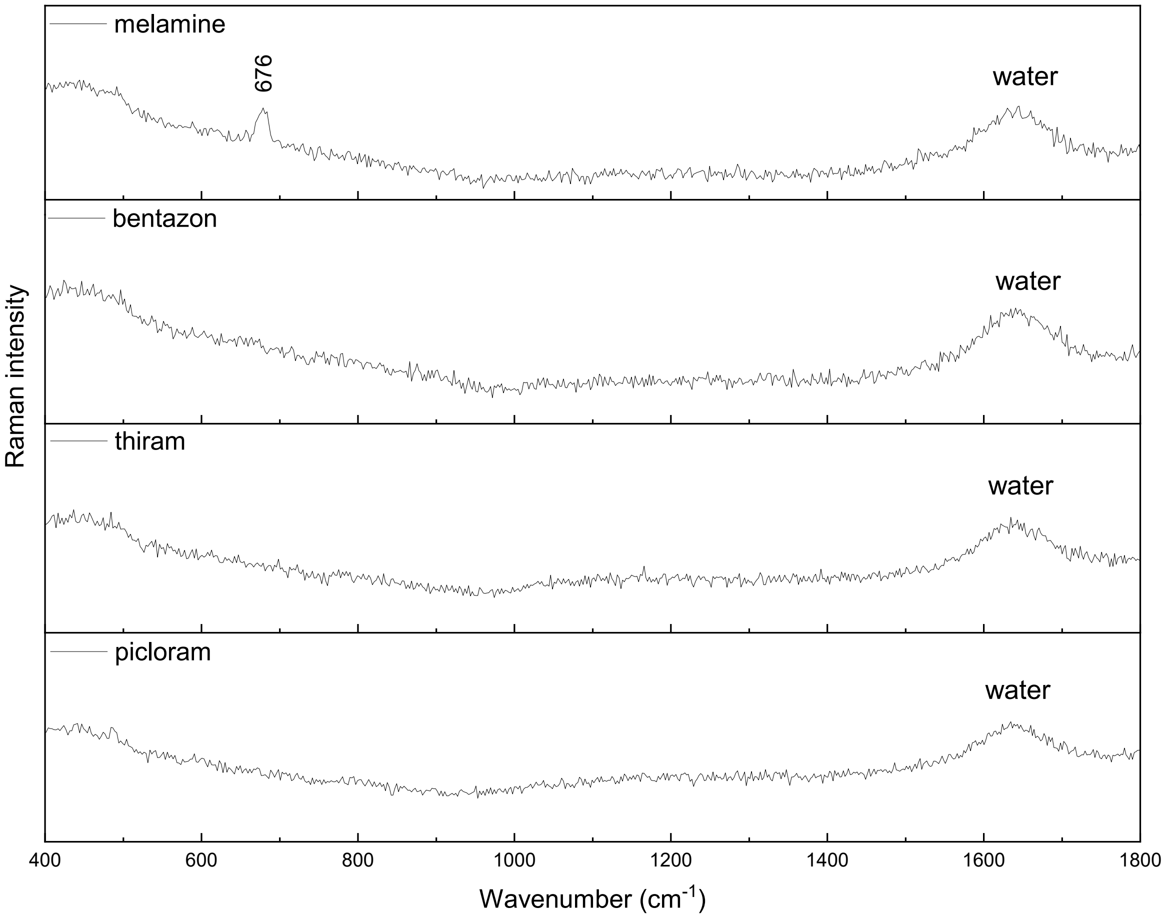

Figure S2: Raman spectra of stock solutions of studied contaminants melamine, bentazon, thiram and picloram.

A.8 Insights into thiram fungicide: A comparative study of solution and solid phases through Raman, DCDR, and SERS measurements and DFT simulations

VALÁŠKOVÁ, Martina; KUIŽOVÁ, Alžbeta; KOČIŠOVÁ, Eva; PROFANT, Václav. Insights into thiram fungicide: A comparative study of solution and solid phases through Raman, DCDR, and SERS measurements and DFT simulations. *Journal of Raman Spectroscopy.* **2023**, vol. 54, no. 9, pp. 950-965.

Available from doi: 10.1002/jrs.6581

Received: 18 April 2023 | Revised: 17 July 2023 | Accepted: 17 July 2023

DOI: 10.1002/jrs.6581

SPECIAL ISSUE - RESEARCH ARTICLE

Journal of RAMAN SPECTROSCOPY WILEY

Insights into thiram fungicide: A comparative study of solution and solid phases through Raman, DCDR, and SERS measurements and DFT simulations

Martina Valášková | **Alžbeta Kuižová** | **Eva Kočišová** | **Václav Profant**

Institute of Physics, Faculty of Mathematics and Physics, Charles University, Prague 2, Czech Republic

Correspondence
Václav Profant, Institute of Physics, Faculty of Mathematics and Physics, Charles University, Ke Karlovu 5, Prague 2 121 16, Czech Republic.
Email: profant@karlov.mff.cuni.cz

Funding information
Charles University Research Centre, Grant/Award Numbers: UNCE/SCI/010, SVV-2023-260716

Abstract

Thiram, a widely known fungicide, has evinced a negative impact on the environment and human health that led to the banning of its use in plant protection products on all commodities in the European Union. Therefore, there is a need for monitoring possible illicit use, which requires sensitive and accurate detection methods. In this study, the behavior of thiram in different phases was investigated in order to better understand its properties. Raman spectra were obtained from thiram in the solid state as a crystalline powder, dissolved in different solvents, and from dried deposits using the drop coating deposition Raman (DCDR) method. The analyses of acquired Raman spectra revealed evidence of hydrogen bonding between thiram and chloroform in the solution phase. The reliability and sensitivity of DCDR measurements were also highlighted, with high-quality spectra obtained from a dried pattern from droplet at a 40 μM concentration. Moreover, the study identified the most abundant conformer of intact (undegraded) thiram molecule and enabled reliable band assignment and vibrational analysis based on DFT simulations, providing a better understanding of the compound's properties. The results also suggested that thiram can be coordinated to silver in nanostructured SERS active substrates not only in the degraded form but also in the undegraded form. Overall, this study provides valuable insights into thiram's behavior and can be helpful in the further development of efficient and effective methods for its detection and analysis.

KEYWORDS

density functional theory (DFT), drop coating deposition Raman (DCDR), SERS, Thiram, vibrational assignment

1 | INTRODUCTION

Thiram (Figure 1), a sulfur-containing fungicide, is widely utilized to protect cereals, fruits, seeds, and vegetables from fungal infections and to prevent harvested crops from deterioration during transportation or storage. Additionally, high doses of thiram can act as a repellent for various animals such as rabbits, rodents, birds, and deer.[1,2]

Belonging to the dithiocarbamate family, the thiram molecule releases carbon disulfide within an animal's body, leading to liver damage and digestion issues.[3–6] Acute exposure to thiram can result in symptoms such as throat irritation, coughing, dizziness, and headaches.[7]

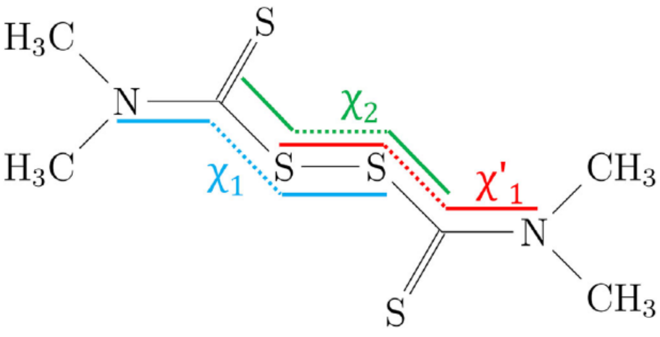

FIGURE 1 Structure of thiram molecule with highlighted dihedral angles χ_1 (blue), χ_2 (green), and χ'_1 (red).

Thiram induces oxidative stress and oxidative modification of cellular components in human erythrocytes,[8] and it causes thyroid dysfunction in aquatic organisms.[9] Due to these negative impacts,[2,10] the European Union has banned the use of thiram in plant protection products on all commodities, as per Commission Regulation (EU) 2022/1406, which amended Regulation (EC) No. 396/2005.[11] Therefore, the monitoring of possible illicit use is necessary.

The detection of thiram residues in fruit and vegetable samples using surface-enhanced Raman spectroscopy (SERS) has been extensively studied.[12–17] These studies have been focused on the selection and manufacture of the most suitable substrate in the form of a solid surface or colloid. However, there have been fewer studies conducted on the SERS or normal Raman spectrum measurement of thiram itself and the assignment of its spectral bands.[18–21] There are significant differences between the solid-phase Raman spectra and SERS spectra of thiram, which might be attributed to various individual aspects. For instance, the Raman signal from crystalline powder may be influenced by packing or conformational polymorphism or even by different crystal grain sizes.[22,23] In SERS measurements, the analyte is dissolved in a suitable solvent and allowed to adsorb onto the SERS-active substrate. Spectra are then measured from a colloidal solution or from dried deposits formed on the solid surface. Therefore, changes seen in the SERS spectrum can be produced by solvent–solute interactions, the drying process, and/or interaction with a SERS-active substrate. Samples for SERS measurements and further analysis are mostly prepared as a diluted aqueous solution, in which thiram is rather unstable.[20,24] Given the high affinity of sulfur atoms for binding to SERS-active substrates, it is generally believed that the degraded form of thiram is measured, where the central disulfide bridge is cleaved, and resulting dimethyldithiocarbamate ions are directly bound to Ag atoms. However, the spectra of thiram and dimethyldithiocarbamate ions bound to Ag atoms are highly similar, as shown in a recent theoretical study by Oliviera et al.,[18] making it difficult to provide a definitive answer. Alternatively, it was shown recently[25] that thiram in low concentrations, relevant to groundwater contamination, can be detected also by a drop coating deposition Raman (DCDR) approach,[26] which does not require nanostructured SERS active substrate. DCDR method was already proven to be efficient approach for detection and identification of small molecules from low concentrated solutions.[27–30]

The aim of this study is to investigate and gain a deeper understanding of thiram fate after dissolution in different solvents and during drying processes. To achieve this, we obtained Raman spectra of thiram in various phases, including the solid state (crystalline powder), solution phase (dissolved in chloroform, benzene, and tetrachloromethane), and from dried deposits using the DCDR method. Due to the limited solubility of thiram, solution phase measurements have not been done previously. In addition, we utilized quantum mechanical calculations and spectra simulations to analyze the obtained spectra from different methods, including SERS spectra, and to assign specific spectral bands to corresponding vibrations in the thiram molecule.

2 | METHODS

2.1 | Samples

A commercial thiram sample was purchased from Merck (Sigma-Aldrich) in crystalline powder form—product number 43966, purity ≤100%, certified reference material. The solvents used—deionized water, chloroform, benzene, and tetrachloromethane—were of spectroscopic purity. Samples and solvents were used without further refinement or purification.

2.2 | Experimental setups

Macro-measurements (solution in cuvette) were performed on a Raman spectrometer based on the spectrograph SPEX 270M from the Jobin-Yvon company with a focal length of 270 mm and a collimating mirror diameter of 50 mm. The second harmonic wavelength of a Nd:YAG laser was used as an excitation source of 532 nm with ~600 mW power at the sample. The spectrometer uses rectangular geometry where the incident excitation beam passes through the polished bottom cuvettes and the scattered radiation is collected at right angle geometry. Scattered radiation passes through an edge filter to filter out Rayleigh scattering and enters the spectrograph, where it is diffracted by grating with 1,200 grooves/mm. The recorded spectral region spanned from ∼ −50 to 2,325 cm^{-1} with the Rayleigh filter cut-off at ∼53 cm^{-1}. The signal was detected by a liquid nitrogen-cooled CCD detector with 1,340 × 100 pixels. Quartz cuvettes with 1- and 10-mm widths were used; the standard sample volume was 100 μl and 1 ml, respectively. The thiram concentrations used for measurements were chosen to be close to the solubility limit in a particular solvent, that is, 100 mg/ml (416 mM) in benzene and chloroform and ∼10 mg/ml (41.6 mM) in tetrachloromethane.

Solid phase measurements (crystalline powder, DCDR, and SERS) were performed on a Raman microspectrometer Alpha 300 from WITec. The instrument possesses an ultra-high throughput spectrometer (UHTS) with a focal length of 30 cm and 600 grooves/mm grating. A 532 nm laser was used as an excitation source during the measurement with ∼10 mW power at the sample (0.5 mW in the case of SERS measurements). Carl Zeiss 50×/0.55 LD was chosen as the microscope objective. The recorded spectral range (∼ −160 to 3,610 cm^{-1}) enabled the acquisition of high-quality spectra in the whole region of fundamental molecular vibrations. The Rayleigh filter cut-off was at ∼81 cm^{-1}. The crystalline powder form was measured directly from a small amount of sample on a glass slide. DCDR spectra were acquired from dried deposits (on a pure glass slide) of various initial sample concentrations. SERS spectra were measured from dried deposits on the commercial SERS substrate manufactured by SERSitive (www.sersitive.eu). In all cases, spectral maps of ∼20 × 20 μm areas were measured and further statistically processed. The laser power and the accumulation time were chosen so as not to degrade the sample.

2.3 | Experimental data treatment

Spectra measured on a Raman spectrometer were calibrated using the spectrum of the Ne discharge lamp and interpolated to a 1 cm^{-1} sampling interval. Calibration was followed by solvent signal subtraction and cubic-spline-based background correction in GRAMS/AI software version 9.2 (Thermo Fisher Scientific Inc.). Spectra measured on an Alpha300 RS confocal Raman microscope were processed in the associated software from the WITec Suite SIX package (Oxford Instruments, WITec) with automatic calibration. Raw spectra were purged of cosmic ray spikes by available software procedures. Where appropriate, the "True Component Analysis" tool[31,32] was then used. This procedure involves fitting each spectrum of the spectral map with a linear combination of basis spectra using the least squares method. The process begins by identifying the dominant spectral contribution, which serves as the base spectrum. Subsequently, a residual image is calculated based on this base spectrum. If the residual image exhibits structure, additional cycles are performed automatically to incorporate additional components and calculate corresponding residual images. This iterative process continues until it is determined that the residual image primarily consists of noise. Final graphs were created in the OriginPro program 2020b version 9.7.5.184 (OriginLab Corporation).

2.4 | Quantum mechanical calculations and spectra simulations

Thiram structure optimization was done using Gaussian09 (Revision D.01) program,[33] using the density functional theory (DFT), B3LYP hybrid functional,[34,35] 6-311++G** basis set,[36] and implicit solvent model COSMO[37] to mimic the solvent environment. The starting conformations were generated by 1D and 2D scans of the potential energy surface (PES) along chosen coordinates using a smaller basis set (6-31G). Raman intensities for individual conformers were obtained within the harmonic approximation at the same level of theory (DFT/B3LYP/6-311++G**/COSMO); backscattered spectral profiles were generated by convolution of the intensities with a Lorentzian function of 10 cm^{-1} full width at half-height and a Boltzmann factor corresponding to 298 K. Final simulated spectra were acquired as a Boltzmann average corresponding to DFT energies. We used various weightings based on the electronic energy (ΔE), zero-point vibrational energy (ΔE_0), enthalpy (ΔH), and Gibbs energy (ΔG).

3 | RESULTS

3.1 | Crystalline phase Raman spectra

The solid phase Raman spectra of thiram in crystalline powder form were acquired as a spectral map of 12 × 15 μm comprised of 2,880 spectra (4 spectra/μm in both axes). These were processed by True Component Analysis (see Section 2 for details), and three main components were identified: The first was attributed to the background signal, the second and third were labeled as Thir A and Thir B. The spatial distribution of these components within the measured area is shown in Figure 2, left. To enable quantitative analysis, the spectra of both components were compared in three spectral regions (Figure 2, right) corresponding to (A) skeletal and lattice vibrations, (B) fingerprint region, and (C) CH stretching

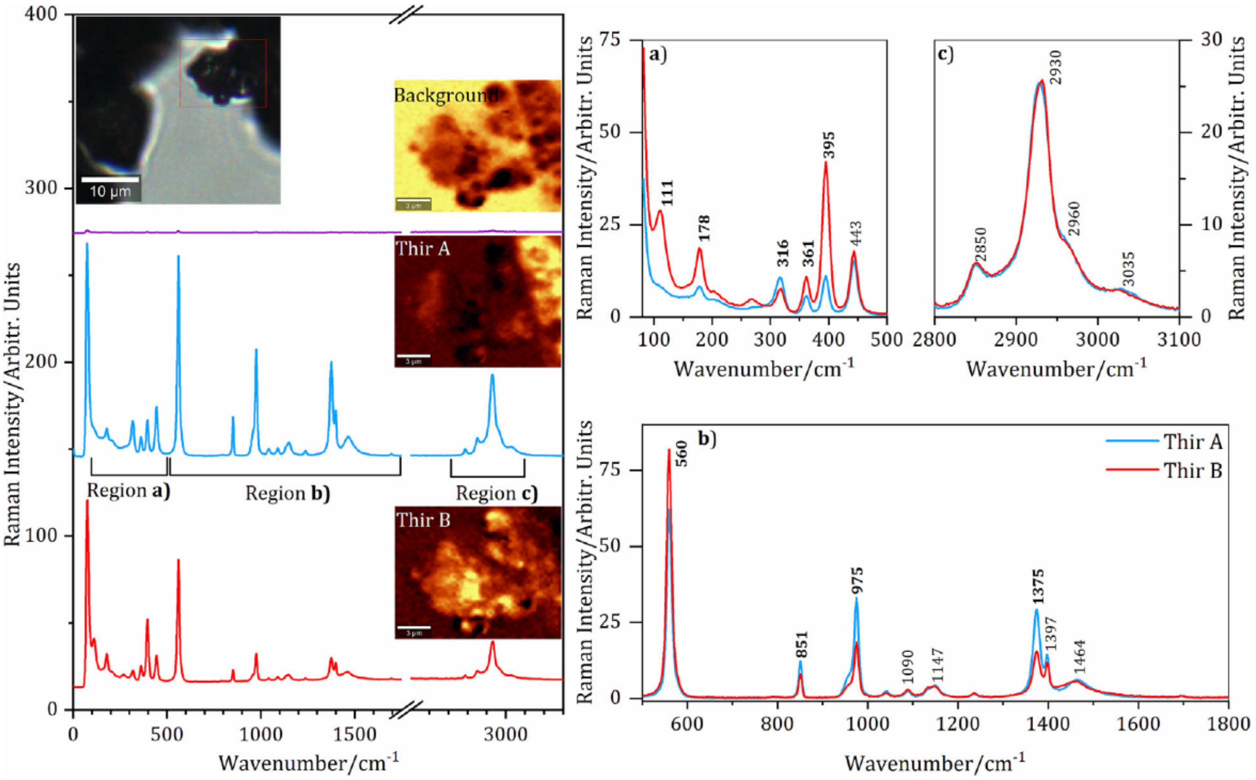

FIGURE 2 (Left) Three main components (Thir A, Thir B, and background signal) obtained from a spectral map of thiram crystalline powder form on the glass slide. The image of the scanned area and the spatial distribution of the components are shown in insets; brighter color indicates a higher signal intensity. (Right) The overlap of Raman spectra of components Thir A and Thir B in three spectral regions (A–C). Spectra were normalized to the same integral intensity in region C.

TABLE 1 The maximum band intensities in the Raman spectra of thiram crystalline powder form.

	Intensity/ (Intensity @ 2930 cm^{-1})		
Wavenumber (cm^{-1})	**Thir A**	**Thir B**	**Region**
111	0.32	1.14	a
178	0.33	0.74	
395	0.44	1.65	
560	2.45	3.32	b
975	1.31	0.73	
1,375	1.16	0.61	
2,930	1.00	1.00	c

region. Normalization was done to the same integral intensity in region (C), which was found identical for both components. Additionally, both spectral components exhibited the same number and positions (wavenumbers) of Raman bands. However, significant differences were observed in the relative intensities of six major bands, three in Region (B), and other three in Region (A), as summarized in Table 1. Specifically, Thir A showed ~80% increase in the intensity of bands at 975 and 1,375 cm^{-1} (corresponding to the modes 30 and 41/42 in Table 3, respectively) and ~25% decrease in the intensity of the ν(S-S) band at 560 cm^{-1} (mode 22 in Table 3) in Region (B). In the low-wavenumber region (A), the band at 178 cm^{-1}, corresponding to the bending of the central part of the molecule (Modes 10 and 11 in Table 3), had twice the intensity in Thir B, while the bands at 395 and 111 cm^{-1} (Modes 18/19 and 8/9 in Table 3, respectively), corresponding mostly to vibrational movement of the whole methyl groups, were almost four times more intense in Thir B.

3.2 | Solution phase Raman spectra

Obtaining high-quality Raman spectra of thiram in the solution that cover the entire range of fundamental vibrations is a difficult task. The best solvent for Raman measurements, water, is not suitable, as saturated thiram aqueous solution has a low concentration of only 0.03 mg/ml. Therefore, it is necessary to use organic solvents, which, however, generally exhibit intense Raman signals. To obtain all vibrational bands of the studied sample, spectra from several solvents that have their own vibrations in different spectral regions must be combined. After tests, benzene and chloroform were identified as the most suitable solvents (see Figure S1), in which thiram could be dissolved up to a concentration of 100 mg/ml. By combination of acquired Raman spectra from both solutions, it was possible to obtain almost the entire range of thiram molecular vibrations except for a narrow gap between 1,160 and 1,240 cm^{-1} (Figure 3). A complementary measurement in tetrachloromethane at thiram concentration of 10 mg/ml (Figure S2) revealed that this gap does not contain any Raman band of thiram.

Figure 3 illustrates that the spectra obtained from different solvents are highly similar, indicating that the conformational preferences of the thiram molecule were unaffected by the choice of solvent. Generally, wavenumber shifts are insignificant. The detailed assignment of Raman bands is shown in Table 3 and Figure 10 in Section 3.7. It is noteworthy that when measuring in chloroform, an additional band at 2,985 cm^{-1} was detected in the CH valence region (indicated by a dagger in Figure 3), which was not present in the spectra obtained from other solvents. This band is believed to correspond to the valence vibration of the C-H bond in the chloroform molecule (3,019 cm^{-1}), which is downshifted by 34 cm^{-1} due to hydrogen bonding to the thio group in the thiram molecule.

The Raman spectra of thiram solution were successfully obtained at high quality primarily from measurements in chloroform and benzene, with the additional measurements in tetrachloromethane providing complementary information. Although performed in organic solvents, the results were of good quality and reproducible.

3.3 | DCDR spectra

The DCDR measurements were performed using thiram solutions in benzene and chloroform at different initial concentrations (~4 mM, 0.4 mM, and 40 μM). The deposited drops were dried freely at room temperature on a pure glass microscope slide without any surface treatment. The resulting deposits consisted mainly of clustered (bulk) structures, with a thin film observed between the clusters. A spectral map of 20 × 25 μm was acquired and evaluated, consisting of 500 spectra (1 spectrum/μm in both axes). Using the True Component Analysis, we have consistently identified two main spectral components along with the signal corresponding to the background (Figure S3). The first (most prevalent) component emerging from the clusters was assigned to the intact thiram molecule based on the presence of a prominent band at ~560 cm^{-1} (corresponding to the ν(S-S) vibration) and overall spectral similarity to the results of solution phase measurement. Well-resolved thiram spectra were obtained using both solvents and at all concentrations and with good quality even at 40 μM initial concentration (Figure 4). It is likely that thiram could be identified by DCDR even at concentrations 1 or

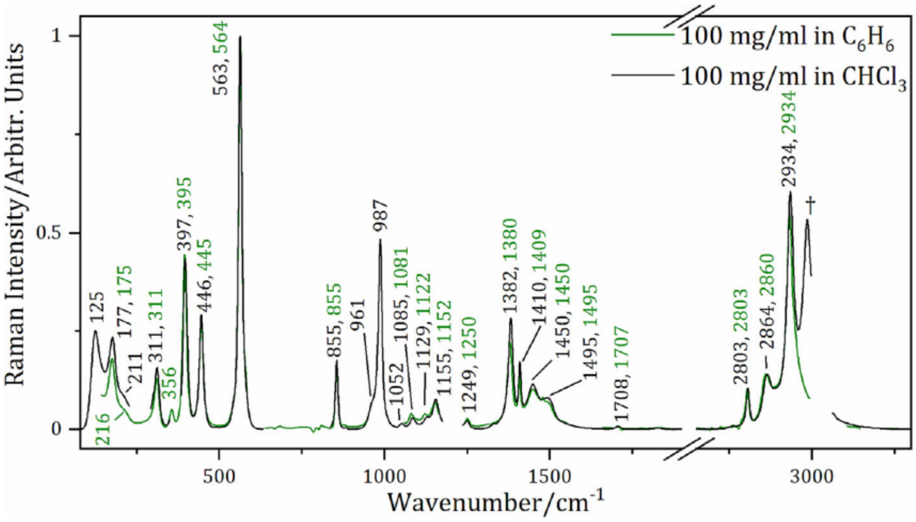

FIGURE 3 Overlaid Raman spectra of thiram dissolved to 100 mg/ml (416 mM) concentration in chloroform (black) and benzene (green). Regions with high solvent signal were omitted. Spectra were baseline corrected and normalized to the same intensity of the band at ~563 cm^{-1}. Raman band corresponding to the ν(C-H) vibration of chloroform H-bonded to thiram is marked by a dagger.

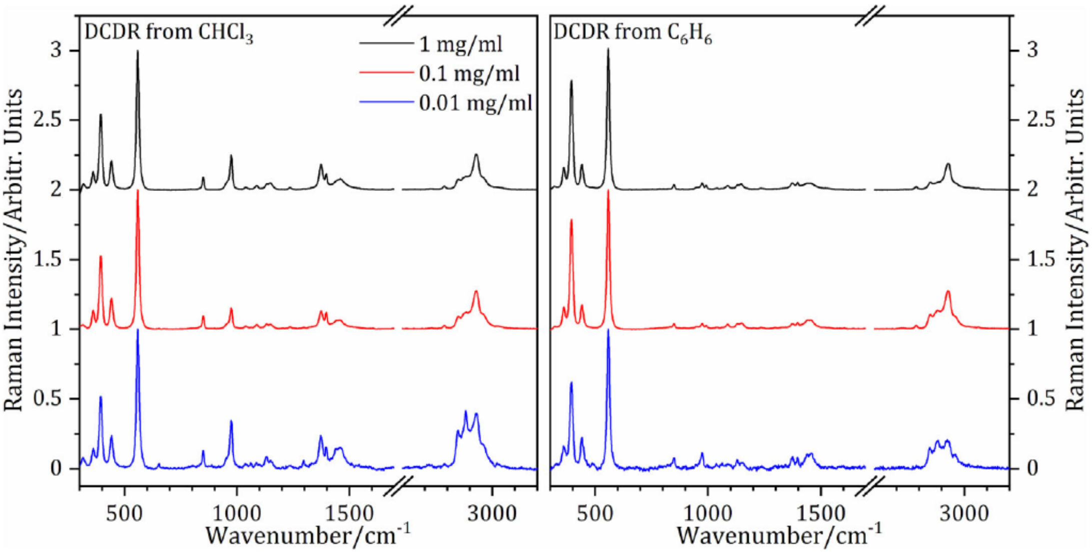

FIGURE 4 DCDR spectra of thiram measured from dried deposits (bulks) from solutions of 1 mg/ml (4.2 mM, black), 0.1 mg/ml (0.4 mM, red), and 0.01 mg/ml (40 μM, blue) concentration in chloroform (left) and benzene (right). Spectra were acquired from selected areas of spectral maps that did not show evidence of thiram decomposition.

2 orders of magnitude lower. The overall spectral shape was highly similar to the thiram signal obtained from solution measurements, with band assignments provided in Table 3.

The second spectral component, coming primarily from the thin films, lacked the characteristic band at ~560 cm^{-1} and exhibited downshifted bands in the CH stretching region. The increase in its signal was observed in the case of deposits originating from 40 μM thiram solution in benzene and in all samples originating from chloroform solution (Figure S3). Therefore, this component may correspond to the degraded forms of thiram, which tends to undergo S-S bond cleavage to form two dimethylthiocarbamate ions that can further degrade to dimethylamine and carbon disulfide. The rate of degradation was lower when benzene was used as solvent, which could be related to the existence of hydrogen bonds between thiram and chloroform weakening the disulfide bond.

3.4 | SERS spectra

SERS spectra of thiram were obtained using commercial nanostructural substrate from SERSitive. This was prepared using the electrodeposition of silver nanoparticles on an indium tin oxide glass surface. As declared, the structure of silver nanoparticles obtained using this approach gives excellent and uniform signal enhancement. To achieve high-quality spectra, a relatively high concentration of samples (10^{-4} M) and two types of solvents were utilized: first, water, with which thiram is most often encountered when used as a fungicide and repellent in industry, and second, benzene, in which thiram underwent minimal degradation in the solution phase and DCDR experiments. The samples were deposited (2 μl) onto the substrate and measured after drying. Similar to previous cases, spectral maps of 25 × 25 μm containing 2,500 spectra were acquired (2 spectra/μm in both axes). Upon map evaluation (using the True Component Analysis tool), two main components were identified (Figure S4)—the first with a homogeneous distribution corresponding to thiram and the second localized in several small areas (even points) where the sample was photodecomposed (burned) to graphitic carbon. Formation of bulks of clusters has not been observed. The resulting SERS spectra of thiram are shown in Figure 5.

The spectra of both samples match well above 700 cm^{-1}, except for a shoulder at around 1,575 cm^{-1}, which could be attributed to imperfect background subtraction or residual signal of photodecomposed sample. Nevertheless, notable differences were observed in the low-wavenumber region. The sample prepared from a water solution exhibited a significant decrease (by more than 50%) in the intensity of the bands at 563, 443, and 347 cm^{-1}, and a new band emerged at 255 cm^{-1}. This observation is particularly significant for the band at 563 cm^{-1}, which is known to correspond to the ν(S-S) vibration in standard Raman and DCDR measurements. In SERS, the relative intensities of bands are typically different from those observed in standard Raman scattering and therefore cannot be directly compared. However, if two SERS measurements only differ in the solvent used,

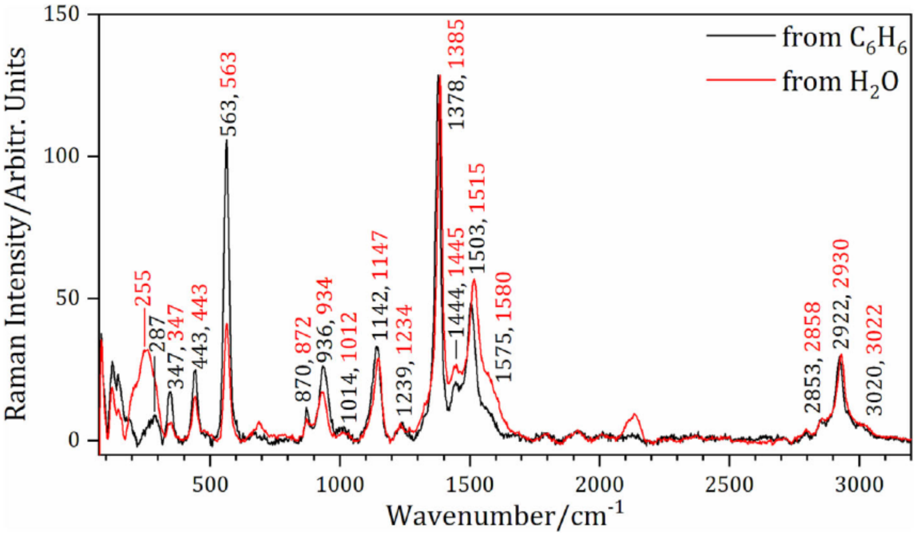

FIGURE 5 SERS spectra of thiram measured from dried deposits from 1 mg/ml solutions in benzene (black) and water (red). Spectra were corrected for the signal of photodecomposed (burned) sample and baseline and normalized on the same intensity to the band at 1,378 cm^{-1}.

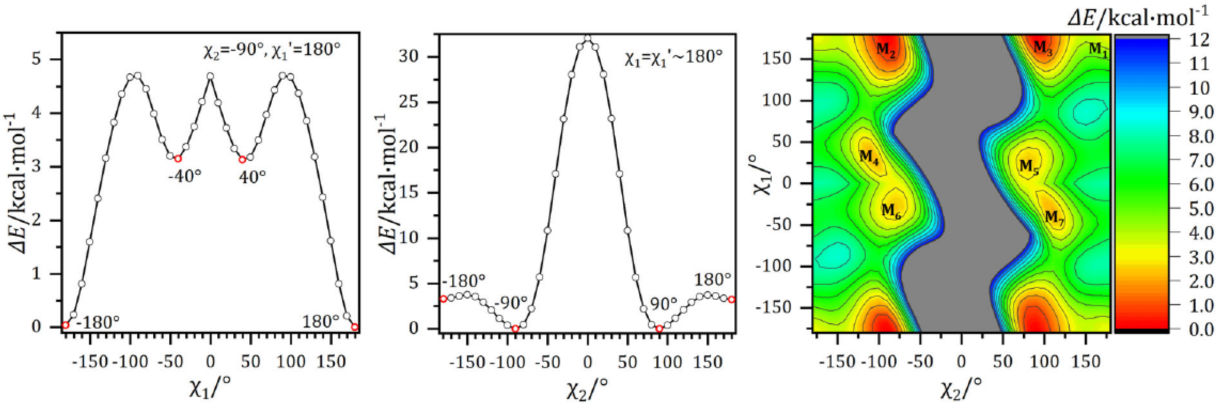

FIGURE 6 One-dimensional PES scans of thiram dihedral angles χ_1 (left) and χ_2 (middle). Energy minima are highlighted in red color. Two-dimensional PES scan of thiram dihedral angles χ_1 and χ_2 (right). χ'_1 angle was kept at 180° during the scan. Energy minima are sequentially labeled M$_1$–M$_7$ according to their depth.

changes in the relative intensities of the bands are significant and meaningful. The implications of such changes are discussed in detail in Section 4.

3.5 | PES scan

The thiram molecule consists of two dimethyldithiocarbamate groups connected by a disulfide (S-S) bond (as shown in Figure 1). These groups are planar due to the resonance character, similarly to the peptide group. However, because of the disulfide bond, there are three dihedral angles—χ_1 (N-C-S-S), χ_2 (C-S-S-C), and χ'_1 (S-S-C-N)—which give the molecule flexibility in its conformation.

The angles χ_1 and χ'_1 have the same range of possible values because of symmetry, but the preferred values for the angle χ_2 are different. The favored conformational arrangements were determined by performing PES scans along specific coordinates (dihedral angle) at B3LYP/6-31G/cpcm (chloroform) level of theory. The starting point for these scans was an optimized structure of the "stretched" conformer, which had the dihedral angles of (χ_1, χ_2, χ'_1) ~ (180°, −90°, and 180°). The 1D scan of the dihedral angle χ_2, with χ_1 and χ'_1 set to 180°, revealed two additional minima at +90° and 180° (as shown in Figure 6, left). Similarly, the 1D scan of torsion angle χ_1, with χ_2 set to −90° and χ'_1 to 180°, identified two other minima at approximately +40° and −40° (as shown in Figure 6, middle). To account for the mutual influence of the conformational preferences of the angles χ_1 and χ_2, a two-dimensional (2D) scan was also performed, with χ'_1 restricted to 180°. This scan identified a total of seven local energy minima, labeled as M$_1$–M$_7$, (see Figure 6, right), with values of (χ_1, χ_2) ∈ {(180°, 180°), (180°, −90°), (180°, 90°), (32°, −108°), (28°, 80°), (−28°, −80°), (−32°, 108°)}, which correspond well to the values observed in the 1D scans.

To determine the most stable conformations of thiram, 27 different structures were created (combining the favored values of angles of χ_1, χ_2, and χ'_1) and optimized at a higher level of theory (B3LYP/6311++G**/cpcm (chloroform)). After optimization, 11 unique structures were obtained, consisting of five pairs of enantiomers (structures that are mirror images to each other, such as A_1 and A_2 in Figure 7) and one non-chiral structure. Since Raman scattering cannot differentiate between enantiomers, it is possible to group them together, resulting in a total of six possible thiram structures. The geometry parameters, thermochemical properties, and molar ratios of each conformer (calculated using the Boltzmann statistics) are presented in Table 2. Each conformer is also described using the conventional notation, where *t* (*trans*), g+ (*gauche plus*), and g− (gauche minus) are used for χ_1 and χ'_1 values of ~180°, +40°, and −40°, respectively. For the angle χ_2, ***t***, ***d***, and ***g*** stand for 180°, +90°, and −90°, respectively. The molar ratios of conformers slightly vary depending on the thermodynamic potential used, but in all cases, the A conformer (***tgt*** or ***tdt***) is the most prevalent with 80.7–95.7%.

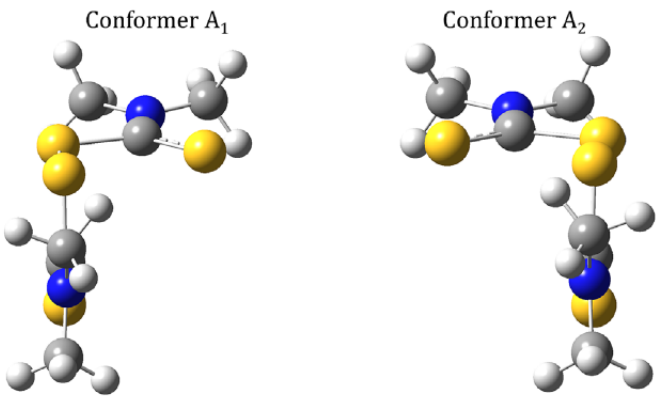

FIGURE 7 Enantiomeric thiram conformers A_1 and A_2; the corresponding geometry parameters are shown in Table 2. Atomic types are labeled by color: sulfur, yellow; carbon, gray; nitrogen, blue; and hydrogen, white.

3.6 | Spectral markers of different conformers

The thiram conformers differ not only in their energies but also in their Raman spectra. These spectral differences can be used to identify and confirm the relative proportions of the different conformations determined solely based on energies. For this purpose, it is convenient to divide the Raman spectrum of thiram into three main regions:

i. The *CH stretching region* (2,900–3,300 cm^{-1}), which is not very useful for distinguishing between conformations because the wavenumbers of the methyl group stretching vibrations do not vary enough, as shown in Figure S5. The only exception is the fully

TABLE 2 Geometric and thermodynamic parameters of unique thiram conformers.

					Thermodynamics				η			
	χ_1	χ_2	$\chi_{1'}$		ΔE	ΔE$_0$	ΔH	ΔG	ΔE	ΔE$_0$	ΔH	ΔG
Conformer	(°)			Type	(kcal/mol)				(%)			
A_1	177	91	177	***tdt***	0.00	0.00	0.00	0.00	80.8	87.2	83.1	95.7
A_2	−177	−91	−177	***tgt***								
B_1	28	81	170	***g$^+$dt***	1.27	1.51	1.34	2.28	9.5	6.8	8.7	2.0
B_2	−170	−81	−28	***tgg$^-$***								
C_1	−31	108	179	***g$^-$dt***	1.69	1.88	1.75	2.34	4.7	3.7	4.3	1.8
C_2	−179	−108	31	***tgg$^+$***								
D_1	38	80	39	***g$^+$dg$^+$***	1.92	2.49	2.11	3.92	3.2	1.3	2.3	0.1
D_2	−39	−80	−38	***g$^-$gg$^-$***								
E_1	32	100	−38	***g$^+$dg$^-$***	2.35	2.82	2.51	4.28	1.5	0.7	1.2	0.1
E_2	−32	−100	38	***g$^-$gg$^+$***								
F	180	−180	180	***ttt***	3.28	3.27	3.24	3.67	0.3	0.3	0.3	0.2

Abbreviations: ΔE, the energy difference between the current conformer and conformer with the lowest energy; ΔE$_0$, zero point energy difference; ΔH, enthalpy difference; ΔG, Gibbs energy difference; η, molar ratio conformer calculated based on the Boltzmann distribution at 20°C, level of calculations B3LYP/6-311++G**/cpcm (chloroform).

stretched conformation F (*ttt*), which has a slightly different NH stretching bands' profile. Also, the changes in band intensities between conformations are too small to enable conformer recognition when compared to the experimental spectrum.

ii. The *CH deformations and thiocarbamate vibrations region* (1,000–1,600 cm^{-1}), in which spectra can be divided into three groups based on the degree of stretching or packing of the molecule. These groups include "stretched" conformers A and F, "semi-packed" conformers B and C, and "packed" conformers D and E. The spectra of the stretched conformers are slightly more diverse due to a large change in the value of χ_2 angle, but the spectra in the remaining two groups match well (see Figure 8). This behavior is caused by the spectral band, which wavenumber is very sensitive to the value of the χ_1 and χ'_1 angle (modes 39 and 40, $\rho[\text{CH}_3] + \nu[\text{N-CH}_3]$; see Tables S1 and 3). When at least one of these angles has a *trans* conformation, the band is found at 1,267 cm^{-1} (conf. A), 1,273 cm^{-1} (conf. F), or approximately 1,260 cm^{-1} (conf. B and C). On the other hand, if at least one of these angles has a *gauche* conformation, the band is found at approximately 1,243 cm^{-1} (conf. B, C, D, and E). In the experiment, only one band is observed in the 1,200–1,300 cm^{-1} region; therefore, semi-packed conformers B and C can be excluded. For the further assignment, a direct comparison to the experiment is not possible as there is a shift between experimental and calculated band positions. However, by comparing the relative distances to the nearest two bands in both experimental and calculated spectra, it is possible to estimate which conformation thiram favors. The measurement in chloroform provided a trio of bands at 1,155, 1,249, and 1,382 cm^{-1}, with distances of 94 and 133 cm^{-1}. The calculation resulted in distances of 94 and 134 cm^{-1} for conformer A and 81 and 168 cm^{-1} for conformer D. Additionally, in the spectrum of conformer F, a rather intense band at 1,037 cm^{-1} was observed that is not present in the experiment. Therefore, the comparison to the experimental spectrum strongly indicates that conformer A dominates the conformer ratio.

iii. The *C-S and S-S stretching and skeletal vibrations region* (0–1,000 cm^{-1}), in which the differences among the conformers are most prominent (as shown in Figure 9). Again, the conformers can be divided into three categories: stretched (A, F), half-packed (B, C), and packed (D, E) based on their band positions (wavenumber) and intensity. The most significant difference between categories is seen in the S-S stretching vibration band (Mode 22 in Table 3). For stretched conformers A and F, the band is

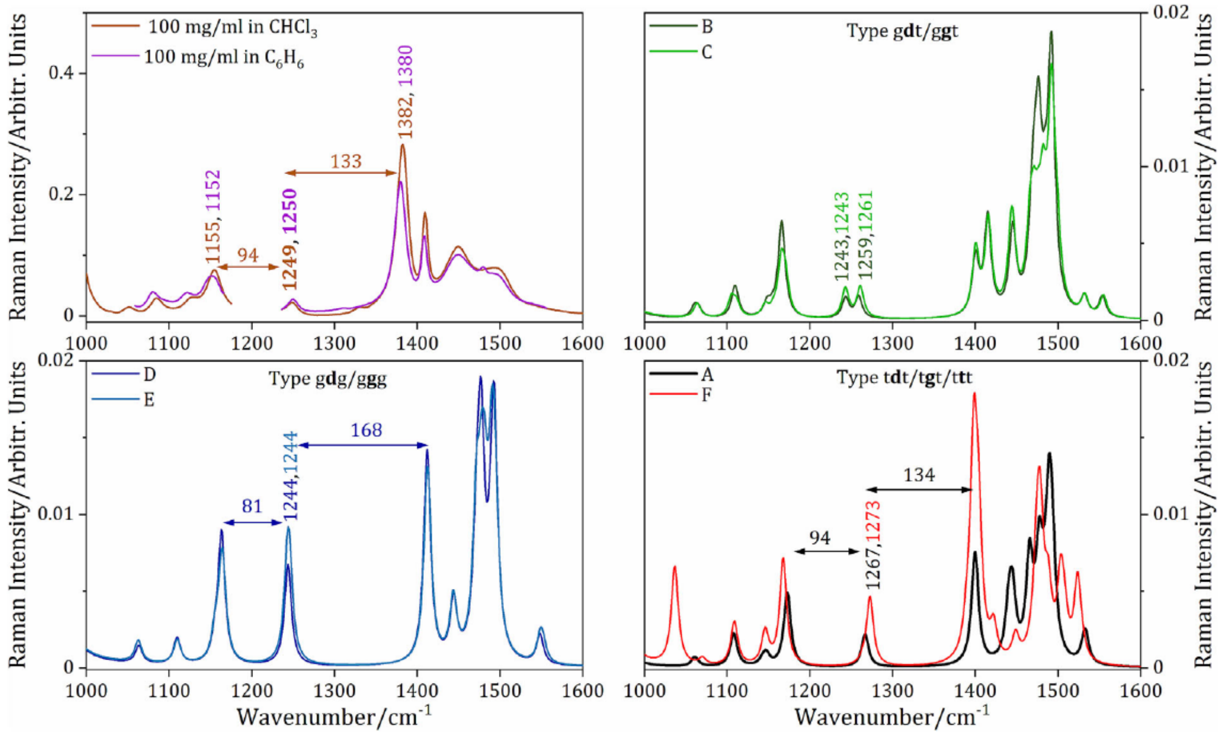

FIGURE 8 Comparison of solution phase Raman spectra of thiram (top, left) with calculated spectral profiles of the thiram conformers in 1,000 to 1,600 cm^{-1} region; B3LYP/6-311++G**/cpcm (water) level of theory.

TABLE 3 Vibrational mode assignment of the bands in the experimental Raman spectra from various phases and SERS

CHCl$_3$	CCl$_4$	C$_6$H$_6$	Powder	SERS		
Wavenumber (cm^{-1})					Mode	Description
125	116	-	111	-	8,9	τ(C-H$_3$)
177	175	175	178	-	10, 11	δ(C-S-S-C) sym.
211	-	216	213	-	12, 13, 14	ν(N-C-S-S-C-N), δ(N-C [CH$_3$]$_2$)
-	-	-	270	-	15	δ(S=C-N-CH$_3$)
311	-	311	317	347	16	δ(S-C=S)
-	-	356	363	347	17	δ(S-C=S)
397	**395**	**395**	**395**	-	**18, 19**	**ν(S-C) + δ(N-[CH$_3$]$_2$) rocking**
446	-	445	443	443	20, 21	δ(N-[CH$_3$]$_2$) scissoring
563	**565**	**564**	**561**	**563**	**22**	**ν(S-S)**
			585	-	24–26	δ(C-NS$_2$) + δ(N-[CH$_3$]$_2$) scissoring op
855	857	855	851	870	27	ν(C-S) + ν(N-CH$_3$) sym.
961	961	-	958	**936**	29	ν(C=S) + ρ(C-H$_3$) ip
987	**992**	-	**975**		**30**	**ν(C=S) + ρ(C-H$_3$) ip**
1,052	-	-	1,041	1,014	32	ρ(C-H$_3$) op + ν(N-CH$_3$) asym. Op
1,085	1,082	1,081	1,088	-	33, 34	ρ(C-H$_3$) op
1,129	1,127	1,122	1,132	-	35, 36	ρ(C-H$_3$) ip
1,155	1,156	1,152	1,149	1,142	38	ρ(C-H$_3$) ip
1,249	1,254	1,250	1,240	1,239	39, 40	ρ(C-H$_3$) op + ν(N-CH$_3$) asym. Ip
1,382	**1,379**	**1,380**	**1,375**	**1,378**	**41, 42**	**ν(C-N)**
1,410	1,410	1,409	1,399	-	43, 44	δ(C-H$_3$) sym. Op
1,450	1,450	1,450	1,466	1,444	47–52	δ(C-H$_3$) asym.
1,490	-	1,490	1,510	1,503	53, 54	δ(C-H$_3$) sym. Ip
2,864	2,853	2,860	2,851	2,853	55, 56	ν(C-H$_3$) sym. Op
2,934	2,931	2,934	2,930	2,922	58	ν(C-H$_3$) sym. Ip
-	-	-	2,970	-	59–61	ν(C-H$_3$) asym.
-	-	-	3,028	3,020	63–66	ν(C-H$_3$) asym. Ip

Note: The most distinct bands in the experimental spectra are highlighted in bold.

Abbreviations: τ, twisting; ρ, rocking; ν, stretching; δ, deformation; asym., asymmetrical; ip, in phase; op, out of phase; sym., symmetrical; -, not measured or observed.

located at 538 and 540 cm^{-1}, respectively. For half-packed conformers B and C, the band has a slightly higher intensity and is downshifted by approximately 70 cm^{-1} to 467 and 474 cm^{-1}, respectively. And for packed conformers D and E, the band has a very high intensity (about 5 times higher than in A) and is further downshifted by another ~70 cm^{-1} to 396 and 387 cm^{-1}, respectively. In experiments, the S-S stretching vibration can be seen at ~564 cm^{-1}, which is most consistent with the stretched conformers.

The analysis showed that experimental thiram spectra agree with the calculated spectrum of conformer A, which is characterized by the ***tgt*/*tdt*** stretched conformation. This dominance of conformer A is also supported by the comparison of the weighted spectra of thiram obtained based on the ΔE, ΔE_0, ΔH, and ΔG of individual conformers, as shown in Figure S6. Weighted spectra are very similar due to the overwhelmingly dominant contribution of conformer A. Therefore, it is difficult to determine the most appropriate weighting method when compared to the experimental spectrum. The indicators enabling differentiation might be the intensity ratio of bands at 841 and 874 cm^{-1}, the presence of a band at 468 cm^{-1}, and the presence of a band at 276 cm^{-1}. However, none of these features are observed in the experimental spectra (see, e.g., Figures 2 or 3). Therefore, the

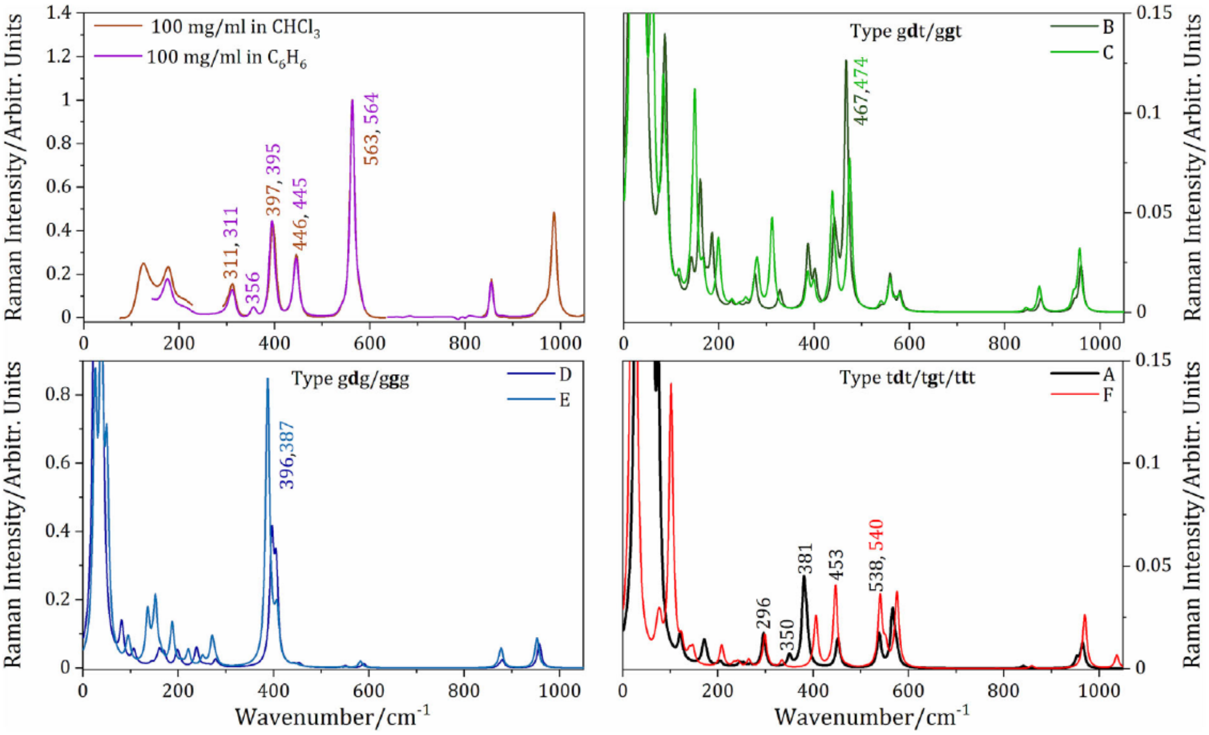

FIGURE 9 Comparison of solution phase Raman spectra of thiram (top, left) with calculated spectral profiles of the thiram conformers in 0 to 1,000 cm^{-1} region; B3LYP/6-311++G**/cpcm (water) level of theory.

weighting based on the Gibbs energy with the highest ratio of conformer A (95.7%) appears to be the most accurate.

3.7 | Vibrational analysis

Based on the analysis in the previous two sections, it was found that at standard pressure and temperature (20°C), the stretched conformer A has the highest probability of occurrence. The vibrational analysis of thiram was therefore made based on its Raman spectrum (see Table 3 and Figure 10; the in-detail assignment of all vibrational modes is made in Table S1). A thiram molecule has 24 atoms and thus 66 fundamental vibrations. Due to the symmetry of thiram, we distinguish two variants for each vibration—A (symmetrical to the C_2 axis of symmetry) or B (asymmetric to the C_2 axis of symmetry). For each dithiocarbamate, the group contains two methyls, whose vibrations often combine in phase or in antiphase. In general, the thiram Raman spectrum is dominated by the bands corresponding to vibrations with symmetry A and related to the movement of methyl groups (region of CH valence vibrations and the region of 1,000–1,700 cm^{-1}) or movement of sulfide groups (0–1,000 cm^{-1}). The agreement between the calculated and experimental spectra is very good, which made it possible to assign practically all vibrational modes to the corresponding spectral bands (except for the region below 100 cm^{-1}). Also, the relative ratios between the intensities of the individual bands are reliably reproduced in the simulations. The only significant deviation is swapped intensity of bands 22 and 24–26.

The vibrational analysis was successful for all experimental spectra, regardless of the chosen phase or measurement technique. The four most characteristic thiram vibrations (Raman markers) are illustrated in Figure 10 (bottom) and highlighted in bold in Table 3. These are related to vibrations of the disulfide group (Modes 18 and 22), thiocarbonyl groups (Mode 30), and dithiocarbamate (Mode 41).

4 | DISCUSSIONS

4.1 | Reproducibility of experimental features in simulations

The spectra of different conformers exhibited sufficient variability to enable the identification of the preferred conformation, not only on the basis of calculated conformer energies (Table 2) but also because of the similarity of calculated and experimental spectral profiles (Figures 8 and 9). Conformer A, with a ***tgt*/*tdt*** conformation (Figure 7), was found to be predominant in

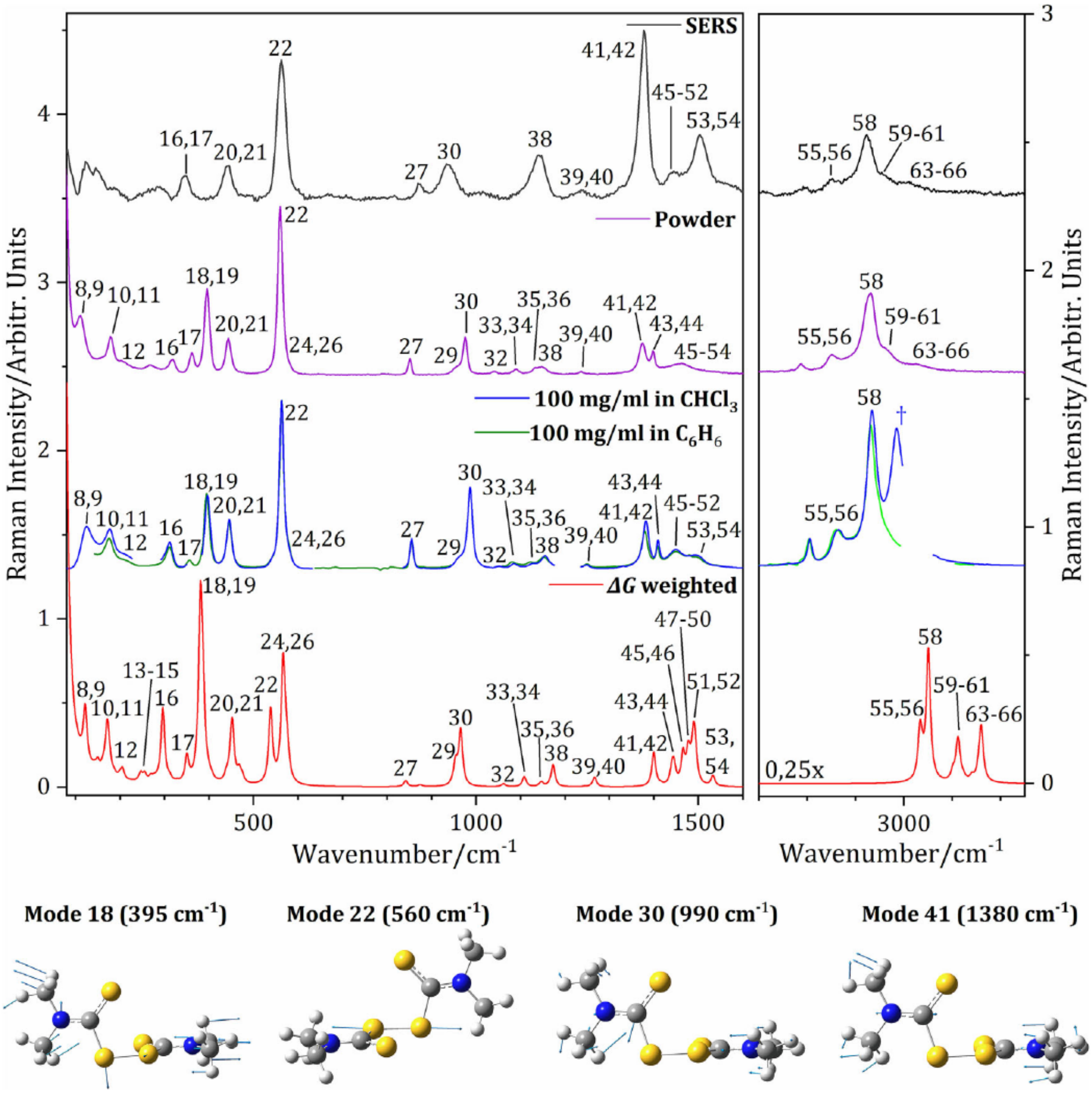

FIGURE 10 (Top) Comparison of the calculated thiram spectrum based on the *ΔG* weighting of conformers with experimental Raman spectra obtained in solution and solid phase (Thir B) and SERS spectrum. Corresponding bands are labeled, and the numbers correspond to the individual vibrational modes as shown in Tables 3 and S1. (Bottom) Illustration of the four vibrational modes corresponding to the most characteristic spectral bands of thiram.

the equilibrium by both approaches. This finding is readily explicable since this conformer possesses the lowest steric hindrance.

A high degree of concordance between experimental and simulated spectra allowed for a detailed vibrational analysis and the assignment of all observed experimental bands in the solution, as well as the vast majority of bands from the crystalline powder, DCDR, and SERS measurements (Table 3). Although the level of calculation employed for Raman spectra simulation (B3LYP/6-311++G**/cpcm [chloroform]) was adequate, the calculated wavenumber of S-S stretching vibration was somewhat imprecise. While most calculated spectral bands are slightly upshifted, the *ν*(S-S) band is slightly downshifted, a known effect for which a scaling factor of 1.05 has been proposed specifically for *ν*(S-S) vibration to improve the correspondence between experimental and calculated spectra.[38] However, because this factor is arbitrary and empirical, we chose to present calculated spectra without additional wavenumber scaling.

The findings of our calculations can be compared to the recent studies conducted by Oliviera et al.[18] and Ivanov et al.[19] However, it should be noted that these studies primarily focused on the interaction between degraded thiram molecules and silver atoms/surfaces. Both papers do present DFT simulated Raman spectra for the intact thiram molecule, but the specific conformation used is not mentioned. From a plain comparison of their molecular schemes and simulated spectra, it appears that the former paper likely employed conformation A (which we identified as the prevalent one), while the latter paper probably used the linear conformation F, which has a negligible abundance. This inference is supported by the shape of the molecular scheme and the calculated band positions in the lower wavenumber region (e.g., the band at 420 cm^{-1} should be approximately at 390 cm^{-1}).

Consequently, our research contributes clarity regarding the behavior and conformational flexibility of the undegraded (intact) thiram molecule. It showcases the reproducibility of experimental features in simulations, enabling the identification of the preferred conformation of thiram based on calculated conformer energies and the agreement between calculated and experimental spectral profiles.

4.2 | Resemblance of thiram and other disulfide group containing systems

The molecular structure of thiram closely resembles the central part of cystine, or diethyldisulfide, which is frequently utilized as an S-S bridge model. The conformation of these molecules, as determined by the value of three central dihedral angles, is described in the same manner, and there is a comparable correlation between the wavenumber of ν(S-S) vibration and conformation in all these systems. A rule proposed in 1970s[39,40] states that Raman bands attributed to disulfide bond stretch motion, observed at ~500, ~520, and ~540 cm^{-1}, should be assigned to three rotamers defined along the three successive bonds of the -C-S-S-C- moiety, designated as *ggg*, *ggt*, and *tgt*. This rule fits well for diethyldisulfide[41–43] and is also utilized for Raman-based assignment of S-S bridges conformation in peptides,[44–46] although recent observations suggest that the situation is more complex and requires refinement of this basic rule.[38,47] Nevertheless, our DFT simulations (Figure 8) revealed a similar trend, with Raman bands corresponding to the ν(S-S) vibration of *ggg*, *ggt*, and *tgt* conformers found at ~390, ~470, and ~540 cm^{-1}, respectively (~410, ~495, and ~565 cm^{-1} if a scaling factor of 1.05 is employed). The primary difference is the increase in the wavenumber gap between these bands, which rises from ~20 cm^{-1} for diethyldisulfide to ~80 cm^{-1} for thiram.

4.3 | Comparison of experimental spectra

Figure 10 and Table 3 can be utilized to facilitate the discussion of similarities and differences observed in thiram spectra obtained by various techniques and in different phases. Based on the calculations, the conformation of thiram molecule in the solution phase has been identified as ***tgt*/*tdt*** in both benzene and chloroform. This preferred arrangement is not altered by drying, as evidenced by the similarity of DCDR spectra obtained from dried deposits with spectra from solution (Figure S7). Furthermore, the Thir B component from crystalline powder measurements exhibits similar band positions and intensities to solution thiram spectra (Figure S7), while the spectrum of Thir A component exhibits minor differences related only to relative band intensities, particularly in the region below 700 cm^{-1}, however without any band shifts (Figure 2).

The disparity between the spectra of Thir A and Thir B components therefore cannot be attributed to conformational polymorphism, for spectra of different conformers manifest a number of band shifts. Instead, it could arise from either packing polymorphism or the influence of crystal grain size. Previous studies have demonstrated that the intensity of low wavenumber vibrational modes in Raman measurements of crystalline powder samples can be affected by the size of crystal grains.[22,23,48,49] Considering that the observed differences between Thir A and Thir B spectra are mostly subtle and confined to the region below 500 cm^{-1}, we deem the latter explanation to be the most plausible.

4.4 | Stability of thiram molecule in different phases

Thiram exhibits relative instability and is susceptible to degradation, starting with the cleavage of the disulfide bond into two dimethyldithiocarbamate anions. UV radiation and humidity have been identified as triggers of this process.[24,50,51] The present study aimed to investigate the stability of thiram crystalline powder and solutions in different solvents, namely, benzene, chloroform, and water, with a focus on the effect of drying methods and solvent-solute interactions. The results showed that thiram crystalline powder and solutions in benzene and chloroform are generally stable. However, evidence of degradation was observed in DCDR and SERS measurements, suggesting that the combination of the drying process and the solvent's capability to create intermolecular H-bonds with thio groups make the disulfide bond more vulnerable to degradation. The SERS spectra of dried samples from benzene and water solutions (Figure 5) showed that the intensity of 560 cm^{-1} band was less than half in the latter case. Additionally, DCDR measurements revealed increased thiram degradation when dissolved in chloroform (Figure S3) in which evidence of hydrogen bonds between chloroform and thiram was detected (Figure 2). Therefore, these observations suggest that the choice of solvent and drying process are crucial factors in maintaining the stability of thiram. It is important to note that our findings were not influenced by the specific spot chosen on the dried deposit, indicating that the results are consistent and reproducible. The only observed heterogeneity was associated with DCDR measurements and was related to the variations in the shape of the dried deposits, which however did not impact the identification of the spectral components.

4.5 | Differences in thiram SERS spectra

Generally accepted mechanism of enhancement of thiram SERS spectrum (measurements done on Ag aqueous colloids[20] and Au films[21]) is based on the idea of cleavage of thiram disulfide bond after adsorption on the metal surface, leading to the formation of monodentate or bidentate coordination of resulting dimethyldithiocarbamate anions to metal atoms.[20] This ligation should lead to the charge redistribution and strong enhancement of the ν(C-N) band at 1,378 cm^{-1}. In other words, it is expected that not thiram itself but products of its degradation are observed in SERS measurements. Recent studies supported this hypothesis, showing that simulated SERS spectra of dimethyldithiocarbamate ions bound to silver are highly similar to the spectra of thiram.[18,19] Even the band at 560 cm^{-1} (corresponding to ν(S-S) in undegraded thiram molecule) is still present but corresponds to ν(S-C-S) and δ (CH_3-N-CH_3) vibrations of dimethyldithiocarbamate anion.

However, our results (Figure 6) suggest that the situation can be more complex and the type of solvent used for sample preparation plays a crucial role. The intensity of bands below 600 cm^{-1} is over two times higher in benzene than in other solvents, indicating that another type of adsorption occurs when the solvent does not facilitate thiram degradation. Thiram may adsorb to Ag through weak interaction when only thiocarbonyl groups are coordinated to the surface and the molecule does not undergo degradation, similar to the case of ziram absorbed on Au surfaces.[21] This is supported by the notable downshift in modes 29 and 30 related to the ν(C=S) vibration and changes in other modes (16–19) associated with the vibrations of the C=S group in the low-wavenumber region (Figure 10 and Table 3). The favored ***tgt*/*tdt*** conformation of thiram remains unchanged, as the ν(S-S) vibration does not shift in wavenumber.

Our findings indicate that both types of coordination to the metal surface occur and the sum of thiram and dimethyldithiocarbamate anion SERS spectra is recorded in different proportions depending on the solvent used. The choice of solvent plays a crucial role due to its ability to form intramolecular hydrogen bonds to the thiocarbonyl group, which weakens the thiram disulfide bond and makes it susceptible to degradation.

5 | CONCLUSIONS

The study conducted on thiram revealed several significant findings. The spectra of the crystalline powder phase of thiram exhibited slight variability in relative intensities attributable to the variable crystal grain size. The solution phase Raman spectrum of thiram was obtained for the first time using a combination of measurements in three different solvents: chloroform, benzene, and tetrachloromethane, providing valuable insights into the interaction between thiram and solvent used. Evidence of hydrogen bonding between thiram and chloroform was observed.

The study has also highlighted the reliability and sensitivity of DCDR measurements, with high-quality thiram DCDR spectra obtained at a concentration of 40 μM. The spectra were highly similar to those obtained from the solution phase measurements, validating the accuracy of the results. Moreover, the observation of a higher rate of thiram degradation during drying when a solvent capable of forming intramolecular hydrogen bonds with thiram was used provides valuable information for future research.

The detailed conformational analysis of thiram allowed the identification of the most abundant conformer (adopting ***tgt*/*tdt*** conformation) based on both calculated thermodynamic properties and spectral resemblance to the experiment. This enabled reliable band assignment and vibrational analysis, providing a better understanding of the compound's properties.

The differences observed in thiram SERS spectra based on the solvent used for sample preparation indicate that thiram can be coordinated not only in the degraded form but also in the undegraded form. However, further experiments and simulations are required to verify this observation.

Overall, this study provides valuable insights into the behavior of thiram in different phases and solvents used, as well as into the differentiation and detection of its degraded and undegraded forms. This knowledge can be very beneficial in further work towards a viable Raman-based sensing and quantitative detection of thiram. At present, its detection is based on several SERS platforms (silver and/or silver/gold nanoparticles in different forms and states) as well as on the use of standard chromatography separation methods. In further prospect, the SERS and DCDR spectra complementing each other as well as the spectra coming from the synergy of both techniques could lead to the extension of their detection potential for thiram.

ACKNOWLEDGMENT

This work has been supported by Charles University Research Centre program UNCE/SCI/010 and SVV-2023-260716.

ORCID

Martina Valášková https://orcid.org/0009-0000-2154-9084
Alžbeta Kuižová https://orcid.org/0000-0002-2184-6537
Eva Kočišová https://orcid.org/0000-0001-5758-595X
Václav Profant https://orcid.org/0000-0001-8161-305X

REFERENCES

[1] T. S. Thind, D. W. Hollomon, *Pest Manage. Sci.* **2018**, *74*, 1547.
[2] V. K. Sharma, J. S. Aulakh, A. K. Malik, *J. Environ. Monit.* **2003**, *5*, 717.
[3] R. R. Dalvi, T. J. Robbins, M. K. Williams, D. P. Deoras, F. Donastorg, C. Banks, *J. Environ. Sci. Health, Pt. B: Pestic., Food Contam., Agric. Wastes* **1984**, *19*, 703.
[4] R. R. Dalvi, D. P. Deoras, *Acta Pharmacol Toxicol (Copenh)* **1986**, *58*, 38.
[5] P. S. Dalvi, T. Wilder-Kofie, B. Mares, R. R. Dalvi, L. H. Billups, *Pestic. Biochem. Physiol.* **2002**, *74*, 85.
[6] K. Maita, S. Tsuda, Y. Shirasu, *Fundam. Appl. Toxicol.* **1991**, *16*, 667.
[7] J. Siwiec, E. Siek, A. Grzywa-Celinska, B. Mackiewicz, E. Czekajska-Chehab, *Ann. Agric. Environ. Med.* **2019**, *26*, 672.
[8] S. Salam, A. Arif, R. Mahmood, *Pestic. Biochem. Physiol.* **2020**, *164*, 14.
[9] X. Chen, M. Fang, M. Chernick, F. Wang, J. Yang, Y. Yu, N. Zheng, H. Teraoka, S. Nanba, T. Hiraga, D. E. Hinton, W. Dong, *Gen. Comp. Endocrinol.* **2019**, *271*, 73.
[10] K. Liu, Y. Li, M. Iqbal, Z. Tang, H. Zhang, *Chemosphere* **2022**, *295*, 133928.
[11] Commission Regulation (EU), *Off. J. Eur. Union.* **2022**, *L215*, 65.
[12] M. B. Bhavya, R. B. Prabhu, B. M. Shenoy, P. Bhol, S. Swain, M. Saxena, N. S. John, G. Hegde, A. K. Samal, *Environ. Sci. NANO* **2020**, *7*, 3999.
[13] K. Wang, Z. Yue, X. Fang, H. Lin, L. Wang, L. Cao, J. Sui, L. Ju, *Sci. Total Environ.* **2023**, *856*, 159108.
[14] A. L. Picone, M. L. Rizzato, A. R. Lusi, R. M. Romano, *Food Chem.* **2022**, *373*, 131570.
[15] C. Yao, X. Gao, X. Liu, Y. Shen, A. Xie, *J. Mater. Res. Technol.* **2021**, *11*, 857.
[16] T. C. Dao, T. Q. N. Luong, T. A. Cao, N. M. Kieu, *Adv. Nat. Sci.: Nanosci. Nanotechnol.* **2019**, *10*, 10.
[17] J. Wu, Y. Huang, J. Miao, K. Lai, *J. Sci. Food Agric.* **2022**, *102*, 6211.
[18] M. J. S. Oliveira, C. S. Martin, R. J. G. Rubira, A. Batagin-Neto, C. J. L. Constantino, R. F. Aroca, *J. Raman Spectrosc.* **2021**, *52*, 2557.
[19] E. Ivanov, R. A. Ando, P. Corio, *Vib. Spectrosc.* **2016**, *87*, 116.
[20] S. Sánchez-Cortés, M. Vasina, O. Francioso, J. V. García-Ramos, *Vib. Spectrosc.* **1998**, *17*, 133.
[21] S. Sanchez-Cortes, C. Domingo, J. V. Garcia-Ramos, J. A. Aznarez, *Langmuir* **2001**, *17*, 1157.
[22] R. B. Patel, V. Stepanov, H. Qiu, *Appl. Spectrosc.* **2016**, *70*, 1339.
[23] P. K. Duy, S. Chun, H. Chung, *Anal. Chem.* **2017**, *89*, 11937.
[24] B. Gupta, M. Rani, R. Kumar, *Biomed. Chromatogr.* **2012**, *26*, 69.
[25] A. Kuižová, M. Přikryl, M. Procházka, E. Kočišová, *Spectrochim. Acta, Pt. a: Mol. Biomol. Spectrosc.* **2021**, *262*, 120109.
[26] A. Kuižová, E. Kočišová, *J. Raman Spectrosc.* **2023**, *54*, 694.
[27] D. Zhang, Y. Xie, M. F. Mrozek, C. Ortiz, V. J. Davisson, D. Ben-Amotz, *Anal. Chem.* **2003**, *75*, 5703.
[28] E. Kočišová, M. Procházka, *J. Raman Spectrosc.* **2015**, *46*, 280.
[29] E. Kočišová, M. Procházka, *J. Raman Spectrosc.* **2018**, *49*, 2050.
[30] E. Kočišová, S. Sayedová, M. Procházka, *J. Raman Spectrosc.* **2020**, *51*, 871.
[31] T. Dieing, W. Ibach, in *Confocal Raman Microscopy*, (Eds: T. Dieing, O. Hollricher, J. Toporski), Springer Berlin Heidelberg, Berlin, Heidelberg **2011** 61.
[32] I. Benito-González, M. Martínez-Sanz, A. López-Rubio, L. G. Gómez-Mascaraque, *J. Raman Spectrosc.* **2020**, *51*, 2022.
[33] M. J. Frisch, G. W. Trucks, H. B. Schlegel, G. E. Scuseria, M. A. Robb, J. R. Cheeseman, G. Scalmani, V. Barone, G. A. Petersson, H. Nakatsuji, X. Li, M. Caricato, A.V. Marenich, J. Bloino, B.G. Janesko, R. Gomperts, B. Mennucci, H. P. Hratchian, J. V. Ortiz, A.F. Izmaylov, J. L. Sonnenberg, W. F. Ding, F. Lipparini, F. Egidi, J. Goings, B. Peng, A. Petrone, T. Henderson, D. Ranasinghe, V. G. Zakrzewski, J. Gao, N. Rega, G. Zheng, W. Liang, M. Hada, M. Ehara, K. Toyota, R. Fukuda, J. Hasegawa, M. Ishida, T. Nakajima, Y. Honda, O. Kitao, H. Nakai, T. Vreven, K. Throssell, J.A. Montgomery Jr., J. E. Peralta, F. Ogliaro, M. J. Bearpark, J. J. Heyd, E. N. Brothers, K. N. Kudin, V. N. Staroverov, T.A. Keith, R. Kobayashi, J. Normand, K. Raghavachari, A. P. Rendell, J. C. Burant, S. S. Iyengar, J. Tomasi, M. Cossi, J. M. Millam, M. Klene, C. Adamo, R. Cammi, J. W. Ochterski, R. L. Martin, K. Morokuma, O. Farkas, J. B. Foresman, D. J. Fox, Gaussian 09, Rev. D.01. Gaussian Inc. Wallingford CT, **2016**.
[34] K. Kim, K. D. Jordan, *J. Phys. Chem.* **2002**, *98*, 10089.
[35] P. J. Stephens, F. J. Devlin, C. F. Chabalowski, M. J. Frisch, *J. Phys. Chem.* **2002**, *98*, 11623.
[36] R. Ditchfield, W. J. Hehre, J. A. Pople, *J. Chem. Phys.* **1971**, *54*, 724.
[37] A. Klamt, G. Schüürmann, *J. Chem. Soc., Perkin Trans.* **1993**, *2*, 799.
[38] B. Hernández, F. Pflüger, E. López-Tobar, S. G. Kruglik, J. V. Garcia-Ramos, S. Sanchez-Cortes, M. Ghomi, *J. Raman Spectrosc.* **2014**, *45*, 657.
[39] H. Sugeta, A. Go, T. Miyazawa, *Chem. Lett.* **1972**, *1*, 83.
[40] H. Sugeta, A. Go, T. Miyazawa, *Bull. Chem. Soc. Jpn.* **1973**, *46*, 3407.
[41] H. E. van Wart, F. Cardinaux, H. A. Scheraga, *J. Phys. Chem.* **1976**, *80*, 625.
[42] H. E. van Wart, H. A. Scheraga, *J. Phys. Chem.* **1976**, *80*, 1812.
[43] H. E. van Wart, H. A. Scheraga, *Proc. Natl. Acad. Sci. U. S. a.* **1986**, *83*, 3064.

[44] B. Hernandez, Y. M. Coic, S. G. Kruglik, C. Carelli, R. Cohen, M. Ghomi, *J. Phys. Chem. B* **2012**, *116*, 9337.

[45] E. Podstawka-Proniewicz, D. Sobolewski, A. Prahl, Y. Kim, L. M. Proniewicz, *J. Raman Spectrosc.* **2012**, *43*, 51.

[46] S. Schlucker, C. Liang, K. R. Strehle, J. J. DiGiovanna, K. H. Kraemer, I. W. Levin, *Biopolymers* **2006**, *82*, 615.

[47] M. Pazderková, V. Profant, P. Maloň, R. K. Dukor, V. Čeřovský, V. Baumruk, L. Bednárová, *Symmetry* **2020**, *12*, 12.

[48] T. R. M. de Beer, W. R. G. Baeyens, Y. V. Heyden, J. P. Remon, C. Vervaet, F. Verpoort, *Eur. J. Pharm. Sci.* **2007**, *30*, 229.

[49] D. A. Gómez, J. Coello, S. Maspoch, *Vib. Spectrosc.* **2019**, *100*, 48.

[50] M. M. Haque, M. Muneer, *Chem. Technol.* **2005**, *12*, 68.

[51] S. Heise, H. Weber, L. Alder, *Fresenius' J. Anal. Chem.* **2000**, *366*, 851.

SUPPORTING INFORMATION

Additional supporting information can be found online in the Supporting Information section at the end of this article.

How to cite this article: M. Valášková, A. Kuižová, E. Kočišová, V. Profant, *J Raman Spectrosc* **2023**, 1. https://doi.org/10.1002/jrs.6581

A.9 Exploring drying-induced separation of main constituents in melamine-blended milk infant formula using DCDR spectroscopy

KUIŽOVÁ, Alžbeta; KOČIŠOVÁ, Eva. Exploring drying-induced separation of main constituents in melamine-blended milk infant formula using DCDR spectroscopy. *Microchemical Journal.* **2024**, vol. 199, pp. 110206.

Available from doi: 10.1016/j.microc.2024.110206

Microchemical Journal 199 (2024) 110206

Contents lists available at ScienceDirect

Microchemical Journal

journal homepage: www.elsevier.com/locate/microc

Exploring drying-induced separation of main constituents in melamine-blended milk infant formula using DCDR spectroscopy

Alžbeta Kuižová, Eva Kočišová [*]

Charles University, Faculty of Mathematics and Physics, Institute of Physics, Ke Karlovu 5, 121 16, Prague 2, Czech Republic

ARTICLE INFO

Keywords:
Infant formula
Melamine
Carbohydrates
Lactose
Lipids
Drop coating deposition Raman
DCDR

ABSTRACT

Drop coating deposition Raman (DCDR) spectroscopy was employed to investigate the melamine compound susceptibility to milk infant formula main constituents as lactose and lipids (specifically 1,2-dioleoyl-*sn*-glycero-3-phosphocholine (DOPC), and 1,2-dioleoyl-*sn*-glycero-3-phosphoethanolamine (DOPE)). DCDR approach is based on the deposition and drying of a small droplet (a few μl) of liquid sample on a hydrophobic substrate. After complete evaporation, the analyte is preconcentrated into the dried pattern from which the classical Raman spectra are acquired. A simple melamine-blended model reactions were tested (melamine-blended lactose, DOPC, and DOPE). From these, lactose was shown to be the most potent reaction partner for melamine, where a significant difference in dried pattern between pure and blended lactose was noticed, and the relevant Raman spectral changes were observed. Pure and melamine-blended infant formula solutions from two kinds of powdered infant formula purchased in the local market were then studied. For pure milk solutions, the drying process, as an integral part of the DCDR approach, led to the spatial separation of lipids and carbohydrates in the resulting pattern. Acquired Raman spectra revealed that the ring edge of the dried pattern was composed mainly of lipids, while the thin film in the central part contained mainly carbohydrates, especially lactose. For the melamine-blended formula, the DCDR approach identified that melamine was present only in the central part of the dried pattern together with carbohydrates. As a result, it was assumed that melamine has a higher susceptibility for carbohydrates than for lipid molecules, even in milk infant formula.

1. Introduction

Melamine, as a small organic molecule characterised by a high nitrogen content, is industrially produced from urea. It is widely used in diverse industrial applications, including adhesive resin in wood-based panels and flooring or material for durable kitchenware, and fertiliser in agriculture or impregnation [1–3]. Besides that, melamine is also known for its harmful effects on the animal and human body. As early as 1966, it was shown that melamine-adulterated animal feed had a negative impact on sheep [4], nearly 30 years later, a harmful effect was shown on rats [5]. Then, in 2004 in Asia and in 2007 in the USA, melamine was illegally added to pet food for dogs and cats, which led to stone formation and kidney failure [6]. Global attention on melamine's adverse effects arose when the melamine-contaminated infant formula in China in 2008 was uncovered, where melamine was illegally misused for the apparent elevation of protein content [7]. The detailed mechanism of melamine-induced toxicity from adulterated infant formula has not yet been fully described. However, it is known that co-digestion of melamine with cyanuric acid produces insoluble co-crystals present in kidney tubules where the physical blockage leads to renal impairment [8].

Focusing on melamine contamination, the evaluation of the possible interaction of melamine with main milk constituents is still of high importance. Considering lactose, the most abundant sugar in infant formula, it was found that melamine is due to its three amino groups targeted for non-enzymatic glycation of reducing sugars yielding different products with unknown effects on the human body [9,10]. Raman spectroscopy was then applied to study a simple "wet-blended" and then spray-dried lactose-melamine mixture [11]. Acquired Raman spectra showed a shift of the melamine breathing vibration spectral band due to the melamine interaction with lactose, supporting the hypothesis of melamine glycation.

As Raman spectroscopy is sensitive to melamine Raman spectral features, we focused on investigating possible melamine competitive reactions with the main constituents of milk infant formula (lactose and lipids). We employed the drop coating deposition Raman (DCDR)

---

[*] Corresponding author.
E-mail address: kocisova@karlov.mff.cuni.cz (E. Kočišová).

https://doi.org/10.1016/j.microc.2024.110206
Received 23 November 2023; Received in revised form 26 January 2024; Accepted 20 February 2024

spectroscopy [12], a vibrational spectroscopic method providing unique information about molecular vibrations based on depositing a small droplet (a few μl) of low concentrated liquid sample on a hydrophobic substrate and allowing it to dry, generally at room temperature. After complete evaporation, the analyte is preconcentrated to the dried deposit of different forms (ring pattern, spots, crystals…), from which classical Raman spectra (single spectra or spectral maps) are accumulated and further analysed. Because of the drying-induced preconcentration, sensitivity for low-concentrated samples is significantly improved compared to the classical Raman spectra from the solution [13,14]. Choosing a suitable substrate is crucial for optimising a DCDR experiment and performance, where hydrophobic substrates are preferred. Hydrophobicity affects the resulting pattern's size, the analyte's final preconcentration, and its spatial separation. Generally, the formed pattern is an interplay among more factors, such as the type of molecular solution (or analyte), i.e. molecular size, charge, concentration, used solvent, and a selected substrate.

DCDR spectroscopy introduces a simple and rapid method convenient for sensitive detection of low-concentrated analyte solution or suspension with minimal or no sample preparation. This approach has already been widely used to study biological molecules, molecular mixtures, and real samples [15–20].

This study further aimed to investigate the feasibility of detecting and identifying melamine based on its interaction with the main milk constituents, such as lactose and lipids, in concentrations relevant to adulterated infant formulas. Thanks to the symmetrical ring structure of the melamine molecule, it has a strong Raman signal around 676 cm^{-1} corresponding to the breathing vibration [21–23]. Using the DCDR approach and commercial hydrophobic substrate SpectRIM$^{\mathrm{TM}}$ from Tienta Sciences, it was shown that melamine from an aqueous solution can be detected at μM concentrations [24]. Concerning infant formula, we also focused on the drying-induced spatial separation of main milk constituents into dried deposit pattern for pure and melamine-blended milk. For the contaminated sample, powder melamine was added to and mixed with lactose powder, lipids (1,2-dioleoyl-*sn*-glycero-3-phosphocholine - DOPC, 1,2-dioleoyl-*sn*-glycero-3-phosphoethanolamine - DOPE) and powder milk infant formula and subsequently dissolved in water to mimic real situation when illegally blended. In this work, we demonstrate that a small drop of the prepared low-concentrated samples allowed, after drying, the study of a deposit from which a high-quality Raman spectrum could be obtained to determine spatial separation and interaction for main milk constituents and melamine.

2. Material and methods

2.1. Material

α-lactose monohydrate (product number L3625) and melamine in the form of crystalline powder (product number M2659) were purchased from Sigma-Aldrich at the highest possible purity. Lipids 1,2-dioleoyl-*sn*-glycero-3-phosphocholine powder (DOPC, product number 850375) and 1,2-dioleoyl-*sn*-glycero-3-phosphoethanolamine powder (DOPE, product number 850725) were purchased from Avanti polar lipids. Two powder milk infant formulas – Sunar and Nutrilon, referred to as Sun and Nut, respectively - were obtained at the local market. All solutions were prepared in deionised water (Milipore-Q 18.2 MΩ) of spectroscopic purity.

2.2. Sample preparation

For obtaining Raman spectra by DCDR approach of pure melamine, lactose, DOPC, DOPE, Sun and Nut, separate solutions and suspension (for lipids) were prepared. The melamine powder was dissolved to the final 0.1 mg/ml concentration. Lactose solution was prepared at a final concentration of 1.3 mg/ml, and solutions of both infant formulas, Sun and Nut, were prepared at a concentration of 7.83 mg/ml in deionised water (concentration corresponding to twenty times diluted one dose of infant formula). For lipids, samples were prepared as pure liposomal suspensions from DOPC and DOPE. The preparation consists of the complete lipid dissolution (1 mg/ml in both cases) in a chloroform–methanol mixture in a glass flask. A stream of nitrogen gas was used to remove the solvent to form a thin lipid layer on a glass surface. Spontaneous vesicle formation began when deionised water was added and mixed to hydrate the lipids. Applying an ultrasonic bath achieved complete hydration to cloudy nonunillamelar liposome suspension. The detailed standard preparation procedure can be seen elsewhere [25]. The summary of pure samples used in the study is listed in Table 1.

Concerning mixtures, a lactose-melamine solution (Lac_Mel) was prepared by blending the melamine powder with lactose powder and then dissolved in deionised water. Lipid-melamine mixtures (DOPC_Mel, DOPE_Mel) were achieved by adding melamine powder to a thin lipid layer spread on a glass flask after removing the organic solvent (chloroform–methanol mixture) with subsequent hydration by deionised water. Then, melamine powder was intentionally added to the powder of two kinds of infant formula and dissolved in deionised water in three different concentrations of melamine in the milk (Sun A, Sun B, Sun C, Nut A, Nut B, Nut C). The final concentrations of all prepared mixtures are summarised and listed in Table 2.

2.3. DCDR spectroscopy measurements

To perform DCDR measurements, we used a commercial μ-RIM slide from BioTools, a highly reflective stainless steel hydrophobic substrate with no detectable Raman or IR background signal. A 2-μl drop of each studied solution (pure and mixture ones) and suspension were deposited onto the slide and left to dry at room temperature for approximately 45 min. The substrate was covered with a Petri dish to avoid dust pollution during drying. The formed dried pattern was then analysed.

2.4. Instrumentation

Raman spectra of dried patterns were acquired by Raman microspectrometer Alpha 300 from WITec. The microspectrometer was equipped with a 532 nm laser as an excitation source with the power tuned to the 5 mW. A Carl Zeiss 50×/0.55 LD objective was chosen to focus the laser onto the sample and collect back-scattered radiation. The chosen objective reduced laser power on the sample by a factor of 0.698. The instrument uses an ultra-high throughput spectrometer (UHTS) with a focal length of 30 cm. All spectra were recorded with 600 grooves/mm grating using a nitrogen-cooled CCD detector. Each single Raman spectrum was collected by 60 × 3 s accumulation. For measuring a spectral map of pure DOPC, DOPC-melamine mixture and lactose-melamine mixture dried patterns, an area of 40 × 40 μm was scanned comprising 1600 spectra with a resolution of 1 spectrum/μm with a 1 s accumulation per spectrum. For pure DOPE, and DOPE-melamine mixture dried patterns, the area of 20 × 80 μm comprising 1600 spectra was measured with a resolution of 1 point/μm with a 1 s accumulation per spectrum. To acquire a spectral map of milk solutions, an area of 20 × 20 μm comprising 100 spectra was scanned with a resolution of 1 point per 2 μm with a 5 s accumulation per spectrum. The laser power and the accumulation time were chosen to prevent a sample

Table 1
Final concentrations of pure aqueous solutions and lipid suspensions.

Reactant	Final concentrations of pure samples **(mg/ml)** for DCDR spectroscopy
Melamine	0.1
Lactose	1.3
DOPC	1
DOPE	1
Sunar	7.83
Nutrilon	7.83

Table 2
Final concentrations of reactants in the mixtures for model reactions.

Reactant	Reactant final concentration in aqueous mixtures (mg/ml) for DCDR spectroscopy								
	Lac_Mel	DOPC_Mel	DOPE_Mel	Sun A	Sun B	Sun C	Nut A	Nut B	Nut C
Melamine	0.006	0.006	0.007	0.1	0.05	0.025	0.1	0.05	0.025
Lactose	1								
DOPC		1							
DOPE			1						
Sunar				7.83	7.83	7.83			
Nutrilon							7.83	7.83	7.83

degradation. For a more detailed image, white light images of dried patterns were taken using objectives Carl Zeiss 5× /0.15 and Carl Zeiss 50×/0.55 LD.

2.5. Data analysis

All spectra (single spectra, Raman spectral maps) measured on an Alpha300 RS confocal Raman microscope were processed in the associated software from the WITec Suite SIX package (Oxford Instruments, WITec) with automatic calibration. All measured spectra were first treated with the software's "Cosmic Ray Removal" procedure to detect and remove recorded cosmic rays' spikes. For processing the Raman spectral map, where appropriate, the "True Component Analysis" software tool was used to obtain and identify dominant spectral components in the scanned area. This procedure involves fitting each spectrum of the acquired Raman map with a linear combination of basis spectra (components) using the least square method. The intensity distribution of different components and their averaged spectra are simultaneously created. The appropriate software procedure in the WITec suite SIX package was used to calculate an average spectrum of Raman spectral maps. Spectra were then treated by the orthogonal-differences baseline-correction method using in-house-developed software, also employed for the intensity normalisation [26]. The final presented graphs were prepared in the OriginPro program 2020b (OriginLab Corporation).

3. Results and discussion

3.1. Melamine

Firstly, a 2-μl drop of melamine solution (0.1 mg/ml) was deposited onto the μ-Rim substrate. After drying, we could observe the resulting pattern depicted in Fig. 1a. This pattern contained long, thin crystals, which are typical for melamine due to its molecular structure allowing the formation of melamine complexes by hydrogen bonds [27–31]. The observed pattern agreed with dried deposits from the previous work [24], where similarly nonuniform patterns with crystals were formed. A spectrum accumulated from preconcentrated locations served as a reference for melamine's classical Raman spectrum for further comparison and analysis. The single point characteristic spectrum in Fig. 1b shows the lower spectral region with the most intense spectral band at position 673 cm^{-1}, which belongs to the symmetric breathing vibration of the melamine ring structure [23,32]. Further protonation or complexation of melamine by hydrogen bonds increases the ring's rigidity and results in the shift of the breathing vibration frequency to higher wavenumbers by units of cm^{-1} [32–35]. This vibration played a key role in identifying melamine in real samples and investigating its interaction in mixtures [36–38].

3.2. Lactose-melamine mixture

The DCDR approach was then employed for the pure lactose and Lac_Mel mixture solutions. After evaporation, a significant difference was observed between dried patterns from the pure solution and the mixture (Fig. 2a, Fig. 2b, Fig. 2c for pure lactose, and Fig. 2e for the mixture). Dried pure lactose consisted of crystals clearly visible through polarising filters (Fig. 2c), unlike the dried pattern from the Lac_Mel mixture, which was formed by the homogeneous thin film pattern with no sign of crystallinity (Fig. 2e). Lactose lost its crystalline character after mixing with melamine and subsequent dissolving and drying. Moreover, the dried pattern from the Lac_Mel mixture showed no lactose-melamine spatial separation, which indicated melamine glycation. The acquired single-point Raman spectrum from the dried pattern of crystalline lactose and the average spectrum from spectral mapping obtained from the Lac_Mel mixture amorphous deposit are presented in Fig. 2d and Fig. 2g, respectively.

Crystalline solid lactose can occur in either one of three forms (α-lactose monohydrate, α-lactose anhydrous and β-lactose anhydrous) with different vibrational signatures confirmed experimentally as well as by quantum chemical calculations [39–41]. α- and β-lactose are present in the equilibrium in the aqueous solution due to mutarotation. Therefore, it is challenging to assign Raman bands to specific vibrations of different lactose forms [42]. To identify anomer measured here from

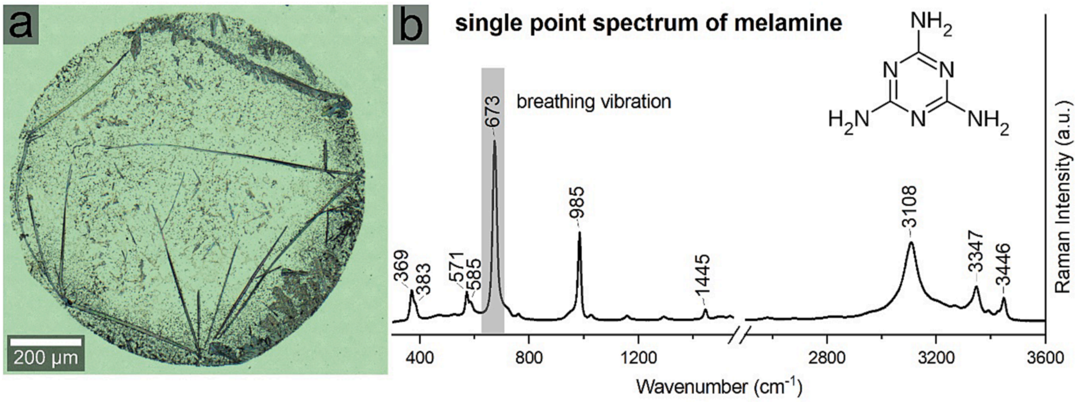

Fig. 1. DCDR measurement of melamine. a) The white light image of the dried pattern of the drop of melamine solution (0.1 mg/ml) deposited onto the μ-Rim substrate, and b) the single point DCDR spectrum providing further as a reference. Inset: chemical structure of melamine.

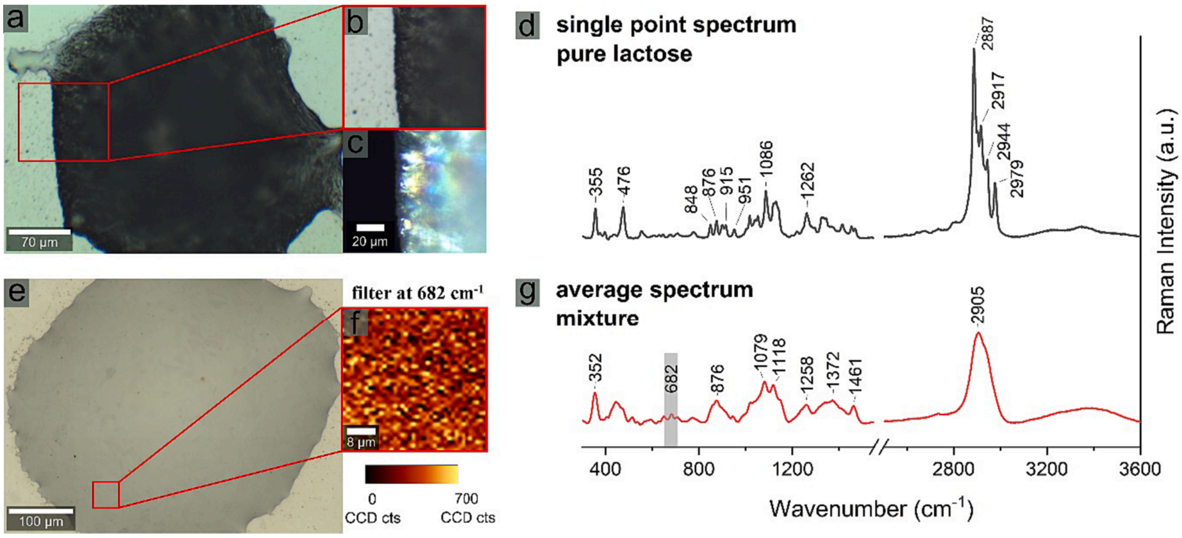

Fig. 2. DCDR measurement of lactose and Lac_Mel mixture. a), b) White light images of pure lactose dried pattern with c) the image under polarised light and d) single point Raman spectrum from pure lactose dried pattern. e) The white light image of Lac_Mel mixture dried deposit with the indicated area selected for spectral mapping, f) showing melamine distribution throughout the scanned area using a spectral filter for the spectral band of melamine breathing vibration at 682 cm^{-1}, and g) average Raman spectrum from this selected area.

pure dried lactose deposit, a very distinctive band at 1086 cm^{-1} assigned to the ν(CC) and ν(CO) modes of the glycosyl unit can be used as a characteristic fingerprint band for α-lactose [41–43]. More spectral bands can be used for anomer identification, for instance, the intense band at 355 cm^{-1} is attributed to the τ(COHO) and τ(HOH) [41,44]. Detailed band assignments of lactose Raman bands can be found elsewhere [39,42–44]. Moreover, the 1086 cm^{-1} band can be used to identify the crystalline or amorphous lactose form as it is sensitive to polarisation [40]. Generally, the Raman spectrum of crystalline lactose significantly differs from the Raman spectrum of amorphous lactose, which agrees with our measurements from the pure dried pattern and the Lac_Mel mixture. Amorphous lactose shows the broadening of bands with similar Raman shifts, intensity decrease, and the absence of band splitting [40].

Concerning the Lac_Mel mixture, spectral mapping clearly demonstrated the melamine band at the position of 682 cm^{-1} and its homogeneous distribution in the measured area by using a filtering procedure to show an intensity distribution for a specific spectral region (Fig. 2f, Fig. 2g). The difference in the Raman spectrum between pure lactose (Fig. 2d) and the Lac_Mel mixture (Fig. 2g), together with the presence of the melamine spectral band, confirmed that lactose interacts with melamine when mixed, which is also related to the loss of lactose crystalline character evident in the dried pattern change.

3.3. Lipid-melamine mixture

To investigate the possible reaction between melamine and lipids present in infant formulas, we chose two model lipids, DOPC and DOPE. These phospholipids with different head groups (phosphatidylcholine for DOPC and phosphatidylethanolamine for DOPE) comprise the same acyl chain formed by oleic acids, the most prominent fatty acid in the infant formulas. After the evaporation process of deposited pure liposomal suspensions of DOPC and DOPE and blended mixtures DOPC_Mel and DOPE_Mel, formed dried patterns were compared. The details of formed ring structures of both blended mixtures are shown in Fig. 3a and Fig. 4a. There was no significant visible difference between deposits

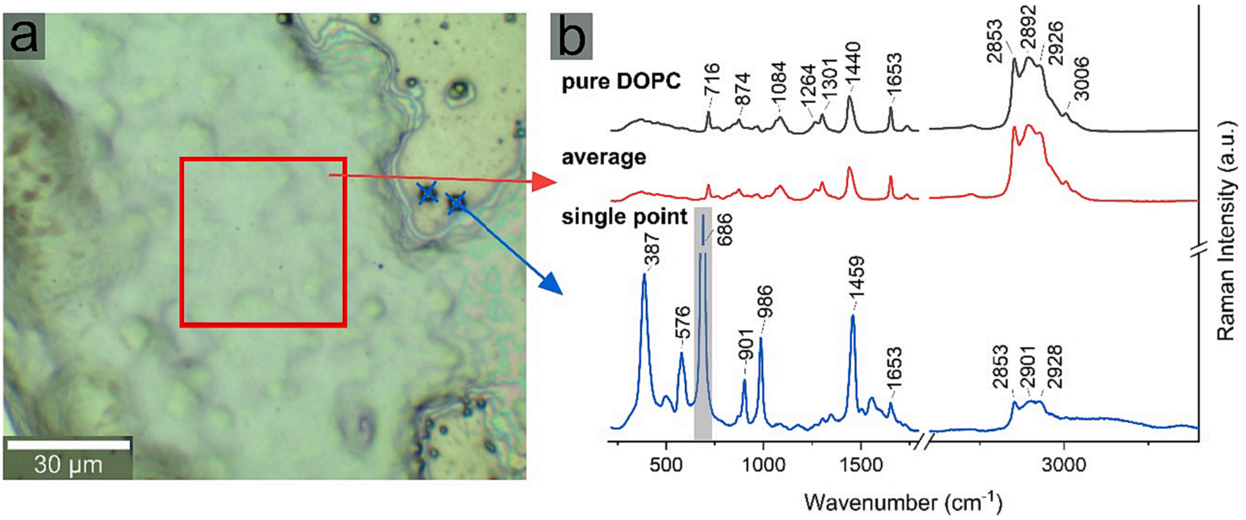

Fig. 3. DCDR measurement of DOPC_Mel mixture. a) The white light image of DOPC_Mel mixture with indicated area for spectral mapping, and b) spectra from pure DOPC dried deposit, average Raman spectrum from spectral mapping and single Raman spectra from the points indicated on the white light image.

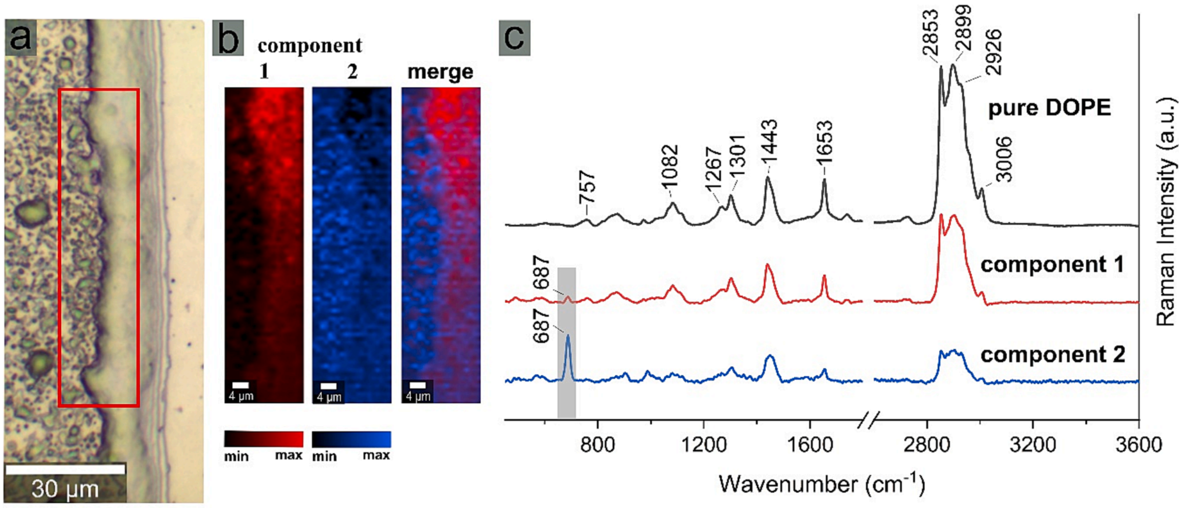

Fig. 4. DCDR measurement of DOPE_Mel mixture. a) The white light image of the DOPE_Mel mixture with indicated area for spectral mapping with b) showing the spatial distribution of two components identified in the scanned area, stronger colour indicates a higher signal. c) Average spectrum from pure DOPE dried deposit and average Raman spectra of both components obtained from a spectral map.

from pure samples and mixtures, unlike we observed for lactose (patterns from pure suspensions not shown). Four spectral maps, one from each dried pattern (DOPC, DOPE, DOPC_Mel, DOPE_Mel) were acquired. The average spectra calculated from the mapping of pure samples were used as reference spectra for blended lipids (Fig. 3b and Fig. 4c). For the DOPC_Mel sample, we obtained additional single point spectra from specific sites absent in the dried pattern of pure DOPC located in the centre of the ring pattern. Acquired Raman spectra consisted of a strong signal belonging to the melamine. The spatial separation of melamine to the inner part of the dried pattern in the form of small spots indicated in Fig. 3a was thus revealed. The average spectrum of the spectral map of the ring structure of the DOPC_Mel pattern expressed a signal only from DOPC, as shown in Fig. 3b (no melamine band), with no visible differences compared to the reference spectrum of pure DOPC. Lipid DOPC was preconcentrated to the ring pattern, and the melamine tended to form small spots in the inner part of the ring pattern. Based on the Raman spectra acquired from dried deposits, we could clearly identify the spatially separated melamine and lipid molecules. Melamine did not interact with DOPC and remained separated after mixing and subsequent drying process.

Raman spectral mapping from the DOPE_Mel ring pattern (Fig. 4a) showed that the dried ring deposit is not composed solely of lipids (Fig. 4b and Fig. 4c). Employing a “True component analysis” procedure to identify the spectral components, we determined specific locations within the scanned area with the most intense melamine band at 687 cm^{-1} corresponding to component 2. Subsequently, an average spectrum based on the components’ intensity distribution was computed (Fig. 4c). It is clear from the measured spectra that the lipid tended to preconcentrate in the ring pattern, as seen for component 1 spatial distribution, and melamine was partially separated in the inner parts of the ring. The acquired Raman spectral map revealed that DOPE and melamine partially interacted during mixing and drying, whereas component 2 consists of intense features from both DOPE and melamine. Unlike DOPC, DOPE consists of an amine group in the hydrophilic part of the lipid. We supposed that this group was prone to react with melamine molecules through hydrogen bonding, resulting in non-homogeneous melamine co-localisation with a DOPE in the dried pattern. To conclude, from tested melamine-blended lipid mixtures, we did not observe any relevant interactions that could be attributed to the melamine interaction with the oleic acid acyl present in infant formulas.

3.4. *Melamine–milk mixture*

Finally, we deposited droplets of pure milk solutions, Sun and Nut. The dried patterns of such droplets are shown in Fig. 5a and Fig. 5c. For both samples, we observed the formation of distinct rings with the remaining thin film spread in the central part. This pattern may result from either a high concentration of analyte in the solution or, a possible spatial distribution of solvent constituents, or both effects. After measuring single Raman spectra from the ring edge and the thin inner layer (Fig. 5b and Fig. 5d), we could observe significant differences, such as different intensity ratios of spectral bands and the appearance/disappearance of some bands. These results demonstrated the possible contribution of the drying process to separating milk constituents from the solution.

Similarly, variation and changes in Raman spectra obtained across the ring width related to molecular separation were discussed by Filik and Stone from tears samples [20]. Regarding spectra from both tested milk solutions, Sun and Nut, we observed only subtle differences between the spectra obtained from ring edges and thin films. Thus, we could see a similar separation of solution constituents for both studied kinds of milk with slightly different compositions. For clear-cut identification of melamine and analysis of its interaction in the contaminated milk solutions, it is advantageous that both milk spectra (from the ring edge and the thin layer) do not overlap with the main spectral feature of melamine.

We examined the spectral features of both acquired Raman spectra (ring edge and central part) to determine what constituents are separated during the drying process. According to infant formula composition, the main constituents were unsaturated fats, specifically oleic acid, and carbohydrates such as lactose, galactooligosaccharides, and fructooligosaccharides. Achieving the optimal concentration of the milk solution played a key role in the drying-induced separation process. Due to the high concentration, the dried pattern did not show evidence of constituents’ separation, for example, at the concentration corresponding to the one dose of infant formula.

Concerning spectra from the ring edge, we compared our measured spectra with the Raman spectra of different lipids [45]. A long chain of fatty acids (FAs) has several characteristic spectral regions in the Raman spectra. Unsaturated FAs have specific doublet in the region 1200–1400 cm^{-1} visible in our spectra at 1264 cm^{-1} and 1302 cm^{-1} assigned to the in-plane = C-H deformation in an unconjugated cis double bond and δ(CH$_2$) twisting, respectively [46]. The intense band at 1655 cm^{-1} assigned for C = C stretching vibration is characteristic of unsaturated

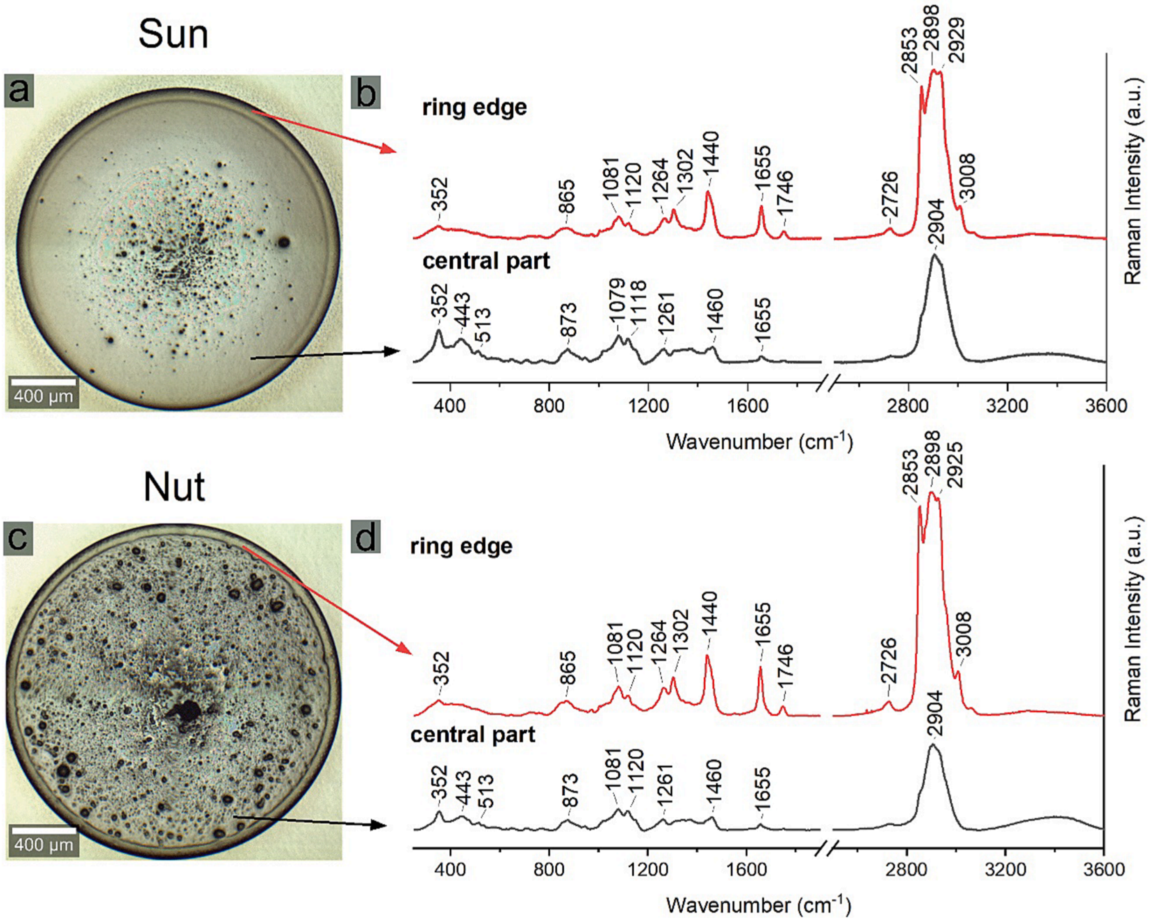

Fig. 5. DCDR measurement of infant formulas. a) The white light image of a dried pattern of the Sun milk droplet with b) corresponding DCDR spectra accumulated from the edge ring and central part. c) The white light image of a dried pattern of Nut milk droplet with d) corresponding DCDR spectra accumulated from the edge ring and central part.

FAs, and the band at the position of 1746 cm^{-1} is a typical lipid band attributed to the C = O stretching vibration [46]. FAs also differ in the region for C-H stretching vibrations. Unsaturated FAs have an additional feature around 3000 cm^{-1} related to the stretching modes of the = C-H moieties visible at 3008 cm^{-1} in our spectra. Spectral bands at 2853 cm^{-1} and 2898 cm^{-1} are assigned to the CH_2 stretching vibration, and the band at 2927 cm^{-1} is related to the CH_3 vibration. According to the mentioned characteristic spectral features for FAs and our Raman spectra of ring edge, we concluded that the ring edge of milk deposit is mainly formed of oleic acid, the most dominant lipid constituent in measured infant formula. This is consistent with a study on milk fat composition that showed that oleic acid has the highest proportion of all present fatty acids [47]. Further, the preconcentration and segregation of lipid molecules to the ring structure are in agreement with previously published works focused on the DCDR approach of different lipids in the form of liposomes [15,48,49].

Focusing on the spectra of the central part acquired from the thin film inside the ring structure, we could see a noticeable difference compared to spectra taken from the ring edge. We assumed that the central part is mainly composed of carbohydrates, the most abundant carbohydrate present in milk is lactose, known as milk sugar. The spectral region from 300 to 1500 cm^{-1} in Fig. 5b and Fig. 5d acquired from the central part strongly corresponds to the Raman spectra of amorphous lactose [40,50]. The lactose fingerprint region (950 – 1200 cm^{-1}) contains two strong bands at 1087 cm^{-1} and at 1123 cm^{-1}, with shoulders at 1027 cm^{-1} and 1149 cm^{-1} [50]. Measured DCDR spectra from the deposit central part from both kinds of milk showed a wavenumber shift of these bands to positions at 1079 cm^{-1} and 1118 cm^{-1} for Sun and 1081 cm^{-1} and 1120 cm^{-1} for Nut. These shifts can be attributed to the presence of carbohydrate mixture (oligosaccharides and polysaccharides), not only lactose, in tested milk solutions. Other spectral regions such as the low wavenumber region (bands at 352, 443, and 513 cm^{-1}), anomeric region (600–950 cm^{-1}) and also the CH_2 and COH deformations region (1200–1500 cm^{-1}) correspond to the lactose Raman bands [50]. The high wavenumber region (>2600 cm^{-1}) in our measured spectra from the central part exhibited the broader overlapped bands assigned to the CH_2 and CH_3 vibrations [44]. For carbohydrates, these broader bands are specific for oligosaccharides and polysaccharides, also present in the measured infant formula or amorphous lactose. From the above-mentioned analysis, it is clear that the spatial distribution of the main milk constituents is observed after the evaporation process of the diluted milk solution. The ring structure is created mainly of lipid molecules, and the thin layer in the central part of the formed deposit is composed mainly of carbohydrate lactose.

To determine a melamine influence in a real formula sample, we intentionally contaminated (blended) two infant formulas. Deposited 2-µl droplets blended milk mixtures for both tested formulas were left to dry at room temperature (Sun A (20 ×), Sun B (20 ×), Sun C (20 ×), Nut A (20 ×), Nut B (20 ×), Nut C (20 ×)). The formed patterns (an example seen in Fig. 6b) were indistinguishable from patterns of dried pure milk solutions in Fig. 5a and Fig. 5c, with a significant ring structure at the edge and the inner central part as a thin film of the spread analyte. After Raman spectra acquisition from the ring structure for each pattern, we did not observe any spectral feature belonging to the melamine molecule. Therefore, we focused on the thin inner film of the pattern, where accumulated single spectra (Fig. 6a) revealed the

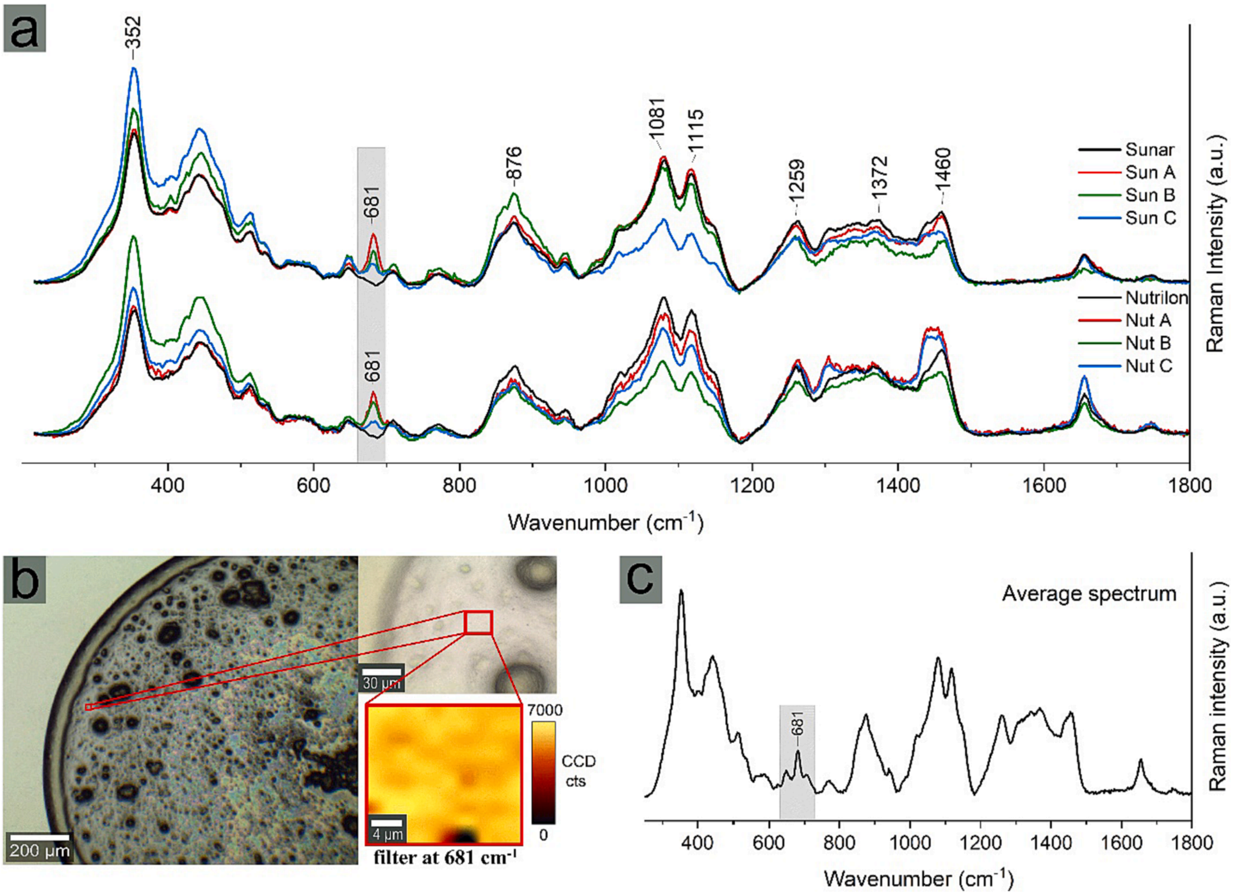

Fig. 6. DCDR measurement of infant formula blended with melamine. a) Set of spectra normalised to the overall intensity of Sun and Nut, the spectral window (in grey) shows the melamine breathing vibration. Spectra demonstrate that the intensity of the featured spectral band decreases with the concentration of melamine in milk. b) The white light image of the Nut B (20x) dried pattern of intentionally contaminated (blended) infant formula with a detailed indicated area for spectral mapping and an indication of melamine distribution throughout the scanned area using a spectral filter for the spectral band of melamine breathing vibration at 681 cm^{-1}, and c) an average Raman spectrum obtained from scanned area.

presence of melamine thanks to its breathing vibration. We could recognise an evident spectral band at 681 cm^{-1} for each tested melamine concentration for both formulas. Comparing the position of the spectral band for the breathing vibration of melamine, we observed a slight shift to higher wavenumbers for the melamine-contaminated samples. It agrees with the previously discussed shifts for melamine breathing vibration where melamine molecule interacts by hydrogen bonding. Fig. 6a demonstrates that the intensity of the featured spectral band decreased with the concentration of melamine in milk. Considering the drying-induced separation of milk solution constituents, we assume that melamine has a significant susceptibility to substances present in the inner thin film, namely lactose and other carbohydrates, which agrees with the results of the tested simple melamine-blended reaction models.

Moreover, we employed Raman spectral mapping to investigate melamine distribution in the thin spread layer in the pattern. We focused on a small area of the pattern from the Nut B (20 ×) sample and accumulated Raman spectra (Fig. 6b and Fig. 6c). To observe the presence of melamine, we used a filter for the spectral band for breathing vibration at 681 cm^{-1}. The spectral map and the average spectrum calculated from all measured spectra (Fig. 6b and Fig. 6c) indicated homogeneous melamine distribution throughout the scanned area of the pattern, similar to the Lac_Mel mixture. If the amount of melamine in the contaminated sample continued to decrease, its distribution in the central part of the pattern was no longer homogeneous but only partial in some selected places.

4. Conclusions

We utilised the DCDR spectroscopy to readily determine the susceptibility of the melamine compound to main components of milk infant formula, such as lactose and lipids (specifically 1,2-dioleoyl-*sn*-glycero-3-phosphocholine (DOPC), and 1,2-dioleoyl-*sn*-glycero-3-phosphoethanolamine (DOPE)) and its subsequent identification from the dried pattern of intentionally contaminated milk infant formula. For this purpose, two kinds of powder infant formula were used and tested. Firstly, DCDR spectroscopy was applied to pure melamine and lactose solutions and to pure liposomal suspensions to obtain reference spectra. Simple melamine-blended model reactions were then investigated where melamine was added to lactose, DOPC, and DOPE. We observed and compared the formed dried patterns of pure and blended samples together with their Raman spectra. Lactose was found to be the most potent reaction partner for melamine, where a significant difference in dried pattern and Raman spectra between pure and melamine-blended lactose was revealed. Moreover, lactose lost its crystalline character after mixing with melamine, as seen from the dried pattern and Raman spectra. Melamine presence was identified thanks to the spectral band corresponding to its breathing vibration. For melamine-blended lipid mixtures, Raman spectra revealed spatial separation of melamine and lipid molecules, where lipids tend to preconcentrate into a ring while melamine was present in the central part of the pattern. Only a slight reaction potential was observed between melamine and DOPE, which we believe is due to the possible hydrogen bonding of the lipid head amino group and three amino groups of melamine.

To test the affinity of melamine to the main milk constituents in the real sample, we employed the DCDR approach to pure milk solution and diluted melamine-contaminated one. When completely evaporated, the main milk constituents' spatial distribution and separation were observed for pure infant formula solution. The formed dried deposit consists of a visible edge ring structure and a thin film in the central part of the ring. The separation of the constituents was further analysed using the Raman spectra obtained from the ring edge and the central part of the dried deposit. It was concluded that the ring edge was composed mainly of lipid molecules, and the thin film in the central part was composed mainly of carbohydrates, specifically lactose. Even with slightly different compositions of the two kinds of purchased milk, the exhibited separation was the same. Achieving the optimal concentration of the milk solution played a key role in the drying-induced separation process. The dried pattern showed no evidence of constituents' separation at the concentration corresponding to the one dose of infant formula.

Then, melamine powder was intentionally mixed with infant formula powder in three different concentrations. Formed dried patterns from blended formulas were indistinguishable from the pure infant formula dried patterns. The DCDR approach applied to the blended formula revealed that the melamine compound was present only in the thin film in the central part of the dried patterns. From the previously mentioned separation of milk constituents, we assumed that melamine has a higher susceptibility to substances present in the inner thin layer, which is composed mainly of carbohydrates, namely lactose. Therefore, melamine retains its high reaction potential to lactose rather than lipid molecules, which are also present in the milk infant formula. These findings represent a promising utilisation of the DCDR approach as the efficient method for detecting and identifying compounds (contaminants) based on the spatial distribution throughout the dried deposit pattern and thanks to the reaction potential of the compound to the main constituents of solution of interest. Further progress could be achieved by optimising the characteristics of the used substrates where the great potential is represented by e.g. nanostructured surfaces with designed/tailored hydrophobicity.

CRediT authorship contribution statement

Alžbeta Kuižová: Writing – original draft, Visualization, Investigation, Formal analysis, Data curation, Conceptualization. **Eva Kočišová:** Writing – review & editing, Supervision, Project administration, Investigation, Conceptualization.

Declaration of competing interest

The authors declare that they have no known competing financial interests or personal relationships that could have appeared to influence the work reported in this paper.

Data availability

Data will be made available on request.

Acknowledgement

This work was supported by the Charles University Research Centre program UNCE/SCI/010 and SVV-2023-260716.

References

[1] S. Członka, A. Strąkowska, K. Strzelec, A. Kairytė, A. Kremensas, Melamine, silica, and ionic liquid as a novel flame retardant for rigid polyurethane foams with enhanced flame retardancy and mechanical properties, Polym. Test. 87 (2020) 106511, https://doi.org/10.1016/j.polymertesting.2020.106511.

[2] A. Dorieh, M. Farajollah Pour, S. Ghafari Movahed, A. Pizzi, P. Pouresmaeel Selakjani, M. Valizadeh Kiamahalleh, H. Hatefnia, M.H. Shahavi, R. Aghaei, A review of recent progress in melamine-formaldehyde resin based nanocomposites as coating materials, Prog. Org. Coat. 165 (2022) 106768, https://doi.org/10.1016/j.porgcoat.2022.106768.

[3] A.S. Giroto, R.H.S. Garcia, L.A. Colnago, A. Klamczynski, G.M. Glenn, C. Ribeiro, Role of urea and melamine as synergic co-plasticisers for starch composites for fertiliser application, Int. J. Biol. Macromol. 144 (2020) 143–150, https://doi.org/10.1016/j.ijbiomac.2019.12.094.

[4] R. Clark, Melamine crystalluria in sheep, J. S. Afr. Vet. Assoc. 37 (3) (1966) 349–351, 10520/AJA00382809_3500.

[5] H. Ogasawara, K. Imaida, H. Ishiwata, K. Toyoda, T. Kawanishi, C. Uneyama, S. Hayashi, M. Takahashi, Y. Hayashi, Urinary bladder carcinogenesis induced by melamine in F344 male rats: correlation between carcinogenicity and urolith formation, Carcinogenesis 16 (11) (1995) 2773–2777, https://doi.org/10.1093/carcin/16.11.2773.

[6] C.A. Brown, K.-S. Jeong, R.H. Poppenga, B. Puschner, D.M. Miller, A.E. Ellis, K.-I. Kang, S. Sum, A.M. Cistola, S.A. Brown, Outbreaks of renal failure associated with melamine and cyanuric acid in dogs and cats in 2004 and 2007, J. Vet. Diagn. Invest. 19 (5) (2007) 525–531, https://doi.org/10.1177/104063870701900510.

[7] J.R. Ingelfinger, Melamine and the global implications of food contamination, N. Engl. J. Med. 359 (26) (2008) 2745–2748, https://doi.org/10.1056/NEJMp0808410.

[8] R.L. Dobson, S. Motlagh, M. Quijano, R.T. Cambron, T.R. Baker, A.M. Pullen, B. T. Regg, A.S. Bigalow-Kern, T. Vennard, A. Fix, R. Reimschuessel, G. Overmann, Y. Shan, G.P. Daston, Identification and characterisation of toxicity of contaminants in pet food leading to an outbreak of renal toxicity in cats and dogs, Toxicol. Sci. 106 (1) (2008) 251–262, https://doi.org/10.1093/toxsci/kfn160.

[9] W. Liu, M.A. Cohenford, L. Frost, C. Seneviratne, J.A. Dain, Non-enzymatic glycation of melamine with sugars and sugar like compounds, Bioorg. Chem. 46 (2013) 1–9, https://doi.org/10.1016/j.bioorg.2012.08.004.

[10] J. Ma, X. Peng, K.-W. Cheng, R. Kong, I.K. Chu, F. Chen, M. Wang, Effects of melamine on the maillard reaction between lactose and phenylalanine, Food Chem. 119 (1) (2010) 1–6, https://doi.org/10.1016/j.foodchem.2009.07.007.

[11] B.J. Yakes, M.M. Bergana, P.F. Scholl, M.M. Mossoba, S.R. Karunathilaka, L. K. Ackerman, J.D. Holton, B. Gao, J.C. Moore, Effects of wet-blending on detection of melamine in spray-dried lactose, J. Agric. Food Chem. 65 (28) (2017) 5789–5798, https://doi.org/10.1021/acs.jafc.7b00834.

[12] A. Kuižová, E. Kočišová, Drop coating deposition Raman (DCDR) spectroscopy of biologically important molecules, J. Raman Spectrosc. 54 (7) (2023) 694–705, https://doi.org/10.1002/jrs.6524.

[13] E. Kočišová, M. Procházka, Drop-coating deposition Raman spectroscopy of porphyrins, J. Raman Spectrosc. 46 (2) (2015) 280–282, https://doi.org/10.1002/jrs.4637.

[14] E. Kočišová, M. Procházka, Drop coating deposition Raman spectroscopy of dipicolinic acid, J. Raman Spectrosc. 49 (12) (2018) 2050–2052, https://doi.org/10.1002/jrs.5493.

[15] E. Kočišová, M. Procházka, Drop-coating deposition Raman spectroscopy of liposomes, J. Raman Spectrosc. 42 (8) (2011) 1606–1610, https://doi.org/10.1002/jrs.2915.

[16] C. Ortiz, D. Zhang, Y. Xie, V.J. Davisson, D. Ben-Amotz, Identification of insulin variants using Raman spectroscopy, Anal. Biochem. 332 (2) (2004) 245–252, https://doi.org/10.1016/j.ab.2004.06.013.

[17] D. Zhang, Y. Xie, M.F. Mrozek, C. Ortiz, V.J. Davisson, D. Ben-Amotz, Raman detection of proteomic analytes, Anal. Chem. 75 (21) (2003) 5703–5709, https://doi.org/10.1021/ac0345087.

[18] J. Filik, N. Stone, Drop coating deposition Raman spectroscopy of protein mixtures, Analyst 132 (6) (2007) 544–550, https://doi.org/10.1039/B701541K.

[19] J. Filik, N. Stone, Analysis of human tear fluid by Raman spectroscopy, Anal. Chim. Acta 616 (2) (2008) 177–184, https://doi.org/10.1016/j.aca.2008.04.036.

[20] J. Filik, N. Stone, Investigation into the protein composition of human tear fluid using centrifugal filters and drop coating deposition Raman spectroscopy, J. Raman Spectrosc. 40 (2) (2009) 218–224, https://doi.org/10.1002/jrs.2113.

[21] J. Goubeau, E.L. Jahn, A. Kreutzberger, C. Grundmann, Triazines. X. The Infrared and Raman Spectra of 1,3,5-triazine, J. Phys. Chem. 58 (12) (1954) 1078–1081, https://doi.org/10.1021/j150522a008.

[22] N.E. Mircescu, M. Oltean, V. Chiş, N. Leopold, FTIR, FT-raman, SERS and DFT study on melamine, Vib. Spectrosc 62 (2012) 165–171, https://doi.org/10.1016/j.vibspec.2012.04.008.

[23] W. Sawodny, K. Niedenzu, J.W. Dawson, Vibrational Spectrum and Assignment of Normal Vibrations of Melamine, J. Chem. Phys. 45 (8) (1966) 3155–3156, https://doi.org/10.1063/1.1728077.

[24] A. Kuižová, M. Přikryl, M. Procházka, E. Kočišová, Drop coating deposition raman (DCDR) spectroscopy of contaminants, Spectrochim. Acta A Mol. Biomol. Spectrosc. 262 (2021) 120109, https://doi.org/10.1016/j.saa.2021.120109.

[25] R. MacDonald, R. Macdonald, B. Menco, K. Takeshita, N. Subbarao, L.-R. Hu, Small-volume extrusion apparatus for preparation of large, unilamellar vesicles, BBA 1061 (1991) 297–303, https://doi.org/10.1016/0005-2736(91)90295-J.

[26] J. Palacký, P. Mojzeš, J. Bok, SVD-based method for intensity normalisation, background correction and solvent subtraction in Raman spectroscopy exploiting the properties of water stretching vibrations, J. Raman Spectrosc. 42 (7) (2011) 1528–1539, https://doi.org/10.1002/jrs.2896.

[27] B. Froschauer, M. Weil, Melaminium hydrogen malonate, Acta Crystallographica Section E: Crystallographic Commun. 68 (8) (2012) o2553–o2554, https://doi.org/10.1107/S1600536812033016.

[28] H. Su, Y.-K. Lv, Y.-L. Feng, Bis(melaminium) tartrate dihydrate, Acta Crystallographica Section E: Crystallographic Commun. 65 (4) (2009) o933, https://doi.org/10.1107/S1600536809011143.

[29] L. Vella-Zarb, D. Braga, A. Guy Orpen, U. Baisch, The influence of hydrogen bonding on the planar arrangement of melamine in crystal structures of its solvates, co-crystals and salts, CrstEngComm 16 (35) (2014) 8147–8159, https://doi.org/10.1039/C4CE00748D.

[30] G.J. Perpétuo, J. Janczak, Melaminium acetate acetic acid solvate monohydrate, Acta Crystallographica Section C: Struct. Chem. 58 (2) (2002) o112–o114, https://doi.org/10.1107/S0108270101021631.

[31] G.J. Perpétuo, J. Janczak, Supramolecular architectures in crystals of melamine and aromatic carboxylic acids, J. Mol. Struct. 891 (1) (2008) 429–436, https://doi.org/10.1016/j.molstruc.2008.04.032.

[32] P.J. Larkin, M.P. Makowski, N.B. Colthup, The form of the normal modes of s-triazine: infrared and Raman spectral analysis and ab initio force field calculations, Spectrochim. Acta A Mol. Biomol. Spectrosc. 55 (5) (1999) 1011–1020, https://doi.org/10.1016/S1386-1425(98)00244-3.

[33] M.K. Marchewka, Infrared and Raman spectra of melaminium chloride hemihydrate, Mater. Sci. Eng. B 95 (3) (2002) 214–221, https://doi.org/10.1016/S0921-5107(02)00235-0.

[34] C.Y. Panicker, H.T. Varghese, A. John, D. Philip, H.I.S. Nogueira, Vibrational spectra of melamine diborate, $C_3N_6H_62H_3BO_3$, Spectrochim. Acta A Mol. Biomol. Spectrosc. 58 (8) (2002) 1545–1551, https://doi.org/10.1016/S1386-1425(01)00608-4.

[35] B. Sigdel Regmi, A. Apblett, Spectroscopic characterisation, thermal, and flame retarding properties of melaminium cyanoacetate monohydrate, Polym. Bull. (2022), https://doi.org/10.1007/s00289-022-04594-4.

[36] Y. Gao, N. Yang, T. You, C. Zhang, P. Yin, Superhydrophobic “wash free” 3D nanoneedle array for rapid, recyclable and sensitive SERS sensing in real environment, Sens. Actuators B 267 (2018) 129–135, https://doi.org/10.1016/j.snb.2018.04.025.

[37] K. Ge, Q. Wu, Y. Li, Y. Gu, High and stable surface-enhanced Raman spectroscopy activity of h-BN nanosheet/Au_1Ag_3 nanoalloy hybrid membrane for melamine determination, Spectrochim. Acta A Mol. Biomol. Spectrosc. 271 (2022) 120952, https://doi.org/10.1016/j.saa.2022.120952.

[38] C. Huang, S. Jiang, F. Kou, M. Guo, S. Li, G. Yu, B. Zheng, F. Xie, C. Zhang, H. Yu, J. Wang, Development of jellyfish-like ZNO@AG substrate for sensitive SERS detection of melamine in milk, Appl. Surf. Sci. 600 (2022) 154153, https://doi.org/10.1016/j.apsusc.2022.154153.

[39] F. Fan, P. Xiang, L. Zhao, Vibrational spectra analysis of amorphous lactose in structural transformation: water/temperature plasticisation, crystal formation, and molecular mobility, Food Chem. 341 (2021) 128215, https://doi.org/10.1016/j.foodchem.2020.128215.

[40] B.M. Murphy, S.W. Prescott, I. Larson, Measurement of lactose crystallinity using Raman spectroscopy, J. Pharm. Biomed. Anal. 38 (1) (2005) 186–190, https://doi.org/10.1016/j.jpba.2004.12.013.

[41] H. Susi, J.S. Ard, Laser-raman spectra of lactose, Carbohydr. Res. 37 (2) (1974) 351–354, https://doi.org/10.1016/S0008-6215(00)82924-9.

[42] M.J. Márquez, A.B. Brizuela, L. Davies, S.A. Brandán, Spectroscopic and structural studies on lactose species in aqueous solution combining the HATR and Raman spectra with SCRF calculations, Carbohydr. Res. 407 (2015) 34–41, https://doi.org/10.1016/j.carres.2015.01.019.

[43] P.H. Rodrigues Júnior, K. de Sá Oliveira, C.E.R.D. Almeida, L.F.C. De Oliveira, R. Stephani, M.D.S. Pinto, A.F.D. Carvalho, Í.T. Perrone, FT-raman and chemometric tools for rapid determination of quality parameters in milk powder: classification of samples for the presence of lactose and fraud detection by addition of maltodextrin, Food Chem. 196 (2016) 584–588, https://doi.org/10.1016/j.foodchem.2015.09.055.

[44] E. Wiercigroch, E. Szafraniec, K. Czamara, M.Z. Pacia, K. Majzner, K. Kochan, A. Kaczor, M. Baranska, K. Malek, Raman and infrared spectroscopy of carbohydrates: a review, Spectrochim. Acta A Mol. Biomol. Spectrosc. 185 (2017) 317–335, https://doi.org/10.1016/j.saa.2017.05.045.

[45] K. Czamara, K. Majzner, M.Z. Pacia, K. Kochan, A. Kaczor, M. Baranska, Raman spectroscopy of lipids: a review, J. Raman Spectrosc. 46 (1) (2015) 4–20, https://doi.org/10.1002/jrs.4607.

[46] H. Sadeghi-Jorabchi, P.J. Hendra, R.H. Wilson, P.S. Belton, Determination of the total unsaturation in oils and margarines by fourier transform Raman spectroscopy, J. Am. Oil Chemists’ Soc. 67 (8) (1990) 483–486, https://doi.org/10.1007/BF02540752.

[47] R.M. El-Abassy, P.J. Eravuchira, P. Donfack, B. von der Kammer, A. Materny, Fast determination of milk fat content using Raman spectroscopy, Vib. Spectrosc 56 (1) (2011) 3–8, https://doi.org/10.1016/j.vibspec.2010.07.001.

[48] E. Kočišová, M. Petr, H. Šípová, O. Kylián, M. Procházka, Drop coating deposition of a liposome suspension on surfaces with different wettabilities: “coffee ring” formation and suspension preconcentration, PCCP 19 (1) (2017) 388–393, https://doi.org/10.1039/c6cp07606h.

[49] A. Kuižová, A. Kuzminova, O. Kylián, E. Kočišová, Nanostructured plasma polymerized fluorocarbon films for drop coating deposition raman spectroscopy (DCDRS) of liposomes, Polymers 13 (22) (2021), https://doi.org/10.3390/polym13224023.

[50] M. Dudek, G. Zajac, E. Szafraniec, E. Wiercigroch, S. Tott, K. Malek, A. Kaczor, M. Baranska, Raman optical activity and Raman spectroscopy of carbohydrates in solution, Spectrochim. Acta A Mol. Biomol. Spectrosc. 206 (2019) 597–612, https://doi.org/10.1016/j.saa.2018.08.017.